Doctoral School in Environmental Engineering

On the role of mixing in controlling transport of aqueous species in heterogeneous formations

Francesca Boso

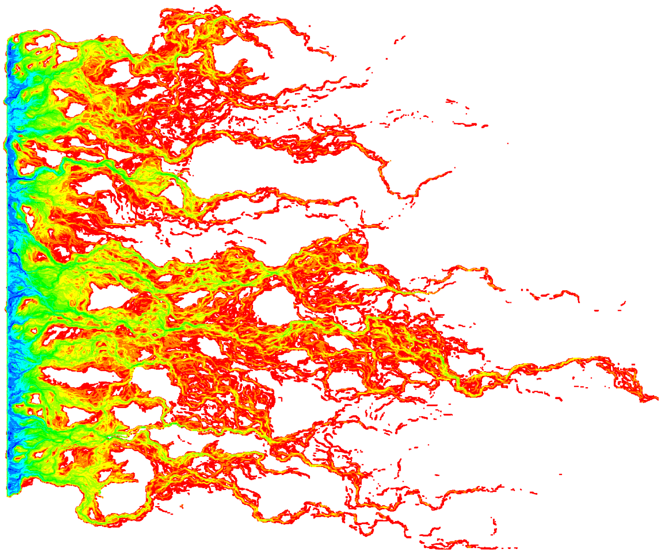

UNIVERSITÀ DEGLI STUDI DI TRENTO

Dipartimento di Ingegneria Civile
e Ambientale

Based on the Doctoral Thesis in Environmental Engineering (XXIV Cycle) defended in April 2012 at the Faculty of Engineering, University of Trento, Italy

On the role of mixing in controlling transport of aqueous species in heterogeneous formations, PhD Thesis

Supervisor: Prof. A. Bellin

Abstract

The fate of reactive solutes in groundwater is largely determined by mixing, since dilution and reactions are controlled by mixing rates. By mixing we refer to the overlap of solute bodies with a different composition, which makes possible the encounter between reacting molecules. Therefore the quantification of mixing has an important role in contamination and risk assessment and remediation technology, when they rely on processes of natural attenuation, biodegradation or chemical delivery. As porous formations are ubiquitously heterogeneous, and heterogeneity features, besides being deterministically unknown, belong to a hierarchy of scales, the description of transport processes has to deal with two main issues: epistemic uncertainty and reference scale. While the heterogeneous nature of porous media interferes with physical and chemical processes (which are inherently related to the quantification of mixing and mixing-controlled processes), the choice of the reference scale is related to the means of modeling the phenomena.

In order to have an accurate representation of mixing at the continuum scale, we develop a few numerical tools, all belonging to the Lagrangian framework, and compare them with classic Eulerian and Eulerian-Lagrangian schemes. Typical transport scenarios are characterized by highly fingered plumes and sharp fringes, and pose several numerical problems (e.g. artificial diffusion and spurious oscillations). In particular, artificial diffusion can in some cases overcome the actual local dispersion, thereby possibly determining gross overestimations of reaction rates. Our numerical tests provide a set of guidelines for a conscious choice of the numerical scheme according to the objectives of the investigation and to the heterogeneity level, highlighting the drawbacks of the numerical schemes on both the evaluation of dilution and of the overall effect of reactions.

Under the assumption of complete mixing at the Darcy scale, we model both instantaneous and kinetically-controlled reactive transport on synthetic bi-dimensional hydraulic conductivity fields in order to investigate the complex interplay among velocity non-uniformities, local dispersion and reaction rates at increasing levels of physical heterogeneity. We also compare the effects of different local dispersion models and injection modes (uniform vs non-uniform), still analyzing the results on a single-realization basis. Realizations share the same log-conductivity structure ($Y = \ln K$, where K is the hydraulic conductivity) but are characterized by variances ranging from low ($\sigma_Y^2 = 0.2$) to high ($\sigma_Y^2 = 10$).

Resorting to single-realization analysis is uncommon in the literature, unless when ergodicity conditions are fulfilled. On the other hand, ensemble analysis is insensitive to local features and does not often offer a reliable representation of actual field phenomena, especially in non-ergodic conditions. Hence single-realization scenarios

can be used for understanding the key processes and their interaction, or for grasping aggregated information on the whole solute body behavior.
Under simplified conditions, that is, limiting the investigation to low heterogeneity fields, these numerical results are compared to simplified Lagrangian semianalytical relations aiming at reproducing plume-averaged quantities. This Lagrangian theory provides relevant information relying on a limited amount of information, i.e. low-order geostatistical properties of the formation, aquifer's geometry, reactive parameters and problem forcings (e.g. initial and boundary conditions for the flow field and the concentration of the involved species). The match between empirical and theoretical global moments is very good in all tested conditions (two different Péclet numbers, a few heterogeneity levels up to $\sigma_Y^2 = 2$ and three different source sizes), and also Beta Cumulative Frequency Distributions (CFDs) with shape parameters obtained by substituting the theoretical global moments compare well with the numerical CFDs. As expected, coherent estimates of peak concentration are not equally good, because of an inherently different nature of this quantity as opposed to plume-scale concentration moments.
The a-priori information expressed by statistical analysis both at the global scale and at the local scale for a conservative tracer z can be transferred to reactive species in case of very fast kinetics. Given this useful property of equilibrium reactions, we develop explicit semianalytical relations for the moments and the probability distribution functions of the concentration of chemical species reacting according to a bimolecular equilibrium homogeneous reaction. We assume that the conservative tracer probability distribution function, both at the local scale and at the global scale, can be modeled with a Beta distribution, fully characterized by the mean and the variance of z. Rigorous numerical testing on highly heterogeneous velocity fields confirms that this assumption holds. A few illustrative cases shed some light on the role of the reaction on the time evolution of (local and global) concentration for the different reactive species, and on the different quality of information contained in local statistics as opposed to global statistics. The Beta distribution is a powerful predicting tool for the space and time evolution of passive concentration and, by extension, also for reactive species in particular chemical conditions. Analytical procedures are needed for predicting the z moments, as for example the Lagrangian ones used in the present work, which are limited to weakly heterogeneous formations.
Finally we explore, analytically and numerically, the upscaling from the pore scale to the Darcy scale. Via multiple scale analysis we identify a homogenizability region, in terms of the dimensionless numbers regulating a multicomponent precipitation/dissolution reactive problem, where Darcy-scale (upscaled) transport equations can be used, regardless of sub-Darcy scale inhomogeneities.

Acknowledgements

First I'd like to thank prof. Alberto Bellin, for sharing his experience and for his constant and patient support over three long years. I'd like to thank also prof. Aldo Fiori, for his generous help and for going through most of my thesis, prof. Daniel Tartakovsky, for the weeks spent in San Diego and the months to come, and prof. Ilenia Battiato, for her contagious enthusiasm. I'm grateful I had the opportunity to learn from them. Thanks also to Laura Martuscelli for her precious work.

Un grazie particolare a Ale, Lorenzo, Oscar e Vale, per innumerevoli ragioni che non possono stare in qualche riga. Grazie per aver condiviso un pezzo di strada con me.

Grazie al gruppo pranzo per i sempre interessanti discorsi sui massimi sistemi in Skype come a tavola, ai miei roommates per la sopportazione (in particolare a Bruno, per avermi risparmiato le ore di esercitazione), e alle coinquiline del superattico in Via Suffragio nr 13 per la comprensione. Grazie anche ai miei amici, cittadini e valligiani, per aver perdonato le lunghe parentesi di asocialità.

Infine grazie alla mia famiglia, per essere quello che è.

Trento, February 2012

Contents

List of Figures

List of Tables

Chapter 1

Introduction

As assessed by the U.N. Millennium Development Goals to be achieved before 2015, the quality of water resources and the equitable access to clean drinking water and sanitation are among the human rights which require the utmost attention. Therefore reliable and fast procedures of risk assessment, and localized and predictable interventions of remediation (i.e. natural attenuation and chemical delivery) are needed. Unfortunately, understanding fate and transport of contaminants in groundwater is a heavily complicated matter because of the complex interplay between the hydraulic and geochemical heterogeneity of the formation properties and the reaction dynamics. In nearly one century of studies in this field, a huge variety of techniques - analytical, numerical and practical - have tried to tackle these problems by facing several challenges such as site characterization, parameter definition, and modelization, mainly related to the epistemic uncertainty which pervades hydrogeology. In particular, in the last ten years a number of scientists has been focusing on mixing and its key role in controlling the fate of solutes reacting upon mixing.

In fluid systems, mixing is generally indicated as the process of stretching, chaotic deformation and expansion of a solute body; in fluid-solid settings, also the interaction of the solute with the solid phase can contribute to mixing (Ottino, 1989). Such processes are ubiquitous in nature, thus they have been studied in different fields and from different perspectives. The investigation of mixing in aquifer environments is relatively recent, as recent is the general investigation of hydrogeology as a stand-alone discipline. A longer history has the study of mixing in fluid mechanics (either oceans, lakes, natural streams or atmospheric physics), as well as in chemical engineering, especially related to combustion and to industrial processes. These early works approached for the first time the multiple complexities posed by uncertain or chaotic setting where mixing takes place, either in turbulent flows or in geometrically complex/irregular or unknown environments (Csanady, 1973). More recently mixing was addressed also by biomedical research, for investigating transport processes in biological fluids and through biological tissues.

Clearly each single discipline tackles the problem from different perspectives, and aims at different objectives. For example, fluid mechanics has to deal with temporal random velocity fluctuations, whereas chemical engineering generally aims at designing geometric reactors and devices which promote mixing, thus accelerating reactions or making combustion more efficient. Anyway, similar tools have often been developed, with significant superposition and exchange. In fact in all cases analyses are usually performed on a stochastic basis due to the uncertainty which concerns the settings where mixing takes place (Koochesfahani and Dimotakis, 1986; Ottino, 1989; Pope, 2000).

By mixing, we refer here to the processes which cause the overlap of solute bodies moving in porous formations, and therefore the encounter among chemical species and possibily their chemical interaction. Mixing may be due to different mechanisms: (1) Dilution due to the action of local scale dispersion; (2) Different mobility of the involved chemical species; (3) Mass transfer kinetics. In case of non-sorbing compounds, that is, solute uptake by the solid matrix, mixing shows up as the increase of the plume volume as an effect of dilution solely. The main distinction to be done is between mixing and spreading (among others, Cao and Kitanidis, 1998; Cirpka and Kitanidis, 2000b; Dentz and Carrera, 2007), since mixing refers to the dilution of the plume itself, driven by diffusive/dispersive mechanisms and spreading refers to the advective deformation experienced by the plume while exploring the porous medium.

1.1 Framework

The solution of the transport problem at the pore scale requires the solution of conservation equations for both the fluid mass and momentum (e.g. Bear, 1972), and the solute mass (e.g. Bear and Bachmat, 1990). In the following we state the complete differential system in case of stationary flow, to be completed by correspondent initial conditions and boundary conditions along solid/liquid interfaces in a definite pore geometry:

$$\mu \nabla^2 \tilde{\mathbf{v}}(\mathbf{x}) = \nabla \tilde{p}(\mathbf{x}) - \rho_f \mathbf{g} \tag{1.1a}$$

$$\nabla \cdot \tilde{\mathbf{v}}(\mathbf{x}) = 0 \tag{1.1b}$$

$$\frac{\partial \tilde{c}_i(\mathbf{x},t)}{\partial t} + \tilde{\mathbf{v}}(\mathbf{x}) \cdot \nabla \tilde{c}_i(\mathbf{x},t) = \nabla \cdot \left(\mathbf{D}_{m,i} \nabla \tilde{c}_i(\mathbf{x},t)\right) + \tilde{r}_i(\tilde{\mathbf{c}}) \tag{1.1c}$$

Eq. 1.1a represents the Stokes conservation equation for the momentum, where $\tilde{\mathbf{v}}(\mathbf{x})$ is the interstitial velocity, $\tilde{p}(\mathbf{x},t)$ is the fluid pressure, $\mathbf{g}$ is the gravity acceleration and μ and ρ_f represent the fluid viscosity and the fluid density, respectively, which are regarded as constant and uniform. Eq. 1.1b states the fluid mass conservation in case of incompressible fluid. Finally Eq. 1.1c represents the solute mass conservation for species i, where the time evolution of the small scale concentration $\tilde{c}_i(\mathbf{x},t)$ varies as a result of the non-uniform velocity field $\tilde{\mathbf{v}}(\mathbf{x})$, of molecular diffusion $\mathbf{D}_{m,i}$ and possibly of reactions $\tilde{r}(\tilde{\mathbf{c}})$ which complete the solute mass balance of the equation and couple Advection-Diffusion-Reaction Equations (Eq. 1.1c) for species i reacting with each other. These reaction terms do not represent actual molecular mechanisms which do occur at an even smaller scale. Generally any coupling between the solute mass conservation and the fluid flow is neglected, thus ignoring the influence of concentration on fluid density. Clearly, such a system is numerically cumbersome and above all, generally indefinite because the pore geometry cannot be deterministically known.

By volume averaging (Whitaker, 1999), all the conservation laws can be referred to a Reference Elementary Volume (REV), whose effective hydraulic properties are assumed as homogeneous over the REV:

$$\mathbf{u}(\mathbf{x}) = -\frac{\mathbf{K}}{\phi}\nabla H(\mathbf{x}), \tag{1.2a}$$

$$\nabla \cdot (\mathbf{K}\nabla H) = 0, \tag{1.2b}$$

$$\frac{\partial c_i}{\partial t} + \mathbf{u}(\mathbf{x},t) \cdot \nabla c_i(\mathbf{x},t) = \nabla \cdot (\mathbf{D}\nabla c_i(\mathbf{x},t)) + \frac{r_i(\mathbf{c})}{\phi}. \tag{1.2c}$$

The flow equations 1.2a and 1.2b are written here for the case of stationary flow. The Darcy velocity $\mathbf{u}(\mathbf{x})$ is related through Darcy's law (Eq. 1.2a) to the hydraulic conductivity tensor $\mathbf{K}(\mathbf{x})$, which depends on the permeability of the soil matter $\mathsf{k}(\mathbf{x})$ and on the hydraulic properties of the fluid (i.e. density and viscosity). Hence $\mathbf{K}$ epitomizes the properties of both the porous medium and the fluid. $H(\mathbf{x}) = \frac{p(\mathbf{x})}{\rho_f g} + z_g$ is the piezometric head, which has a pressure component $p(\mathbf{x})$, averaged at the continuum scale, and a topographic component z_g.

Also the Advection Dispersion Reaction Equation (Eq. 1.2c) refers this time to the continuum scale. Concentration $c_i(\mathbf{x}, t)$ of species i is regarded as homogeneous over the REV, thus implying a 'well-mixed REV' assumption. In fact reactions rely on this concentration value for estimating the overall reaction rate, which is generally concentration dependent. A large part of the studies assumes complete mixing at the pore scale (Dentz et al., 2011), simply paying adequate attention to the choice of the effective parameters for dispersion $\mathbf{D}$ and reaction r in Eq. 1.2c. $\mathbf{D}$ and r are generally introduced by closure assumptions during the upscaling process. In general, this is acceptable in case of homogeneous reactions (Battiato *et al.*, 2009; Meile and Tuncay, 2006) and provided that pore-scale diffusion is fast as compared to reaction timescales within the pore (Battiato *et al.*, 2009; Dentz *et al.*, 2011; Kechagia *et al.*, 2002; Tartakovsky, Tartakovsky, and Scheibe, 2009). Otherwise, incomplete mixing at the pore scale can cause segregation effects, which affect the movement of the contaminants and the overall reaction rates, especially when reactions are fast with respect to pore-scale dilution dynamics (Tartakovsky, Tartakovsky, and Scheibe, 2009). These segregation effects could result in pseudokinetic behavior (Binning and Celia, 2008), with kinetic reaction rates emerging from the upscaling of equilibrium pore-scale systems. As a result, when well-mixed pore-scale volumes cannot be guaranteed, attaining to pore-scale modeling or at least resorting to hybrid (Battiato *et al.*, 2011; Scheibe *et al.*, 2008; Steefel, DePaolo, and Lichtner, 2005; Tartakovsky *et al.*, 2008) or stochastic models (Tartakovsky, 2010; Tartakovsky, Tartakovsky, and Meakin, 2008) is recommended, although this may be often impractical. Hot spots of mixing, in fact, are necessarily related to the unknown spatial distribution of hydraulic properties (Cao and Kitanidis, 1998; Werth, Cirpka, and Grathwohl, 2006; Willingham *et al.*, 2010) and are thus not deterministically located in space.

Attention has to be paid to the choice of the effective values and mathematical shape of both $\mathbf{D}$ and r, which need to compensate for the loss of information due to volume averaging. $\mathbf{D}$ is the effective, hydrodynamic dispersion tensor which takes into account the molecular diffusion and the sub-Darcy scale velocity non-uniformities (Aris, 1956; Bear, 1972; Brenner, 1980; Brenner and Adler, 1980; Taylor, 1953). Assuming a Fickian closure for the dispersive term imposes a linear dependence between the dispersive flux and the concentration gradient through D

coefficients. Both experimental and field measurements have proven that this is not always valid, because of a time delay in the response of solute fluxes to the generation of concentration gradients (Dentz and Tartakovsky, 2006). As a result also non-local transport models have been developed, with the aim of reproducing non-Fickian features of transport. Non-local formalism (Kubo, Toda, and Hashitsume, 1991) may apply either to parameters (see e.g. Dagan, 1988; Edwards, Shapiro, and Brenner, 1993; Gelhar, Welty, and Rehefeldt, 1992; Han, Bhakta, and Carbonell, 1985; Kechagia *et al.*, 2002; Koch and Brady, 1987; Li, Peters, and Celia, 2006; Lichtner, 1993; Meile and Tuncay, 2006; Porta, Riva, and Guadagnini, 2012; Quintard and Whitaker, 1994) or to processes (among others, Carrera *et al.*, 1998; Ginn, 2001; Haggerty and Gorelick, 1995; Haggerty, McKenna, and Meigs, 2000; Harvey and Gorelick, 1995; Willmann, Carrera, and Sanchez-Vila, 2008; Willmann *et al.*, 2010, for the integro-differential models; Berkowitz and Scher, 1998; Berkowitz *et al.*, 2006; Cortis *et al.*, 2004; Dentz *et al.*, 2004; Metzler and Klafter, 2000; Montroll and Weiss, 1965; Scher and Lax, 1973, for the Continuous Time Random Walk Method; Benson, Wheatcraft, and Meerschaert, 2000; Berkowitz *et al.*, 2006; Meerschaert, Benson, and Baumer, 1999, for the fractional ADE methods).

Also reaction terms have to be made effective in order to express mass conservation over the REV (e.g. Battiato and Tartakovsky, 2011; Battiato *et al.*, 2009; Edwards, Shapiro, and Brenner, 1993; Kechagia *et al.*, 2002; Lichtner, 1993; Meile and Tuncay, 2006; Quintard and Whitaker, 1994; Whitaker, 1999; Wood, 2009).

The hydrodynamic dispersion is the primary driving force of mixing processes, since it determines the overlap of waters with different composition/concentration over the same small volume. Actual mixing processes occur at an even smaller scale, and are physically due to the action of molecular diffusion solely. By a process of scale cascade, what occurs at the molecular scale affects transport up to the field scale. Hence there is the need to account for microscale effects in order to provide macroscale predictions (both at the continuum scale and at the largest scales of the field). Besides, the ubiquitous velocity non-uniformities (that is, spanning a hierarchy of scales) interact with molecular diffusion to enhance the overall dispersive dilution of the plume (mechanical dispersion). Hence hydrodynamic dispersion tensors take primarily into account the compound molecular diffusion (corrected for the effect of tortuosity due to the irregular setting of solute dilution), but also the main features of the pore-scale velocity field, such as the module (which is proportional to the intensity) and the direction (which determines the orientation of the tensor) of the local velocity, as well as the mean size of the pores (Bear, 1972; Delgado, 2006). The assessment of mechanical dispersion, that is, the velocity-dependent component of hydrodynamic dispersion, is strictly related to the length scale of the REV (Ham *et al.*, 2004; Olsson and Grathwohl, 2007). Moreover, depending on the case, $\mathbf{D}$ could also depend on the hydraulic properties of the fluid, as well as on its thermodynamical state (pressure and temperature), as reviewed by Delgado, 2006.

The representation of flow and transport through porous media cannot prescind from the representation of the spatial variability of the hydraulic (and geochemical) properties of the medium. Dealing with heterogeneity implies considering the interaction between mixing and spreading, since the advection-driven fingering experienced by the plume enhances dilution by amplifying the surface of the plume fringe across which local scale dispersion acts (Werth, Cirpka, and Grathwohl, 2006;

Willingham *et al.*, 2010). The continuum scale differential system senses the spatial variability of the hydraulic properties of the medium through the hydraulic conductivity field $\mathbf{K}$. Unfortunately, the deterministic knowledge of the spatial variability of $\mathbf{K}$ is not feasible, despite the progresses in direct and indirect instruments for site characterization (Hubbard and Rubin, 2000). Hence we cannot have a certain representation of the actual flow field for the aquifer of interest.
The complex and most of all unknown spatial variability of $\mathbf{K}$ and thus of $\mathbf{u}(\mathbf{x}, t)$ and $c(\mathbf{x}, t)$ prevents from having analytical solutions of the differential system (1.2), except in very simplified settings such as homogeneous or stratified formations. As a result, this kind of problems has been necessarily tackled with massive numerical simulation or stochastic means, so that the description of fate and transport of solute plumes can be carried out in an ensemble sense. Geostatistics provides the analytical means for describing the spatial variability of the hydraulic properties, referring to the spatial correlation of the log-hydraulic conductivity which lends itself to geostatistical analysis. Probabilistic tools describe the possible outcome of a transport scenario as an ensemble, that is, it reflects what would be obtained by simulating transport on a theoretically infinite number of equivalent independent realizations of the formation of interest. All these realizations share equal low-order statistics, but a different punctual distribution of the hydraulic conductivity. Approximated semianalytical solutions can be obtained in case of weak heterogeneity under the first order approximation in σ_Y^2 (Dagan, 1984, 1989), with σ_Y^2 indicating the variance of the log-conductivity $Y = \ln K$. Numerically, Monte Carlo simulations, that is, a large number of flow and transport scenarios modeled on independent equivalent realizations, can provide spatial averages which converge more or less fast towards ensemble averages. The larger the source area as compared to the integral scale of the formation (that is, moving toward ergodic conditions) and the weaker the heterogeneity level, the faster spatial averages approach ensemble values. Monte Carlo simulations can be very cumbersome and time consuming. Besides, especially when heterogeneity is strong and ergodicity is not fulfilled, the final conclusions can have little to do with actual transport scenarios in the real aquifer. As a matter of fact, the real aquifer is nothing else than one of the multiple realizations which belong to the Monte Carlo series, coherently with the inherent deterministic nature of hydrogeology (Tartakovsky, 2007).

The solution of the continuum mathematical model stated above on a deterministic hydraulic conductivity field poses several numerical challenges, namely: (1) Artificial diffusion and spurious oscillations which arise across steep fronts; (2) Nonlinear source/sink terms; (3) Spatial variability of the coefficients, with even large variations in short distances (4) Large size of the domains; (5) Coupling among different partial differential equations expressing mass conservation for different species interacting with each other (Quarteroni and Valli, 1994). The choice of the numerical method depends on the objective of the analysis. When mixing and its accurate representation is the main concern, a numerical method free of numerical diffusion is crucial since numerical diffusion can overcome, in some cases largely, real dilution. As regards reactive transport, algebraic manipulation typically allows to reduce the number of unknowns by exploiting chemical laws among species in case of fast reactions (Rubin, 1983). Several works take advantage of this kind of procedure for investigating reactive transport in a simplified manner (Bellin, Severino, and Fiori, 2011; Cirpka, 2010; Cirpka and Valocchi, 2007; Cirpka *et al.*, 2008; De Simoni *et al.*, 2005, 2007; Luo *et al.*, 2008) or by relaxing some of the hypotheses (Sanchez-Vila, Dentz, and Donado, 2007; Sanchez-Vila *et al.*, 2010). However we usually need to include unelidible reaction terms into the equations for taking into account the slow, kinetically-controlled reactions belonging to the original reactive system.

Upscaling from the continuum scale to the macroscale is required for developing easy-to-use large-scale models, which do not provide accurate information on the local distribution of concentrations, but give practical estimates at the field scale, or estimate the solute arrivals at cross sections located downstream. A further volume averaging step (through the definition of effective regional velocity, macrodispersion and large scale reaction parameters, as proposed by the seminal work by Gelhar and Axness, 1983) has been demonstrated to provide wrong predictions. First macrodispersion models typically overestimate dilution and hence mixing and reaction rates (among others, Kapoor, Gelhar, and Miralles-Wilhelm, 1997; Kitanidis, 1988; MacQuarrie and Sudicky, 1990; Molz and Widdowson, 1988). Second, actual breakthrough curves in fact display non-Fickian characteristics such as steep fronts and long tails due to anomalous early and late arrival times, which cannot be reproduced by a macroscale Fickian model. Hence non-local models (both in time and in space) have been developed for taking into account the verified non-Markovianity of transport (see e.g. Berkowitz *et al.*, 2006; Cushman, Bennethum, and Hu, 2002; Cushman and Ginn, 1993; Neuman and Tartakovsky, 2009). Thus a multiplicity of process-upscaling methods have been proposed (Berkowitz *et al.*, 2006; Dentz *et al.*, 2011), such as a wide variety of traveltime-based methods (Carrera *et al.*, 1998; Cirpka and Kitanidis, 2000a; Ginn, 2001; Ginn, Simmons, and Wood, 1995; Haggerty and Gorelick, 1995; Haggerty, McKenna, and Meigs, 2000; Luo and Cirpka, 2008; Rubin, Cushey, and Wilson, 1997; Shapiro and Cvektovic, 1988, 1990; Simmons, Ginn, and Wood, 1995; Willmann *et al.*, 2010), or Random-Walk based methods, for example the continuous time random walk (Berkowitz and Scher, 1998; Berkowitz *et al.*, 2006; Montroll and Weiss, 1965; Scher and Lax, 1973) and the fractional ADE (Benson, Wheatcraft, and Meerschaert, 2000; Meerschaert, Benson, and Baumer, 1999). In particular these methods can handle heterogeneity in a continuous framework which ranges from the pore-scale to the largest field scales.

1.2 Outline of the thesis

In the present thesis we address some of the issues outlined in the previous section. In particular, the inherent Lagrangian nature of mixing processes calls for numerical and analytical Lagrangian investigation methods (Ottino, 1989) which we pursue in different activities.

We test the accuracy of several numerical schemes in the solution of the Advection Dispersion Reaction Equation (1.2c) at the continuum scale in severe, although common, conditions. We aim at obtaining suggestions for a conscious choice of the numerical tools according to the objectives and features of the numerical investigation, with particular attention on dilution and mixing-controlled processes in strongly heterogeneous media. Modeling advection-dominated transport in highly heterogeneous formations requires the accurate reproduction of both the disordered velocity field and the local dispersive solute mass fluxes, which are particularly strong along the irregular boundaries of the plumes. In these conditions, which are typical of most aquifers, numerical methods are generally affected by artificial diffusion which determines the overestimation of mixing and thus of reactions controlled by it. We compare five different numerical schemes, some of them commonly used in groundwater modeling, such as the Total Variation Diminishing (TVD) and the Method of Characteristics (MOC), distributed by the USGS (Zheng and Wang, 1999), and evaluate their performance in modeling transport of nonreactive and reactive solutes in heterogeneous formations at several levels of heterogeneity. Besides TVD and MOC, we implement three Lagrangian schemes: the classic Random Walk Particle Tracking method (RWPT), the Smoothed Particle Hydrodynamics (SPH) in the version proposed by Herrera, Massabó, and Beckie, 2009, and a new Streamline-Based (SB) method, modified from the method proposed by Herrera, Valocchi, and Beckie, 2010. The comparison is performed by considering several indicators of dilution, such as second central moments, dilution index, maximum concentration, which are typically considered for evaluating dilution and mixing-controlled processes. The results of the numerical comparison as well as a brief although exhaustive description of the numerical schemes is included in Chapter 2.

As the outgrowth of a collaboration with Aldo Fiori (Universitá degli Studi Roma Tre, Rome, Italy), the numerical SPH simulations are employed in Chapter 3 for testing new semianalytical Lagrangian tools to assess a priori dilution at the plume scale in nonreactive conditions. These relations require the definition of a few parameters for the real aquifer (namely, its structural statistics, the possible anisotropy of the formation, and the hydrodynamic dispersion coefficients), but are subordinate to a set of assumptions, mainly the weak heterogeneity of the formation, which requires numerical validation. In particular, we compare the global mean and the global variance of concentration, as well as the cumulative frequency distribution of concentration within the solute body. All these quantities describe the overall dilution experienced by the plume in a quantitative manner. The global mean $\langle \bar{c} \rangle$, for example, defines an average value of concentration over the plume volume, which can be estimated as well. As dilution proceeds, $\langle \bar{c} \rangle$ tends to the global well-mixed condition for the plume, but it cannot distinguish between a well homogenized plume, where the mean concentration is close to the mode of the distribution, and a set of disordered separate solute blobs spread throughout the domain. A measure of this disorder is given by the global variance, which tends to zero as apparent complete dilution is approached. Finally, the CFDs provide a more complete information on the distribution of concentration over the whole variation range. Such a framework meets a need for simplification sought by practitioners, who approach with distrust, or do not accept at all, the use of stochastic tools in applications (Pappenberger and Beven, 2006; Tartakovsky, 2007; Tartakovsky, Nowak, and Bolster, 2012).

As a first approach to reactive transport, and still moving within the stochastic framework, we develop a procedure for analytically linking the conservative transport statistics to reactive transport in case of equilibrium bimolecular homogeneous reactions of the kind $A + B \rightleftharpoons C$. The activity, described in Chapter 4, begins from assuming that the Beta distribution adequately models the concentration distribution for passive tracers. Exploiting the speciation analytical relations which link the reactive species concentration to the reference conservative component, we provide semianalytical expressions also for the moments (mean and variance) and the probability distribution functions for the three species reacting upon mixing. We then draw both local and global statistics for the reactive species as well as cumulative probability functions, which are somehow related to both volume fraction and mass fraction. Whereas local scale statistics cannot be directly related to dilution (because dramatically affected by uncertainty), global statistics can. Unlike conservative transport moments (Chapter 3), reactive global mean and variance are crucially affected by the reaction. Further information is provided by the cumulative frequency distribution, which shows how concentration within the plume is distributed considering the range of all the admissible concentrations.

Unfortunately the semianalytical tools considered in the previous chapters rely on a set of assumptions (mainly weak heterogeneity, and conservative transport or very fast reaction kinetics) which are not in principle valid when it comes to more realistic highly heterogeneous formations and kinetically-controlled reactions. In these cases we cannot prescind from the use of numerical simulations. Hence in Chapter 5 we present some numerical results about instantaneous and kinetic reactive transport in heterogeneous field characterized by log-conductivity variance up to $\sigma_Y^2 = 10$. The results of the simulations are analyzed on a single-realization basis in order to give some insight on the interplay among the heterogeneity structure of the formation, the Péclet number (which expresses the ratio between the timescale of dispersion and the timescale of advection) and the Damköhler number (which quantifies the balance between dispersion and reaction timescales). We choose the SPH algorithm because it is resistent to both advection-dominated conditions and highly non-uniform velocity fields, and it also allows to include non-linear reaction terms with relative ease. The phenomenological analysis comprehends the effects of the hydrodynamic dispersion model, the injection mode and the source size on a set of dilution indicators (e.g. the Dilution Index, the Peak Concentration, the Cumulative Frequency Distribution of concentration, the Break Through Curves) in both conservative and reactive conditions.

Describing transport at the continuum scale implies accepting that at the reference scale (REV) well-mixed conditions are fulfilled. In general, this implies verifying that the action of diffusion within the pore is fast enough to cancel the inhomogeneities created by the local velocity field, or by the interference of reactive processes. In Chapter 6, which is the result of an activity carried out at the University of California, San Diego, under the co-supervision of prof. Daniel M. Tartakovsky, we determine a set of sufficient conditions for the upscaling from the pore-scale to the continuum scale which guarantees the decoupling between the pore-scale system and the continuum system. We apply the multi-scale expansion homogenization procedure (Hornung, 1997) to upscale a bimolecular precipitation/dissolution reactive system of the kind $A + B \rightleftharpoons C \rightleftharpoons C\downarrow$. The upscaled bimolecular reactive systems considered in the previous chapters can be considered as special cases of this basic pore-scale reactive mechanism. The sufficient conditions for homogenizability apply on the dimensionless numbers which identify the reactive transport problem, namely the Péclet number and three Damköhler numbers; they delimit a homogenizability region in a 4D phase diagram. Here effective parameters at the continuum scale can be determined through the solution of a decoupled boundary value problem on a unit cell which represents the periodic microstructure of the macroscopic domain. The boundaries of the homogenizability region delineated in the phase diagram are investigated through numerical simulations, by comparing the averaged results of pore-scale simulations to direct results of macroscale simulations in a bidimensional fracture setting.

Finally, in Chapter 7 we present our overall conclusions and directions for future work.

Each chapter is thought as a stand-alone piece of work, thus concepts and equations are sometimes repeated for the sake of clarity. More considerable connections and links between chapters are opportunely signalled. For convenience, symbols are independently redefined in each chapter.

Chapter 2

Numerical simulations of solute transport in highly heterogeneous formations: A comparison of alternative numerical schemes

2.1 Introduction

A distinctive character of advection-dominated transport processes in heterogeneous porous media is the disordered distribution of solute concentration with sharp interfaces at the fringes of the plume. This situation is typically encountered in many branches of physics and engineering when the transport of an agent is controlled by a spatially non-uniform velocity field. In the present work we focus on passive and reactive transport in highly heterogeneous geological formations, but the results can be applied also to other cases.

Modeling multi-species reactive solute transport and biological processes in advection dominated environments requires special care in treating the advective component of the Advection Dispersion Reaction Equation (ADRE). In highly heterogeneous geological formations the Darcian velocity field shows strong spatial variability at a hierarchy of scales. This variability leads to a disordered spatial distribution of the concentration with sharp fronts which enhance mixing of the aqueous species, thereby exerting a strong control on the reaction. The accurate reproduction of these features in numerical simulations is essential to correctly model multi-species solute reactions and biochemical processes as well.

In such scenarios, obtaining accurate numerical solutions of the transport equation is challenging because the traditional methods used to approximate the advective term adds numerical diffusion, often accompanied by spurious oscillations. These pathologies, which are common to most grid-based numerical methods, deteriorate the accuracy of the numerical schemes, in particular in proximity of large concentration gradients, such as those emerging in heterogeneous formations. When more than one agent is transported, such as in the case of two aqueous species reacting upon mixing, errors may increase further because of the nonlinear dependence of the reaction rate on the local concentration of the reacting species. Moreover, existing spurious oscillations can be amplified through reaction.

Low-order Eulerian schemes with fixed grids of either finite elements or finite volumes are perhaps the most used schemes in applications. These numerical schemes have been shown to be plagued by artificial diffusion (see e.g., Cirpka, Helmig, and Frind, 1999; Quarteroni and Valli, 1994; Toro, 1999), which can be partially alleviated by increasing the order of accuracy. However, high-order schemes are prone to develop spurious oscillations in high gradient regions, which can be somehow controlled by reducing both grid size and time-step, or by using higher order nonlinear schemes, such as essentially non-oscillatory (ENO, Harten *et al.*, 1987) or weighted essentially non-oscillatory (WENO) methods (Jiang and Shu, 1996). These methods are also available on general unstructured meshes to deal with complex geometries (Dumbser and Käser, 2007; Dumbser *et al.*, 2007; Hu and Shu, 1999). When simulations are multidimensional and formations are highly heterogeneous, grid refinement and smaller time-steps are often unfeasible solutions, because of the high computational burden and the large memory requirement needed to reach adequate accuracy.

Conversely, Lagrangian methods refer to a mobile reference system determined by the Lagrangian velocity at each location, such that along each streamline the total time variation of concentration is caused by local dispersion and reaction, solely. In general, Lagrangian methods are structured such that global mass conservation is granted, whereas local mass conservation requires a careful solution of the flow field (LaBolle, Fogg, and Tompson, 1996).

Among the Lagrangian methods, the classic random walk particle tracking subdivides the total solute mass in a large number of particles moving according to the velocity field; a Brownian component is added in the form of particle jumps to mimic the effect of local dispersion. Other methods, such as Smoothed Particle Hydrodynamics (Monaghan, 2005), refer to mobile fluid particles and discretize the Fickian local dispersion operator by means of an integral interpolation.

Finally, Eulerian-Lagrangian methods use a combination of Lagrangian and Eulerian schemes applied to the advection and dispersion terms, respectively. The method of characteristics (Zheng and Wang, 1999), for example, relies on particle tracking for computing an intermediate concentration field on a fixed reference grid, which is then updated by solving the dispersion term with a Eulerian scheme. A continuous re-mapping of particle configuration is required in order to reduce the computational effort, thereby introducing numerical diffusion to an extent which is cumulative and difficult to quantify. Other methods apply Eulerian algorithms to streamline-oriented grids of elements, thus limiting artificial diffusion at least in the transverse direction. A comparison between streamline-based and grid-based solutions of the transport problem is present in Cirpka, Helmig, and Frind, 1999, in a two-dimensional setup. Although possible, the extension of this approach to a three-dimensional flow field is cumbersome. As an alternative, the transport equation is first solved along a set of streamlines, and successively the dispersive step is added by operator-splitting: Obi and Blunt, 2004, included a finite-difference dispersion discretization, whereas Herrera, Valocchi, and Beckie, 2010, modeled dispersion as SPH-like mass exchange across streamlines. The main difficulty here is to obtain an adequate resolution throughout the domain, since streamlines become highly irregular as the heterogeneity of the formation increases.

In the present work we compare the performance of five numerical schemes to model passive and reactive solute transport in heterogeneous formations. First we analyze how numerical diffusion influences dilution of a passive tracer, and successively, by using the same set of numerical simulations, we analyze the impact of numerical diffusion on the transport of two reactive aqueous species reacting upon mixing. This is possible because the condition that the two species are in equilibrium with their product allows to formally write their concentration as a function of the concentration of a fictitious nonreactive tracer through suitable stoichiometric algebraic equations (see e.g., De Simoni *et al.*, 2005). We simulate transport in bidimensional heterogeneous formations with a log-conductivity variance ranging from 0.2 to 10. Working with high heterogeneity is particularly challenging because of the large deformation that the plume experiences, which leads to large concentration gradients, in particular at the plume's fringes.

In Section 2.3 we briefly describe the numerical methods, in Section 2.4 we present the numerical setup, and finally in Section 2.5 we discuss the results for transport of both conservative and reactive solutes. Finally, conclusions are drawn in Section 2.6.

2.2 Mathematical model

The governing equation for multi-species solute transport in a heterogeneous velocity field is as follows:

$$\frac{\partial c_i}{\partial t} + \mathbf{u} \cdot \nabla c_i = \nabla \cdot (\mathbf{D}\, \nabla c_i) + \frac{r_i}{\phi}, \qquad i = 1, ..., m \tag{2.1}$$

where c_i is the concentration of the i-th species, ϕ is the porosity, assumed constant (uniform) through the computational domain, $\mathbf{u}$ is the spatially variable velocity field, $\mathbf{D}$ is the local dispersion tensor and m is the number of aqueous species belonging to the reactive system. If the fluid can be regarded as incompressible, the velocity field is divergence-free: $\nabla \cdot \mathbf{u} = 0$, which for a stationary velocity field obeying the Darcy's law:

$$\nabla \cdot (\mathbf{K}\, \nabla H) = 0 \tag{2.2}$$

leads to the following mass-conservation equation:

$$\mathbf{u} = -\frac{\mathbf{K}}{\phi} \cdot \nabla H \tag{2.3}$$

where $\mathbf{K}$ is the hydraulic conductivity tensor and H is the piezometric head. Equations (2.1), (2.2) and (2.3) are written at the Darcy's scale, i.e. a scale at which the porous media can be considered as a continuum equivalent (see e.g., Bear, 1972). The interplay between molecular diffusion and the heterogeneous water velocity profile within the pores causes solute mass transfer at the sub-Darcy's scale, which is mimicked in Eq. (2.1) as a hydrodynamic dispersive mass flux: $\mathbf{F}_D = -\mathbf{D} \cdot \nabla c_i$, where c_i is the Darcy's scale concentration of the species i defined over a support volume with characteristic size corresponding to the Darcy's scale. A commonly adopted parametrization of local dispersion is the following (see e.g., Bear, 1979):

$$D_{ij} = (D_{m,i} + \alpha_T \left|\mathbf{u}\right|)\delta_{ij} + (\alpha_L - \alpha_T)\frac{u_i u_j}{\left|\mathbf{u}\right|} \tag{2.4}$$

where $D_{m,i}$ is the effective compound-dependent molecular diffusion (or pore diffusion coefficient), corrected for the effect of tortuosity, $\mathbf{u}$ is the local Darcian velocity, while α_L and α_T are the longitudinal and transverse dispersivities, respectively. The dispersion tensor becomes diagonal if one axis of the orthogonal reference system is parallel to the velocity vector.

For reactive tracers, additional expressions for the reactive source/sink terms, $r_i(c_1, c_2, ..., c_m)$, either linear or non-linear, are required. A slightly non-linear dependence of the longitudinal dispersion coefficient on the local velocity has been evidenced by Bear, 1972, in two-dimensional laboratory experiments. However, we prefer to use the linear model because simpler and widely used in field applications.

In addition to a passive tracer, we choose to model the simple case of a bimolecular instantaneous equilibrium reaction of two aqueous species, A and B, to produce a precipitate C according to the following reaction equation $\nu_1\, A + \nu_2\, B \rightarrow \nu_3 C \downarrow$, where $\nu_i, i = 1, 3$ are the stoichiometric coefficients for species i. For instantaneous bimolecular reactions (see e.g., Denbigh and Denbigh, 1981) whose product is a precipitate, the mass action law reduces to the following algebraic expression $c_1^{\nu_1}\, c_2^{\nu_2} = K_{eq}$ relating the concentration of the two aqueous species to an equilibrium constant K_{eq}. Here c_1 and c_2 are the concentrations of the species A and B, respectively. With the additional assumptions that the two aqueous species have the same molecular diffusion coefficient and that the stoichiometric coefficients are unitary the problem reduces to an ADE for a fictitious nonreactive solute with concentration $\mathsf{u} = c_1 - c_2$ supplemented by the following two speciation equations (De Simoni *et al.*, 2005; Rubin, 1983):

$$c_{1,2} = \frac{1}{2}\left(\mathsf{u} \pm \sqrt{\mathsf{u}^2 + 4K_{eq}}\right), \tag{2.5}$$

where the sign $+$ between the two terms within the bracket is applied for c_1 and the sign $-$ is applied for c_2.

The reaction rate, which in this case is the same for the two species $r = r_1 = r_2$, assumes the following expression:

$$\frac{r}{\phi} = \frac{2K_{eq}}{(\mathsf{u}^2 + 4K_{eq})^{3/2}}\left(\nabla \mathsf{u}^T \mathbf{D} \nabla \mathsf{u}\right) \tag{2.6}$$

This approach belongs to a well established class of methods, called chromatography, used in chemistry and chemical engineering to simplify multispecies transport problems (Hellferich and Klein, 1970), and has been brought into the hydrologic community by the pioneering work of Valocchi, Street, and Roberts, 1981, followed by the studies of Rubin, 1983, Friedly and Rubin, 1992, Saaltink, Ayora, and Carrera, 1998, and De Simoni et al. (2005,2007), among others.

2.3 Numerical schemes

Numerical methods for solving the ADE (Eq. 2.1 with $r_i = 0$) are typically classified as Eulerian or Lagrangian, according to the adopted spatial reference system. These methods attempt to overcome the many difficulties arising in advection-dominated transport processes by using different strategies, the main challenges being the accurate reproduction of sharp moving fronts and of mixing-controlled reactions.

In the present chapter we apply five numerical schemes to the same heterogeneous velocity field in both weakly and strongly heterogeneous formations. In the latter case numerical schemes may show pathologies not evident in weakly heterogeneous formations. Therefore, the focus of the present work is on the impact of formation's heterogeneity on the accuracy of these numerical schemes. In particular, we consider three among the most widely used numerical schemes: the Total Variation Diminishing (TVD) Finite Volume Method, the Method of Characteristics (MOC) and the Random Walk Particle Tracking (RWT) method. The first two schemes are included into the popular MT3DMS package distributed by USGS and hence are widely diffused among practitioners. In addition, we consider other two Lagrangian schemes recently proposed by Herrera et al. (Herrera, Massabó, and Beckie, 2009; Herrera, Valocchi, and Beckie, 2010). For the sake of completeness, subsequently we provide a short description of these numerical schemes.

In all cases saturated flow is solved by applying the classic finite volumes scheme implemented in MODFLOW (Harbaugh, Banta, and McDonald, 2000) to a very fine grid, which we verify capable of reproducing the strong velocity non-uniformities typical of highly heterogeneous formations.

2.3.1 TVD and MOC schemes

In this section we describe the Eulerian TVD and the Eulerian-Lagrangian MOC schemes included into the popular MT3DMS package (Zheng and Wang, 1999). Further details concerning these two numerical schemes and their implementation can be obtained from the user's manual of MT3DMS (Zheng and Wang, 1999).

The literature offers several finite volume TVD schemes constructed in such a way that the Total Variation $TV = \int |\nabla c| \, d\mathbf{x}$ of the numerical approximate solution diminishes as time increases. Among the several TVD schemes available, MT3DMS includes the ULTIMATE TVD scheme, in which the concentration at the interfaces between adjacent cells is obtained through a third-order polynomial interpolation of nodal concentrations. In general, practitioners prefer this scheme because it is computationally effective (both in term of CPU time and memory requirements) and available in the popular package MT3DMS (Zheng and Wang, 1999). The tendency of higher order polynomial interpolations to develop spurious oscillations is controlled through flux limitation, thus ensuring that TV diminishes, whereas the order of accuracy is raised by the polynomial reconstruction of concentration within the cell. This numerical scheme is mass conservative and the accuracy achieved along sharp fronts depends on grid refinement and the time step. Its use is recommended in dispersion-dominated scenarios where the high-order of accuracy is particularly beneficial to obtain accurate reproductions of the concentration with relatively large grid cells. In advection dominated transport problems the use of TVD can be in principle questioned because it deliberately adds numerical diffusion at the edges of sharp fronts, as typical of most Eulerian schemes.

MOC solves the ADE (Eq.2.1 for $i = 1$ and $r_1 = 0$) in two steps. In the first step an intermediate concentration is computed through particle tracking assuming that only the advective term contributes to the variation of the solute concentration. Then, in the second step, this intermediate concentration is updated by adding the variation associated to the dispersive term approximated by a finite difference operator. Although particle tracking is free of numerical diffusion, errors are introduced when the intermediate concentration is computed on the computational grid as the (weighted) average of the concentration of the particles contained within the computational cell of volume ΔV. The accuracy can be increased by reducing ΔV, which in turn calls for an increase of the number of particles, as discussed in Section 2.3.2. In order to contain memory requirements, particles number and position can be dynamically redefined at each time-step. MOC has been shown to minimize numerical diffusion also in advection-dominated scenarios, but unfortunately the scheme is not mass-conservative. Mass balance errors increase with the heterogeneity of the velocity field and when the computational grid is irregular.

2.3.2 Random Walk Particle Tracking

The classic Random Walk Particle Tracking (RWPT) is one of the most intuitive methods for modeling transport of solutes in heterogeneous porous formations. Details on this meshless and virtually free of artificial diffusion method can be found in the review paper by Salamon, Fernández-Garcia, and Jaime Gómez-Hernandez, 2006.

The mass of the solute is divided into a large number of particles, such that each particle carries a small fraction of the total mass. The number of particles is selected as a tradeoff between accuracy and computational burden and, for an instantaneous injection, depends on the ratio between the volumes of the source area V_0 and the computational cell ΔV (see e.g., Salamon, Fernández-Garcia, and Jaime Gómez-Hernandez, 2006; Tonina and Bellin, 2008). An important characteristic of this method is that each particle conserves its initial mass since no mass exchange occurs between adjacent particles. The particles are then moved independently at small time steps Δt by successive jumps which have a drift component, dependent on the underlying velocity field, and an additional Brownian component, which is introduced to simulate hydrodynamic dispersion.

The trajectory of a particle is then computed as follows:

$$\mathbf{X_p}(t+\Delta t) = \mathbf{X_p}(t) + \mathbf{A}(\mathbf{X_p}, t)\Delta t + \mathbf{B}(\mathbf{X_p}, t) \cdot \boldsymbol{\xi}(t)\sqrt{\Delta t} \qquad (2.7)$$

where $\mathbf{X_p(t)}$ is the position of the p-th particle at time t, $\mathbf{A}$ is the drift vector which accounts for the effect of both the velocity field and the divergence of the dispersion tensor, $\mathbf{B}$ is the displacement matrix which depends upon velocity and dispersion, and $\boldsymbol{\xi}(t)$ is a standard random deviate array, whose components have zero mean and unit variance. For $N_p \to \infty$ the local density of the particles provides the solution of the ADE (Eq. 2.1). The error associated to this method reduces as the number of particles increases and their number is typically chosen as a tradeoff between accuracy and computational burden since the CPU time increases linearly with the number of particles. Another source of error, also decreasing when the number of particles increases, is associated to the computation of the mean concentration within the computational cells of an Eulerian grid. This step is typically performed by counting the number of particles located within a cell, assuming that particle's mass is collapsed to its center of mass. The approximation associated to this step is influenced by both the density of particles within the injection volume V_0, representing the initial concentration c_0, and the volume ΔV of the reference grid's cells.

In order to obtain an accurate representation of the concentration distribution the dimensions of ΔV should be much smaller than the respective integral scales of the log-conductivity, which in turn calls for using a large number of particles. This is related to an intrinsic limitation of the forward tracking scheme of Eq. (2.7). As discussed in Tonina and Bellin, 2008, the minimum concentration than can be resolved with the forward scheme (2.7) in the case of an instantaneous injection of a solute mass $M = c_0\, V_0\, \phi$ within the initial volume V_0, is given by: $c_{min} = c_0\ V_0/(N_p\ \Delta V)$, such that, to maintain the sensitivity, a reduction of ΔV should be accompanied by an increase of the total number of particles N_p. Consequently, a large number of particles is needed when the ratio $V_0/\Delta V$ is large, i.e. for wide source areas or small, point-like, ΔV, to better reproduce the spatial variability of the solute concentration. Back-particle tracking may be used in this case to alleviate the computational burden (Tonina and Bellin, 2008).

Moreover, since velocity is known along interfaces between the cells of the grid where the flow is solved, a velocity mapping is required in order to reconstruct a continuous information which can be used for computing **A** and **B** in Equation (2.7). We choose hybrid interpolation in order to fulfill both local fluid and solute mass conservation (LaBolle, Fogg, and Tompson, 1996; Salamon, Fernández-Garcia, and Jaime Gómez-Hernandez, 2006). If these requirements were not satisfied, we would experience particle accumulation in low-permeability regions.

The scheme is natively mass conservative and free of numerical diffusion and spurious oscillations. The main limitations are related to local fluctuations of concentration occurring when the concentration is mapped on a grid, which are usually enhanced by non-linear reactive relations, and to the difficult implementation of reaction terms other than simple linear sorption (Kinzelbach, 1987).

2.3.3 Smoothed Particle Hydrodynamics

Smoothed Particle Hydrodynamics (SPH) is a Lagrangian meshless method whose nodes are moving fluid particles with an assigned fluid volume larger than the Representative Elementary Volume (REV) of the flow. The effect of advection is directly provided by the movement of the particles along the streamlines, whereas dispersion is modeled as Fickian solute mass exchange among particles. As a result, SPH is suitable for pure advection simulations since it can provide strictly bimodal concentration distributions by switching off mass exchange among particles. The concentration of the $i-$th particle, which at time t is at the position $\mathbf{x} = \mathbf{x}_i$, is approximated through the following Monte Carlo integration scheme (Monaghan, 2005) :

$$c(\mathbf{x}_i, t) = \frac{1}{N_p(\mathbf{x}_i)} \sum_{j=1}^{N_p(\mathbf{x}_i)} \frac{c(\mathbf{x}_j)\ W(\mathbf{x}_i - \mathbf{x}_j, h)}{\omega(\mathbf{x}_j)/N_p(\mathbf{x}_j)} \tag{2.8}$$

where W is a suitable kernel function with compact support $\mathcal{H}$ centered on $\mathbf{x} = \mathbf{x}_i$, h is the smoothing length which is proportional to the radius of the smoothing area $\mathcal{H}$, and $N_p(\mathbf{x}_i)$ is the number of particles within $\mathcal{H}$. In addition, the particle density ω assumes the following approximate expression:

$$\omega(\mathbf{x}_j) = \sum_{k=1}^{N_p(\mathbf{x}_j)} W(\mathbf{x}_j - \mathbf{x}_k, h) \tag{2.9}$$

Eq. 2.8 discretizes the integral in the following approximate equality:

$$c(\mathbf{x}) \approx c_I(\mathbf{x}) = \int_{\mathcal{H}} c(\mathbf{x}')W(\mathbf{x} - \mathbf{x}', h)d\mathbf{x}', \tag{2.10}$$

which becomes exact if the kernel function W coincides with the delta function $\delta(\mathbf{x} - \mathbf{x}')$. In order to reduce the error associated to the integral approximation of $c(\mathbf{x})$ through $c_I(\mathbf{x})$, which increases with the size of $\mathcal{H}$, W has to fulfill the following consistency conditions: $\int_{\mathcal{H}} W(\mathbf{x}')d\mathbf{x}' = 1$ and $\int_{\mathcal{H}} \nabla W(\mathbf{x}')d\mathbf{x}' = 0$, which mimic the behavior of the delta function δ. Besides, $\lim_{h\to 0} W(\mathbf{x} - \mathbf{x}') = \delta(\mathbf{x})$. Eq. 2.8 is also affected by an error related to the distribution of the j particles within $\mathcal{H}$, which reduces as h increases. As a result, the accuracy of the Monte Carlo integration does not depend only on the number of particles within $\mathcal{H}$, but also on their distribution. That is why the SPH algorithm cannot be considered a consistent scheme, since increasing the number of particles does not guarantee higher accuracy (Liu and Liu, 2003). In this case the physical constraints posed by the flow continuity equation ensure that the distribution of the particles remain homogeneous throughout the domain, though disordered, thus reducing the error associated with the discretization of the integral. The integral approximation of the dispersive fluxes is borrowed from the SPH solution of the heat conduction equation (Brookshaw, 1985; Cleary and Monaghan, 1999; Jubelgas, Springel, and Dolag, 2004) and reads (Herrera, Massabó, and Beckie, 2009; Tartakovsky *et al.*, 2007a):

$$\frac{dc_i}{dt} = 2 \sum_{j}^{N_p(\mathbf{x}_i)} \frac{1}{\omega_{ij}} D_{ij}(c_j - c_i) \frac{\mathbf{r}_{ij}}{|\mathbf{r}_{ij}|^2} \cdot \nabla W\left(\mathbf{r}_{ij}, h\right) \tag{2.11}$$

where c_i is the concentration associated to the $i-$th particle, which at time t occupies the position $\mathbf{x}_i$ and dc_i/dt is its total time rate of change. In addition, $\mathbf{r}_{ij}$ is the distance vector between the two locations $\mathbf{x}_i$ and $\mathbf{x}_j$, whereas ∇W is the gradient of the kernel function W. Finally $\omega_{ij} = 2\omega_i\, \omega_j/(\omega_i + \omega_j)$ and $D_{ij} = 2D_iD_j/(D_i + D_j)$ are the harmonic means of the values assumed by ω and D at $\mathbf{x}_i$ and $\mathbf{x}_j$, respectively. Harmonic means assure the symmetry of the mass exchanges among particles.

Following Monaghan, 2005, we use for W the following cubic B spline function:

$$W(q) = \frac{K_m}{h^m} \begin{cases} \frac{2}{3} - q^2 + \frac{1}{2}q^3, & \text{for } 0 \le q < 1 \\ \frac{1}{6}\left(2 - q\right)^3, & \text{for } 1 \le q < 2 \\ 0, & \text{for } q > 2 \end{cases} \tag{2.12}$$

where $q = |\mathbf{r_{ij}}|/h$, m is the space dimensionality of the problem and K_m a normalization constant which depends on m. The uniform smoothing length h over which W

is defined is related to the mean particle distance and is the reference length of the numerical scheme. Similarly to RWPT methods, particle tracking is performed by using a linear interpolation of the velocity inside the computational cells (LaBolle, Fogg, and Tompson, 1996) and is computed by using a second-order explicit Taylor scheme. Furthermore, fluid particles are introduced at a density proportional to local flow from the inflow boundary of the domain. The local conservation of fluid mass, guaranteed by the linear interpolation of velocity within the cell and the dynamic upstream particle injection, allow to obtain a nearly constant particle density within the computational domain. The numerical scheme is virtually free of numerical diffusion.

The stability of the solution requires that the time step is limited according to the following expression: $\Delta t \leq \epsilon h^2/D$, where ϵ is a tuning empirical coefficient. The main drawback of this numerical scheme is that it produces spurious oscillations for anisotropic local dispersion and consequently its use is currently limited to isotropic dispersion (Herrera, Valocchi, and Beckie, 2010; Tartakovsky, Tartakovsky, and Scheibe, 2009). Furthermore, it is computationally very expensive, with the most demanding step being the search for neighboring particles, although alleviated by searching within predefined macro-cells as suggested by Ferrari *et al.*, 2009. The most important advantage of this numerical scheme is the possibility to control the accuracy in reproducing sharp changes of solute concentration in highly heterogeneous formation when advection dominates over local dispersion.

2.3.4 Streamline-based numerical method

In an attempt to reduce the computational burden associated with SPH and allow to use anisotropic local dispersion, Herrera, Valocchi, and Beckie, 2010, proposed a two-step streamline based (SB) method for solving Eq. (2.1). As in classic streamline methods the ADE is first written in an orthogonal local coordinate system along a given streamline (Gelhar and Collins, 1971):

$$\frac{\partial c_i}{\partial t} + |\mathbf{u}|\frac{\partial c_i}{\partial s} = \nabla \cdot \left(\hat{\mathbf{D}}\nabla c_i\right) + \frac{r_i}{\phi} \tag{2.13}$$

where s is the longitudinal curvilinear coordinate measured along the streamline. Working with a mobile reference system attached to a particle that moves along the streamline has the advantage that the tensor of local dispersion $\hat{D}$ becomes diagonal (Bear, 1972). Eq. (2.13) can therefore be solved in two steps by using an operator splitting algorithm (Herrera, Valocchi, and Beckie, 2010). At the first step the dispersion tensor is modified by including only a longitudinal component given by the difference between longitudinal and transverse dispersion coefficient $\hat{D}_{11} = D_L - D_T$, all the other components $\hat{D}_{ij}$ being zero. Therefore Eq. (2.13) reduces to a one-dimensional ADE in the curvilinear coordinate s:

$$\frac{\partial c_i}{\partial t} + |\mathbf{u}|\,\frac{\partial c_i}{\partial s} = (\alpha_L - \alpha_T)|\mathbf{u}|\frac{\partial^2 c_i}{\partial s^2} \tag{2.14}$$

where we adopt the Scheidegger dispersion model (2.4) with the dispersion coefficients varying linearly, through constant longitudinal α_L and transverse α_T dispersivities, with the module of the local darcian velocity $|\mathbf{u}|$ (Scheidegger, 1957). The alternative model of spatially constant local dispersion coefficients can be obtained by replacing $|\mathbf{u}|$ with U in Eq. 2.14.

In the second step of the procedure an isotropic dispersion equation in m dimensions has to be solved, adding the remaining part of the dispersive flux :

$$\frac{\partial c_i}{\partial t} = (D_m + \alpha_T\,|\mathbf{u}|)\left(\frac{\partial^2 c_i}{\partial s^2} + \frac{\partial^2 c_i}{\partial \eta^2} + \frac{\partial^2 c_i}{\partial \zeta^2}\right) + \frac{r_i}{\phi} \tag{2.15}$$

where η and ζ are the two local moving coordinates orthogonal to s. In the case of a two-dimensional flow field the term $\partial c_i/\partial\zeta$ on the right hand side of Eq. (2.15) drops and the concentration depends on the two orthogonal spatial coordinates s and η. The overall time variation of c_i over each timestep Δt is given by the sum of the rates of change provided by Eq. 2.14 and 2.15.

The one-dimensional problem (2.14) can be solved numerically by one of the several available Eulerian schemes applied to a fixed number of nodes positioned along the streamline. The solution of Eq. (2.15) is obtained by using the SPH scheme presented in Section 2.3.3, or a suitable transformation. The above splitting algorithm enjoys two main advantages: a strong reduction of the computational burden associated with the SPH-operator due to the fixed position of the nodes with respect to the standard SPH method operating on moving nodes and, most importantly, the possibility to use anisotropic local dispersion tensors. Streamlines are obtained by means of the particle tracking algorithm (Eq. 2.7) with $\mathbf{A} = \mathbf{u}$ and $\mathbf{B} = 0$. The computational nodes along the streamlines are chosen at a constant spacing ds equal to a fraction of the smoothing length h.

The main source of error of the SPH scheme is in the Monte Carlo integral (2.11) used to evaluate the modification of the particle's concentration due to the interaction with the neighborhood particles. The accuracy of this numerical integration depends on the number and distribution of particles within the support volume $\mathcal{H}$ of W. To correct for non-uniform distributions of particles the integral (2.8) is weighted with respect to the inverse of the local particles density ω. In the classic SPH the weights $\omega(\mathbf{x}_j)$ assigned to the particles in the approximation (2.8) vary slightly if an adequately large number of particles is used. This calls for an accurate and detailed discretization of the flow field, especially at high σ_Y^2, such as to obtain a distribution of particles as homogeneous as possible, although disordered. In highly heterogeneous three-dimensional formations both the number of particles and the number of grid cells required to accurately reproduce the velocity field may be very large. Notice that contrary to the RWPT method the number of particles is not proportional to the injected mass, but depends on the size of the computational domain, which may be cumbersome in large domains.

In SB the computational burden is alleviated with respect to SPH by placing the particles at fixed positions along a given number of streamlines. Early simulations showed that in highly heterogeneous formations frequent flow focusing and expansion leads to inhomogeneous particle distribution which impacts negatively on the accuracy of Monte Carlo integration.

To improve the accuracy of the SB method we assume a spatially varying smoothing length $h_i = 2\,(1/\omega_i(\mathbf{x}_i))^{1/m}$, which is adapted to the local particle density. Given the inhomogeneous distribution of the particles we propose to replace the weight ω in the Monte Carlo integration (2.8), with the inverse of the volume associated to the node, as in the classic SPH implementation (Tartakovsky *et al.*, 2007a). Therefore, at the node $\mathbf{x}_j$ along a streamline we assign the volume $V(\mathbf{x}_j) = A(\mathbf{x}_j)\,ds$, where ds is the constant spacing of the nodes along the streamline. The cross-sectional area $A(\mathbf{x}_j)$ of the corresponding streamtube is computed by imposing mass conservation along the streamline:

$$A(\mathbf{a}_j)\,u(\mathbf{a}_j) = A(\mathbf{x}_j)\,u(\mathbf{x}_j) \tag{2.16}$$

where u is the local velocity and $\mathbf{a}$ is the position from which the streamline originates. Node volumes are explicitly included in the discretized integral approximation for c_i:

$$c(\mathbf{x}_i, t) = \sum_{j=1}^{N_p(\mathbf{x}_i)} c(\mathbf{x}_j) V_j W(\mathbf{x}_i - \mathbf{x}_j). \tag{2.17}$$

Coherently, also Eq. 2.11 needs to be modified by setting $\omega_{ij} = 1/V_j$.

The solution of the one dimensional ADE (2.14) along the streamlines is obtained by applying the TVD Finite Volume method described in Section 2.3. Notice that, for isotropic local dispersion, Equation (2.14) reduces to a purely advective transport equation, whose solution with the TDV algorithm is error prone. In this case the classic SPH algorithm should be preferred to SB.

2.4 Numerical set-up

In order to compare the above numerical schemes under the same conditions we consider transport of a passive solute in a multi-Gaussian log-conductivity field with constant mean m_Y and variance varying from $\sigma^2_Y = 0.2$ to $\sigma^2_Y = 10$. The latter is used as an upper limit of the observed log-conductivity. Furthermore, we adopt the classic exponential model of spatial variability $C_Y(r'_1, r'_2) = \exp[-r']$, where $r' = \sqrt{(r'^2_1 + r'^2_2)}/I_Y$ is the dimensionless, with respect to the integral scale I_Y, two-point separation distance with components r'_1 and r'_2 in longitudinal and transverse directions, respectively. We generate four log-conductivity fields with the same ensemble mean and $\sigma^2_Y = 0.2$, 1, 4 and 10, obtained by rescaling a correlated Random Space Function (RSF) y with zero mean and $\sigma^2_{\mathsf{y}} = 1$ through the following expression: $Y(\mathbf{x}) = m_Y + \sqrt{\sigma^2_Y}\mathsf{y}(\mathbf{x})$. In doing that the resulting four fields share the same spatial structure but show fluctuations of different amplitude. y is generated by Hydro_Gen (Bellin and Rubin, 1996), an evolution of the sequential simulator algorithm introduced by Gomez-Hernandez and Srivastava, 1990.

We conduct numerical simulations of transport of both non-reactive and reactive solutes, the latter for two aqueous species reacting instantaneously upon mixing. We solve the flow equations (2.3) and (2.2) by using MODFLOW (Harbaugh, Banta, and McDonald, 2000) in a computational domain $L_1 = 40 I_Y$ long and $L_2 = 20 I_Y$ large, with very fine square cells of size $I_Y/20$ and permeameter-like boundary conditions of impervious longitudinal boundaries at $x_2 = 0$ and $x_2 = L_2$ and constant heads at the other two sides ($x_1 = 0$ and $x_1 = L_1$) such as to induce a mean head gradient of $J = 0.03$. It has been shown that with this grid's size the numerical solution converges to the right solution with negligible effect of the adopted numerical scheme (Cainelli, Bellin, and Putti, 2011). The resulting velocity field is then used as advective component in the solution of the transport equation (Eq. 2.1) with the numerical schemes described in Section 2.3. Since in all cases the velocity field is the same, the observed differences in the numerical solutions can be used to highlight specific pathologies of the numerical schemes, such as artificial (numerical) diffusion, for example.

In order to better evidence the impact of numerical diffusion on dilution, in a first set of simulations we consider the local dispersion spatially constant (uniform) and isotropic, i.e. $D_L = D_T = D$ and $\mathrm{Pe}_L = \mathrm{Pe}_T = \mathrm{Pe} = U\, I_Y / D = 1000$, where Pe is the Péclet number and U is the effective mean velocity obtained by dividing the total flux per unit thickness crossing the downstream boundary by the product between the width L_2 of the computational domain and the formation's porosity ϕ. The hypothesis of spatially constant D is consistent with the first-order analysis of flow and transport (see e.g., Dagan, 1989; Rubin, 2003), but it cannot be taken for granted in highly heterogeneous formations where the model of local dispersion is expected to have a significant impact on dilution. For this reason, successively we compare the results obtained by using the Scheidegger model (Eq. 2.4), which postulates a linear dependence of local dispersion from the local velocity. As discussed in Bear, 1972, the Scheidegger model is able to represent the increase of local dispersion with the Péclet number of the grain: $\mathrm{Pe}_g = u\, d_{50}/D_m$, for $\mathrm{Pe}_g > 100$, where d_{50} is the mean grain size.

We perform the simulations for a uniform instantaneous injection of a passive tracer with a unitary dimensionless initial concentration within the initial volume V_0 centered on $\mathbf{x} = (5I_Y, 10I_Y)$. V_0 has a squared horizontal projection of side $L = I_Y$ and thickness equal to the aquifer's thickness b. The resulting simulated concentrations are therefore dimensionless with respect to the initial concentration c_0: $z = c/c_0 \in [0, 1]$. The same concentrations, after rescaling with the following expression: $\mathsf{u} = (u_{\text{inj}} - u_{\text{amb}})\, z + u_{\text{amb}}$, can be substituted into the speciation Eqs. (2.5) to obtain the concentration of two aqueous species, A and B, reacting instantaneously upon mixing to produce the precipitate C according to the following simplified stoichiometry: $A + B \to C \downarrow$. The resulting concentrations of the two aqueous species are normalized with respect to $\sqrt{K_{eq}}$, which is a more convenient choice for making dimensionless the concentration of the two aqueous species. The initial conditions of the nonreactive tracer transport problem in term of the fictitious concentration u are of constant $u_{inj} = C_{1,\text{inj}} - C_{2,\text{ inj}}$ within the initial volume V_0 and of constant $u_{\text{amb}} = C_{1,\text{amb}} - C_{2,\text{amb}}$ in the ambient water, with C_i indicating the dimensionless concentration of species i. The dimensionless values of $C_{\text{i, inj}}$ and $C_{\text{i,amb}}$, with $i = 1, 2$ used in the simulations are shown in Table 2.1. Given the initial conditions listed in Table 2.1, reaction always occurs in the direction of precipitation (Rubin, 1983).

A comprehensive comparison of different numerical schemes requires that equivalent conditions are established on the parameters. In most cases a comparison criterion is the computational burden. In the present work, we decide not to consider the smaller computational burden as a preference criterion although a few comparative indications can be found in Herrera, Massabó, and Beckie, 2009; Herrera, Valocchi, and Beckie, 2010. Instead, our preference criterion is the numerical

Table 2.1: Parameters for the bimolecular reactive transport model: $C_{1,\,\mathrm{inj}}$ and $C_{2,\,\mathrm{inj}}$, and $C_{1,\mathrm{amb}}$ and $C_{2,\mathrm{amb}}$ are the dimensionless concentrations of the two aqueous species in the water injected instantaneously within the volume V_0 and in the ambient water, respectively. The initial concentrations values are the same for all the numerical methods. Specific parameters of the numerical schemes are as follows. SPH: $\overline{N}_p$ is the mean number of particles within the support volume of the weighting function W with uniform smoothing length h; SB: $h_{\min}$ and $h_{\max}$ are the minimum and maximum values of the variable smoothing length; RWPT: N_p is the total number of particles and $c_{\min}$ is the minimum concentration that can be resolved in the numerical simulations.

Numerical scheme	Parameter	Value
All	$C_{1,\mathrm{inj}}$, $C_{2,\mathrm{inj}}$	10, 0.1
All	$C_{1,\mathrm{amb}}$, $C_{2,\mathrm{amb}}$	0.1, 10
SB	$h_{\min}/I_Y$	0.025
SB	$h_{\max}/I_Y$	$[0.28, 0.53, 1.91, 16.8]$
SPH	h/I_Y	0.05
SPH	$\overline{N}_p$	50
RWPT	N_p	$4.84 \cdot 10^6$
RWPT	$c_{\min}/c_0$	$8.26 \cdot 10^{-5}$

diffusion, which should be reduced as much as possible, particularly when dealing with transport of aqueous species reacting upon mixing. Therefore, we select optimal parameters for each numerical scheme without imposing the condition of equal computational burden. Given that, TVD, MOC and RWPT are applied on the same uniform staggered grid used for the solution of the flow equation (i.e. a square grid with side $\Delta = I_Y/20$), which is also the smoothing length we adopt in SPH as well as the uniform distance ds of adjacent nodes along the streamlines in the SB method. Moreover, for SB streamlines are traced starting from the inlet boundary at $x_1 = 0$ at a constant mean transverse distance equal to $I_Y/20$. The number or particles used in SPH is fixed such as to obtain convergence of the concentration Cumulative Frequency Distribution (CFD) computed by considering the sample of all the particles used in the numerical simulation. Given the finiteness of the sample, the CFD can show unphysical discontinuities at high concentration values.

The strategies adopted to control this problem include increasing the number of particles, reducing the smoothing length in zones with high contrasts in the spatial distribution of the concentration (Cabezon, Garcia-Senz, and Relano, 2008) and adding an artificial diffusive flux as discussed in the work by Ferrari *et al.*, 2009. Here we do increase the number of particles to a level above which additional particles do not change the empirical concentration CFD. As for SB, in order to obtain a mean density of particles within the smoothing area similar to that used in SPH, we add particles in low density areas and trace them forward and backward such as to increase the density of the nodes where needed. Finally, we assign similar values to the concentration detection limit of RWPT and the concentration convergence limit of TVD and MOC.

2.5 Results

Here we present the results of the transport exercises conducted by applying the numerical schemes described in Section 2.3 to the same velocity field with increasing σ_Y^2 values. All the results are presented in dimensionless form.

2.5.1 Conservative tracer

We start by considering the time evolution of the spatial second order moments, which are good descriptors of the plume's deformation (spreading) and, except for computation performed with RWPT, are sensitive, though to a lesser extent than other indicators, to numerical diffusion.

The second order spatial plume moments assume the following general expressions:

$$S_{ij}(t) = \frac{1}{M(t)} \int_{\Omega} \phi\, c(\mathbf{x},t)\ (x_i - R_i)(x_j - R_j)\ d\mathbf{x} \tag{2.18}$$

with

$$R_i(t) = \frac{1}{M(t)} \int_{\Omega} \phi\, x_i\ c(\mathbf{x},t) d\mathbf{x} \tag{2.19}$$

and $M(t) = \int_{\Omega} \phi\, c(\mathbf{x},t)\ d\mathbf{x}$, where Ω is the computational domain.

An interesting property of RWPT is that these spatial moments are very well approximated by the moments of inertia $\mathcal{S}_{ij}(t)$ of the cloud of points marking the position of the particles at time t, without requiring the computation of the spatial distribution of the concentration:

$$\mathcal{S}_{ij}(t) = \frac{1}{N_p} \sum_{k=1}^{N_p} \left(X_i(t;\mathbf{a}_k) - \overline{X}_i(t)\right)\ \left(X_j(t;\mathbf{a}_k) - \overline{X}_j(t)\right) \tag{2.20}$$

with

$$\overline{X}_i(t) = \frac{1}{N_p} \sum_{k=1}^{N_p} X_i(t;\mathbf{a}_k) \tag{2.21}$$

where $X_i(t;\mathbf{a}_k)$ is the i-th component of the position of the particle k that originated at time $t = 0$ at the position $\mathbf{a}_k$ within the source V_0. Notice that in our two-dimensional simulations the volume V_0 is intended as the volume per unit thickness and planar area A_0. The moments computed through expressions 2.20 and 2.21 are free of numerical diffusion because RWPT does not resort to a discretization of the advective term of Eq. 2.1.

In the simulations conducted with RWPT we use a large number of particles (Table 2.1), which are enough to stabilize both $\mathcal{S}_{11}$ and $\mathcal{S}_{22}$ at all times considered in the simulations. The plume moments obtained by RWPT are therefore assumed as benchmark since they are not affected by numerical diffusion.

The second order moments $\mathcal{S}_{11}$ and $\mathcal{S}_{22}$, obtained by simulating transport of a nonreactive tracer with the five numerical schemes described in Section 2.3 are shown in Figure 2.1. The dash-dotted lines depict the moments obtained by simulating transport with RWPT and in the absence of local dispersion. We observe that the effect of local dispersion on the spatial moments is generally weak, although

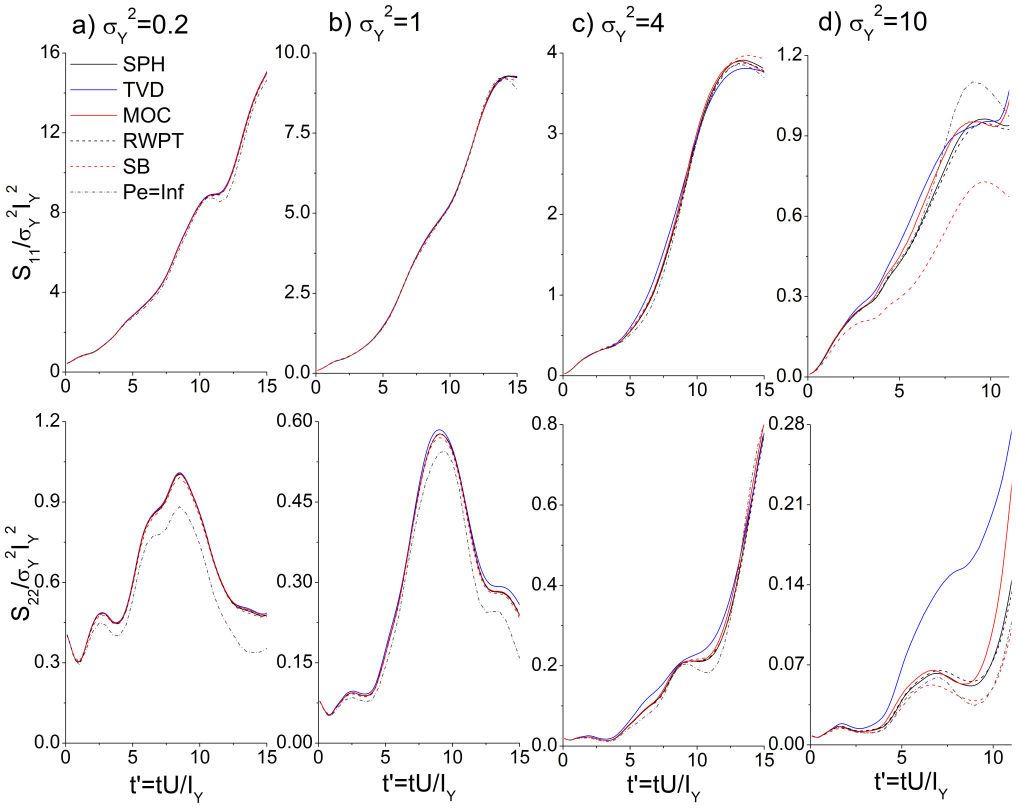

Figure 2.1: Longitudinal (upper row) and transverse (lower row) second central plume moments as a function of the dimensionless time $t' = t\,U/I_Y$ for: a) $\sigma_Y^2 = 0.2$; b) $\sigma_Y^2 = 1$; c) $\sigma_Y^2 = 4$; d) $\sigma_Y^2 = 10$. A combination of color and line type is used to refer to the numerical scheme.

larger in the transverse direction and when σ_Y^2 is high. Therefore, the second order central plume moments can hardly be used to quantify dilution, and the interplay between heterogeneity and local dispersion in controlling the evolution of dilution, since there are no clear ways to distinguish between spreading and dilution effects, except comparing the moments obtained with and without local dispersion. As shown in Figure 2.1 both $\mathcal{S}_{11}$ and $\mathcal{S}_{22}$ show a pulsating behavior, which indicates that transport is in non-ergodic conditions.

For a weakly heterogeneous formation ($\sigma_Y^2 = 0.2$) all the numerical schemes produce nearly the same $\mathcal{S}_{11}$ with the largest relative difference with respect to RWPT of 3 % for SB. The largest relative difference is very small (1.5%) also for $\mathcal{S}_{22}$ obtained by using the TVD method. The relative differences remain generally small, except for the TVD method, up to $\sigma_Y^2 = 4$, although for a given σ_Y^2 it is larger for $\mathcal{S}_{22}$ than for $\mathcal{S}_{11}$. For $\sigma_Y^2 = 10$ larger relative differences are observed in particular for $\mathcal{S}_{22}$. Figure 2.1 shows that TVD overestimates both spatial moments, while SB underestimates them, though to a lesser extent. Similar results have been obtained when local dispersion is let to vary linearly with the local velocity.

Global mass conservation is an important condition that numerical schemes are required to satisfy. It should be noted, however, that respecting this condition is not necessarily indicative of an accurate numerical solution, but on the other hand failing

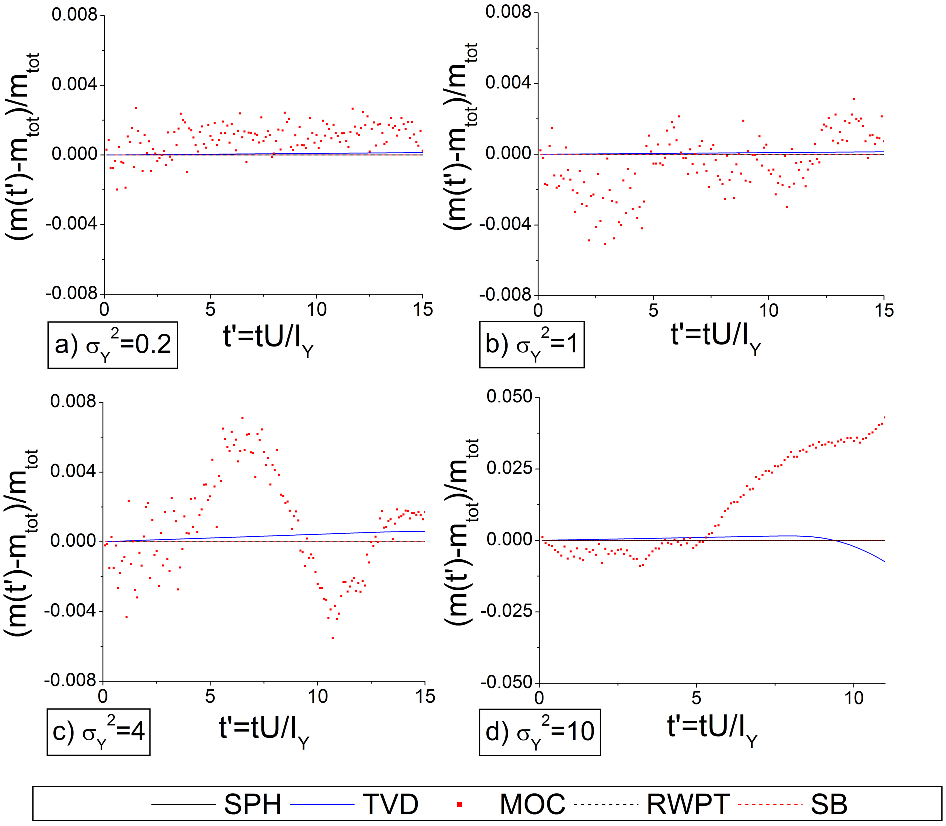

Figure 2.2: Global mass conservation for the conservative solute in relative terms for the different heterogeneity fields: a) $\sigma_Y^2 = 0.2$; b) $\sigma_Y^2 = 1$; c) $\sigma_Y^2 = 4$; d) $\sigma_Y^2 = 10$.

global mass conservation is certainly symptomatic of a problematic numerical scheme with possible large inaccuracies at the local level. Global mass conservation for the five numerical schemes is shown in Figure 2.2. For a correct interpretation of this figure one should notice that RWPT is strictly conservative, since mass conservation implies finding all the released particles within the computational domain at all times spanning between solute injection and the earliest arrival at the downstream boundary. As shown by Herrera, Massabó, and Beckie, 2009, and confirmed here, mass conservation holds for SPH simulations as well, since mass exchanges within the smoothing volume $\mathcal{H}$ are inherently mass conservative.

The mass is conserved also for SB and TVD. However, the latter shows the signs of an early reduction of the mass within the computational domain due to outflow from the downstream boundary, associated to anticipated early arrivals, of which the larger longitudinal second moment shown in Figure 2.1 is a clear manifestation. Finally, Figure 2.2 shows that MOC is not conservative, with the total amount of mass within the computational domain showing oscillations of amplitude that increase with σ_Y^2. While the global mass balance error of MOC is relatively low for $\sigma_Y^2 = 0.2$ (i.e., 0.3%), it increases to the remarkable value of 5% for $\sigma_Y^2 = 10$. This value is quite large because related to a global quantity that it is expected to remain quite stable and casts some doubts on the accuracy of this numerical scheme.

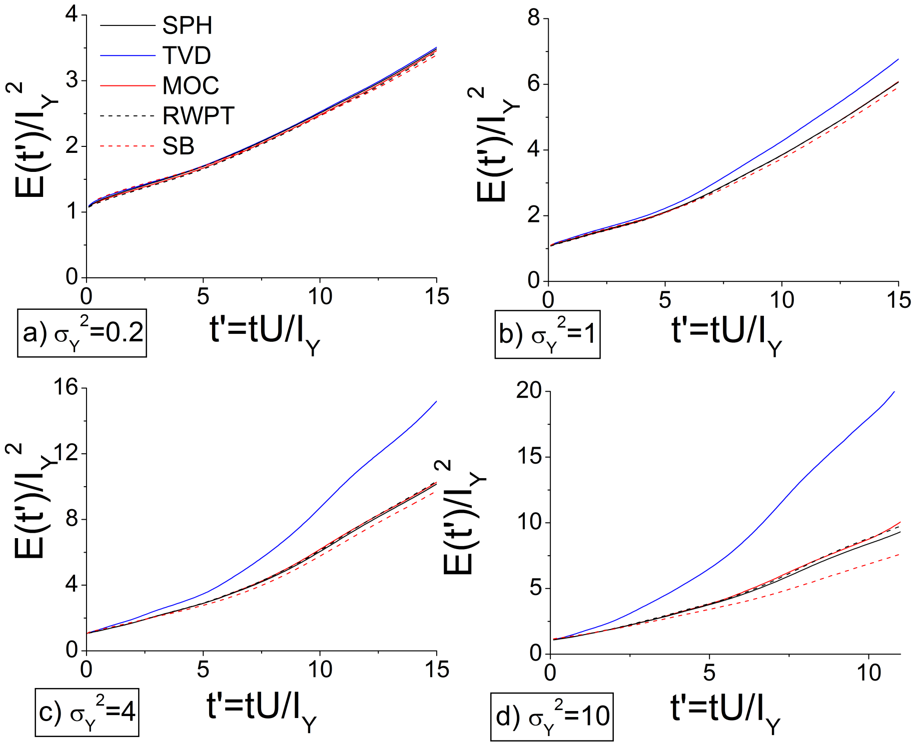

Figure 2.3: Dilution index E for the different heterogeneity fields for the conservative solute z as a function of time $t' = tU/I_Y$. I_Y is the (isotropic) integral scale of the formation.

A frequently used measure of mixing is the dilution index introduced by Kitanidis, 1994, in analogy with information theory, to quantify the amount of entropy, or disorder, in a system represented in our case by a disordered distribution of solutes concentrations. For a set of discrete concentration data, i.e. concentrations defined over a given support volume ΔV, which in our case coincides with the cell's or the particle's volume, the dilution index assumes the following expression (Kitanidis, 1994):

$$E(t) = \Delta V \exp(-\sum_{k=1}^{N} p_k \ln p_k) \tag{2.22}$$

where $p_k = c(\mathbf{x}_k, t)/M(t)$ and N is the number of concentration data. In Equation (2.22) we choose to consider only the cells whose concentration is larger than the dimensionless concentration threshold of $z_{\mathrm{lim}} = c_{\mathrm{lim}}/c_0 = 10^{-3}$. The dilution index is a measure of the volume occupied by the solute, whose evolution depends on the nonlinear interplay between local dispersion and concentration gradients (Kitanidis, 1994), both depending on the spatial distribution of the velocity field. Consequently, the numerical diffusion introduced by the approximation of the advective term causes local variations of dilution which affect the dilution index (Chilakapati and Yabusaki, 1999). However, as a global quantity the dilution index is rather insensitive to localized variations of dilution.

Figure 2.3 compares the evolution of $E(t)$ for σ_Y^2 ranging from 0.2 to 10. As

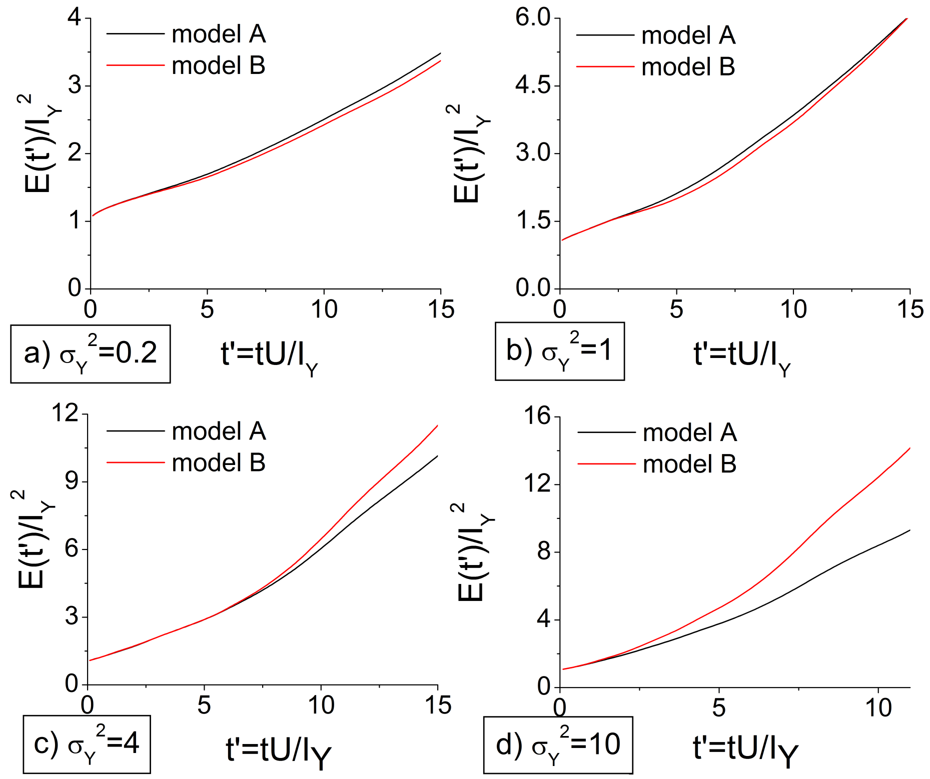

Figure 2.4: Dilution index E for the different heterogeneity fields for the conservative solute z as a function of time $t' = tU/I_Y$. I_Y is the (isotropic) integral scale of the formation. Black lines refer to the hydrodynamic dispersion model A (that is, uniform dispersion) and red lines refer to model B (that is, uniform dispersivity). Numerical simulations are performed with SPH.

expected, the dilution index increases more than linearly with time showing in all cases larger values when transport is simulated by TVD. On the other hand, SPH, RWPT and MOC provide very similar results, whatever the heterogeneity level. The dilution index of SB is slightly larger than for SPH and the other numerical schemes at early times but becomes smaller at intermediate and large times. Consequently, except at early times when the difference is negligible, SB underestimates E with respect to SPH, RWP and MOC, to an amount that increases with σ_Y^2. At all σ_Y^2 values considered in the present study the underestimation of E by SB is however much less than the overestimation by TVD. This is in agreement with the results shown in Figures 2.1 and 2.2 and confirms that TVD introduces numerical diffusion, while SB slightly underestimates dilution. The performance of SB at large σ_Y^2 is possibly penalized by the difficulty to compute correctly the volume of the nodes with errors that are expected to increase with σ_Y^2.

Overall, SPH, RWPT and MOC reproduce correctly, with very small reciprocal differences, the dilution index, therefore minimizing the impact of numerical diffusion. The large overestimation of E shown in Figure 2.3 suggests that TVD is unable to reproduce accurately dilution for moderately to high heterogeneous formations (i.e., $\sigma_Y^2 \geq 1$). All the numerical schemes reproduce accurately E in weakly heterogeneous formations.

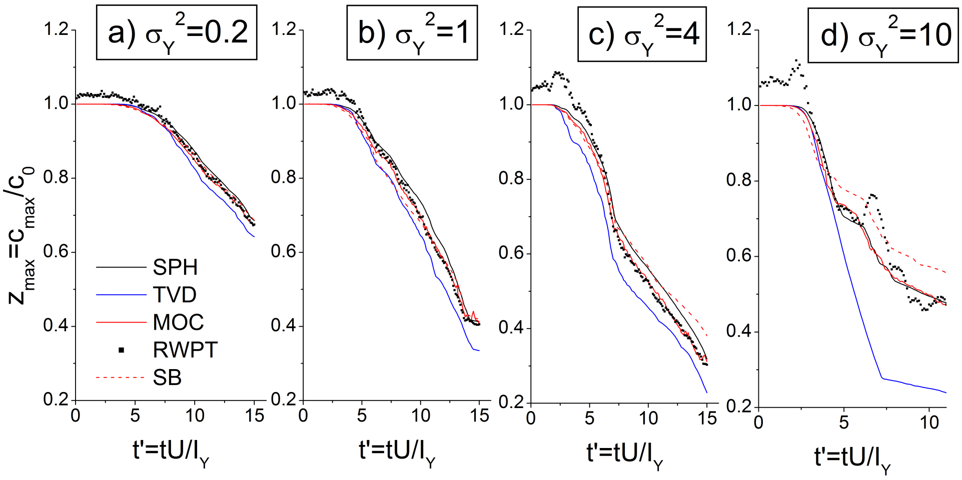

Figure 2.5: Peak concentration for the different heterogeneity fields for the passive tracer z as a function of time $t' = tU/I_Y$.

Figure 2.4 shows the dilution index obtained by solving the ADE (Eq. 2.1 for $i = 1$ and $r_1 = 0$) with SPH considering two different dispersion models: spatially constant dispersion (model A) and dispersion coefficients linearly dependent on the local velocity according to the Scheidegger model (2.4) with uniform dispersivity (model B). The difference between the two models of local dispersion is small to negligible for $\sigma_Y^2 = 0.2$ and $\sigma_Y^2 = 1$, but increases with σ_Y^2 and time, becoming large in highly heterogeneous formations, i.e. for $\sigma_Y^2 = 4$ and 10. In low velocity regions model A leads to a larger dispersive flux with respect to model B, whereas along fast paths it is the model B that introduces the largest local dispersion. Generally, the second effect is the strongest, so that the predicted dilution is larger for model B than for model A. The impact of the local dispersivity model is evident at large σ_Y^2 as an effect of the larger velocity variance which determines also larger differences between local dispersion coefficients.

A further measure of dilution is the maximum concentration of the conservative solute $z_{\max} = c_{\max}/c_0$. Unlike the dilution index, which is a global measure, the attenuation of the peak concentration with respect to the initial concentration c_0 is a local measure of dilution. Consequently, a faster attenuation with time of the peak concentration is symptomatic of a larger dilution and therefore a larger numerical diffusion, with all the other conditions unchanged. On the other hand, solute spreading affects the location of the peak concentration, whose position at a given time changes in each realization. This inverse relation between the overall dilution and the peak concentration is respected only in the case of small injection areas (Kapoor and Kitanidis, 1998).

In terms of accuracy of the numerical solution we observe for $z_{\max}$ the same problems evidenced with the dilution index (Fig. 2.5), with the difference that here for $\sigma_Y^2 \geq 4$ RWPT provides spurious oscillations on the value of $z_{\max}$ due to errors in computing the mass within the cell, whose size is $\Delta = I_Y/20$. The oscillations attenuate and progressively disappear as the cell is enlarged up to $\Delta = I_Y/5$. Notice that this size has been indicated as suitable to obtain reliable estimates of the

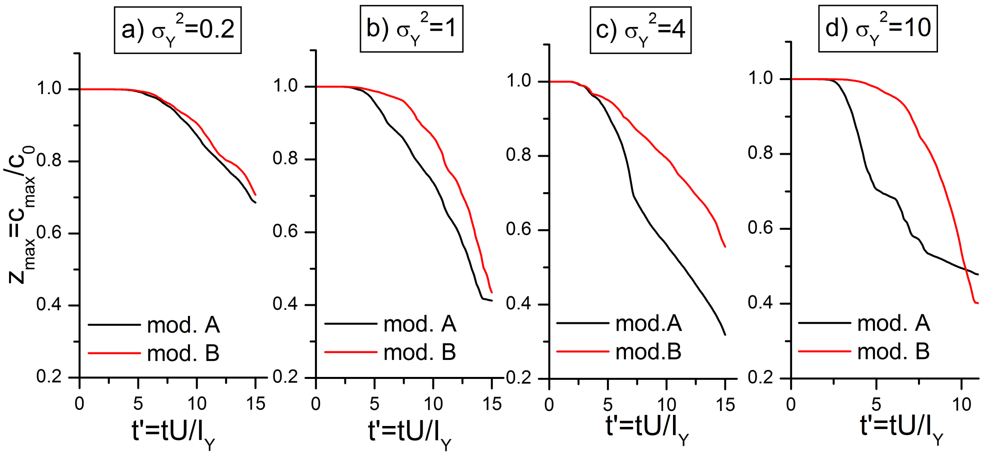

Figure 2.6: Peak concentration for the different heterogeneity fields for the passive tracer z as a function of time $t' = tU/I_Y$. Black lines refer to the hydrodynamic dispersion model A (that is, uniform dispersion) and red lines refer to model B (that is, uniform dispersivity). Numerical simulations are performed with SPH.

point concentration (Bellin, Rubin, and Rinaldo, 1994). This calls for a careful choice of the number of particles and the cell's size as discussed by Tonina and Bellin, 2008. While no detectable differences are observed between MOC and SPH, TVD underestimates $z_{\max}$ to an extent that increases with σ_Y^2. On the other hand, detectable differences between SB and SPH appear only for $\sigma_Y^2 \geq 4$, when SB tends to overestimate $z_{\max}$, and this confirms the tendency of SB to underestimate dilution, as already evidenced in Fig. 2.3.

Figure 2.6 compares the maximum concentration obtained with the models A and B of local dispersion by solving transport with SPH. The difference between the two models depends on the initial distribution of concentration, and in particular on the local transmissivity values. In this case $z_{\max}$ declines faster with time when the model A is used. The difference between the two models is small for $\sigma_Y^2 = 0.2$, thereby supporting the hypothesis of constant local dispersion introduced in first-order theories (Dagan, 1989), but increases fast with σ_Y^2 and the differences are larger than those observed for the same σ_Y^2 for the dilution index. Inspection of Figures 2.4 and 2.6 reveals that $z_{\max}$ is much more sensitive to the model of local dispersion than the dilution index (2.22). This indicates that $z_{\max}$ is a more sensitive indicator of dilution than the dilution index, because of its local nature confronted with the global nature of E.

2.5.2 Reactive transport

We consider here the case of an instantaneous injection of water containing a certain species A in an ambient water containing a species B. The two aqueous species react instantaneously upon mixing. This case is approximated by considering an injection water with a very small concentration of species B in equilibrium with species A, while the opposite is true for the ambient water, as shown in Table 2.1. We need to resort to this approximation because the equilibrium reaction requires

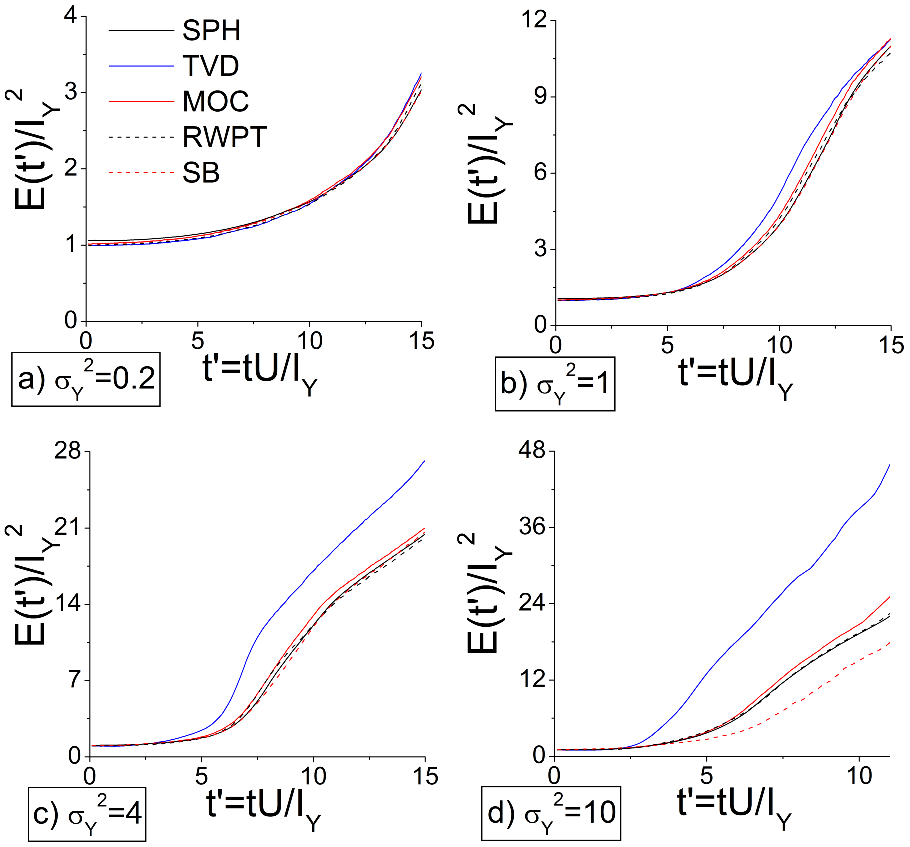

Figure 2.7: Dilution index E for the different heterogeneity fields for the reactive species A as a function of time $t' = tU/I_Y$.

that the product of the concentration of the two aqueous species remains locally constant.

Figure 2.7 shows the dilution index computed for the species A, whose concentration within the plume reduces as a combined effect of dilution and reaction with the species B, which is more abundant in the ambient water. At early times the dilution index remains nearly constant with the decay of the mass of the species A which compensates for the increase of E due to the dispersive flux. At later times, when the rate of consumption of the two reacting species reduces as shown in Figure 2.8, dilution dominates over mass consumption and the dilution index increases with time. Like in the nonreactive case, TVD overestimates dilution to an extent that is small to negligible in weakly heterogeneous formations, but becomes relevant for $\sigma_Y^2 > 1$.

Finally, Figure 2.8 shows the total mass of the species A consumed by the reaction, normalized over the mass of the injected species A. Coherently with the previously discussed results, when transport is modeled with TVD the injected mass of the species A is consumed more quickly than for the other numerical schemes. As expected the largest difference is observed for $\sigma_Y^2 = 10$, when also SB diverges from the prediction of the other numerical schemes, but to a lesser extent. In general, the consumption rate is initially fast until the almost complete consumption

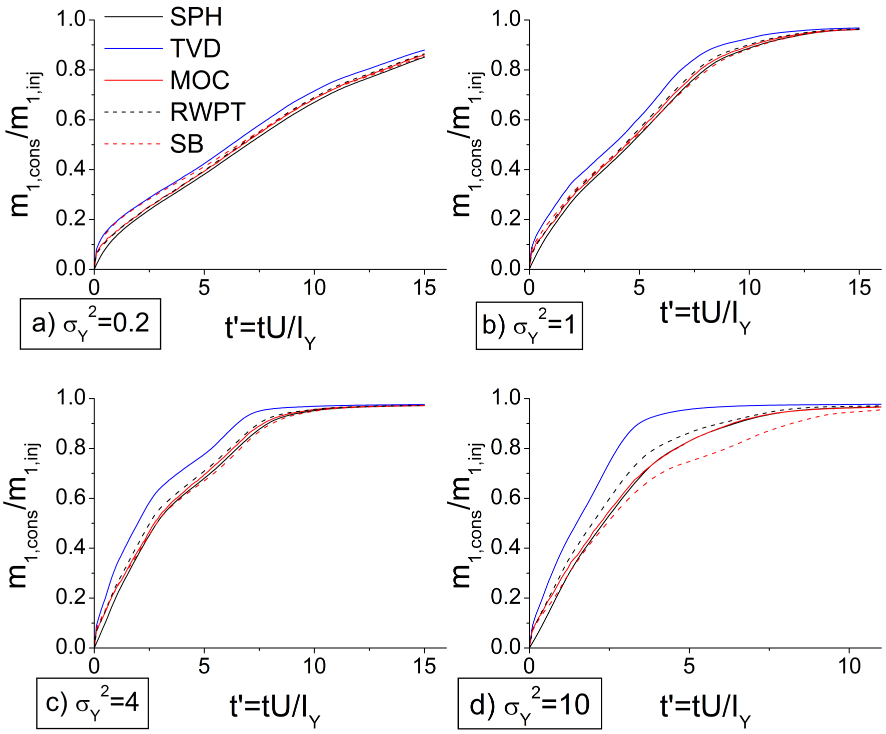

Figure 2.8: Relative fraction of mass of species A which is consumed by the reaction as a function of time $t' = tU/I_Y$ for the different heterogeneity fields.

of the injected A is approached. This asymptotic state is reached at larger times for weakly heterogeneous formations, as a result of a lower consumption rate due to slower dilution.

2.6 Conclusions

We compared the accuracy of several numerical schemes in solving the transport equation of nonreactive and reactive tracers in heterogeneous formations with increasing levels of heterogeneity. We considered the following numerical schemes: the Eulerian TVD Finite Volume method, the Eulerian-Lagrangian Streamline-Based method and the Method of Characteristics, and finally the Lagrangian Random Walk Particle Tracking and Smoothed Particle Hydrodynamics. In particular, we analyzed the numerical diffusion that these methods introduce in the discretization of the advective term, because of its negative impact on dilution and mixing-controlled reactions. A reliable, though not particularly sensitive, benchmark for evaluating artificial diffusion is constituted by the longitudinal and transverse spatial central moments evaluated by simulating transport with RWPT, because they are directly computed as inertial moments of the particle cloud and are thereby not affected by numerical diffusion. However, spatial moments are mostly sensitive to the spreading of the plume as an effect of the non-uniformity of the velocity field, though local dispersion influences these moments, especially in the transverse direction. Both SPH and MOC match these spatial moments, thanks to the accurate reproduction of particle trajectories and the zero or small amount of artificial diffusion. On the contrary, TVD and SB show larger differences, which emerge also at low heterogeneity levels for the Eulerian TVD method. We considered also several quantities differently related to the dilution process: the dilution index for both the conservative and the reactive species, the maximum value of concentration and the total consumed mass of the injected reactive species. All indicators show that TVD overestimates dilution, to an extent which increases as heterogeneity increases. SB provides different estimates of all the considered parameters for the highest heterogeneity case (σ_Y^2), generally underestimating dilution as an effect of the non-uniform distribution of particles used in the Monte Carlo integration of the diffusive term. In case of highly heterogeneous formations RWPT may be a good choice, but limited to conservative transport or simple reactions. Moreover local concentration values may be unreliable because of strong local concentration fluctuations. More complex reaction terms can be handled by SPH, which is in turn limited to isotropic dispersion tensor models (Herrera, Valocchi, and Beckie, 2010). In highly heterogeneous formations MOC shows significant mass balance errors and SB underestimates dilution. However, both numerical schemes are a valuable alternative to SPH at low heterogeneity.

Finally we considered how the model of local dispersion influences dilution in both weakly and highly heterogeneous formations. Considering local dispersion constant or linearly dependent on the local velocity does not make any difference in weakly heterogeneous formations, confirming what is suggested by classic results of first-order analysis in σ_Y^2 (Dagan, 1989). However, as heterogeneity increases, the two models result in large differences in the dilution index, indicating that the dependence of the local dispersion on the local velocity cannot be neglected for $\sigma_Y^2 > 1$.

Chapter 3

On the assessment of plume-scale concentration moments

3.1 Introduction

Dealing with aquifer contamination requires to provide fast and reliable tools for risk assessment. The prediction of the fate and transport of solute contaminants in groundwater is plagued by uncertainty, which is mostly due to the unknown spatial distribution of the hydraulic properties of the medium. Geostatistics gives the analytical means to mathematically investigate this issue. Stochastic hydrogeology was born from the merging between geostatistical tools and hydrogeological equations. Basically after thirty years of investigation, the scientific community has provided a mature set of stochastic quantities thanks to the fundamental work of several scientists.

On the one hand, local concentration moments and local probability distributions (pdfs) of concentration are useful for estimating the probability rates to exceed a threshold at specific locations, for example wells or localized receptors. Clearly these quantities are severely affected by uncertainty, whose role is even larger in case of small plumes, low values of local dispersion and high heterogeneity. Analytical or semianalytical means for quantifying this uncertainty are available in case of weak heterogeneity, in the framework of the first order approximation in the log-hydraulic conductivity variance (σ_Y^2) theory (Dagan, 1984). On the other hand, spatial moments should provide a global representation of the plume space and time evolution at the field scale. In particular, second central moments have been used for assessing the time-increasing volume of the solute body and have been related to the macrodispersion coefficients which describe the asymptotic behavior of the plume (see e.g. Aris, 1956; Dagan, 1990; Kitanidis, 1988). Unfortunately, because of the fluctuations of the plume's centroid registered by the particle displacement covariances, the second central moments and therefore also the macrodispersion values generally overestimate the actual dilution experienced by the real plume (Attinger *et al.*, 1999; Dentz *et al.*, 2000; Rajaram and Gelhar, 1993b). As a result adjustments to this kind of predictions are required (see e.g. Cirpka, 2002, Cushman and Ginn, 1993,Rubin *et al.*, 1999).

There remains a need for simplified and fast solutions to be used in practical applications (Pappenberger and Beven, 2006; Tartakovsky, Nowak, and Bolster, 2012; Tartakovsky and Winter, 2008). De Barros, Fiori, and Bellin, 2011, for example, moved in this direction providing simplified analytical solutions valid for transport in weakly heterogeneous anisotropic formations on the basis of existing well-known and easy-to-use solutions for homogeneous porous media. We focus on global averages calculated over the plume volume, aiming to describe the behavior of each single-realization plume and renouncing to obtain information referred to deterministic points in space. These global moments can provide useful information which could be representative of the whole dilution process, though necessarily lumped. The global mean, for example, decreases as dilution progresses, although it does not allow to distinguish between a well-mixed plume and a collection of patches with high and low concentration. The global variance, conceptually and operatively different from the global variance introduced by Kapoor and Gelhar, 1994b, measures the fluctuations of the local concentration values towards the global mean, thus sheds some light also on the concentration distribution within the plume volume. We consider different integral expressions for both the global mean and variance, and compare them to empirical single-realization numerical scenarios in different conditions, characterized by different log-conductivity variance σ_Y^2 (up to $\sigma_Y^2 = 2$), Peclet number ($Pe = UI_Y/D = 100$ and 1000) and source size. All the theoretical estimates are based on the integration of the local expected value of concentration, and are by construction valid at weak heterogeneity. In particular we consider (1) the equivalent plume in a homogeneous medium, subject to the local value of dispersion; (2) the equivalent plume subject to macrodispersion coefficients as computed from the rate of change of the particle displacement covariances X_{ij}; (3) the equivalent plume subject to corrected effective dispersion coefficients related to the rate of change of relative particle displacement covariances W_{ij}, coherently with a mobile reference system developed in Fiori, 2001a. In general model (1) overestimates and model (2) underestimates systematically the empirical moments, while model (3) could provide much more reliable a-priori estimations. We extend the comparison also to the peak concentration, even if it is more difficult to predict because of its very local nature, and to the Cumulative Frequency Distribution (CFD). Both quantities may be very useful for risk assessment purposes. The peak concentration is in fact directly comparable to concentration thresholds set by Environmental Law. As regards the CFDs, they provide the volume fraction of the plume whose concentration is below a given concentration threshold. We consider two theoretical estimates of the CFDs, related to the fully Lagrangian estimates (3) of the global concentration moments, to be compared to the empirical ones. The first is completely coherent with the structure built to define the global concentration moments according to model (3), whereas the second one assumes a Beta distribution model for the CFD and defines its shape by using the theoretical Lagrangian moments. The Beta choice is supported by a wide portion of the literature (Girimaji, 1991,Fiori, 1996,Pope, 2000,Fiori, 2001a, Fiorotto and Caroni, 2002,Bellin and Tonina, 2007,Cirpka *et al.*, 2008,Schwede *et al.*, 2008). Besides, we test the goodness-of-fit of the Beta distribution by also comparing empirical Beta CFDs, that is, Beta CFDs with shape parameters dependent on the empirical (numerical) moments of concentration.

In Sections 3.2 and 3.3 we describe the statistical tools which have been used, with a brief overview on the basic statistical theory. In particular in Section 3.3 we describe

the new theoretical model (3) in a fully Lagrangian framework. Section 3.4 lists the parameters for the numerical simulations. Finally Section 3.5 contains the results for all the compared quantities. For the sake of clarity all graphs are grouped at the end of the chapter.
The material of this chapter is the outgrowth of the collaboration with prof. A. Fiori (Universitá degli Studi Roma Tre, Rome, Italy), who outlined the analytical framework.

3.2 Theoretical framework - Local statistics

Stochastic hydrogeology is based on Random Space Functions whose use is suggested by the unknown spatial variability of the hydraulic properties of the geological formations. Geostatistics gives the instruments to describe the spatial correlation structure of the log-hydraulic conductivity Y of a porous medium. Thus Y is the primary Random Space Function which is used to describe the spatial distribution of the hydraulic properties of the medium. It is mainly defined by the mean m_Y, the variance σ_Y^2, and the two-point covariance function $C_Y(\mathbf{a},\mathbf{b})$ which is typically assumed to be stationary, that is, dependent solely on the distance vector $\mathbf{r}_{\mathrm{ab}} = \mathbf{a}-\mathbf{b}$ between the two quantities $Y(\mathbf{a})$ and $Y(\mathbf{b})$ whose correlation is considered. The integral scale $I_{\mathrm{Y,i}} = 1/\sigma_Y^2 \int_0^\infty C_Y(r_{\mathrm{ab,i}})dr_{\mathrm{ab,i}}$ quantifies the spatial persistence of the correlation of Y values in direction i. Field measurements as well as soft information on the geological history of a medium help to choose a mathematical shape for the covariance function of a formation and also to assign a value to the log-conductivity moments.

Through Darcy's law, the randomness of Y transfers to the velocity. Gelhar and Axness, 1983 found an analytical relation between $\hat{C}_Y$ and the velocity covariance $\hat{u}_{\mathrm{ij}}$ in the Fourier space under the assumption of steady flow and constant medium's porosity:

$$\hat{u}_{ij}(\mathbf{k}) = U_q U_n \left(\delta_{iq} - \frac{k_i k_q}{k^2}\right)\left(\delta_{jn} - \frac{k_j k_n}{k^2}\right)\hat{C}_Y(\mathbf{k}), \quad i,j,q,n = 1,m \tag{3.1}$$

where m is the number of dimensions and U_q is the mean velocity in direction q; $\mathbf{k}$ is the wave number vector with length k, since each covariance is characterized by different components which are related to different wave numbers. This relation has been demonstrated to be valid up to $\sigma_Y^2 = 4$ (Rubin, 2003).

Concentration can be regarded as a Random Space Function as well. Solute transport is in fact determined by the displacement of small solute masses as an effect of the non-uniform velocity field, as well as by diffusive/dispersive fluxes. These solute particles have the size of a few pores, so that they are subject to the punctual value of Darcy's velocity.

Detecting these solute masses in fixed control volumes ΔV centered in $\mathbf{x}$ gives an Eulerian representation of the concentration field $C(\mathbf{x},t)$ throughout the domain. The temporal concentration variation over ΔV is provided by advective and diffusive/dispersive mass exchanges between volumes. By considering $C = \langle C\rangle + C'$ and by ensemble-averaging a constitutive mass balance equation (the Advection Dispersion Equation), we obtain Partial Differential Equations for both the mean concentration $\langle C\rangle$ and the concentration variance σ_C^2. These PDEs require to conjecture closure assumptions, which are typically based on measurements or numerical simulations (Kapoor and Kitanidis, 1998), and rely on a small C' hypothesis.

On the other hand, following single particle displacements along streamlines gives a Lagrangian perspective on transport which is directly based on particle trajectories $\mathbf{X_t}$:

$$\mathbf{X_t}(t;\mathbf{a},t_0,\mathbf{D}) = \mathbf{X}(t;\mathbf{a},t_0,\mathbf{D}) + \mathbf{X_d}(t;\mathbf{D}) \tag{3.2}$$

where the total trajectory $\mathbf{X_t}$ of a particle starting in $\mathbf{a}$ at time t_0 is given by the sum of the advective particle displacement $\mathbf{X}$ and the dispersive displacement $\mathbf{X_d}$. Both $\mathbf{X}$ and $\mathbf{X_d}$ depend on the local value of the dispersion coefficients D_{ij}. $\mathbf{X_t}(t)$ is analytically related to the Lagrangian velocity $\mathbf{V_L}(t;\mathbf{a},t_0,\mathbf{D}) = \frac{d\mathbf{X_t}(t|\mathbf{a},t_0,\mathbf{D})}{dt}$, which has both an advective component $\mathbf{V}(\mathbf{X}(t))$ and a dispersive component $\mathbf{V_d}(\mathbf{D})$. The concentration moments are normalized over the uniform initial concentration c_0 over V_0; if the initial concentration is not uniform, the dimensionless quantity $C_0(\mathbf{a}), \mathbf{a} \in V_0$ takes into account its spatial distribution. The local value of concentration can thus be computed as follows, under the assumption of constant porosity:

$$C(\mathbf{x},t) = \int_{V_0} C_0(\mathbf{a})\delta[\mathbf{x} - \mathbf{X_t}(t;\mathbf{a},t_0,\mathbf{D})]d\mathbf{a} \tag{3.3}$$

where $C_0(\mathbf{a})$ is the dimensionless initial resident concentration in $\mathbf{a} \in V_0$.

The concentration mean $\langle C(\mathbf{x},t)\rangle$ and variance $\sigma_C^2(\mathbf{x},t)$, which characterize the local concentration $C(\mathbf{x},t)$ as a RSF, can be related to the statistics of particle displacements in the Lagrangian framework, as shown by Fiori, 1996.

Through mathematical manipulation (developed by Dagan, 1989), the displacement covariance tensor of $\mathbf{X}$ can be analytically related to the Fourier Transform of the velocity covariance $\hat{u}_{ij}$. The further assumption of uncorrelated particle displacements and uniform-in-the-mean stationary flow $\mathbf{U} = (U,0,0)$, allows a complete statistical characterization of $\mathbf{X}$ through a multi-normal pdf $f_{\mathbf{X}(t)}(\mathbf{x})$ (Rubin, 2003). Under the first order approximation in σ_Y^2 for the trajectory moments (Dagan, 1984), the one-particle covariances $X_{ij}(t;\mathbf{a},t_0,D_{ij})$ read:

$$\begin{aligned} &X_{ij}(t;\mathbf{a},t_0,D_{ij}) = \\ &\quad \frac{1}{(2\pi)^{m/2}} \iint_0^t \int_{-\infty}^{\infty} \hat{u}_{ij}(\mathbf{k}) \exp\left[-I\mathbf{k}\mathbf{U}(t'-t'')\right] \exp\left[-k_p k_r D_{pr}|t'-t''|\right] d\mathbf{k}dt'dt'' \end{aligned} \tag{3.4}$$

where m is the space dimensionality of the problem. The two-particle covariances $Z_{ij}(t;\mathbf{a}-\mathbf{b},t_0,D_{ij})$ can be computed as follows:

$$\begin{aligned} Z_{ij}(t;\mathbf{a}-\mathbf{b},t_0,D_{ij}) = \; & \tfrac{1}{(2\pi)^{m/2}} \iint_0^t \int_{-\infty}^{\infty} \hat{u}_{ij}(\mathbf{k}) \exp\left[-I\mathbf{k}(\mathbf{a}-\mathbf{b})\right] \exp\left[-I\mathbf{k}\mathbf{U}(t'-t'')\right] \\ & \exp\left[-k_p k_r D_{pr}(t'+t'')\right] d\mathbf{k}dt'dt'' \end{aligned} \tag{3.5}$$

Fiori and Dagan, 2000 developed explicit semi-analytical expressions for X_{ij} and Z_{ij} in case of exponential covariance C_Y and weakly heterogeneous formations.

$\mathbf{X_d}$ is a Brownian displacement, which is assumed to have a normal distribution $f_{\mathbf{X_d}}$ with zero mean and the following variance-covariance matrix:

$$X_{d,ij} = \langle \mathbf{X_d}'(t|\mathbf{a},t_0)\mathbf{X_d}'(t'|\mathbf{b},t_0)\rangle = \begin{cases} 2D_{ij}\min(t,t'), & \text{for } \mathbf{a}=\mathbf{b} \\ 0, & \text{otherwise} \end{cases} \tag{3.6}$$

where $\mathbf{X_d}'$ is the fluctuation associated to the dispersive displacement $\mathbf{X_d}$ with respect to its mean $\langle \mathbf{X_d}\rangle = 0$.
Fiori and Dagan, 2000 demonstrated also how, in weakly heterogeneous multi-Gaussian random fields, $\mathbf{X}$ and $\mathbf{X_d}$ can be assumed to be independent, so that $f_{\mathbf{X_t}} = f_{\mathbf{X}} f_{\mathbf{X_d}}$. Coherently with the first order approximation in σ_Y^2, local dispersion coefficients D_{ij} are considered constant and proportional to the mean longitudinal velocity U.

The dimensionless concentration mean $\langle C(\mathbf{x},t)\rangle$ and variance $\sigma_C^2(\mathbf{x},t)$ can be computed as follows:

$$\langle C(\mathbf{x},t)\rangle = \int\int_{V_0} C_0(\mathbf{a}) f_{\mathbf{X},\mathbf{X_d}}(\mathbf{X},\mathbf{x}-\mathbf{X}) d\mathbf{a} d\mathbf{X} \tag{3.7}$$

where $f_{\mathbf{X},\mathbf{X_d}}$ is the joint multi-variate normal pdf of the displacements $\mathbf{X}$ and $\mathbf{X_d}$, and:

$$\begin{aligned} \sigma_C^2(\mathbf{x},t) &= \langle C^2(\mathbf{x},t)\rangle - \langle C(\mathbf{x},t)\rangle^2 \\ &= \iint \iint_{V_0} C_0(\mathbf{a})C_0(\mathbf{b}) f_{\mathbf{XYX_dY_d}}(\mathbf{X},\mathbf{Y},\mathbf{x}-\mathbf{X_d},\mathbf{x}-\mathbf{Y_d}) d\mathbf{a} d\mathbf{b} d\mathbf{X} d\mathbf{Y} \\ &\quad -\langle C(\mathbf{x},t)\rangle^2 \end{aligned} \tag{3.8}$$

where $\mathbf{X}(t;\mathbf{a},t_0,\mathbf{D})$, $\mathbf{Y}(t;\mathbf{b},t_0,\mathbf{D})$, $\mathbf{X_d}(\mathbf{t};\mathbf{a},\mathbf{t_0},\mathbf{D})$ and $\mathbf{Y_d}(t;\mathbf{b},t_0,\mathbf{D})$ are the advective and dispersive displacements of the particles originating in $\mathbf{a},\mathbf{b} \in V_0$, and $f_{\mathbf{XYX_dY_d}}$ is the joint pdf of these displacements.
In the Lagrangian framework, $\langle C\rangle$ and σ_C^2 can thus be simply computed assuming weak heterogeneity and assigning values to $\mathbf{D}$ components.

Finally Fiori and Dagan, 2000 provided a simplified analytical solution for the concentration moments under the assumption of small initial volume V_0, with dimensions L_i $(i = 1, m)$ and uniform constant initial concentration C_0. The small V_0 hypothesis allows to drop the dependence of Z_{ij} on the distance between the points $\mathbf{r}_{\mathrm{ab}} = \mathbf{a} - \mathbf{b}$, and considerably simplifies the integrals in Eq. 3.5:

$$\langle C(\mathbf{x},t)\rangle = C_0 \prod_{i=1}^{m} \frac{1}{2}\left\{ \operatorname{erf}\left[\frac{x_i - U_i t + L_i/2}{\sqrt{2X_{t,ii}}}\right] - \operatorname{erf}\left[\frac{x_i - U_i t - L_i/2}{\sqrt{2X_{t,ii}}}\right]\right\} \tag{3.9}$$

$$\sigma_C^2(\mathbf{x_C},t) = C_0^2 \prod_{i=1}^{m} \int_{-L_i/2}^{L_i/2} \Theta_i(x_{C,i};a_i) da_i - \langle c(\mathbf{x_C},t)\rangle^2 \tag{3.10}$$

where

$$\begin{aligned} \Theta(x_i;a_i) = \quad & \frac{1}{\sqrt{2\pi X_{t,ii}}} \exp \frac{-(x_i - U_i t - a_i)^2}{2X_{t,ii}} \frac{1}{2}\left\{ \operatorname{erf}\left[\frac{L_i X_{t,ii}/2 + (x_i - U_i t)(X_{t,ii} - Z_{ii}) + a_i Z_{ii}}{\sqrt{2X_{t,ii}(X_{t,ii}^2 - Z_{ii}^2)}}\right]\right. \\ & \left. - \operatorname{erf}\left[\frac{-L_i X_{t,ii}/2 + (x_i - U_i t)(X_{t,ii} - Z_{ii}) + a_i Z_{ii}}{\sqrt{2X_{t,ii}(X_{t,ii}^2 - Z_{ii}^2)}}\right]\right\} \end{aligned} \tag{3.11}$$

Concentration is a RSF which is affected by a large amount of uncertainty, which depends on the unknown spatial variability of the velocity field. The uncertainty which affects the local mean concentration $\langle C(\mathbf{x},t)\rangle$ depends on the position of $\mathbf{x}$ with respect to the possible location and shape of the solute body at time t. Looking for the local statistics close to the theoretical centroid of a large solute body reduces the uncertainty on the predictions, as an effect of several, possibly interacting, reasons: (1) local scale dispersion (2) initial large size of the plume (3) large travel times which make the plume similar to the theoretical Gaussian plume. In the absence of pore scale dispersion the concentration variance is the largest, as predicted by Dagan, 1989. On the other hand, uncertainty is larger if we look at the local statistics in positions $\mathbf{x}$ possibly located along plume fringes. Moreover uncertainty is increased by the heterogeneity level which increases the irregularity of the plume and multiplies the possibilities for its development. Overall large plumes close to ergodicity or to Gaussianity are better predictable than small plumes in non-ergodic conditions. Thus one of the main causes of uncertainty is that we are looking for the statistical description of the concentration field in Eulerian locations, deterministically positioned in the domain, whereas the phenomenon develops in a Lagrangian and irregular way in the space.

Hence in order to reduce the impact of the heterogeneity-driven uncertainty Fiori, 2001a improved the classic definition of $C(t,\mathbf{x})$ (Eq. 4.26) by introducing the Lagrangian concentration $C_L(t;\boldsymbol{\xi},\mathbf{c},\mathbf{D_d})$:

$$C_L(t;\boldsymbol{\xi},\mathbf{c},\mathbf{D}) = \int_{V_0} C_0(\mathbf{a})\delta\left[\boldsymbol{\xi} - (\mathbf{X}_t(t;\mathbf{a},\mathbf{D}) - \mathbf{P}(t;\mathbf{c},\mathbf{D}))\right] d\mathbf{a} \tag{3.12}$$

$C_L(t;\boldsymbol{\xi},\mathbf{c},\mathbf{D})$ refers to a mobile system of coordinates $\boldsymbol{\xi} = \mathbf{x} - \mathbf{P}(t;\mathbf{c},\mathbf{D})$ centered in $\mathbf{P}(t;\mathbf{c},\mathbf{D})$. $\mathbf{P}(t;\mathbf{c},\mathbf{D})$ is the trajectory of the centroid of each Darcy's scale particle Δ which starts from $\mathbf{c} \in V_0$. Coherently with the new system of coordinates Fiori introduced also the new relative trajectory $\mathbf{W_t}(t;\mathbf{a},\mathbf{c},\mathbf{D}) = \mathbf{X}_t(t;\mathbf{a},\mathbf{D}) - \mathbf{P}(t;\mathbf{c},\mathbf{D})$ and its statistical properties under the first order approximation in σ_Y^2:

$$\langle \mathbf{W}_t(t;\mathbf{a},\mathbf{c},\mathbf{D})\rangle = \mathbf{a} - \mathbf{c} \tag{3.13a}$$

$$W_{t,ij}(t;\mathbf{a}-\mathbf{c},D_{ij}) = X_{ij}(t;D_{ij}) + 2D_{ij}t + Z_{ij}(t;\mathbf{a}-\mathbf{c}=0,D_{ij}) - 2Z_{ij}(t;\mathbf{a}-\mathbf{c},D_{ij}) \tag{3.13b}$$

These moments fully define the multi-variate normal pdf $f_{\mathbf{W_t}}$. He stated the expressions for the local mean and variance of the Lagrangian concentration:

$$\langle C_L(\boldsymbol{\xi},t;\mathbf{c},\mathbf{D})\rangle = \int_{V_0} C_0(\mathbf{a}) f_{\mathbf{W_t}}(\boldsymbol{\xi};t,\mathbf{a},\mathbf{c},\mathbf{D}) d\mathbf{a} \tag{3.14}$$

$$\begin{aligned}\sigma^2_{C_L}(\boldsymbol{\xi},t;\mathbf{c},\mathbf{D}) &= \textstyle\int_{V_0}\int_{V_0} C_0(\mathbf{a})C_0(\mathbf{b}) f_{W_{t1},W_{t2}}(\boldsymbol{\xi},\boldsymbol{\xi};t,\mathbf{a}-\mathbf{c},\mathbf{b}-\mathbf{c},\mathbf{D}) d\mathbf{a} d\mathbf{b}\\ &\quad - \langle C_L(t;\mathbf{c},\mathbf{D})\rangle^2\end{aligned} \tag{3.15}$$

where $f_{\mathbf{W_t}}$ is the pdf of $\mathbf{W}_t$, $f_{\mathbf{W_{t1}},\mathbf{W_{t2}}}$ is the joint pdf for the two displacements $\mathbf{W}_{t1} = \mathbf{X}_t(t;\mathbf{a}) - \mathbf{P}(t;\mathbf{c},\mathbf{D})$ and $\mathbf{W}_{t2} = \mathbf{X}_t(t;\mathbf{b}) - \mathbf{P}(t;\mathbf{c},\mathbf{D})$. If $\boldsymbol{\xi} = 0$ we are considering the estimates in $\mathbf{P}(t;\mathbf{c},\mathbf{D})$, centroid of each macroparticle Δ leaving from V_0. As stated by Fiori, $\mathbf{W}_t$ is a quantity which is much more stable than $\mathbf{X}_t$ since it is cleansed of the uncertainty on $\mathbf{P}$. Hence $\sigma^2_{C_L}$ is always smaller than σ^2_C, and local predictions are less uncertain. However **P** statistics needs to be considered if we want to have estimates referred to fixed positions in space (see Dentz, 2012; Fiori, 2001a).

A few works try to provide a full local statistical distribution of concentration, providing a more complete and precise measure of the uncertainty of the predictions at a specific location (see e.g. Cirpka and Kitanidis, 2000b; Cirpka *et al.*, 2008; Tartakovsky, Lichtner, and Pawar, 2003; Tartakovsky, Nowak, and Bolster, 2012). Most relevantly, cumulative distribution functions assess the exceeding probability with respect to concentration thresholds, possibly related to law limits. First, these pdfs are bounded by physical upper and lower limits for concentration which depend on the initial and boundary conditions of the system. Second, their shape has to respond to high heterogeneity-driven values of σ_C^2 by assigning high probability rates to the extreme values of the admissible interval. As a result, local mean concentration is definitely far from the mode, or possibly the multiple modes, which characterize the actual local pdf. In the absence of pore-scale dispersion, Dagan, 1982 pointed out that local pdfs are strictly bimodal, since the local value of concentration can be either 0 or C_0 (if C_0 is uniform within the source volume) depending on the position of the reference $\mathbf{x}$ with respect to the actual shape and spatial location of the solute body. Including also uncertainty results in a local pdf which reads: $f(C) = \langle C\rangle\delta\left[C_0 - C\right] + \left[C_0 - \langle C\rangle\right]\delta\left[C\right]$ where δ is the Dirac delta function. Also the cumulative distribution function (cdf) is not a Heaviside function centered on the actual local value of concentration, as it would be if we had no uncertainty on the local estimates, but reads: $F(C) = \left[C_0 - \langle C\rangle\right]H(C) + \langle C\rangle H(C - C_0)$, where H is the Heaviside step function. In this limit case, the variance is high and analytically related to the mean: $\sigma_C^2(\mathbf{x}) = \langle C\rangle\left(C_0 - \langle C\rangle\right)$. On the opposite extreme, as plume grows and time advances, uncertainty reduces and also pdfs get closer to normality (Bellin, Rubin, and Rinaldo, 1994).

Both numerical estimates (Caroni and Fiorotto, 2005; Fiorotto and Caroni, 2002) and theoretical speculations (Bellin and Tonina, 2007; Cirpka *et al.*, 2008; Fiori, 2001a) point towards the Beta distribution as an analytical model capable of reproducing these characteristics. The Beta distribution has a longer history in the description of mixing processes in turbulent settings (Girimaji, 1991; Pope, 2000; Rhodes, 1975) in the framework of 'assumed PDFs methods' (Pope, 1994). The use of the Beta distribution in groundwater problems is further sustained by the good comparison between the Beta pdf and the analytical procedure developed by Schwede *et al.*, 2008 in case of steady plume and continuous injection. For high σ_C^2 the Beta pdf is bimodal, with modes close to the extreme values of the admissible range of concentration, whereas it tends towards the Gaussian unimodal pdf at low σ_C^2. Moreover, the shape of the Beta is completely determined by the first two moments of concentration, for which several analytical and semianalytical theoretical formulations are available, among which the ones listed above.

3.3 Theoretical framework - Global statistics

Since the early times, the necessity to provide sound and practical tools for coping with plume and field-scale solute bodies has suggested to address stochastic hydrogeology from a global perspective (Dagan, 1984, 1990; Gelhar and Axness, 1983; Kitanidis, 1988; Neuman, Larrabee Winter, and Newman, 1987). This issue has been traditionally addressed in an Eulerian framework, by considering the space and time evolution of the mean concentration $\bar{C}$, representing the average concentration over adequately large volumes ΔV. In this simplified setting $\bar{C}$ obeys a macroscale Advection Dispersion Equation

$$\frac{\partial \bar{C}}{\partial t} + \mathbf{U} \cdot \nabla \bar{C} = \nabla \cdot \left(\mathbf{D_{mac}} \nabla \bar{C} \right) \tag{3.16}$$

where $\mathbf{U}$ is the regional average velocity and $\mathbf{D_{mac}}$ is the tensor of macrodispersion, which lumps both diffusive and dispersive effects taking into account all the subscale variability of velocity. A lot of effort has been put in the accurate prediction of the macrodispersion coefficients by linking them to the spatial central moments of the plume.

At this scale in fact the plume is characterized by the following spatial moments, which are obtained by integrating over the domain Ω: the total mass

$$M(t) = \int_\Omega \phi\, C(\mathbf{x}, t) d\mathbf{x} \tag{3.17}$$

which is constant in case of conservative solute (ϕ is the constant porosity); the barycenter of the plume:

$$\mathbf{R}(t) = \frac{1}{M(t)} \int_\Omega \phi\, x_j\, C(\mathbf{x}, t) d^m x, \quad j = 1, m \tag{3.18}$$

where m is the dimensionality of the problem; the second central moments:

$$S_{ij}(t) = \frac{1}{M} \int_\Omega \phi\, (x_i - R_i)\,(x_j - R_j)\, C(\mathbf{x}, t)\, d\mathbf{x}, \quad i, j = 1, m \tag{3.19}$$

Several different analytical or semianalytical approximations for S_{ij} are available in the literature, for instance in case of initially small solute bodies at large t (Rajaram and Gelhar, 1993b) or in stratified aquifers (Rajaram and Gelhar, 1993a). Spatial moments are undoubtedly less error prone than local statistics, but they cannot give a detailed description of the spatial variability of concentration. In addition, S_{ij} can provide an estimate for plume macrodispersion coefficients:

$$D_{\mathrm{mac,ij}}(t) = \frac{d\langle S_{ij}(t) \rangle}{dt} \tag{3.20}$$

which generally overestimate plume dilution (see e.g. Gramling, Harvey, and Meigs, 2002; Kapoor, Gelhar, and Miralles-Wilhelm, 1997; Kitanidis, 1988, 1994; MacQuarrie and Sudicky, 1990; Molz and Widdowson, 1988; Raje and Kapoor, 2000). Through S_{ij}, macrodispersion coefficients are related to both solute spreading and plume meandering, since S_{ij} depend on both solute-particle covariances X_{ij} and centroid trajectory covariances R_{ij} through:

$$\langle S_{ij}(t) \rangle = S_{ij}(t = 0) + X_{ij}(t) - R_{ij}(t) \tag{3.21}$$

Spreading depends on the Darcy's scale velocity non-uniformities which each particle encounters as it moves throughout the domain, whereas plume meandering, epitomized by the location of the plume's center of mass $\mathbf{R}$, depends on larger scale velocity non-uniformities (Fiori, 2001b). Only in case of large ergodic plumes, as travel time increases, R_{ij} as well as the initial size of the solute body become negligible, so $\langle S_{ij} \rangle$ do coincide with X_{ij}; also macrodispersion coefficients become more representative of the actual behavior of asymptotic plumes, but it is difficult to identify conditions which can be safely assumed ergodic (Fiori and Jankovic, 2005). Several attempts have been pursued in order to make macrodispersion coefficients more representative of the actual plume behavior. Rajaram and Gelhar, 1993b and later Attinger *et al.*, 1999 and Dentz *et al.*, 2000 were the first to point out the necessity to distinguish between the average of the S_{ij} of the spatial concentration distribution in every realization and the second moments of the ensemble-averaged concentration distribution. The latter procedure results in the overestimation of $D_{\mathrm{mac,ij}}$ with respect to the former, which somehow filters out part of the plume meandering. As ergodic conditions are approached, spatial and ensemble averages get closer (Kitanidis, 1992; Wang and Kitanidis, 1999). Rubin *et al.*, 1999 and Rubin, Bellin, and Lawrence, 2003, for example, tried to include subscale velocity non uniformities in block effective values of macrodispersion, which converge faster towards the actual representation of real plumes with respect to classic macrodispersion that represents the actual behavior of the plume only, if ever, at asymptotic times and for large plumes. Cirpka, 2002 proposed to determine effective dispersion coefficients obeying solute mass conservation rather than the relation with the spatial moments stated by Eq. 3.20. Others (see e.g. Cushman and Ginn, 1993; Hu, Cushman, and Deng, 1997; Koch and Brady, 1987) relied on non-local dispersion coefficients.

Instead, we focus here on the prediction of the global or integral concentration averages over the volume of the plume, and on the Concentration Frequency Distribution (CFD) within the plume itself. An intermediate step in this direction was performed by Tonina and Bellin, 2008, who provided analytical relations for the mean concentration and the mean variance of concentration on finite sampling volumes by neglecting the r dependence of Z_{ij}, and highlighted the strong impact of PSD on the concentration variance. Both the dimensionless global mean:

$$\langle \bar{C} \rangle = \frac{1}{V_s(C^*)} \int_{V_s(C^*)} C(\mathbf{x}, t) d\mathbf{x} \tag{3.22}$$

and the dimensionless global variance:

$$S_C^2 = \frac{1}{V_s(C^*)} \int_{V_s(C^*)} C(\mathbf{x}, t)^2 d\mathbf{x} - \langle \bar{C} \rangle^2 \tag{3.23}$$

are defined over a plume volume V_s which is enclosed by a iso-concentration curve with corresponds to a fixed concentration threshold C^*. C^* can for example correspond to a technical detection limit for the specific solute compound. These moments characterize the CFDs, which express of the probability $F(C \leq \mathsf{c})$ that any $C(\mathbf{x}, t)$ anywhere within the domain is lower than a reference concentration c:

$$F(C \leq \mathsf{c}) = 1 - \frac{V_s(\mathsf{c})}{V_s(C^*)} \tag{3.24}$$

Basically, $F(C \leq \mathsf{c})$ represents the volume fraction with respect to the total plume volume where $C \leq \mathsf{c}$. Both global moments and CFDs are disjointed from any spatial reference. Unlike local concentration moments, which have an evident stochastic meaning, global concentration moments refer to actual spatial averages for a single plume. They do not conceptually depend on statistics because they aim to describe the deterministic, single-realization case. Nevertheless, estimates for both the global mean and the global variance can be obtained by stochastic means, for example Monte Carlo simulations. Typically the stabilization of these quantities require a limited number of independent realizations, at least in weak and mild heterogeneous formations. Conversely, we use stochastic means belonging to the Lagrangian framework for a-priori estimating both the global mean and the global variance.

The global moments of concentration C can be computed by averaging the local estimates for C over the volume of the plume $V_s(C^*)$. The plume volume is thus defined with respect to a threshold concentration C^* according to the following equation:

$$V_s(C^*) = \int H[\langle C(\mathbf{x},t)\rangle - C^*]d\mathbf{x} \tag{3.25}$$

where H is the Heaviside function. In this way we are simply counting the number of deterministic locations $\mathbf{x}$ where the local estimate of concentration $\langle C(\mathbf{x},t)\rangle$ exceeds a given threshold C^*.
The spatial moments can be computed as follows:

$$\langle \bar{C}\rangle = \frac{1}{V_s(C^*)}\int_{V_s(C^*)} \langle C(\mathbf{x},t)\rangle d\mathbf{x} \tag{3.26}$$

$$S_C^2 = \frac{1}{V_s(C^*)}\int_{V_s(C^*)} \langle C(\mathbf{x},t)\rangle^2 d\mathbf{x} - \langle \bar{C}\rangle^2 \tag{3.27}$$

We compare three different solutions for estimating both $\langle \bar{C}\rangle$ and S_C^2, two traditional ones (labelled as 'Eulerian' and 'Homogeneous') and an original one, fully belonging to the Lagrangian framework. In all cases the initial source volume is characterized by a regular shape (L_i is the length of the side in direction i) and by a uniform initial concentration C_0. Although it would be possible to account for a non uniform but deterministic initial concentration distribution within V_0, this would make the integrals for computing $\langle C(\mathbf{x},t)\rangle$ more cumbersome.

For the Eulerian estimates we substitute the following:

$$\langle C(\mathbf{x},t)\rangle_{\mathcal{E}} = C_0 \prod_{i=1}^{m} \frac{1}{2}\left\{ \text{erf}\left[\frac{x_i - U_i t + L_i/2}{\sqrt{2X_{t,ii}(t)}}\right] - \text{erf}\left[\frac{x_i - U_i t - L_i/2}{\sqrt{2X_{t,ii}(t)}}\right]\right\} \tag{3.28}$$

into integrals 3.26 and 3.27. We refer to this method as 'Eulerian' because it refers to a deterministic location $\mathbf{x}$.

The second procedure equates the analytical solution for the concentration field in case of homogeneous equivalent medium to the estimates map:

$$\langle C(\mathbf{x},t)\rangle_{\mathcal{H}} = C_0 \prod_{i=1}^{m} \frac{1}{2}\left\{ \text{erf}\left[\frac{x_i - U_i t + L_i/2}{\sqrt{4D_{d,ii}t}}\right] - \text{erf}\left[\frac{x_i - U_i t - L_i/2}{\sqrt{4D_{d,ii}t}}\right]\right\} \tag{3.29}$$

Eq. 3.29 was substituted again into Eq. 3.26 and 3.27.

Finally, referring to the mobile reference system $\boldsymbol{\xi}$ centered in $\mathbf{P}(t;t_0,\mathbf{c})$ proposed by Fiori, 2001a, the spatial moments can be computed as follows:

$$\langle \bar{C}\rangle_{\mathcal{L}} = \frac{1}{V_s(C^*)}\int_{V_s(C^*)} \langle C_L(\boldsymbol{\xi},t)\rangle d\boldsymbol{\xi} \tag{3.30}$$

$$S^2_{C,\mathcal{L}} = \frac{1}{V_s(C^*)} \int_{V_s(C^*)} \langle C_L(\boldsymbol{\xi}, t)\rangle^2 d\boldsymbol{\xi} - \langle \bar{C}\rangle^2_{\mathcal{L}} \tag{3.31}$$

where $\langle C_L(\boldsymbol{\xi}, t)\rangle$ and $\langle C_L(\boldsymbol{\xi}, t)\rangle^2$ can be computed through Eq. 3.14 and 3.15. Integrals 3.26 and 3.27 may be cumbersome to compute, because the 'relative' displacement covariances W_{ij} depend on the distance $\mathbf{r}_{\mathrm{ab}} = \mathbf{a} - \mathbf{b}$ between $\mathbf{a}$ and $\mathbf{b}$ in V_0. If we neglect the dependence of W_{ij} on $\mathbf{r}_{\mathrm{ab}}$, $\langle C_L(\boldsymbol{\xi}, t)\rangle$ becomes:

$$\langle C_L(\boldsymbol{\xi}, t)\rangle_{\mathcal{L}} = C_0 \prod_{i=1}^{m} \frac{1}{2} \left\{ \mathrm{erf}\left[\frac{\xi_i + L_i/2}{\sqrt{2W_{t,ii}(t;0)}}\right] - \mathrm{erf}\left[\frac{\xi_i - L_i/2}{\sqrt{2W_{t,ii}(t;0)}}\right] \right\} \tag{3.32}$$

which considerably simplifies the numerical integration of Eq. 3.26 and 3.27. As in the previous cases, we consider also uniform C_0 in V_0; a non-uniform initial distribution could be considered, but it would make the numerical integrals 3.30 and 3.31 heavier.

The theoretical Lagrangian integral estimates of $\langle \bar{C}\rangle_{\mathcal{L}}$ and $S^2_{C,\mathcal{L}}$ can be computed in a number of different conditions which influence W_{ii} through both X_{ii} and Z_{ii}, namely: (1) the heterogeneity level, because both X_{ii} and Z_{ii} scale linearly with σ^2_Y; (2) the anisotropy of the formation, expressed by a non-unitary ratio between the integral scales of Y in different directions; (3) the dimensionality of the problem; (4) the intensity and the direction of the mean flow $\mathbf{U}$; (5) the plume initial size which would influence both Z_{ii} (if we considered its dependence on $\mathbf{r}$) and the limits of integration; (6) finally, the Peclet number which affects the displacement covariances, both in their advective part, although limitedly, and in their purely dispersive part.

In general Eulerian estimates are smaller than Lagrangian ones because of the overestimation of dilution through X_{ii}. On the contrary, homogeneous estimates do not account for the effect of heterogeneity on dilution, thus they overestimate the global moments.

$\langle C_L(\boldsymbol{\xi}, t)\rangle$ maps the local estimate of concentration referring to the centroid of the plume. The theoretical shape under the set of approximations which permits to write Eq. 3.32, is rather regular, and, above all, compact. This regular shape develops (expands) in a mobile reference system $\boldsymbol{\xi}$ centered in $\boldsymbol{P}(0, t)$, which is the trajectory of the centroid of the plume which corresponds at time 0 to the centroid of V_0. Thus the concentration distribution within the plume is more homogenized with respect to the actual frequency distribution of concentration. This means that the global averages (such as the mean and the variance) can be similar to the actual global averages of a real plume, but it could be harder to predict localized quantities, such as the maximum concentration, as well as CFDs.
Nevertheless, the equivalent plume maximum can be computed as follows:

$$\langle C_{\mathrm{L,max}}(t)\rangle_{\mathcal{L}} = C_0 \prod_{i=1}^{m} \mathrm{erf}\left[\frac{L_i/2}{\sqrt{2W_{t,ii}(t, \boldsymbol{\xi} = 0)}}\right] \tag{3.33}$$

whereas the theoretical prediction of the CFD can be predicted through Eq. 3.24 with $V_s(C) = \int H\left[\langle C_L(\boldsymbol{\xi}, t)\rangle - C^*\right] d\boldsymbol{\xi}$ similarly to Eq. 3.25.

3.4 Numerical set-up for the validation

In order to assess the validity of Equations 3.30 and 3.31 in describing the actual global moments of single-realization plumes, and the improvements with respect to the traditional theories, we compare the theoretical estimates to the actual empirical moments.

Simulations are performed in deterministic bidimensional fields, and all quantities are computed on a single-realization basis, coherently with the genesis of the theoretical procedure. The limits of such a procedure reside in the fact that the numerical testing is performed on 2D simulations, despite integral formulae have been derived in a generalized dimensionality. We leave the tests in three dimensions to future work.

Moreover it would be interesting to validate the theoretical approach on non multi-Gaussian Y fields, in order to assess the effect of different correlation structures. It has already been verified (Dagan, 2003; Fiori *et al.*, 2010) that different Y structures, and above all different correlation strengths for different Y classes, impact the behavior of apparent spmacrodispersion at asymptotic times.

The numerical simulations have been performed in a 2D uniform-in-the-mean flow field $\mathbf{U} = (U, 0)$ driven by a longitudinal constant hydraulic gradient. Multi-Gaussian hydraulic conductivity fields are generated with Hydro_Gen (Bellin and Rubin, 1996). The fields are characterized by a constant log-conductivity mean m_Y and an isotropic exponential Y covariance; the heterogeneity structures cover a $100I_Y \times 100I_Y$ domain. The variance σ_Y^2 ranges from 0.2 to 2 in order to test a few heterogeneity levels. Coherently with the first order approximation which lies at the basis of the theoretical predictions, σ_Y^2 are limited, the larger value being $\sigma_Y^2 = 2$, and the dispersion coefficients are constant. The flow field is computed with the classic finite volumes MODFLOW code (Harbaugh, Banta, and McDonald, 2000), developed by the USGS. Transport is computed with an SPH code (see Chapter 2) taking advantage of its adaptability to even highly non uniform velocity fields and its zero artificial diffusion; the number of particles is chosen so that their density remains almost uniform throughout the domain. The local dispersion tensor is uniform and isotropic: $\mathbf{D} = D\mathbf{I}$. Transport originates from instantaneous injection in source areas with different size: (1) small: $0.1I_Y \times 0.1I_Y$; (2) intermediate: $I_Y \times I_Y$; (3) large: $0.25I_Y \times 80I_Y$. The Peclet number is computed as $\mathrm{Pe} = UI_Y/D$. We test the combination of different heterogeneity levels (epitomized by σ_Y^2) and different isotropic Peclet numbers, assuming values typically encountered in real aquifers: $\mathrm{Pe} = 100$ and $\mathrm{Pe} = 1000$.

Results are presented in dimensionless form. Estimates of the actual global moments of the plume and of its volume can be determined once we assign values to U, I_Y, m_Y, σ_Y^2, D, c_0 and V_0, as well as to C^*. Since simulations are bi-dimensional and represent the vertical average of the system, we need also to define the thickness of the aquifer b.

3.5 Results and discussion

We compare several different means for predicting the global moments, the concentration peak and the Cumulative Frequency Distributions of concentration with the empirical quantities resulting from the numerical simulation. The traditional methods, Eulerian and Homogeneous, are shortly indicated with $\mathcal{E}$ and $\mathcal{H}$, whereas the fully Lagrangian method is identified by $\mathcal{L}$. A comprehensive list of the figures is attached at the end of the section, in order to make the consultation easier and the comparison between the different parameter combinations more direct. Figures are grouped on the basis of the quantity and the Peclet number.

Figures 3.4 – 3.9 list the global moments as computed for the different source sizes and the different Peclet numbers. In each group of figures, rows correspond to different σ_Y^2 values. The left column contains for each case the global mean $\langle \bar{C} \rangle$, whereas the right column contains the global variance S_C^2.
In each graph we draw: (1) the empirical moment as obtained from the numerical simulation; (2) the theoretical Eulerian estimate of the moment (Eq. 3.26 and 3.27, and Eq. 3.28); (3) the theoretical Homogeneous estimate of the moment (Eq. 3.26 and 3.27, and Eq. 3.29); (4) the theoretical Lagrangian estimate of the quantities (Eq. 3.30 and 3.31, and Eq. 3.32). Eulerian estimates do depend on both Pe and σ_Y^2 through X_{ii} and generally overestimate the dilution experienced by the plume because X_{ii} represent stochastically an ensemble of realizations. Also Lagrangian estimates do depend on Pe and σ_Y^2, but through W_{ii} which refer to a theoretical, closer to the actual, centroid of the plume and its trajectory. Homogeneous predictions depend on Pe but not on σ_Y^2 since they refer to the equivalent homogeneous field; since the considered $\mathbf{D}$ tensors are isotropic, also the equivalent homogeneous plume has a isotropic shape. The distance among the theoretical curves is larger as heterogeneity increases because of the dilution boost due to enhanced spreading. Obviously heterogeneity does not affect the homogeneous curves, which provide estimates for the equivalent homogeneous medium.

The Lagrangian estimates for both the global mean and the global variance reproduce well the empirical moments in all tested conditions, with a surprising accuracy.
The match with $\mathcal{L}$ is almost perfect in case of ergodic (line) injection for all the considered Peclet numbers (Pe $= 100$ and Pe $= 1000$) and tested levels of heterogeneity ($\sigma_Y^2 = 0.2, 1, 2$). The comparison with the global variance is slightly worst, especially for Pe $= 1000$ and $\sigma_Y^2 = 2$, because the variance, being an upper order moment, is more dependent than the mean on the concentration distribution within the plume volume. On the contrary, $\mathcal{E}$ and $\mathcal{H}$ curves respectively underestimate and overestimate the empirical values in a systematic way.
The finite $(I_Y \times I_Y)$ cases display a match which is just slightly worst between the empirical pattern and the theoretical Lagrangian estimates, despite the fact that these cases are not ergodic. In fact each plume moving in a different realization of the heterogeneous field has a very different shape evolving in time and space, especially as heterogeneity increases. In order to assess the impact of the single-realization on the global statistics, we simulate flow and transport on 25 independent realizations which share the same low order statistics of Y, in case of $(I_Y \times I_Y)$ injection and Pe $= 1000$ for the usual $\sigma_Y^2 = 0.2, 1, 2$ cases (Figure 3.16). The spread of the empirical global curves is not large, though growing with σ_Y^2 (from left to right in Fig. 3.16). The theoretical $\mathcal{L}$ predictions for both $\langle \bar{C} \rangle$ and S_C^2 lay in the middle of the sheaf in all cases, differently from $\mathcal{E}$ and $\mathcal{H}$ models. The match for the single reference realization improves with higher σ_Y^2 and Pe $= 1000$, but it could be an artificial

effect due to the specific realization. Here Homogeneous and Lagrangian predictions are very close for $\sigma_Y^2 = 0.2$ because of the weak contribution of heterogeneity, and thus spreading, to dilution.
In case of small injection, $\mathcal{H}$ and $\mathcal{L}$, but also $\mathcal{E}$, are even closer. The concentration detection limit becomes rapidly smaller than the mean concentration within the plume, and also $V_s(C^*)$ soon contains a much smaller amount of solute mass with respect to the total injected mass. The Eulerian theory overestimates dilution to such an extent that rapidly the mean concentration becomes lower than the prescribed concentration threshold. Empirical dots are always included, for this realization, between $\mathcal{H}$ and $\mathcal{L}$, whereas $\mathcal{E}$ is too low because of the big role of uncertainty which affects X_{ii}. Since the plume size is smaller than I_Y, there is large uncertainty on the Y structures initially involved by the plume, but also on the space-time evolution of the solute body.

Figures 3.10 – 3.15 list the prediction and simulations for the maximum value of concentration and the Cumulative Frequency Distribution at a specific timestep. In general the peak predictions provided by all the three models behave badly, because of the contrast between the nature of the theoretical estimates and the physical phenomena, which keep high, in actual solute bodies, the local concentration values. In particular, Eulerian and Lagrangian estimates underestimate $C_{\max}$ because of the artificial effect, in both theories, which imposes $C_{\max}$ to be inversely proportional to dilution, regardless of the heterogeneity level and of the plume size. In real aquifers, this is not always the case.
In case of large line injection, the Lagrangian and Eulerian predictions compare very poorly to the empirical values. In such scenarios, the empirical peak concentration is located in the low permeability regions which belong to the source volume. Their time decrease depends on the action of local dispersion, which, as the almost sole dilutive effect, slowly smoothen concentration peaks. On the contrary, adjacent regions characterized by higher permeability values are subject also to the effect of advection, which contributes to dilution by moving solute downstream and developing fringe regions where mixing is enhanced. In this way, high concentrations are recorded at the centroid of solute blobs, whose size becomes with time smaller than the original source size. As a result, the homogeneous estimates follow more closely the behavior of the empirical maxima at least at early and intermediate times. Then, as the solute begins to leave the retention low permeability regions, also σ_Y^2 contributes to the decrease of $C_{\max}$. The initially slowly decreasing pattern would persist longer in case of velocity dependent dispersion coefficients (see Chapter 5).
The comparison with the Lagrangian maximum values improves as the plume initial size reduces, as heterogeneity decreases and as Peclet increases. Both Peclet and heterogeneity play a role in determining the erosion of high concentration values. As a result, Lagrangian estimates become more similar to numerical values than Homogeneous estimates. However, these general indications can be controverted by single realizations, since small source volumes mean non-ergodic conditions. As stated above, the maximum concentration dynamics is decisively dependent on local phenomena, and thus on the single case.
This is clear if we look at the series of realizations in case of intermediate injection, where the peak concentration for each Y field spans over a much larger zone than the moments. In fact the maximum concentration depends also on the Y distribution

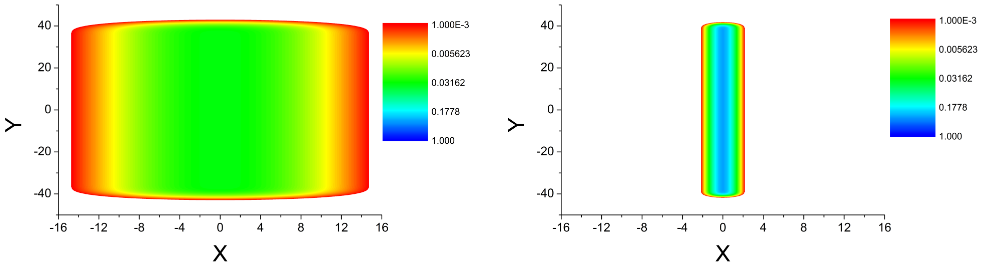

(a) $\mathcal{E}$ theoretical plume **(b)** $\mathcal{H}$ theoretical plume

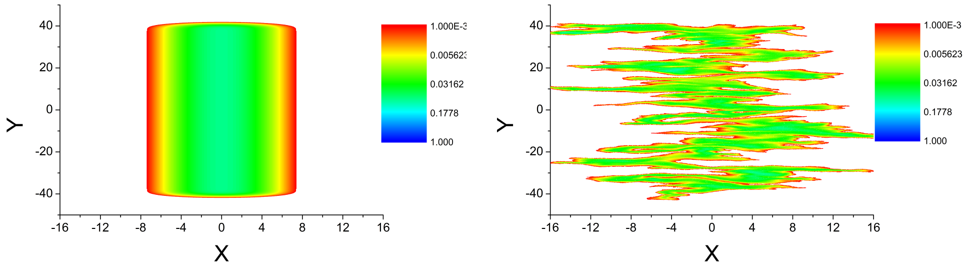

(c) $\mathcal{L}$ theoretical plume **(d)** Numerical plume

Figure 3.1: Snapshots of the plume at time $t' = tU/I_Y = 20$ for the line injection ergodic plume in case of $\sigma_Y^2 = 1$ and Pe $= 100$: Numerical and Theoretical plumes. Notice that the color palette is logarithmic.

within the source area. In the case of $(I_Y \times I_Y)$ injection, the numerical predictions of our reference realization lay between the $\mathcal{H}$ and $\mathcal{L}$ estimates, whereas $\mathcal{E}$ estimates are too low. Anyway, the Lagrangian prediction, although not centered and favored by the large spread of the empirical curves, unlike $\mathcal{E}$ and $\mathcal{H}$, belongs to the empirical sheaf in all cases.

In the limit case of small injection, the best prediction is provided by the homogeneous model, since the shape of the solute body is very similar to the compact regularized theoretical one, and the maximum concentration displays a behavior which is more or less exactly inversely proportional to dilution as in the homogeneous case. However, the small size of the plume allows to state that the larger σ_Y^2, the faster the $C_{\max}$ decrease not only for the theoretical estimate, where this natively happens, but also for the empirical simulations because the plume remains compact.

The same group of Figures (from Fig. 3.10 to Fig. 3.15) contains also the Cumulative Frequency Distributions, both empirical and theoretical. For the ergodic and intermediate cases, CFDs refer to $t' = tU/I_Y = 20$, whereas for the small injection $t' = 5$. The theoretical lines refer to three different theoretical models, two of them relying on the Lagrangian estimates of the global moments, taking advantage of the good comparison between these estimates and the empirical moments:

- 'Theoretical' Beta CFD $F(C \leq \mathsf{c}; p_1, p_2) = \frac{\int_0^{\mathsf{c}} x^{p_1-1}(x-1)^{p_2-1}dx}{\int_0^1 x^{p_1-1}(1-x)^{p_2-1}dx}$, whose shape parameters, $p_1 = \langle \bar{C} \rangle (\langle \bar{C} \rangle (1 - \langle \bar{C} \rangle)/S_C^2 - 1)$ and $p_2 = (1 - \langle \bar{C} \rangle)(\langle \bar{C} \rangle (1 -$

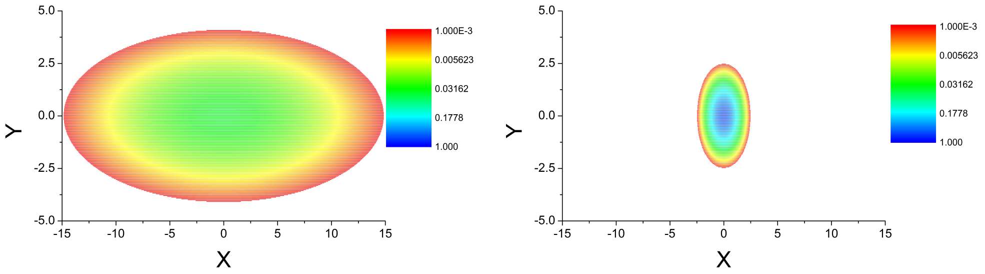

(a) $\mathcal{E}$ theoretical plume **(b)** $\mathcal{H}$ theoretical plume

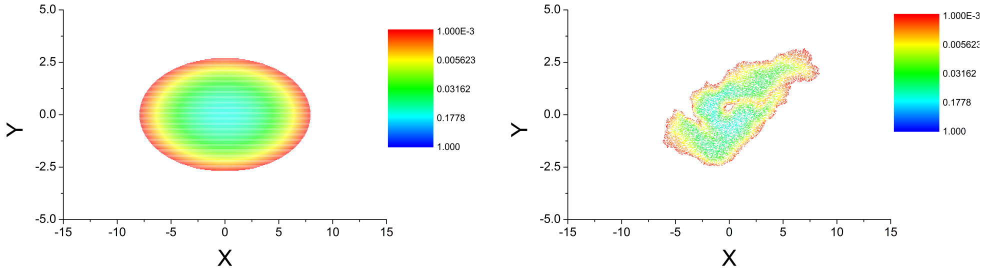

(c) $\mathcal{L}$ theoretical plume **(d)** Numerical plume

Figure 3.2: Snapshots of the plume at time $t' = tU/I_Y = 20$ for the intermediate $(I_Y \times I_Y)$ injection plume in case of $\sigma_Y^2 = 1$ and $\text{Pe} = 100$: Numerical and Theoretical plumes. Notice that the color palette is logarithmic.

$\langle \bar{C} \rangle)/S_C^2 - 1)$, depend on the mean $\langle \bar{C} \rangle$ and the variance S_C^2 of the distribution of concentration. C is the dimensionless random variable varying between 0 and 1, whereas $\mathsf{c} \in [0, 1]$ is the dimensionless concentration threshold for the cumulative frequency distribution. Both p_1 and p_2 are computed with the method of moments, thus substituting to $\langle \bar{C} \rangle$ and S_C^2 the values of the theoretical Lagrangian global moments (Eq. 3.30 and 3.31, and Eq. 3.14);

- 'Empirical' Beta CFD $F(C \leq \mathsf{c}; p_1, p_2) = \frac{\int_0^{\mathsf{c}} x^{p_1-1}(x-1)^{p_2-1}dx}{\int_0^1 x^{p_1-1}(1-x)^{p_2-1}dx}$, whose shape parameters are computed by the method of moments substituting to $\langle \bar{C} \rangle$ and S_C^2 in p_1 and p_2 expressions the numerical global moments for the concentration;

- Theoretical CFD, which is computed according to Eq 3.24 for the whole range of concentrations belonging to $[C^*, 1]$, where C^* is the dimensionless threshold concentration, which in our simulations is equal to 0.001, and 1 is the dimensionless value of initial concentration $C_{\max}(t = 0) = c_0/c_0$. Volumes $V_s(C)$ are approximated in a Lagrangian sense, thus considering $V_s(C) = \int_\Omega H\left[\langle C_L(\boldsymbol{\xi}, t) \rangle - C^*\right] d\boldsymbol{\xi}$;

Hence we consider two Beta models, taking advantage of the fact that the Beta distribution has been demonstrated in the past to be a reliable analytical tool for predicting and describing the concentration distribution at both the local scale and the global scale (Bellin and Tonina, 2007; Caroni and Fiorotto, 2005; Cirpka *et al.*, 2008; Fiori, 1996, 2001a; Fiorotto and Caroni, 2002; Schwede *et al.*, 2008). The Beta

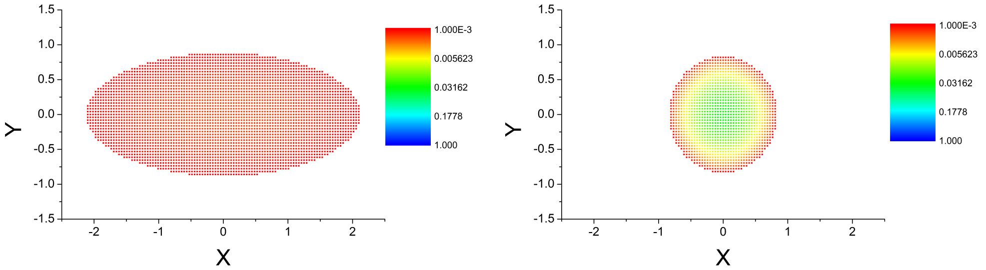

(a) $\mathcal{E}$ theoretical plume **(b)** $\mathcal{H}$ theoretical plume

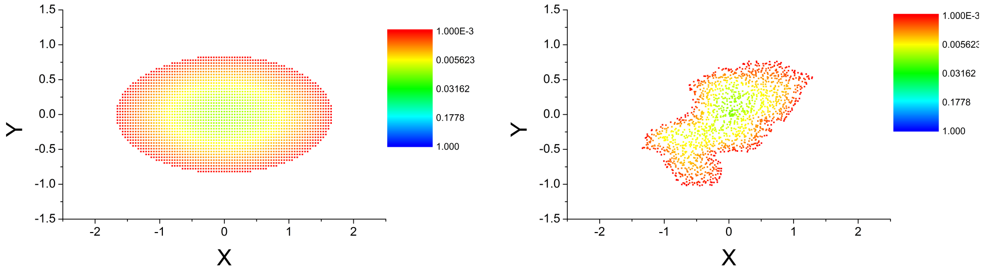

(c) $\mathcal{L}$ theoretical plume **(d)** Numerical plume

Figure 3.3: Snapshots of the plume at time $t' = tU/I_Y = 5$ for the small $(0.1 I_Y \times 0.1 I_Y)$ injection plume in case of $\sigma_Y^2 = 1$ and $\mathrm{Pe} = 100$: Numerical and Theoretical plumes. Notice that the color palette is logarithmic.

distribution is set once the first two moments and thus the shape parameters are provided. The theoretical Lagrangian estimates of the global moments are a-priori known, hence the development of the correspondent Beta distribution is immediate. In this way we would have an analytical tool for predicting the whole concentration distribution within the plume. In the following we try to assess the capability of these Beta CFDs to reproduce the empirical CFDs. For the sake of completeness, and in order to determine the goodness of the Beta distribution as analytical tool for predicting actual CFDs, we also consider the Beta distribution with moments taken from the correspondent numerical simulations.

The theoretical CFD model, based on the prediction of the plume volume for specific iso-concentration contours, is coherent with the Lagrangian representation of the theoretical plume, but suffers the very regular shape that the theoretical plume develops. In particular the theoretical equivalent plumes greatly homogenize the concentration distribution within the plume to a much stronger extent than the real solute bodies, except that they have very similar global low order concentration moments. As an example of the homogenized appearance of $\mathcal{L}$ plumes, in Figures 3.1, 3.2 and 3.3, we represent the snapshots of the actual numerical plumes and of the corresponding theoretical $\mathcal{E}$, $\mathcal{H}$ and $\mathcal{L}$ plumes for the same t' and $C^* = 0.001$. All plumes'centroids are in $(0, 0)$.

The match of the empirical Beta model is in fact almost perfect in all cases, regardless of the initial plume size. Thus the prediction of the theoretical Beta models is better for closer predictions of the theoretical moments to the empirical moments.

For the line injection, both Beta distributions have a good match with the empirical CFDs, with better performances for Pe = 100. On the contrary, the theoretical Lagrangian CFDs do not compare well with the empirical CFDs. This is because the predicted homogenized and regularized theoretical plumes are very different from the actual shape of the solute body, as captured by the snapshots (Figures 3.1) for the Pe = 100 and $\sigma_Y^2 = 1$ case at time $t' = 20$.

In the intermediate injection case, the theoretical Beta distribution is slightly more distant to the empirical CFD. However, in general, looking at the series of 25 independent realizations, the overall performance of the Beta models compares well with the empirical distributions. Also the behavior of the fully theoretical Lagrangian CFD belongs to the range individuated by the multiple realizations, but performs poorly at the highest concentrations.

In the small injection case at the chosen time ($t' = 5$) the plume is almost totally diluted, with the CFD which is completely leant against the $C_{\mathrm{amb}} = 0$ value, especially for Pe = 100. Both theoretical CFDs overpredict dilution in all cases with respect to the empirical CFDs, as a result of the underprediction of the theoretical $\mathcal{L}$ moments compared to the numerical ones.

3.6 Conclusions

We compared a few theoretical estimates for the global statistics to the empirical correspondent values obtained through single-realization numerical simulations of transport as a result of instantaneous injection scenarios. From this perspective, the comparison with single-realization numerical plumes should quantify the capabilities of the semianalytical tools to describe the space and time evolution of actual dilution of solute bodies. The aim is trying to provide reliable a-priori estimates for the global statistics at the plume scale, in order to facilitate risk assessment. Quantifying the global mean and the global variance of concentration over the plume volume provides effective indications also about the dilution experienced by the plume. As a matter of fact, the mean concentration reduces as dilution progresses, because nearly the same amount of mass (if the concentration threshold C^* is sufficiently low) occupies a progressively larger volume, whereas the global variance approaches zero. Nevertheless, we considered also a series of independent realizations in order to assess the spreading of the sheaf of curves for each quantity in response to different hydraulic conductivity fields.

In particular we tested a new fully Lagrangian estimate for the global moments, belonging to the setup developed in Fiori, 2001a. These estimates rely on the theoretical statistical estimate of the relative particle displacements, which are referred to the actual, although not deterministically positioned, centroid of the plume, and are sensitive to both the heterogeneity of the medium (though necessarily weak) and the Peclet number. Differently from the classic models based on the macrodispersion theory, the fully Lagrangian theoretical estimates filter out most of the uncertainty due to the unknown position of the actual plume centroid. Moreover, they include the boosting effect of spreading to dilution which is neglected by the equivalent Gaussian plume, where advection is limited to rigid shift whereas dilution is driven by the effect of pore scale dispersion. As a result, the fully Lagrangian estimates compare much better than the classic theories to the empirical moments, despite the

assumptions which lie at the basis of the computed theoretical models (i.e. weak heterogeneity and two-particle displacement covariances Z_{ij} not dependent on the distance between the two points, as strictly valid only in case of point injection).
However, a coherent theoretical prediction of the peak concentration is not equally good. The development of reliable predictions for the maxima would require a separate analysis on different theoretical bases.
We then used the Lagrangian estimates for the concentration to draw the Cumulative Frequency Distributions (CFDs). The best match between a-priori models and the empirical CDFs is given by the Beta distribution model, where the shape parameters are computed from the theoretical predictions of the moments. Such a instrument allows to predict the spatial distribution of the concentration within the solute body, for example estimating the volume fraction above or below a given threshold. Moreover, we can also assess how the concentration distribution changes in time as a result of the evolution of the global moments.

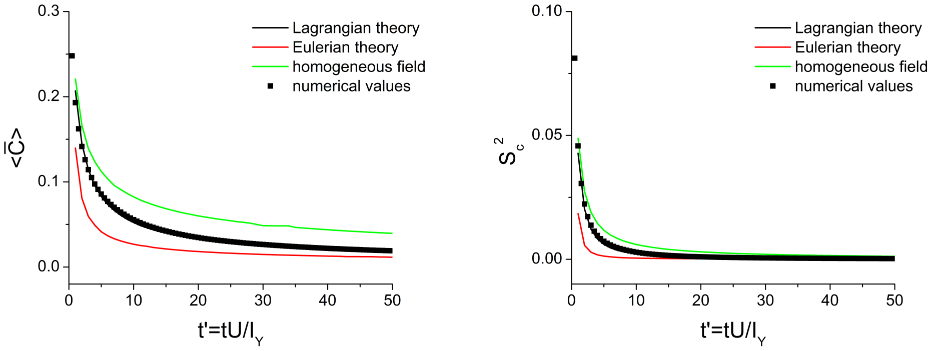

(a) $\sigma_Y^2 = 0.2$ - Pe $= 100$ **(b)** $\sigma_Y^2 = 0.2$ - Pe $= 100$

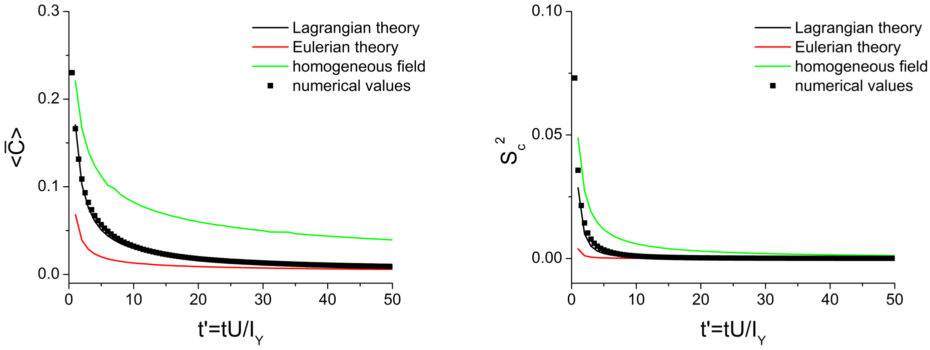

(c) $\sigma_Y^2 = 1$ - Pe $= 100$ **(d)** $\sigma_Y^2 = 1$ - Pe $= 100$

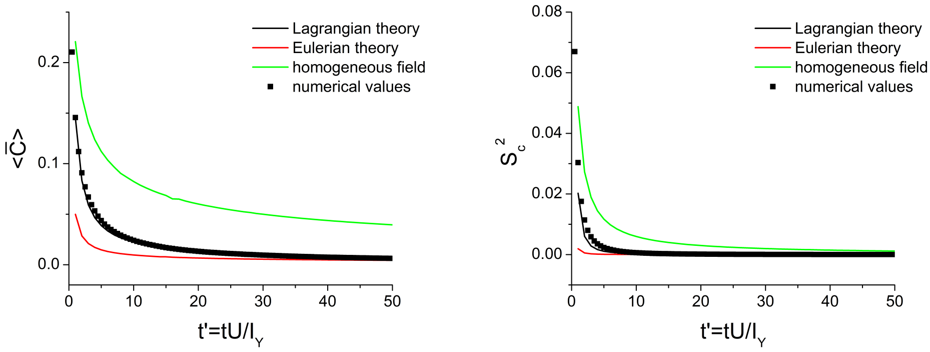

(e) $\sigma_Y^2 = 2$ - Pe $= 100$ **(f)** $\sigma_Y^2 = 2$ - Pe $= 100$

Figure 3.4: Dimensionless global mean $\langle \bar{C} \rangle$ and variance S_C^2 for the line injection case and Pe $= 100$ for the passive solute. Dots represent the empirical moments, whereas lines represent the theoretical models, whose color refers to: Eulerian theory ($\mathcal{E}$, red), Homogeneous theory ($\mathcal{H}$, green) and Lagrangian theory ($\mathcal{L}$, black).

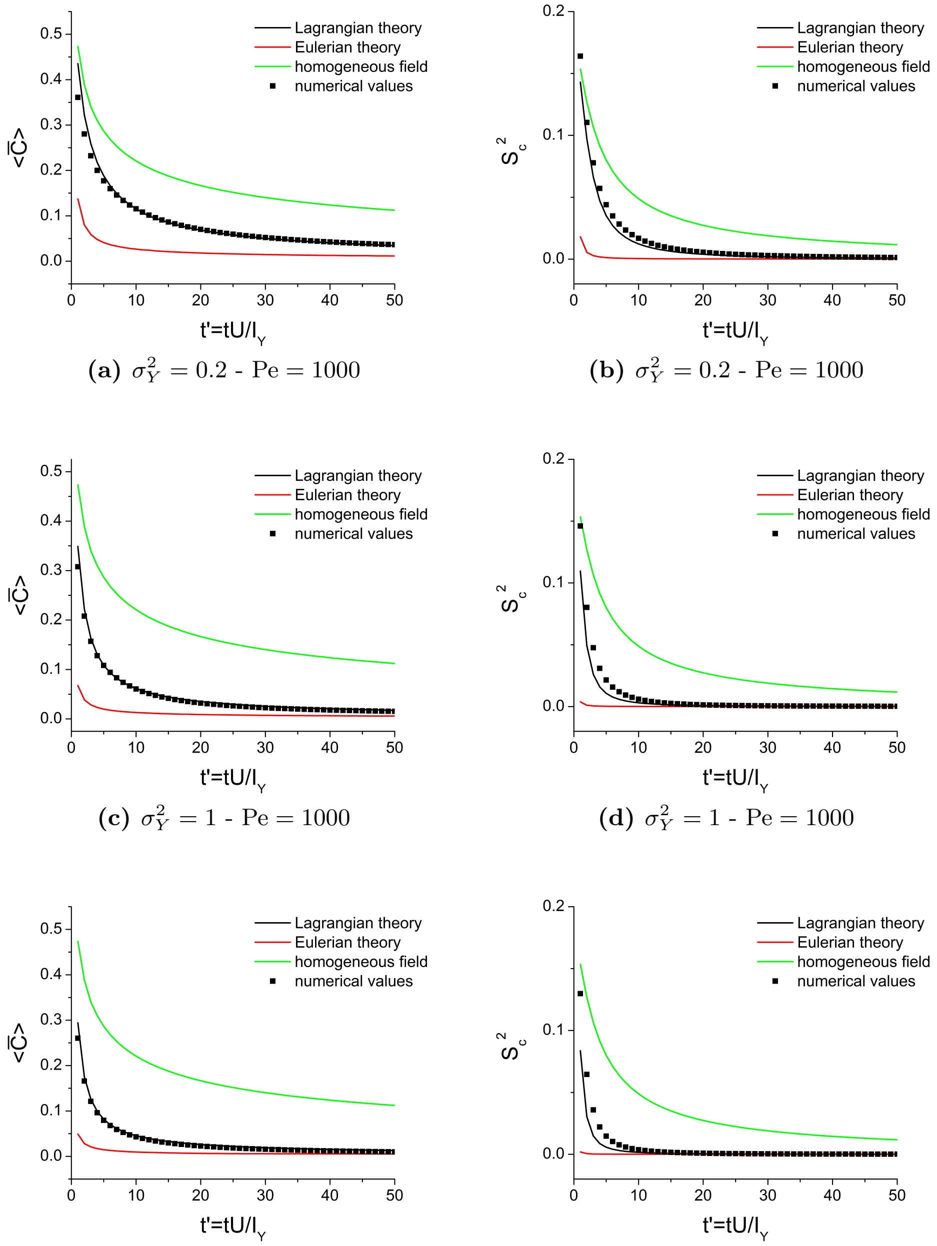

(a) $\sigma_Y^2 = 0.2$ - Pe $= 1000$ **(b)** $\sigma_Y^2 = 0.2$ - Pe $= 1000$

(c) $\sigma_Y^2 = 1$ - Pe $= 1000$ **(d)** $\sigma_Y^2 = 1$ - Pe $= 1000$

(e) $\sigma_Y^2 = 2$ - Pe $= 1000$ **(f)** $\sigma_Y^2 = 2$ - Pe $= 1000$

Figure 3.5: Dimensionless global mean $\langle \bar{C} \rangle$ and variance S_C^2 for the line injection case and Pe $= 1000$ for the passive solute. Dots represent the empirical moments, whereas lines represent the theoretical models, whose color refers to: Eulerian theory ($\mathcal{E}$, red), Homogeneous theory ($\mathcal{H}$, green) and Lagrangian theory ($\mathcal{L}$, black).

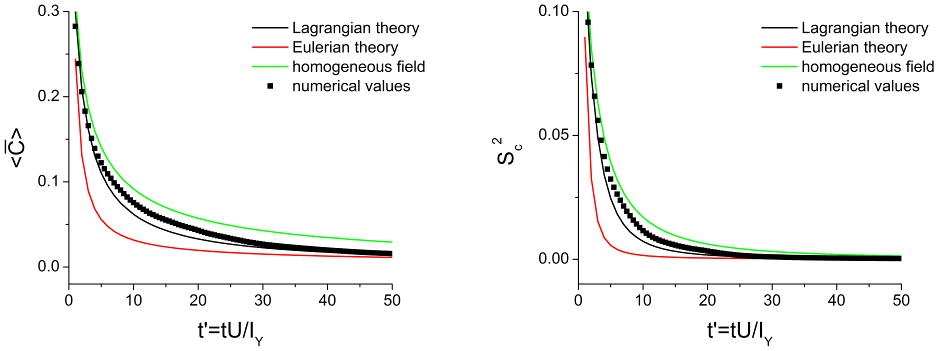

(a) $\sigma_Y^2 = 0.2$ - Pe $= 100$ **(b)** $\sigma_Y^2 = 0.2$ - Pe $= 100$

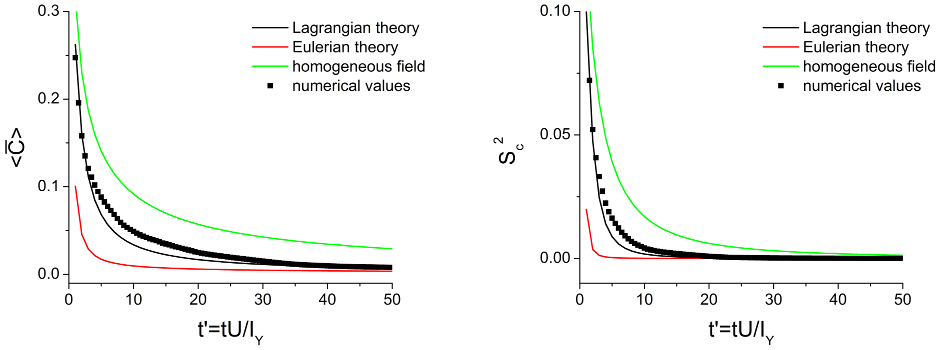

(c) $\sigma_Y^2 = 1$ - Pe $= 100$ **(d)** $\sigma_Y^2 = 1$ - Pe $= 100$

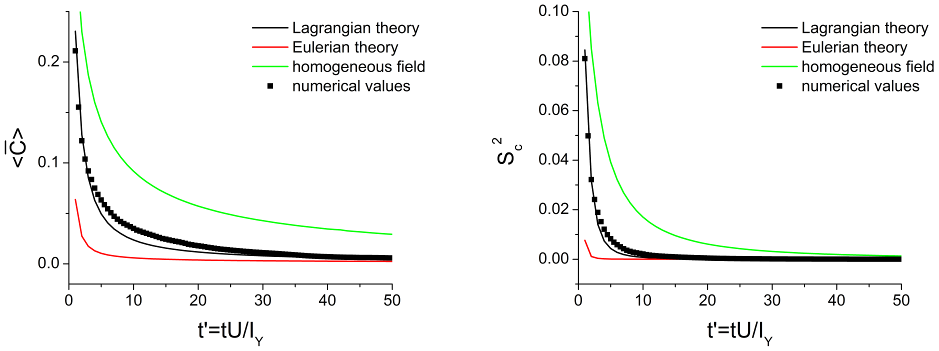

(e) $\sigma_Y^2 = 2$ - Pe $= 100$ **(f)** $\sigma_Y^2 = 2$ - Pe $= 100$

Figure 3.6: Dimensionless global mean $\langle \bar{C} \rangle$ and variance S_C^2 for the intermediate $(I_Y \times I_Y)$ injection case and Pe $= 100$ for the passive solute. Dots represent the empirical moments, whereas lines represent the theoretical models, whose color refers to: Eulerian theory ($\mathcal{E}$, red), Homogeneous theory ($\mathcal{H}$, green) and Lagrangian theory ($\mathcal{L}$, black).

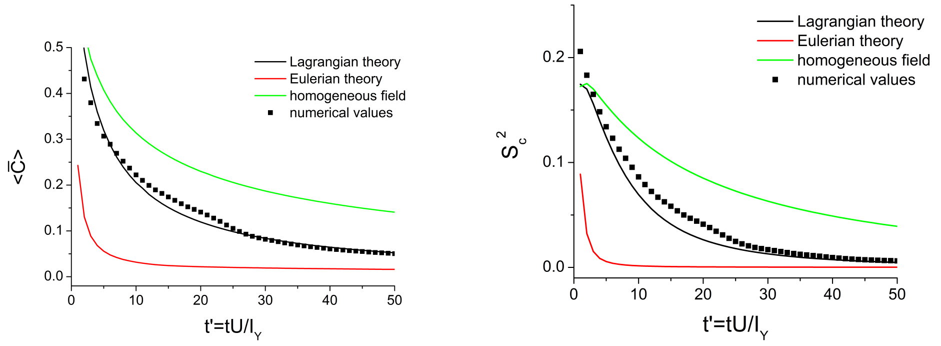

(a) $\sigma_Y^2 = 0.2$ - Pe $= 1000$ **(b)** $\sigma_Y^2 = 0.2$ - Pe $= 1000$

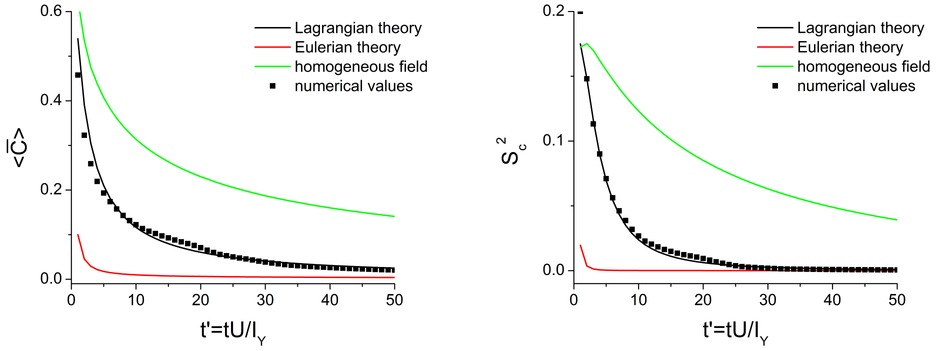

(c) $\sigma_Y^2 = 1$ - Pe $= 1000$ **(d)** $\sigma_Y^2 = 1$ - Pe $= 1000$

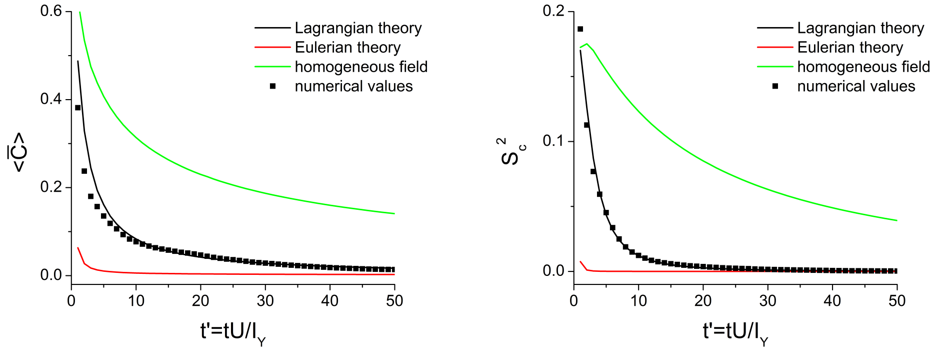

(e) $\sigma_Y^2 = 2$ - Pe $= 1000$ **(f)** $\sigma_Y^2 = 2$ - Pe $= 1000$

Figure 3.7: Dimensionless global mean $\langle \bar{C} \rangle$ and variance S_C^2 for the intermediate $(I_Y \times I_Y)$ injection case and Pe $= 1000$ for the passive solute. Dots represent the empirical moments, whereas lines represent the theoretical models, whose color refers to: Eulerian theory ($\mathcal{E}$, red), Homogeneous theory ($\mathcal{H}$, green) and Lagrangian theory ($\mathcal{L}$, black).

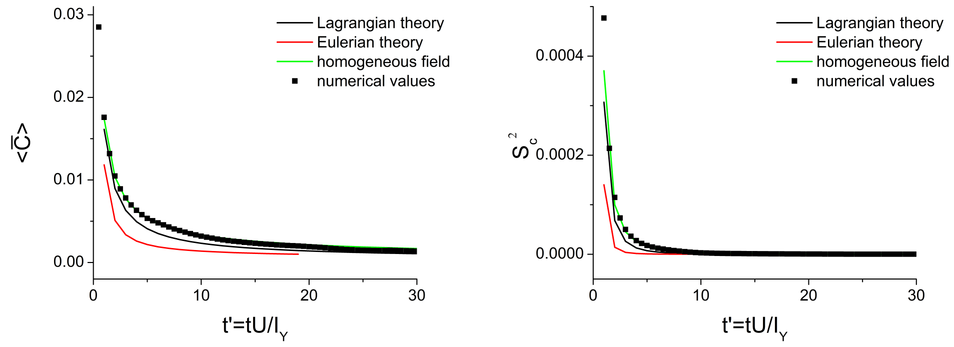

(a) $\sigma_Y^2 = 0.2$ - Pe $= 100$ **(b)** $\sigma_Y^2 = 0.2$ - Pe $= 100$

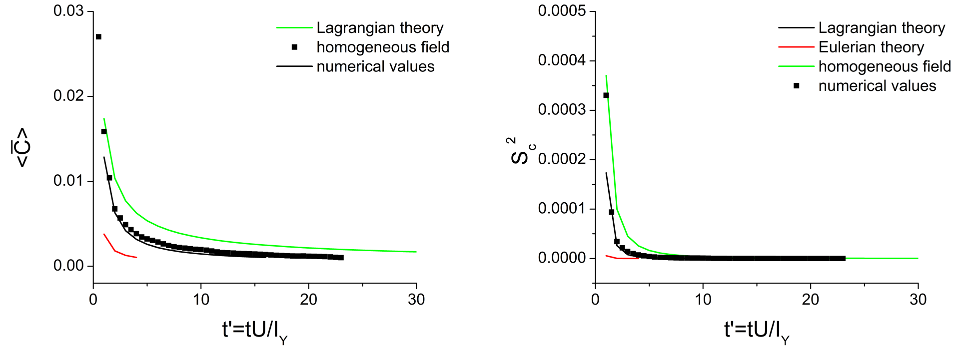

(c) $\sigma_Y^2 = 1$ - Pe $= 100$ **(d)** $\sigma_Y^2 = 1$ - Pe $= 100$

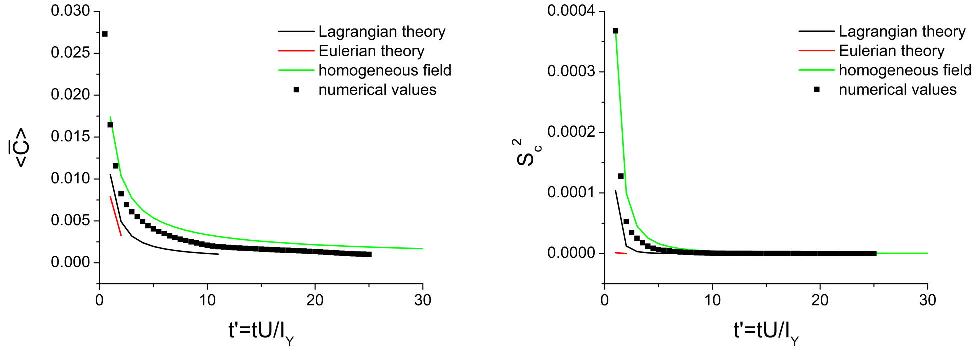

(e) $\sigma_Y^2 = 2$ - Pe $= 100$ **(f)** $\sigma_Y^2 = 2$ - Pe $= 100$

Figure 3.8: Dimensionless global mean $\langle \bar{C} \rangle$ and variance S_C^2 for the small $(0.1 I_Y \times 0.1 I_Y)$ injection case and Pe $= 100$ for the passive solute. Dots represent the empirical moments, whereas lines represent the theoretical models, whose color refers to: Eulerian theory ($\mathcal{E}$, red), Homogeneous theory ($\mathcal{H}$, green) and Lagrangian theory ($\mathcal{L}$, black).

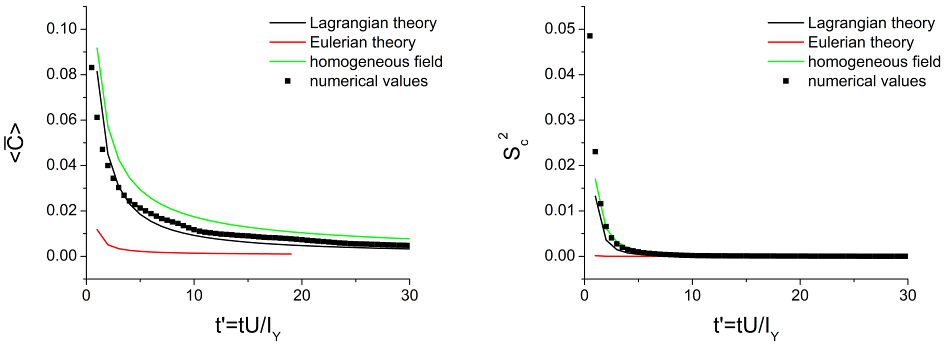

(a) $\sigma_Y^2 = 0.2$ - Pe $= 1000$

(b) $\sigma_Y^2 = 0.2$ - Pe $= 1000$

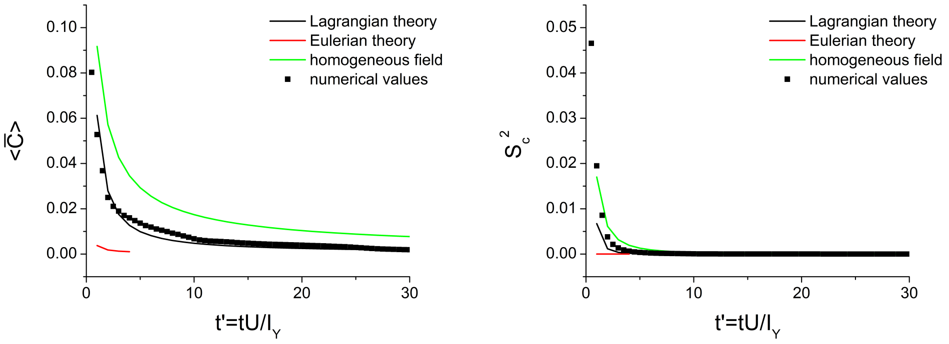

(c) $\sigma_Y^2 = 1$ - Pe $= 1000$

(d) $\sigma_Y^2 = 1$ - Pe $= 1000$

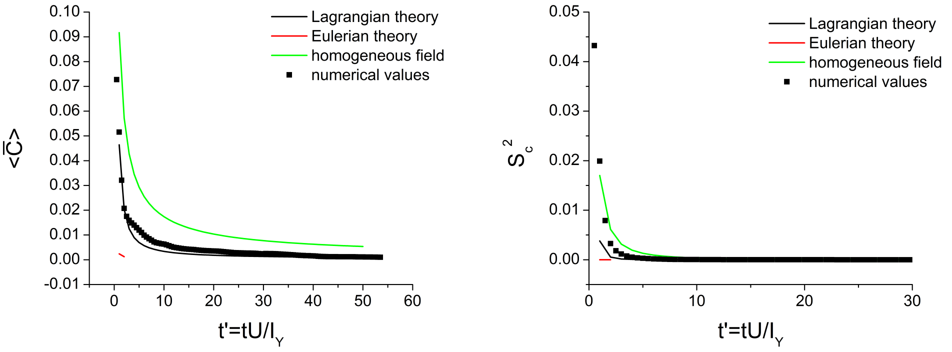

(e) $\sigma_Y^2 = 2$ - Pe $= 1000$

(f) $\sigma_Y^2 = 2$ - Pe $= 1000$

Figure 3.9: Dimensionless global mean $\langle \bar{C} \rangle$ and variance S_C^2 for the small $(0.1 I_Y \times 0.1 I_Y)$ injection case and Pe $= 1000$ for the passive solute. Dots represent the empirical moments, whereas lines represent the theoretical models, whose color refers to: Eulerian theory ($\mathcal{E}$, red), Homogeneous theory ($\mathcal{H}$, green) and Lagrangian theory ($\mathcal{L}$, black).

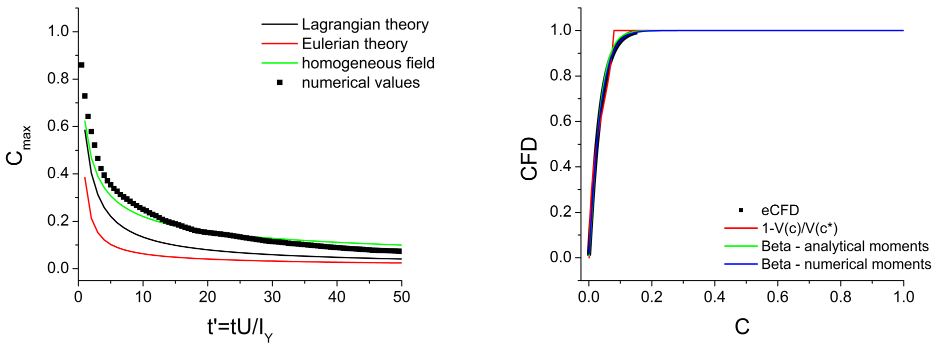

(a) C_{max} ($\sigma_Y^2 = 0.2$ - Pe $= 100$) **(b)** CFD ($\sigma_Y^2 = 0.2$ - Pe $= 100$)

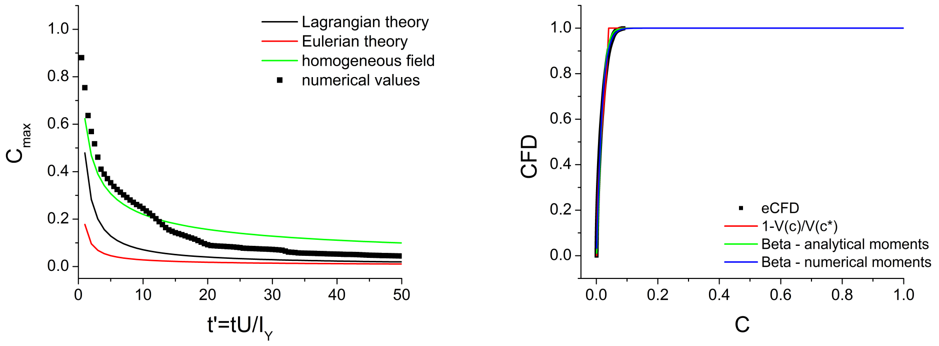

(c) C_{max} ($\sigma_Y^2 = 1$ - Pe $= 100$) **(d)** CFD ($\sigma_Y^2 = 1$ - Pe $= 100$)

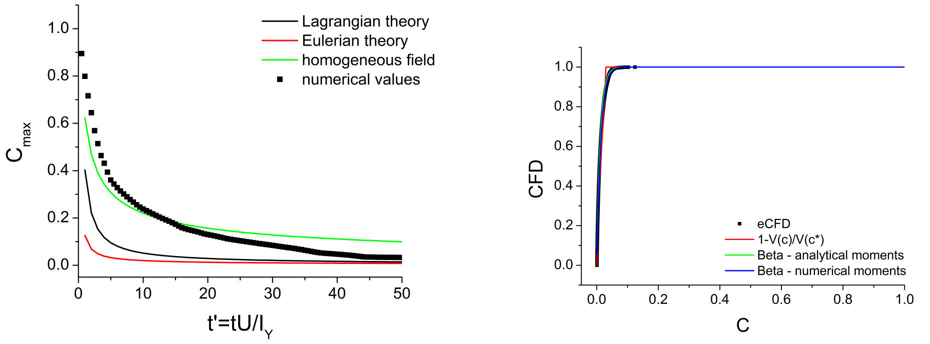

(e) C_{max} ($\sigma_Y^2 = 2$ - Pe $= 100$) **(f)** CFD ($\sigma_Y^2 = 2$ - Pe $= 100$)

Figure 3.10: Dimensionless maximum concentration $C_{\max}$ and CFD for the line injection and Pe $= 100$ for the passive solute. For $C_{\max}$, dots represent the empirical values, whereas lines represent the theoretical models, whose color refers to: Eulerian theory ($\mathcal{E}$, red), Homogeneous theory ($\mathcal{H}$, green) and Lagrangian theory ($\mathcal{L}$, black). For CFDs, black dots represent the empirical CFDs, whereas lines represent the theoretical or semitheoretical models: the theoretical Beta CFD (green lines), the empirical Beta CFD (blue lines) and the theoretical Lagrangian CFD (red lines).

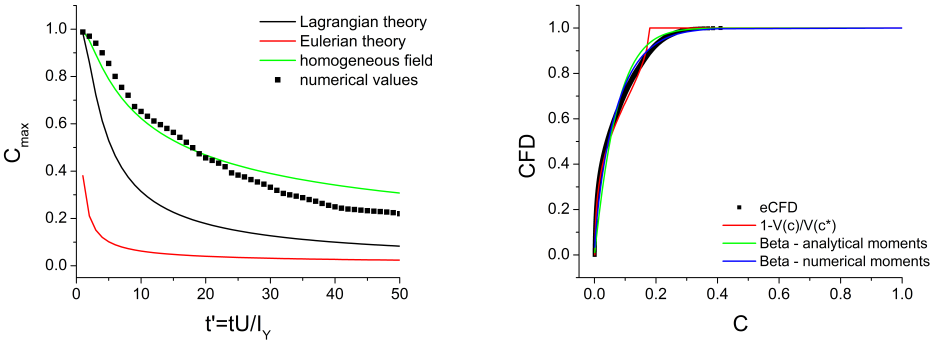

(a) $C_{\max}$ ($\sigma_Y^2 = 0.2$ - Pe $= 1000$) **(b)** CFD ($\sigma_Y^2 = 0.2$ - Pe $= 1000$)

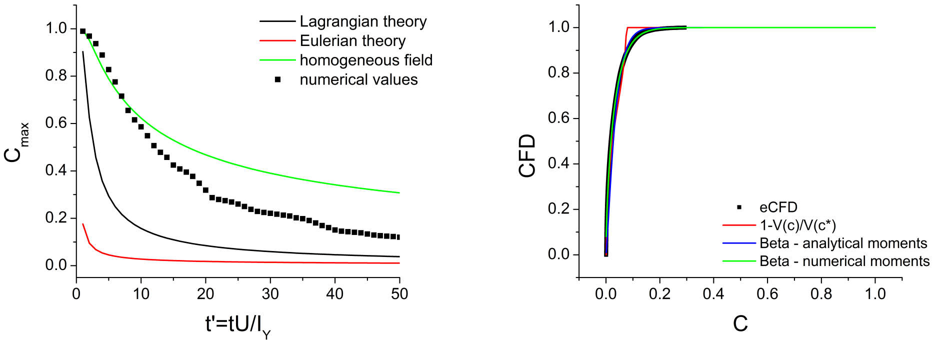

(c) $C_{\max}$ ($\sigma_Y^2 = 1$ - Pe $= 1000$) **(d)** CFD ($\sigma_Y^2 = 1$ - Pe $= 1000$)

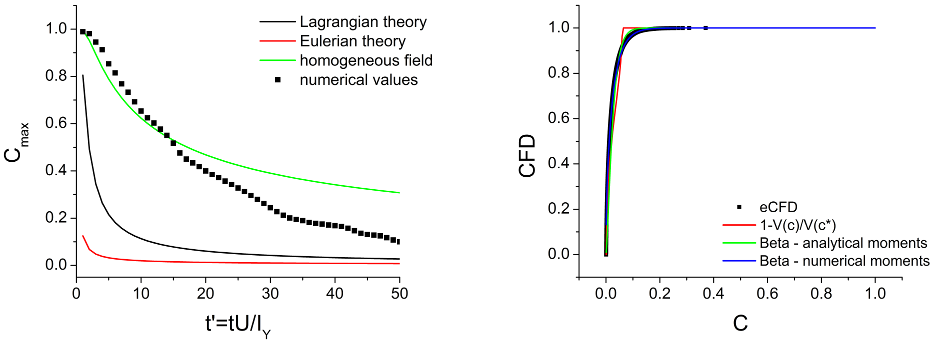

(e) $C_{\max}$ ($\sigma_Y^2 = 2$ - Pe $= 1000$) **(f)** CFD ($\sigma_Y^2 = 2$ - Pe $= 1000$)

Figure 3.11: Dimensionless maximum concentration $C_{\max}$ and CFD for the line injection and Pe $= 1000$ for the passive solute. For $C_{\max}$, dots represent the empirical values, whereas lines represent the theoretical models, whose color refers to: Eulerian theory ($\mathcal{E}$, red), Homogeneous theory ($\mathcal{H}$, green) and Lagrangian theory ($\mathcal{L}$, black). For CFDs, black dots represent the empirical CFDs, whereas lines represent the reference theoretical or semitheoretical models: the theoretical Beta CFD (green lines), the empirical Beta CFD (blue lines) and the theoretical Lagrangian CFD (red lines).

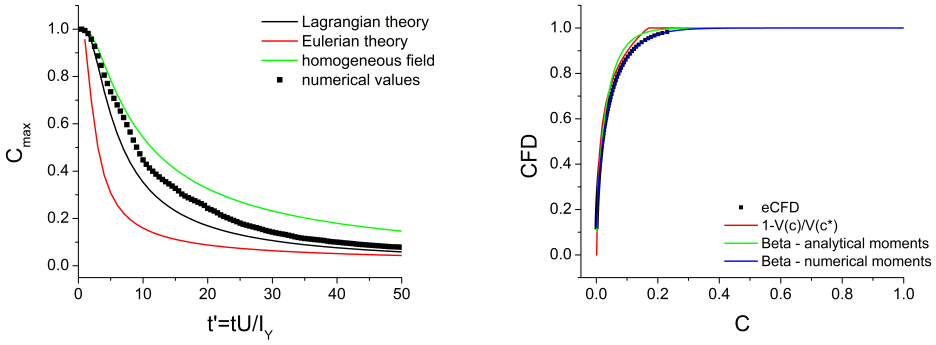

(a) $C_{\max}$ ($\sigma_Y^2 = 0.2$ - Pe $= 100$) **(b)** CFD ($\sigma_Y^2 = 0.2$ - Pe $= 100$)

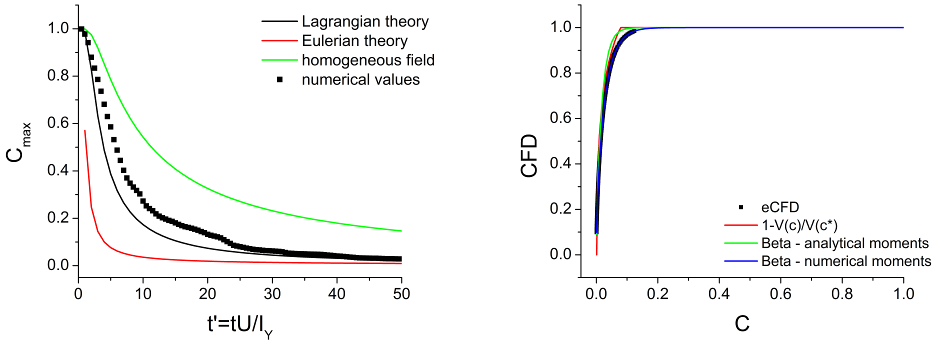

(c) $C_{\max}$ ($\sigma_Y^2 = 1$ - Pe $= 100$) **(d)** CFD ($\sigma_Y^2 = 1$ - Pe $= 100$)

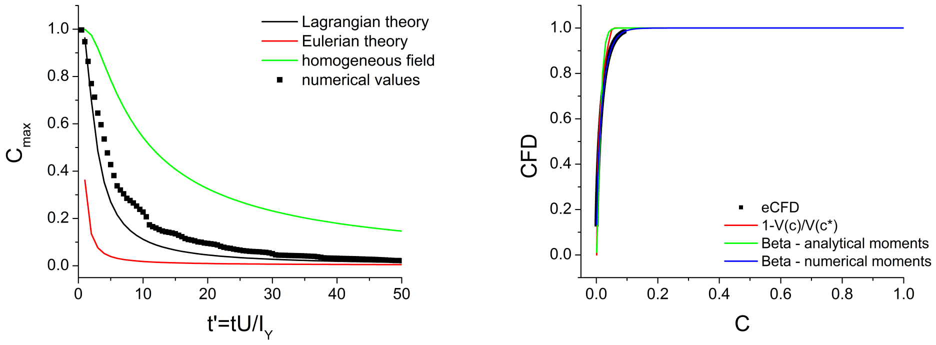

(e) $C_{\max}$ ($\sigma_Y^2 = 2$ - Pe $= 100$) **(f)** CFD ($\sigma_Y^2 = 2$ - Pe $= 100$)

Figure 3.12: Dimensionless maximum concentration $C_{\max}$ and CFD for the finite ($I_Y \times I_Y$) injection and Pe $= 100$. For $C_{\max}$, dots represent the empirical values, whereas lines represent the theoretical models, whose color refers to: Eulerian theory ($\mathcal{E}$, red), Homogeneous theory ($\mathcal{H}$, green) and Lagrangian theory ($\mathcal{L}$, black). For CFDs, black dots represent the empirical CFDs, whereas lines represent the reference theoretical or semitheoretical models: the theoretical Beta CFD (green lines), the empirical Beta CFD (blue lines) and the theoretical Lagrangian CFD (red lines).

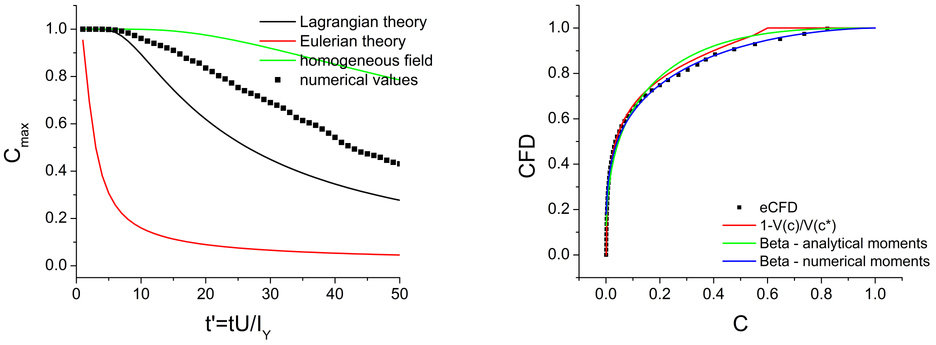

(a) $C_{\max}$ ($\sigma_Y^2 = 0.2$ - Pe = 1000) **(b)** CFD ($\sigma_Y^2 = 0.2$ - Pe = 1000)

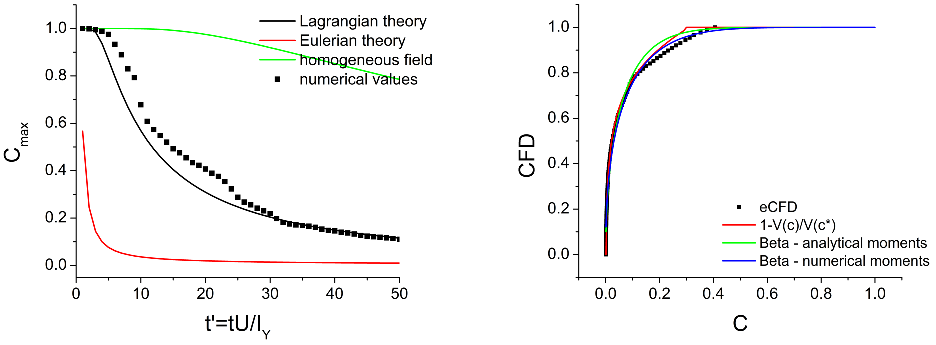

(c) $C_{\max}$ ($\sigma_Y^2 = 1$ - Pe = 1000) **(d)** CFD ($\sigma_Y^2 = 1$ - Pe = 1000)

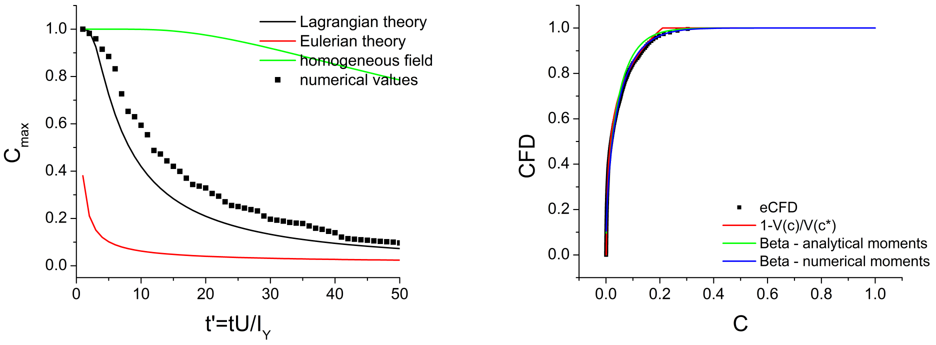

(e) $C_{\max}$ ($\sigma_Y^2 = 2$ - Pe = 1000) **(f)** CFD ($\sigma_Y^2 = 2$ - Pe = 1000)

Figure 3.13: Dimensionless maximum concentration $C_{\max}$ and CFD for the finite ($I_Y \times I_Y$) injection and Pe = 1000. For $C_{\max}$, dots represent the empirical values, whereas lines represent the theoretical models, whose color refers to: Eulerian theory ($\mathcal{E}$, red), Homogeneous theory ($\mathcal{H}$, green) and Lagrangian theory ($\mathcal{L}$, black). For CFDs, black dots represent the empirical CFDs, whereas lines represent the reference theoretical or semitheoretical models: the theoretical Beta CFD (green lines), the empirical Beta CFD (blue lines) and the theoretical Lagrangian CFD (red lines).

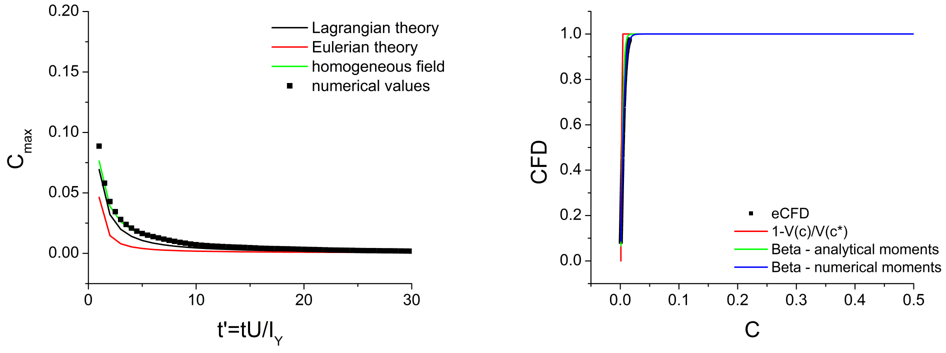

(a) $C_{\max}$ ($\sigma_Y^2 = 0.2$ - Pe $= 100$) **(b)** CFD ($\sigma_Y^2 = 0.2$ - Pe $= 100$)

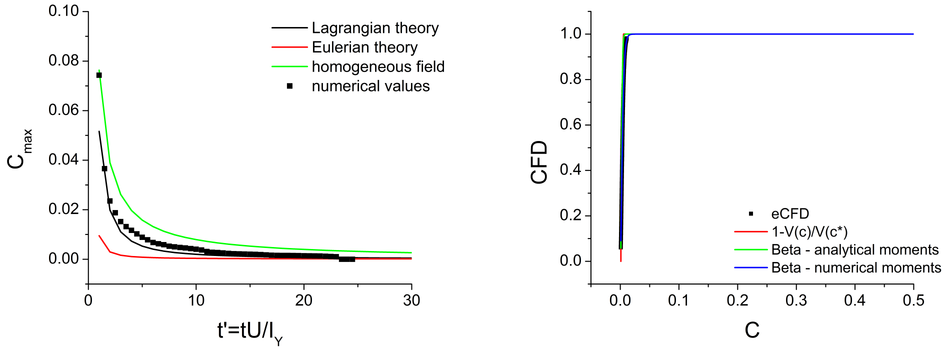

(c) $C_{\max}$ ($\sigma_Y^2 = 1$ - Pe $= 100$) **(d)** CFD ($\sigma_Y^2 = 1$ - Pe $= 100$)

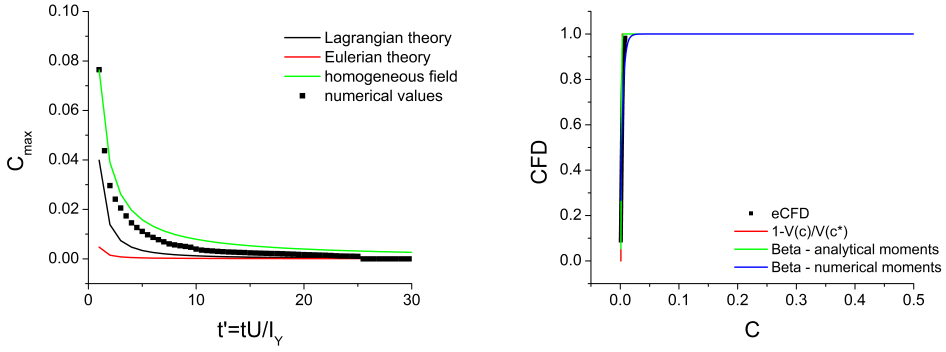

(e) $C_{\max}$ ($\sigma_Y^2 = 2$ - Pe $= 100$) **(f)** CFD ($\sigma_Y^2 = 2$ - Pe $= 100$)

Figure 3.14: Dimensionless maximum concentration $C_{\max}$ and CFD for the small ($0.1 I_Y \times 0.1 I_Y$) injection and Pe $= 100$. For $C_{\max}$, dots represent the empirical values, whereas lines represent the theoretical models, whose color refers to: Eulerian theory ($\mathcal{E}$, red), Homogeneous theory ($\mathcal{H}$, green) and Lagrangian theory ($\mathcal{L}$, black). For CFDs, black dots represent the empirical CFDs, whereas lines represent the reference theoretical or semitheoretical models: the theoretical Beta CFD (green lines), the empirical Beta CFD (blue lines) and the theoretical Lagrangian CFD (red lines).

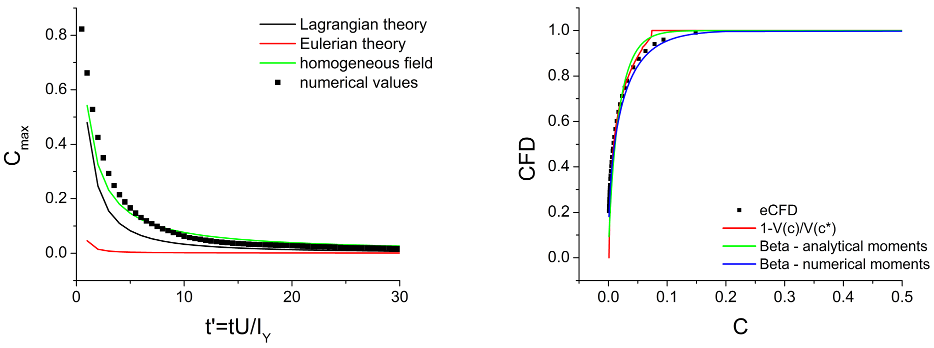

(a) $C_{\max}$ ($\sigma_Y^2 = 0.2$ - Pe $= 1000$) **(b)** CFD ($\sigma_Y^2 = 0.2$ - Pe $= 1000$)

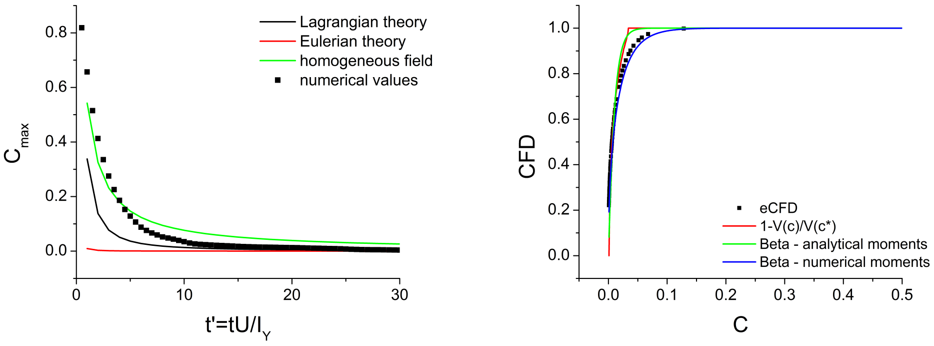

(c) $C_{\max}$ ($\sigma_Y^2 = 1$ - Pe $= 1000$) **(d)** CFD ($\sigma_Y^2 = 1$ - Pe $= 1000$)

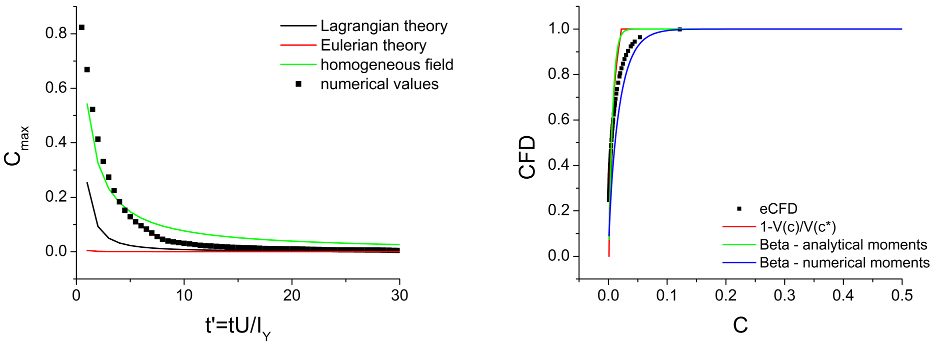

(e) $C_{\max}$ ($\sigma_Y^2 = 2$ - Pe $= 1000$) **(f)** CFD ($\sigma_Y^2 = 2$ - Pe $= 1000$)

Figure 3.15: Dimensionless maximum concentration $C_{\max}$ and CFD for the small ($0.1 I_Y \times 0.1 I_Y$) injection and Pe $= 1000$. For $C_{\max}$, dots represent the empirical values, whereas lines represent the theoretical models, whose color refers to: Eulerian theory ($\mathcal{E}$, red), Homogeneous theory ($\mathcal{H}$, green) and Lagrangian theory ($\mathcal{L}$, black). For CFDs, black dots represent the empirical CFDs, whereas lines represent the reference theoretical or semitheoretical models: the theoretical Beta CFD (green lines), the empirical Beta CFD (blue lines) and the theoretical Lagrangian CFD (red lines).

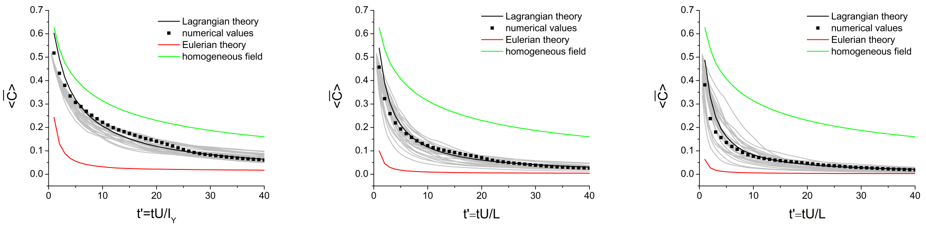

(a) $\langle\bar{C}\rangle$ $(\sigma_Y^2 = 0.2)$ **(b)** $\langle\bar{C}\rangle$ $(\sigma_Y^2 = 1)$ **(c)** $\langle\bar{C}\rangle$ $(\sigma_Y^2 = 2)$

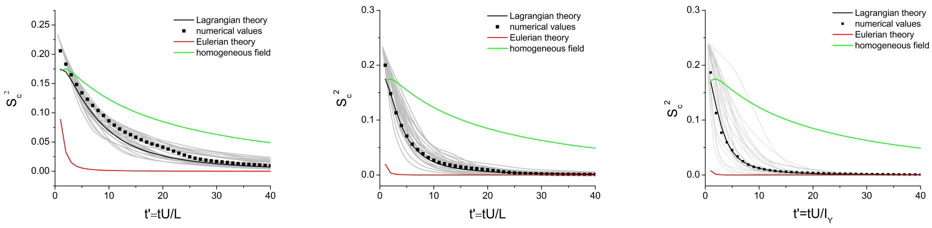

(d) S_C^2 $(\sigma_Y^2 = 0.2)$ **(e)** S_C^2 $(\sigma_Y^2 = 1)$ **(f)** S_C^2 $(\sigma_Y^2 = 2)$

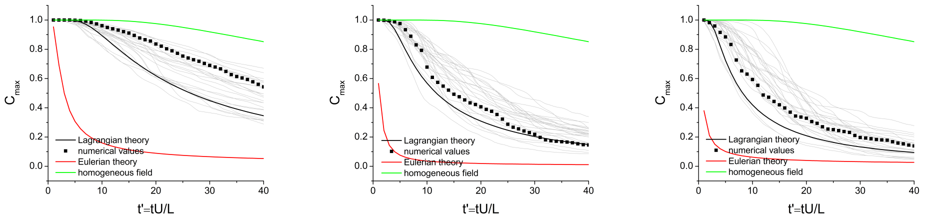

(g) $C_{\max}$ $(\sigma_Y^2 = 0.2)$ **(h)** $C_{\max}$ $(\sigma_Y^2 = 1)$ **(i)** $C_{\max}$ $(\sigma_Y^2 = 2)$

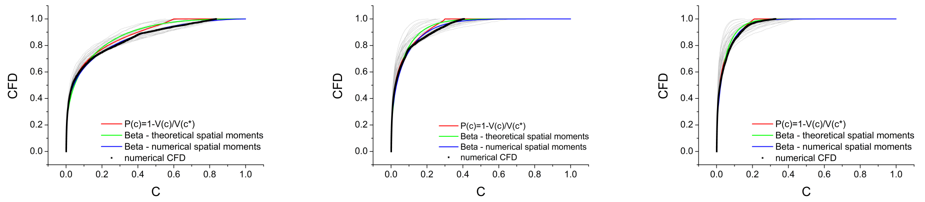

(j) CFD $(\sigma_Y^2 = 0.2)$ **(k)** CFD $(\sigma_Y^2 = 1)$ **(l)** CFD $(\sigma_Y^2 = 2)$

Figure 3.16: Comparison among the series of 25 independent transport simulations, the reference single realization model and the theoretical models. Dots represent the empirical quantities, whereas lines represent the theoretical models. For $\langle\bar{C}\rangle$, S_C^2 and $C_{\max}$ colors refer to: Eulerian theory ($\mathcal{E}$,red), Homogeneous theory ($\mathcal{H}$, green) and Lagrangian theory ($\mathcal{L}$, black). For the CFDs, colors refer to: the theoretical Beta CFD (green lines), the empirical Beta CFD (blue lines) and the theoretical Lagrangian CFD (red lines). Background grey lines represent the sheaf of empirical quantities. From left to right the σ_Y^2 of the Y field increases. The first row shows the global concentration mean $\langle\bar{C}\rangle$; the second row displays the global concentration variance S_C^2; in the third row we draw the maximum concentration $C_{\max}$ and in the last row we compare the Cumulative Frequency Distributions.

Chapter 4

Concentration statistics of solutes reacting upon mixing

4.1 Introduction

Differential reactive systems of equations can be simplified by taking advantage of algebraic relations among species concentrations, which exist for example in case of very fast reaction kinetics (Rubin, 1983). The underlying hypothesis is that all species have to be subject to the same advection and dispersion operators; in particular each species has to be characterized by the same molecular diffusion. The number of unknowns is reduced, thanks to the introduction of components or tenads which can be obtained as a linear combination between single species concentrations. Molins *et al.*, 2004 elaborated a general paradigm for reducing the non-linearities and simplifying the solution of large reactive systems. The resulting Differential Algebraic System consists of a number of conservative Advection Dispersion Equations for independent components, possibly a few original Advection Dispersion Reaction Equations for the slowly reacting species and an adequate number of algebraic relations between the components and the original reacting species. Rubin, 1983 and Friedly and Rubin, 1992 provided several examples of this kind, as well as a classification of the reactions which are typically encountered in environmental systems. Several developments of this basic concept have been presented in the literature so far. Ham *et al.*, 2004 focused on bimolecular instantaneous reactions. De Simoni *et al.*, 2005 and De Simoni *et al.*, 2007, for instance, presented analytical speciation formulae and reaction rates expressions for the case of mixing-controlled bimolecular equilibrium reactions on the basis of the Law of Mass Action (see e.g. Denbigh and Denbigh, 1981), clearly expressing the dependence of the reaction rate r on mixing. Any deviation from local equilibrium, due to transport or external forcings, determines the instantaneous reestablishment of local equilibrium, and consequently local non-zero reaction rates. The same expressions were used for predicting r mapping in a flow-cell experiment (Guadagnini *et al.*, 2009). Sanchez-Vila *et al.*, 2010 extended this procedure for describing a system of n equilibrium reactions and a single kinetically-controlled reaction. When reaction kinetics is not instantaneous, but however fast, reaction rates can be obtained through a perturbation expansion in r, as shown by Sanchez-Vila, Dentz, and Donado, 2007. Cirpka and Valocchi, 2007 presented a semi-analytical approach for a reactive system in steady state in case of bioreactions controlled by a dual Monod kinetics, further developed by Cirpka, 2010 to include also kinetic solute uptake by the biomass.

These analytical relations between species, whenever existent, can be used to assess concentration probability distribution functions (pdfs) of reactive species once these pdfs are established for the conservative components. Several different authors (Bellin and Tonina, 2007; Cirpka *et al.*, 2008; Fiori, 1996; Fiorotto and Caroni, 2002; Schwede *et al.*, 2008) have suggested the assumption of the Beta distribution to estimate the pdf of passive tracers. In particular, Bellin, Severino, and Fiori, 2011 provided analytical pdfs and moments for reactive species interacting according to a bimolecular heterogeneous equilibrium reaction $A + B \leftrightarrows C \downarrow$, treated in De Simoni *et al.*, 2005. Along the same lines, we develop a similar analysis for the bimolecular homogeneous equilibrium reaction $A + B \leftrightarrows C$, considered by De Simoni *et al.*, 2007. Similar work has been done by Cirpka *et al.*, 2008, who opposed the use of perturbative approximations for estimating pdfs, Schwede *et al.*, 2008, who developed an analytical procedure for estimating pdfs in steady state, and Sanchez-Vila, Guadagnini, and Férnandez Garcia, 2009, who developed a simplified methodology for estimating reactive concentration pdfs in stratified aquifers.

In Section 4.2 we summarize the speciation equation for the considered reactive case $A + B \rightleftarrows C$. Section 4.3 contains the analytical expressions for the first two moments of the concentration of the reactive species A, B and C involved in the reactive system, and the pdfs. Sections 4.4 and 4.5 list illustrative examples of both local and global statistics, respectively. We use theoretical moments for the conservative species belonging to the first order Lagrangian statistics (Dagan, 1989) in order to highlight the role of heterogeneity level and local scale dispersion towards reactive concentration statistics. In Section 4.6 different cumulative statistics are considered, focusing on quantities more useful for risk assessment. Finally in Section 4.7 we compare the theoretical global statistics with single-realization numerical simulations, in order to verify the a-priori estimation capabilities of the presented mathematical procedure.

4.2 Reactive problem formulation

The solute mass conservation for each solute i is expressed by means of the following Partial Differential Equation:

$$\frac{\partial c_i}{\partial t} + \mathbf{u} \cdot \nabla c_i = \nabla \left(\mathbf{D} \nabla c_i \right) + \frac{r_i(\mathbf{c})}{\phi} \tag{4.1}$$

where c_i represents the concentration of the i-th species, $\mathbf{u}$ is the local velocity, $\mathbf{D}$ is the local diffusion/dispersion tensor, ϕ is the constant porosity, and $r_i(\mathbf{c})$ represents the source/sink reaction term which may depend on the concentration of different species. $\mathbf{u}$ and $\mathbf{D}$ have to be the same for all species.

When the chemical species react upon an equilibrium reaction, the complete Advection Dispersion Reaction Equations (ADRE, Eq. 4.1) can be simplified by algebraic manipulation and brought back to a set of simpler Advection Dispersion Equations (that is, with $r_i = 0$) plus an adequate number of speciation equations (Rubin, 1983). Such a procedure introduces a corresponding number of conservative quantities which are a linear combination of the concentration of the reactive species which take part in the original reactive system. In particular De Simoni *et al.*, 2005 and De Simoni *et al.*, 2007 provided the speciation equation for the bimolecular equilibrium reaction case $\nu_1 A + \nu_2 B \leftrightarrows \nu_3 C$, both considering a solid or a liquid phase for species C. In the following we refer to the first case as to the heterogeneous case, and to the second one as the homogeneous one, according to the classification by Rubin, 1983. In both cases speciation equations are derived under the hypothesis of compound-independent local dispersion coefficients and considering unitary stoichiometric coefficients ν_i.

For the heterogeneous case, we need to solve the conservative ADE for the quantity $\mathsf{u} = c_1 - c_2$, where c_1 and c_2 are the concentrations of species A and species B, respectively. The speciation equations:

$$c_i = \frac{1}{2}\left(\mathsf{u} \pm \sqrt{\mathsf{u}^2 + 4K_{\text{eq}}}\right), \qquad i = 1,2 \tag{4.2}$$

are obtained by also considering the Law of Mass Action which imposes $c_1 c_2 = K_{\text{eq}}$, where K_{eq} is the equilibrium constant. In addition the reaction rate r, in case of constant K_{eq}, reads:

$$\frac{r}{\phi} = \frac{\partial^2 c_2}{\partial \mathsf{u}^2} \nabla^T \mathsf{u} \mathbf{D} \nabla \mathsf{u} \tag{4.3}$$

where ϕ is the constant porosity.

For the homogeneous case, we need to introduce two different conservative components, $\mathsf{u}_1 = c_1 + c_3$ and $\mathsf{u}_2 = c_2 + c_3$, which both solve the ADE equation provided adequate initial conditions. c_1, c_2 and c_3 refer to the concentration of species A, B and C, respectively. The Law of Mass Action (e.g. Denbigh and Denbigh, 1981), in case of low concentration, imposes in this case $c_1 c_2 / c_3 = K_{\text{eq}}$, and the three speciation equations are the following:

$$c_i = \frac{1}{2}\left(\pm(\mathsf{u}_1 - \mathsf{u}_2) - K_{\text{eq}} + \sqrt{(\mathsf{u}_1 + \mathsf{u}_2 + K_{\text{eq}})^2 - 4\mathsf{u}_1\mathsf{u}_2}\right), \qquad i = 1,2 \tag{4.4}$$

$$c_3 = \frac{1}{2}\left(\mathsf{u}_1 + \mathsf{u}_2 + K_{\text{eq}} - \sqrt{(\mathsf{u}_1 + \mathsf{u}_2 + K_{\text{eq}})^2 - 4\mathsf{u}_1\mathsf{u}_2}\right) \tag{4.5}$$

In Eq. 4.4 the sign '+' refers to species A, while '-' refers to species B. The reaction rate r depends in this case on both $\nabla \mathsf{u}_1$ and $\nabla \mathsf{u}_2$ under the assumption of constant K_{eq}:

$$\frac{r}{\phi} = \frac{\partial c_2^2}{\partial \mathsf{u}_1^2} \nabla \mathsf{u}_1^T \mathbf{D} \nabla \mathsf{u}_1 + \frac{\partial^2 c_2}{\partial \mathsf{u}_2^2} \nabla \mathsf{u}_2^T \mathbf{D} \nabla \mathsf{u}_2 + \frac{\partial^2 c_2}{\partial \mathsf{u}_1 \partial \mathsf{u}_2} \left[\nabla \mathsf{u}_2^T \mathbf{D} \nabla \mathsf{u}_1 + \nabla \mathsf{u}_1^T \mathbf{D} \nabla \mathsf{u}_2\right] \tag{4.6}$$

The Laws of Mass Action for both cases are represented in the species diagrams in Figure 4.1. The red hyperbola in Fig. 4.1a represents the state $c_1 c_2 = K_{\text{eq}}$ of local equilibrium towards which disequilibrium states point. When waters with different (but equilibrium) composition mix, the resulting mixed volume is characterized by a oversaturated composition which depends on the weighted linear combination of the composition of starting waters. Then reaction instantly re-establishes local equilibrium through precipitation. Something similar happens in case of homogeneous

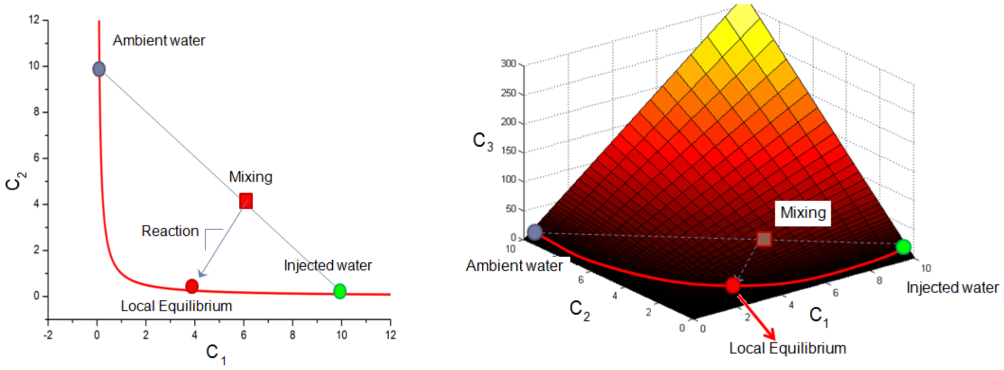

(a) $A + B \leftrightarrows C \downarrow$ **(b)** $A + B \leftrightarrows C$

Figure 4.1: Graphical representation for the bimolecular equilibrium reactions. C_1 and C_2 are the concentration of species A and B, respectively, whereas C_3 is the concentration of species C. (a) represents the bimolecular heterogeneous equilibrium reaction (red hyperbola), while (b) represents the bimolecular homogeneous equilibrium reaction (red surface).

equilibrium reactions (Fig. 4.1b). This time c_3, the concentration of species C, plays a role. The colored surface represents the equilibrium state $c_1 c_2 / c_3 = K_{\mathrm{eq}}$.

For simplicity in each case we refer to the standardized passive tracer z, which is related to the components u_i by the linear relation $\mathsf{u}_i = \Delta u_i z + u_{0,i}$. The coefficients $\Delta u_i = u_{\mathrm{inj,i}} - u_{\mathrm{amb,i}}$ and $u_{0,\mathrm{i}}$ depend on the choice of the initial conditions.

4.3 Concentration statistics and concentration moments

As reviewed in Chapter 3, concentration can be treated as a Random Space Function as a consequence of the unknown spatial distribution of the hydraulic properties of the geological formations. A lot of effort has been put into the development of statistical tools for predictive purposes, both at the local scale and at the global scale. Reasonable agreement has been found on the use of the Beta distribution for modeling the passive concentration distribution at both scales (among others, Bellin and Tonina, 2007; Caroni and Fiorotto, 2005; Cirpka *et al.*, 2008; Fiorotto and Caroni, 2002). The Beta distribution $B(z; p_1, p_2)$

$$f_Z(z) = B(z; p_1, p_2) = \frac{\Gamma(p_1 + p_2)}{\Gamma(p_1)\Gamma(p_2)} z^{p_1 - 1} (1 - z)^{p_2 - 1} \tag{4.7}$$

represents the probability density function (pdf) of a variable Z varying over the range $[0, 1]$. The shape parameters p_1 and p_2 are related to the Z moments $\langle z \rangle$ and σ_Z^2 through:

$$\langle z \rangle = \frac{p_1}{p_1 + p_2} \tag{4.8a}$$

$$\sigma_z^2 = \frac{p_1 \, p_2}{(p_1 + p_2)^2 (p_1 + p_2 + 1)} \tag{4.8b}$$

and their variation determines a wide variety of shapes for the pdf.

The explicit speciation equations for the reactive species concentration c_i can be used for transferring conservative transport results to reactive transport. In particular, Bellin, Severino, and Fiori, 2011, assuming the validity of the Beta distribution for describing the behavior of the passive solute concentration z, provided analytical formulations for both the pdf and the moments of the reactive species concentrations in case of heterogeneous reaction.
In fact, the pdf f_{C_i} for dependent variables $C_i = \mathsf{g}(Z)$ can be brought back to the pdf of Z, f_Z, by the following analytical relation:

$$f_{C_i}(c_i) = \sum_{k=1}^{n(c_i)} \left| \frac{1}{\mathsf{g}'(\mathsf{g}_k^{-1}(c_i))} \right| \cdot f_Z(\mathsf{g}_k^{-1}(c_i)) \tag{4.9}$$

where $n(c_i)$ is the number of monotonic regions k where the function $C_i = \mathsf{g}_k(Z)$ is monotonic, $\mathsf{g}_k^{-1}(c_i)$ is the inverse function of g_k and $\mathsf{g}_k'(c_i)$ is its derivative. The cdf $F_{C_i}(c_i) = \int_0^{c_i} f_{C_i}(c)dc$ can be computed accordingly. Also C_i moments of order μ can be computed through $\langle \mathsf{g}(z)^\mu \rangle = \int_0^1 \mathsf{g}(z)^\mu f_Z(z)dz$.

For the sake of completeness, we report in the following the main findings by Bellin, Severino, and Fiori, 2011. The mean $\langle C_i \rangle$ and the variance σ^2_{Ci} for the concentration of species i read:

$$\langle C_i \rangle = \frac{1}{2} \left(\pm \Delta u \langle z \rangle \pm u_0 + \beta(0) \right) \quad i = 1,2 \tag{4.10}$$

$$\begin{aligned} \sigma^2_{C_i} = & \frac{1}{4} \big(4K_{eq} + u_0^2 - \beta(0)^2 \mp 2\beta(1)\Delta u + 2\Delta u \langle z \rangle u_0 \pm 2\Delta u \langle z \rangle \beta(0) \\ & + 2\Delta u^2 \left(\langle z \rangle^2 + \sigma_z^2 \right), \quad i = 1,2 \end{aligned} \tag{4.11}$$

where

$$\beta(n) = \int_0^1 z^n \sqrt{(\Delta u z + u_0)^2 + 4K_{\text{eq}}} B(z; p, q) dz \tag{4.12}$$

The pdfs f_{C_i} for both c_1 and c_2 can be computed as follows:

$$f_{C_i}(c_i) = \frac{1}{\Delta u} \left(1 + \frac{K_{\text{eq}}}{c_i^2} \right) f_Z \left[\frac{1}{\Delta u} \left(\pm (c_i - K_{\text{eq}}/c_i) - u_0 \right) \right], \qquad i = 1,2 \tag{4.13}$$

In a similar fashion we find now analytical expressions for the moments and the pdf of C_i for the species A, B and C which react according to a homogeneous reaction. For simplicity, we assume the initial conditions for the several species so that Δu_1 is positive and Δu_2 is negative. $\mathsf{c}_1(z)$ and $\mathsf{c}_2(z)$ are monotonic functions of z, whereas $\mathsf{c}_3(z)$ can present different monotonic sections within the range of variability of $z \in [0,1]$. As a result, the inverse function $\mathsf{z}(c_3)$ is not univocal but has to be defined in each section. For our choice of initial conditions, we can individuate two different monotonic regions for the function $c_3 = \mathsf{c}_3(z)$: positive in the range $[0, z_{\text{p}}]$, and negative in the range $[z_p, 1]$. z_p represents the z value within the range $[0,1]$ where $\mathsf{z}(c_3)$ peaks. In the following we list the results in terms of moments for each species:

$$\langle c_i \rangle = \frac{1}{2} \left[\delta(0) \pm (\Delta u_1 - \Delta u_2) \langle z \rangle \pm (u_{1,\text{amb}} + u_{2,\text{inj}}) \mp K_{\text{eq}} \right], \qquad i = 1, 2 \tag{4.14}$$

$$\langle c_3 \rangle = \frac{1}{2} \left[-\delta(0) - (\Delta u_1 + \Delta u_2) \langle z \rangle + (u_{1,\text{amb}} + u_{2,\text{inj}}) + K_{\text{eq}} \right] \tag{4.15}$$

$$\begin{aligned} \sigma_{c_i}^2 = &\frac{1}{4} \{ (u_{1,\text{amb}} - u_{2,\text{inj}})^2 - \delta(0)^2 + K_{\text{eq}}^2 + 2K_{\text{eq}} (u_{1,\text{amb}} + u_{2,\text{inj}} + \Delta u_1 + \Delta u_2) \\ &\pm 2 (\Delta u_1 - \Delta u_2) \delta(1) + \langle z \rangle^2 (\Delta u_1 - \Delta u_2)^2 + 2\sigma_z^2 (\Delta u_1 - \Delta u_2)^2 \\ &+ 2\langle z \rangle [\mp (\Delta u_1 - \Delta u_2) \delta(0) + (\Delta u_1 - \Delta u_2) (u_{1,\text{amb}} - u_{2,\text{inj}})] \}, \quad i = 1, 2 \end{aligned} \tag{4.16}$$

$$\begin{aligned} \sigma_{c_3}^2 = &\frac{1}{4} \{ (u_{1,\text{amb}} - u_{2,\text{inj}})^2 - \delta(0)^2 + K_{\text{eq}}^2 + 2K_{\text{eq}} (u_{1,\text{amb}} + u_{2,\text{inj}} + \Delta u_1 + \Delta u_2) \\ &\pm 2 (\Delta u_1 - \Delta u_2) \delta(1) + \langle z \rangle^2 (\Delta u_1 - \Delta u_2)^2 + 2\sigma_z^2 (\Delta u_1^2 + \Delta u_2^2) \\ &+ 2\langle z \rangle [(\Delta u_1 + \Delta u_2) \delta(0) + (\Delta u_1 - \Delta u_2) (u_{1,\text{amb}} - u_{2,\text{inj}})] \}, \qquad i = 1, 2 \end{aligned} \tag{4.17}$$

with

$$\begin{aligned} \delta(n) = \quad &\textstyle\int_0^1 \sqrt{(K_{\text{eq}} + (\Delta u_1 + \Delta u_2) z + u_{1,0} + u_{2,\text{inj}})^2 - 4(\Delta u_1 z + u_{1,\text{amb}})(\Delta u_2 z + u_{2,\text{inj}})} \\ &z^n B(z; p, q) dz \end{aligned} \tag{4.18}$$

The pdfs read:

$$f(c_1) = \left| \frac{-\Delta u_2 (c_1^2 + u_{1,\text{amb}} K_{eq}) + \Delta u_1 (c_1^2 + 2c_1 K_{\text{eq}} + K_{\text{eq}} (u_{2,\text{inj}} + K_{\text{eq}}))}{(-\Delta u_2 c_1^2 + \Delta u_1 (c_1 + K_{\text{eq}}))^2} \right| B\left(z(c_1)\right) \tag{4.19}$$

$$f(c_2) = \left| \frac{\Delta u_1 (c_2^2 + u_{2,\text{inj}} K_{eq} - \Delta u_2 (c_2^2 + 2c_2 K_{\text{eq}} + K_{\text{eq}} (u_{1,\text{amb}} + K_{\text{eq}})))}{(\Delta u_1 c_2 - \Delta u_2 (c_2 + K_{\text{eq}}))^2} \right| B\left(z(c_2)\right) \tag{4.20}$$

$$\begin{aligned} f(c_3) = &\Bigg| \Bigg[1 + \frac{2\Delta u_1 \Delta u_2 (u_{1,\text{amb}} - 2c_3 + u_{2,\text{inj}} + K_{\text{eq}})}{\sqrt{\varrho(z)} (\Delta u_1 + \Delta u_2)} + \frac{u_{1,\text{amb}} \Delta u_2 - (\Delta u_1 + \Delta u_2) c_3}{\sqrt{\varrho(z)}} \\ &+ \frac{\Delta u_1 u_{2,\text{inj}}}{\sqrt{\varrho(z)}} \Bigg] \frac{(\Delta u_1 + \Delta u_2)}{2\Delta u_1 \Delta u_2} \Bigg| B\left(z(c_{3,p})\right) + \Bigg| \Bigg[1 - \frac{u_{1,\text{amb}} \Delta u_2 + \Delta u_1 u_{2,\text{inj}}}{\sqrt{\varrho(z)}} \\ &+ \frac{(\Delta u_1 + \Delta u_2) c_3}{\sqrt{\varrho(z)}} + \frac{2\Delta u_1 \Delta u_2 (u_{1,\text{amb}} - 2c_3 + u_{2,\text{inj}} + K_{\text{eq}})}{\sqrt{\varrho(z)} (\Delta u_1 + \Delta u_2)} \Bigg] \frac{(\Delta u_1 + \Delta u_2)}{2\Delta u_1 \Delta u_2} \Bigg| \\ &B\left(z(c_{3,n})\right) \end{aligned} \tag{4.21}$$

Table 4.1: Initial conditions for the equilibrium reaction cases. All quantities are dimensionless with respect to $C*$, which is equalled to $\sqrt{K_{\text{eq}}}$ in case of heterogeneous reaction, and to K_{eq} in case of homogeneous reaction.

Case	Parameter	Value
Passive	z_{amb}	0
	z_{inj}	1
Heterogeneous	$(C_1, C_2)_{\text{amb}}$	(0.1, 10)
	$(C_1, C_2)_{\text{inj}}$	(10, 0.1)
Homogeneous	$(C_1, C_2, C_3)_{\text{amb}}$	(0.1, 10,10)
	$(C_1, C_2, C_3)_{\text{inj}}$	(10, 0.1,10)

with

$$\mathsf{z}(c_1) = \mathsf{c_1}^{-1}(z) = \frac{-u_{1,\text{amb}}c_1 + c_1^2 + c_1 u_{2,\text{inj}} - u_{1,\text{amb}}K_{\text{eq}} + c_1 K_{\text{eq}}}{\Delta u_1 c_1 - \Delta u_2 c_1 + \Delta u_1 K_{\text{eq}}} \tag{4.22}$$

$$\mathsf{z}(c_2) = \mathsf{c_2}^{-1}(z) = \frac{-u_{1,\text{amb}}c_2 - c_2^2 + c_2 u_{2,\text{inj}} - c_2 K_{\text{eq}} + u_{2,\text{inj}}K_{\text{eq}}}{\Delta u_1 c_2 - \Delta u_2 c_2 - \Delta u_2 K_{\text{eq}}} \tag{4.23}$$

$$\begin{aligned}\mathsf{z}(c_{3,i}) &= \mathsf{c_{3,i}}^{-1}(z)\\ &= -\frac{1}{2\Delta u_1 \Delta u_2}\left[u_{1,\text{amb}}\Delta u_2 - (\Delta u_1 + \Delta u_2)c_3 + \Delta u_1 u_{2,\text{inj}} \pm \sqrt{\varrho(z)}\right],\ i = p, n\end{aligned} \tag{4.24}$$

where p refers to the positive monotonic region and n refers to the negative monotonic region, and

$$\begin{aligned}\varrho(z) = \ & (u_{1,\text{amb}}\Delta u_2 + (\Delta u_1 + \Delta u_2)c_3 - \Delta u_1 u_{2,\text{inj}})^2 + 4\Delta u_1 \Delta u_2 \left(-c_3^2 - u_{1,\text{amb}}u_{2,\text{inj}}\right.\\ & \left. + c_3(u_{1,\text{amb}}u_{2,\text{inj}} + K_{\text{eq}})\right)\end{aligned} \tag{4.25}$$

4.4 Applications: local statistics

For illustrative purposes, we analyze the behavior of the concentration moments and the probability distribution functions in a 2D formation. The analysis is conducted in the case of instantaneous injection of solute in a small or finite initial square volume with sides $\lambda_i = L_i/I_Y$, in a permeameter like setting with mean velocity $\mathbf{U}(U, 0)$. The initial conditions for all scenarios are listed in Table 4.1 for both the injected water and the ambient water.

We consider the local mean and variance at the theoretical centroid of the plume $\mathbf{x}_C(Ut, 0)$, and the pdf in the same location. All quantities take into account, in an inextricable way, both the dilution process and the uncertainty related to the position and actual shape of the plume, which in turn depends on the uncertainty which plagues the spatial distribution of the hydraulic properties of the medium. All graphs consider the combined effect of two parameters: the local Peclet number $\text{Pe} = UI_Y/D$, where D is the local dispersion and U the effective velocity of the fluid, and the log-conductivity variance σ_Y^2 as a measure of the heterogeneity of the medium.

The time evolution of the moments is drawn in Figures 4.2 as a function of the dimensionless time $t' = tU/I_Y$ in the case of small injection $\lambda = 0.1$. The analytical formulae for both the mean and variance are computed following the classic Lagrangian framework in case of instantaneous uniform injection (Fiori and Dagan, 2000):

$$\langle C(\mathbf{x_c}, t)\rangle = \int_{V_0} C_0(\mathbf{a}) f_{\mathbf{X_t}}(\mathbf{x_C}; t, \mathbf{a}, \mathrm{Pe}) d\mathbf{a} \tag{4.26}$$

$$\sigma_C^2(\mathbf{x_c}, t) = \int_{V_0}\int_{V_0} C_0(\mathbf{a}) C_0(\mathbf{b}) f_{\mathbf{X_t},\mathbf{Y_t}}(\mathbf{x_C}, \mathbf{x_C}; t, \mathbf{a}, \mathbf{b}, \mathrm{Pe}) d\mathbf{a}\mathrm{b} - \langle C(\mathbf{x_c}, t)\rangle^2 \tag{4.27}$$

where $\mathbf{X_t}(\mathbf{t}; \mathbf{a})$ represents the total trajectory of a solute particle originating in $\mathbf{a} \in V_0$, $f_{\mathbf{X_t}}$ is the *pdf* of the displacement $\mathbf{X_t}$ and $f_{\mathbf{X_t},\mathbf{Y_t}}$ is the joint *pdf* of the displacements $\mathbf{X_t}(t; \mathbf{a})$ and $\mathbf{Y_t}(t; \mathbf{b})$. In particular we employ Equations 3.9 and 3.10, which have been derived by Fiori and Dagan, 2000 in the hypotheses of small heterogeneity variance and small initial area of injection. Also the displacement covariances X_{ii} and Z_{ii} are computed according to the relations provided by Fiori and Dagan, 2000 in case of exponential covariance structure of Y in a 2D formation.

$\langle C(\mathbf{x}_c, t)\rangle$ estimates the local value of concentration C at the centroid $\mathbf{x}_C$ of the plume as the expected value of concentration after ensemble-averaging over a theoretically infinite number of log-conductivity realizations. Typically $\langle C(\mathbf{x}, t)\rangle$ is very different from the actual local value of concentration which can be measured at $\mathbf{x}$ in each single realization. The variance $\sigma_C^2(\mathbf{x}_C, t)$ measures the estimated squared value of concentration fluctuations in $\mathbf{x}_C$. These fluctuations can be very large, especially in case of small solute bodies which are very far from ergodic conditions. Because of the bounded nature of concentration, which can vary between ambient concentration values and injection concentration values, high values of local concentration variance result in high probabilities for the extreme values of the range. The local concentration variance is typically large for small solute bodies, when local dispersion is small or when heterogeneity is strong. Moreover it also depends on the reference location $\mathbf{x}$, with typically large coefficient of variation $CV(\mathbf{x}, t) = \sigma_C(\mathbf{x}, t)/\langle C(\mathbf{x}, t)\rangle$ along plume's fringes. Hence $\sigma_C^2(\mathbf{x}, t)$ is regarded as a measure of uncertainty, and exposes the unreliability of the local mean values.

Figures 4.2 show the time evolution of $\langle C\rangle$ and σ_C^2 (in the following we omit the reference to space and time, implying that we are computing the statistics at the centroid of the plume $\mathbf{x_C}$) for the small injection case for the reactive species which take part in the reaction. Species A and B display a behavior which is very similar to the behavior pointed out for analogous quantities by Bellin, Severino, and Fiori, 2011 in case of heterogeneous reaction. In general, the higher the log-conductivity variance σ_Y^2 of the formation and the higher the Peclet number of the problem, the higher σ_C^2 for all the species involved into the reaction. Both higher heterogeneity and smaller local dispersion values increase the uncertainty on the plume location, especially at intermediate times. Higher σ_C^2 peaks also correspond to larger distributions, that is, long-lasting uncertainty.

Local concentration means (left column in Fig. 4.2) suggest that with time the local value of concentration goes from the injection concentration to the ambient

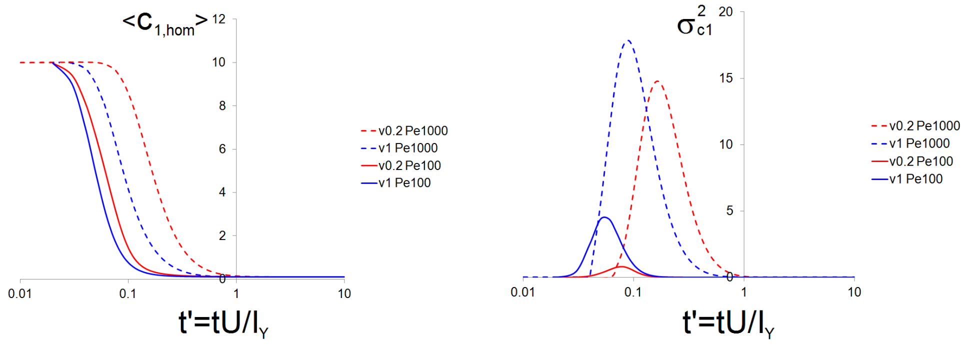

(a) $\langle C_{1,\text{hom}}\rangle$ **(b)** $\sigma^2_{\text{C1,hom}}$

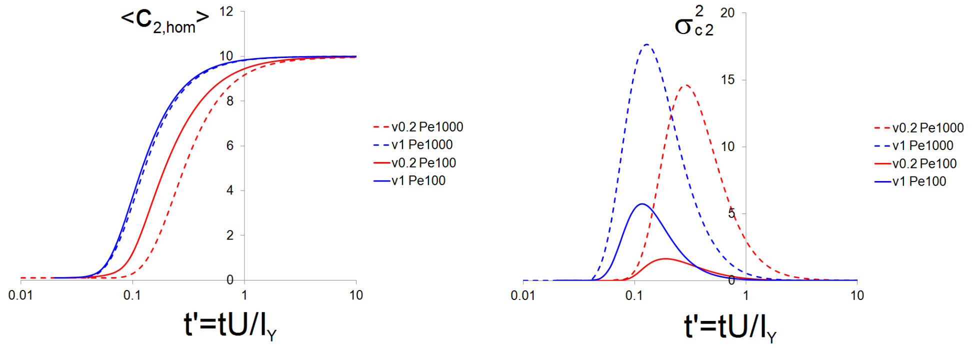

(c) $\langle C_{2,\text{hom}}\rangle$ **(d)** $\sigma^2_{\text{C2,hom}}$

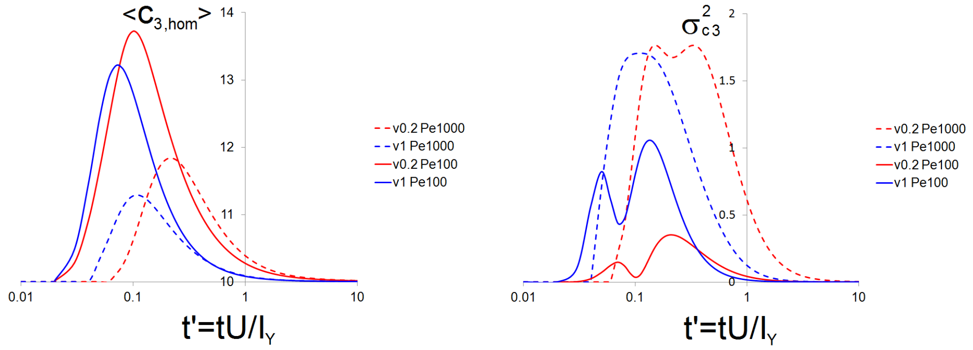

(e) $\langle C_{3,\text{hom}}\rangle$ **(f)** $\sigma^2_{\text{C3,hom}}$

Figure 4.2: Local moments (mean $\langle C_i\rangle$ and variance $\sigma^2_{C,i}$) of concentration for the different reactive species at the centroid $\mathbf{x_C}$ of the plume in case of small ($0.1I_Y \times 0.1I_Y$) instantaneous injection. A combination of color and line type is used to distinguish between Peclet number (Pe = 100 and Pe = 1000) and log-conductivity variance σ^2_Y (v0.2 and v1).

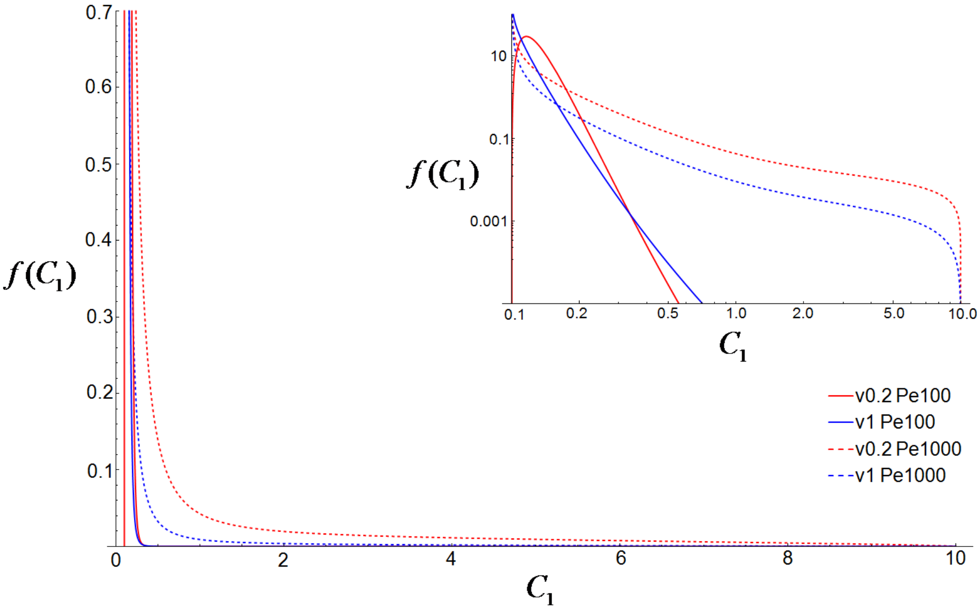

Figure 4.3: Local pdfs $f(C_1)$ for species A at the centroid of the plume in case of small $(0.1I_Y \times 0.1I_Y)$ instantaneous injection at time $t' = tU/I_Y = 0.5$. The inset shows the same curves in a log-log plot. A combination of color and line type is used to distinguish between Peclet number (Pe $= 100$ and Pe $= 1000$) and log-conductivity variance σ_Y^2 (v0.2 and v1).

concentration as an effect of dilution. This transition is slightly sharper and more anticipated for $\sigma_Y^2 = 1$ formations rather than $\sigma_Y^2 = 0.2$ ones, because of stronger spreading. The large uncertainty, evidenced by the variance values, suggests that the local mean values are not reliable. If we compare the local moments also for a non-reactive C_1 with the same initial conditions, we can verify how the reaction anticipates the transition from $C_{1,\text{inj}}$ to $C_{1,\text{amb}}$ for C_1 in all cases, and reduces the time duration of uncertainty because of a faster consumption of the injected solute mass, that is, a faster shrinking of the injected solute body.
Figures 4.2e and 4.2f display $\langle C \rangle$ and σ_C^2 for species C which originates from the mixing of species A and B. We impose $C_{3,\text{amb}} = C_{3,\text{inj}}$ so that C concentration departs and returns to the same value. The peak of $\langle C_3 \rangle$ roughly corresponds to the sharper region in the $\langle C_1 \rangle$ and $\langle C_2 \rangle$ cases. The production of C depends on the contemporaneous presence of species A and B; the relative amount of each species in oversaturated waters determines the rate of production of C. That is why σ_{C3}^2 distributions are much larger than the species A and B ones, resulting as a sort of combination between the two. The most evident feature is the bimodality of the time behavior of the variance, with two distinguishable peaks which approximately correspond to the separate peaks of σ_{C1}^2 and σ_{C2}^2.

The local pdfs complete the information provided by the first two local moments by providing the whole probability distribution referring to each concentration belonging to the physically admissible range. These pdfs take into account both actual mixing processes (due to the action of local dispersion, favored by heterogeneity) and uncertainty. As pointed out by Bellin, Severino, and Fiori, 2011, the Beta dis-

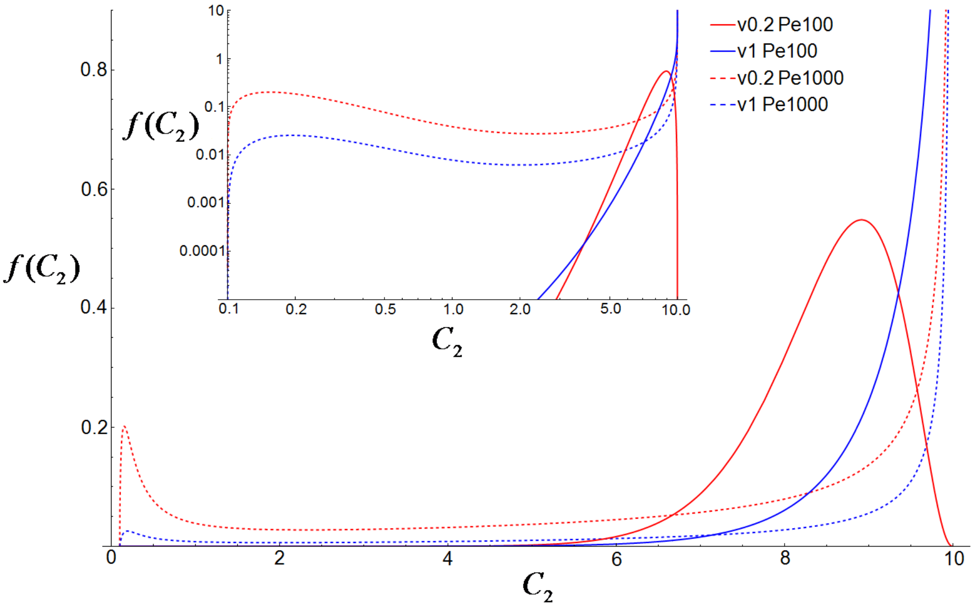

Figure 4.4: Local pdfs $f(C_2)$ for species B at the centroid of the plume in case of small $(0.1I_Y \times 0.1I_Y)$ instantaneous injection at time $t' = tU/I_Y = 0.5$. The inset shows the same curves in a log-log plot. A combination of color and line type is used to distinguish between Peclet number (Pe = 100 and Pe = 1000) and log-conductivity variance σ_Y^2 (v0.2 and v1).

tribution and its modifications, which express the probability distribution of the reactive species, are flexible enough to provide the uncertainty assessment of the local concentration values over the whole admissible range. When the dilution process is slow or early, that is, it is not enhanced by a large pore scale dispersion or by large heterogeneity, pdfs tend to be unimodal. As the dilution process proceeds, favored by pore scale dispersion or by higher heterogeneity, the extreme values tend to be more probable with respect to intermediate values of concentration; pdfs are thus bimodal. At late times, pdfs become unimodal again and centered on the ambient water concentration towards which the system tends once the dilution process approaches completion. Since pdfs are bimodal for long periods of time, the local mean values are confirmed to be far from actual concentration values encountered in single realizations. The level of heterogeneity and the value of the Peclet number change the shape and the actual temporal evolution of the pdf, but not this general evolution.

We consider the pdf for the different species in case of small $(0.1I_Y \times 0.1I_Y)$ instantaneous injection at time $t' = 0.5$. The parameters of $B(z; p_1, p_2)$ are computed by the method of moments, thus substituting the theoretical values obtained by Equations 4.26 and 4.27 into the analytical relations 4.8a and 4.8b. Each line, which corresponds to a different combination of the parameters Pe and σ_Y^2, captures a different phase of the pdf time evolution. In general, dilution grows with the heterogeneity level and decreases with the Peclet number. But variations to this general behavior are provided by the influence of uncertainty, which determines a shift of probability due to heterogeneity and local dispersion.

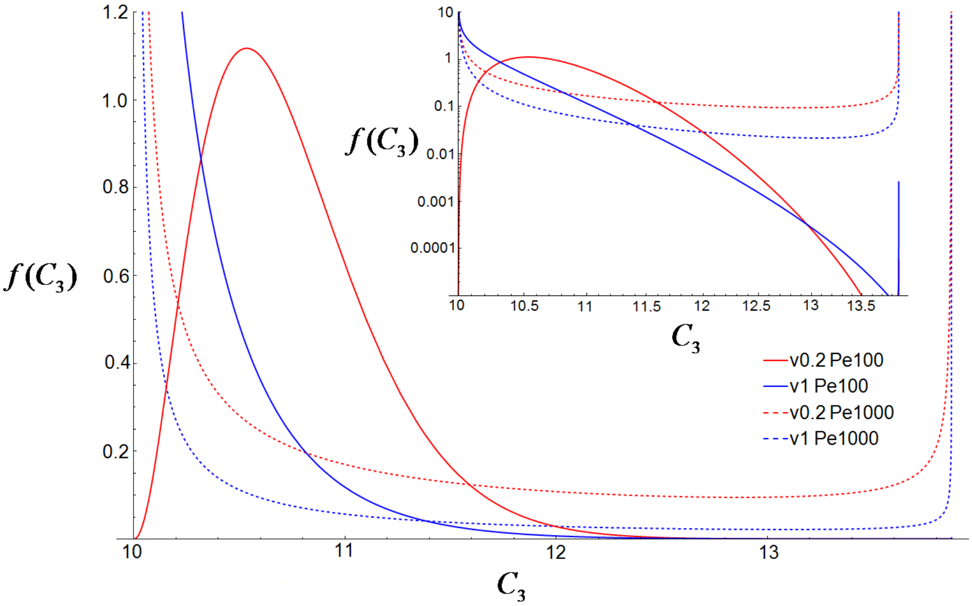

Figure 4.5: Local pdfs $f(C_3)$ for species C at the centroid of the plume in case of small $(0.1I_Y \times 0.1I_Y)$ instantaneous injection at time $t' = tU/I_Y = 0.5$. The inset shows the same curves in a log-log plot. A combination of color and line type is used to distinguish between Peclet number (Pe $=100$ and Pe $=1000$) and log-conductivity variance σ_Y^2 (v0.2 and v1).

The pdfs f_{C_i} are computed for the $\lambda = 0.1$ case, but similar conclusions, although more retarded in time, can be drawn for the $\lambda = 1$ case. Moreover, the $\lambda = 1$ cases are more regular and predictable since the largest size of the plume reduces the amount of uncertainty around the centroid of the plume. In the case of small $\lambda = 0.1$ injection, the mean and the variance are computed neglecting the dependence of Z_{ii}, which cannot be neglected in case of larger $\lambda = 1$ injection.

Figure 4.3 shows the different stages of the pdf evolution referring to species A. At $\sigma_Y^2 = 0.2$ and Pe $= 100$, the pdf is in the last unimodal phase of its evolution, that is, the plume is already rather well mixed, to such an extent that the mean local value at the centroid of the plume is considerably smaller than $C_{1,\text{inj}}$. Looking back at the correspondent local mean and variance, we can see how the transition from the injection condition to the ambient condition at time $t' = 0.5$ is already almost complete, so that also the variance is small. The same happens for the $\sigma_Y^2 = 1$ case, where the pdf is pressed towards the lower boundary of the C_1 range. Also when Pe $= 1000$, that is, lower values of local dispersion, pdfs are unimodal, but higher probability is assigned to larger C_1 values.

An opposite behavior at time $t' = 0.5$ is provided by f_{C2} (Fig. 4.4), since the ambient concentration is located at the upper extreme of the interval $[C_{2,\text{min}}, C_{2,\text{max}}] = [C_{2,\text{inj}}, C_{2,\text{amb}}]$. The dilution dynamics is generally more retarded for species B than for species A, thus $\langle C_2 \rangle$ is still lower than $C_{2,\text{amb}}$, and σ_{C2}^2 values are large, especially for the Pe $= 1000$ cases. Thus these pdfs are bimodal, still predicting not negligible probabilities for low C_2 values close to $C_{2,\text{inj}}$. Lower rates are given to the intermediate values, thus depriving the local mean of all meaning concerning the

prediction of actual local concentrations at the centroid of the plume.
The range of variation of C_3 is determined analytically from the range of z. In all cases σ^2_{C3} at time $t' = 0.5$ is not negligible, thus the pdfs (especially the high σ^2_Y - high Pe ones) assign relevant probability to wide ranges of C_3 values (see Fig. 4.5). The Pe $= 1000$ pdfs display a bimodal behavior, although skewed towards the low, ambient concentration value. For later times, all f_{C3} move decisively toward a unimodal shape leant against $C_{3,\mathrm{amb}}$.
Species C is produced at the highest rates where the gradients $\nabla(C_1 + C_3)$ and/or $\nabla(C_2 + C_3)$ are large, as a result of the reaction between A and B molecules which establishes local equilibrium. At the actual centroid of the plume, the reaction rate is initially slow, because these gradients are small, and increases at later times when the dilution process proceeds further. However, when the plume is small, the uncertainty on the location of the highest gradients involves from the inception also the centroid of the plume, so that also the extreme values of the concentration ranges are involved at early times with not negligible values of f_{C_3}.

4.5 Applications: global statistics

Global statistics can often provide a more useful piece of information, despite its lumped nature, as shown in Chapter 3. We use here the fully Lagrangian estimates for the global moments $\langle \bar{z} \rangle$ and S^2_Z for the passive standard tracer $z = c/c_0$ provided by Equations 3.30 and 3.31 and Equation 3.32 in Chapter 3, and use them for predicting the spatial moments of the species reacting upon the bimolecular equilibrium reactions considered in this Chapter. These semianalytical formulations are not limited by the initial plume size, but estimates are obtained under the hypothesis of weak or mild heterogeneity of the formations. Global moments could be alternatively provided by Monte Carlo simulations; stabilizing global moments requires a much smaller number of realizations than obtaining stable local statistics.
We present the moments for both the heterogeneous and the homogeneous case in the case of finite $I_Y \times I_Y$ instantaneous injection. All simulations share the same heterogeneity structure, characterized by an exponential covariance function, and all quantities are non-dimensional. Figure 4.6 shows the temporal behavior of the theoretical spatial moments as predicted by the first order approximation equations presented in Chapter 3. The line type refers to the Pe number whereas color refers to the heterogeneity level expressed through σ^2_Y. The meaning of the global moments is conceptually and practically different from the local moments'. Global variances $S^2_{C_i}$ are in fact an almost clean measure of dilution, because they average the concentration fluctuations in all points belonging to the plume with respect to the spatial mean concentration. As actual integral moments lack any spatial reference, also the theoretical estimation of spatial moments rely on an undefined reference system hooked to the unknown position of the plume centroid (Fiori, 2001a). Referring to the actual, although unknown, centroid of the plume filters out most of the uncertainty related to the spatial distribution of concentration, as confirmed by both the moments and pdfs pattern. Also the spatial mean $\langle \bar{C}_i \rangle$ acquires a meaning which is closer to actual spatial mean values.
The global means $\langle \bar{C}_1 \rangle$ and $\langle \bar{C}_2 \rangle$ show for species A and B a monotonic pattern towards the ambient concentration value. As opposed to $\langle C_3 \rangle$, $\langle \bar{C}_3 \rangle$ senses the reaction

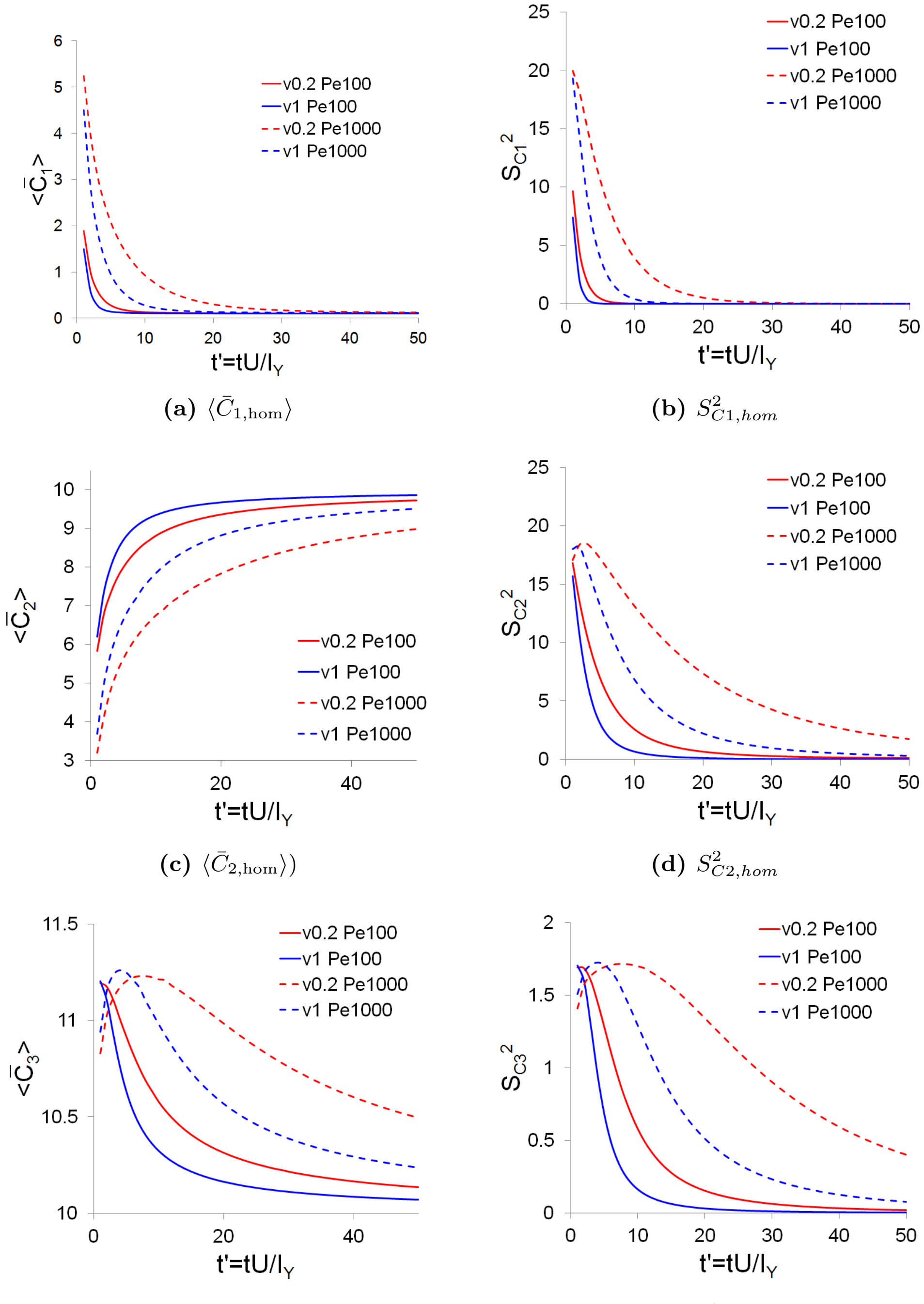

(a) $\langle \bar{C}_{1,\mathrm{hom}} \rangle$

(b) $S^2_{C1,hom}$

(c) $\langle \bar{C}_{2,\mathrm{hom}} \rangle)$

(d) $S^2_{C2,hom}$

(e) $\langle \bar{C}_{3,\mathrm{hom}} \rangle)$

(f) $S^2_{C3,hom}$

Figure 4.6: Global moments (mean $\langle \bar{C}_i \rangle$ and variance S^2_{Ci}) of concentration for the different reactive species in case of finite ($I_Y \times I_Y$) instantaneous injection. A combination of color and line type is used to distinguish between Peclet number (Pe = 100 and Pe = 1000) and log-conductivity variance σ^2_Y (v0.2 and v1).

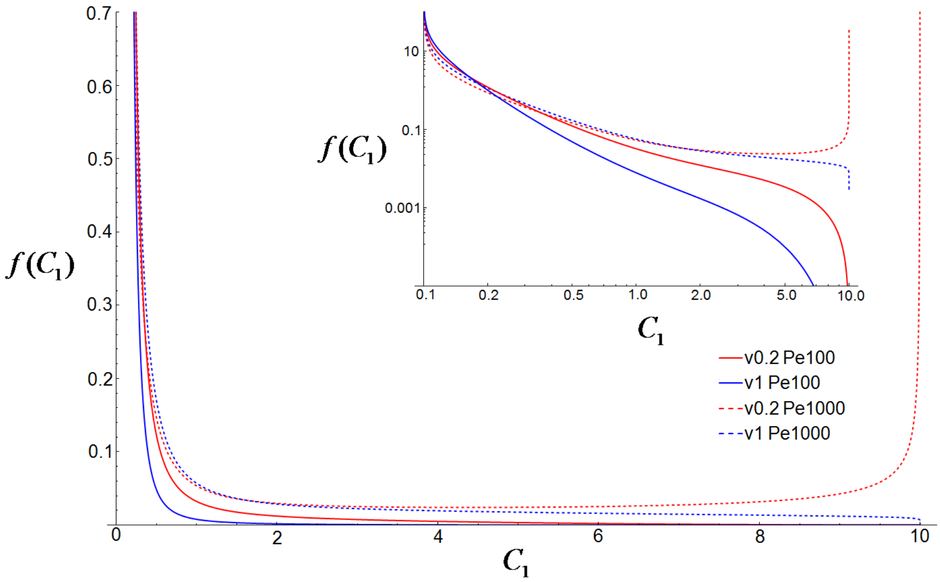

Figure 4.7: Global pdfs $f(C_1)$ for species A in case of finite $(I_Y \times I_Y)$ instantaneous injection at time $t' = tU/I_Y = 5$. The inset shows the same curves in a log-log plot. A combination of color and line type is used to distinguish between Peclet number (Pe = 100 and Pe = 1000) and log-conductivity variance σ_Y^2 (v0.2 and v1).

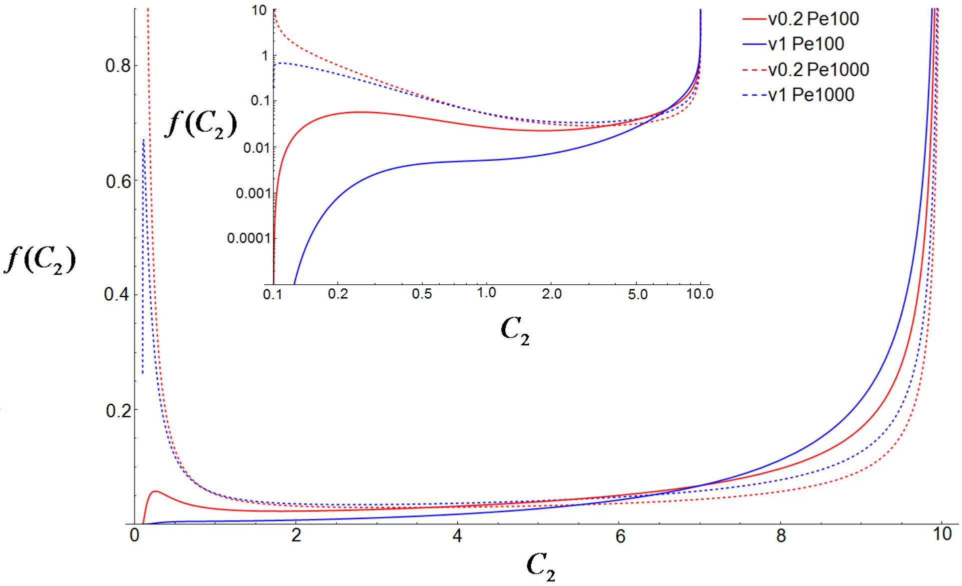

Figure 4.8: Global pdfs $f(C_2)$ for species B in case of finite $(I_Y \times I_Y)$ instantaneous injection at time $t' = tU/I_Y = 5$. The inset shows the same curves in a log-log plot. A combination of color and line type is used to distinguish between Peclet number (Pe = 100 and Pe = 1000) and log-conductivity variance σ_Y^2 (v0.2 and v1).

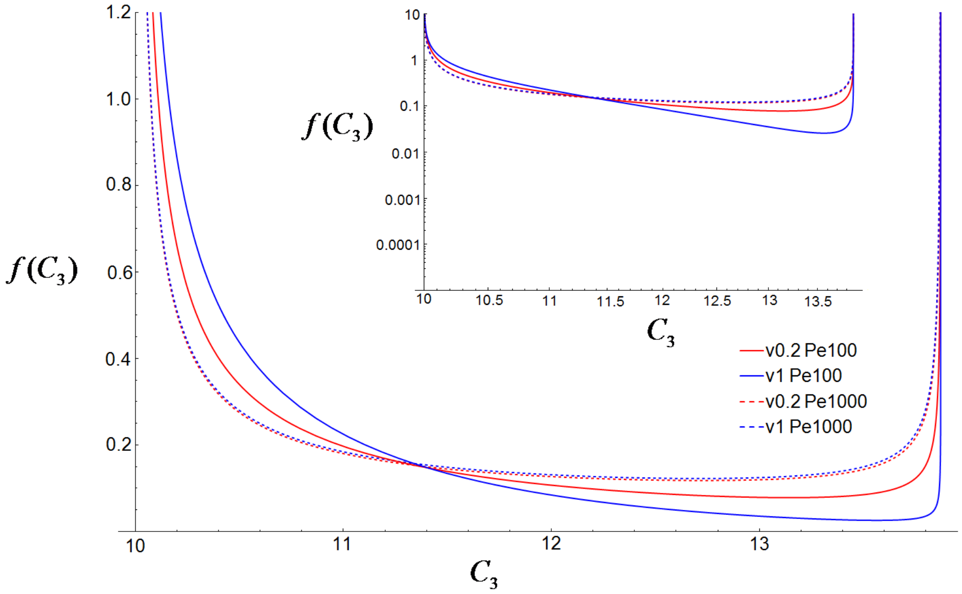

Figure 4.9: Global pdfs $f(C_3)$ for species C in case of finite $(I_Y \times I_Y)$ instantaneous injection at time $t' = tU/I_Y = 5$. The inset shows the same curves in a log-log plot. A combination of color and line type is used to distinguish between Peclet number (Pe $= 100$ and Pe $= 1000$) and log-conductivity variance σ_Y^2 (v0.2 and v1).

from very early times. The initial non monotonic behavior of $\langle \bar{C}_3 \rangle$ is related to the fact that at the beginning the inner portions of the plume are not involved by the reaction, thus locally $C_3 = C_{3,\mathrm{amb}}$. Later C_3 grows as a result of the reaction, which is boosted along plume fringes by ∇C_1 and ∇C_2. Alternatively A and B act as the limiting factor for the reaction. The rate of change of $\langle \bar{C}_i \rangle$ for all species depends on the combination of Pe and σ_Y^2, with both local dispersion and heterogeneity which steepen this trend. In the absence of reaction, C_1 would dilute more slowly because there would be no species A consumption by the reaction. In general in this case the decrease of both the mean $\langle \bar{C}_1 \rangle$ and the variance S_{C1}^2 would be delayed.

As already evidenced by local statistics, the time evolution for both moments is different for the different species. All of them depend on dz/dt, but different non linear relations between C_i and z result in different time dynamics. C_1 is the one which responds faster to z variations, because of a steeper slope at high z values. On the contrary C_2 variations are amplified at low z values. C_3 is sensitive to z variations at both high and low values; its production can be limited by either A or B.

Further calculations for both smaller $(0.1I_Y \times 0.1I_Y)$ and larger $(0.25I_Y \times 80I_Y)$ initial source area have been performed. Small injection causes faster dilution with mean values which become quickly very close to ambient concentration values and variances which are very low, especially for small Pe. Large line (ergodic) injection provides a very similar pattern for the spatial moments as the finite $I_Y \times I_Y$ case, with a larger difference between the Pe $= 100$ and the Pe $= 1000$ cases because of a larger role of heterogeneity.

In case of heterogeneous reaction, the spatial moments of A and B behave in the same manner as in the homogeneous case because of the choice of the initial conditions. Since reactions are mixing-controlled, the development of the reaction is very similar in the two cases.

The pdfs extend the representation of these phenomena over the whole range of admissible concentrations. Pdf values represent the volume fraction of the solute body which is characterized by a given value of concentration. As opposed to local statistics, global statistics are bimodal at time 0, while they gain unimodality very soon moving toward the ambient values of concentration with both the spatial mean and the mode which get closer to $C_{\mathrm{i,amb}}$. As a result, the spatial mean acquires a meaning which is more related to the physical behavior of the plume, despite the disconnection to Eulerian spatial references.
Figures 4.7, 4.8 and 4.9 display the probability distribution functions for species A, B and C, respectively, in case of homogeneous equilibrium reaction at time $t' = 5$. The shape parameters for the distributions are obtained from the theoretical derivation of the spatial moments. As already evidenced by local statistics, the time evolution is different for each species. For instance, for species A (Figure 4.7), the pdf maintains a bimodal shape for the the slowest combination of the parameters, that is, $\sigma_Y^2 = 0.2$ and $\mathrm{Pe} = 1000$. On the contrary C_2 pdfs (Fig. 4.8) at the same timestep $t' = 5$ are still bimodal for almost all parameter combinations, except for the faster one, that is, $\sigma_Y^2 = 1$ and $\mathrm{Pe} = 100$. This means that a non-negligible volume fraction of the solute body at time t' is still characterized by the initial injection concentration $C_{2,\mathrm{inj}}$. Finally for species C (Fig. 4.9) bimodality of f_{C3} lasts longer, and is still evident for all considered cases at time $t' = 5$, although skewed toward $C_{3,\mathrm{amb}}$.
The Beta distribution is thus useful because of its bimodal capabilities and because it allows to assign higher probability close to the extreme values in the range.

4.6 Applications: cumulative distribution functions and mass fractions

For risk assessment purposes it is often more practical to refer to cumulated statistics. Both local Cumulative Distribution Functions (CDFs) and global Cumulative Distribution Functions can be be immediately drawn from the pdfs $f_{C_i}(c_i)$ computed in the previous sections as $F(C_i < \mathsf{c_i}) = \int_{-\infty}^{\mathsf{c_i}} f_{C_i}(c_i) dc_i$, where f represents the local or global probability distribution, respectively. Local CDFs provide for a specific location the exceedance probability with respect to a given concentration threshold, whereas global CDFs assess the probability that the local concentration, anywhere within the plume, exceeds a given concentration threshold. Concentration thresholds can correspond to solute detection limits or Law requirements, or they can be related to health risk, as in case of cancerogenic chemicals, whose threshold concentrations are provided by the Environmental Protection Agencies (Tartakovsky and Winter, 2008).
A similar piece of information is provided by the following quantity:

$$mF(c_i^*) = \frac{\int_0^{c_i^*} c_i f_{C_i}(c_i) dc_i}{\int_0^{c_{\mathrm{i,max}}} c_i f(c_i) dc_i} \tag{4.28}$$

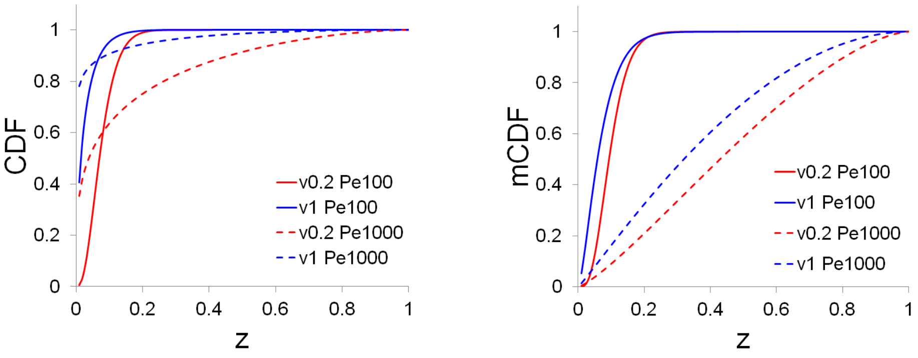

(a) CFD for the passive solute

(b) mCDF for the passive solute

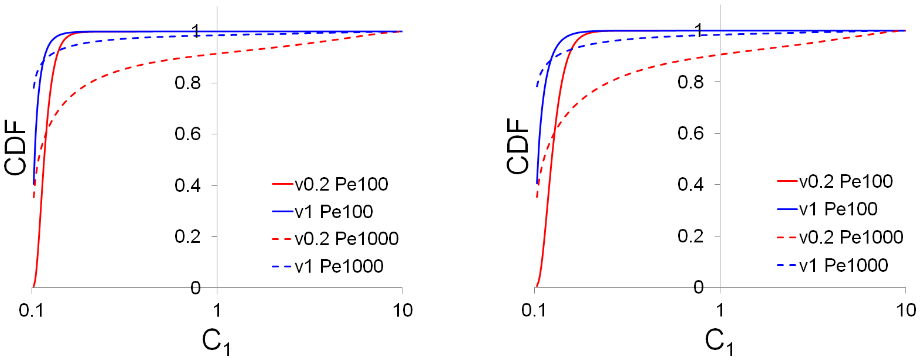

(c) CDF for $C_{1,\text{het}}$

(d) CDF for $C_{1,\text{hom}}$

Figure 4.10: Theoretical local CDFs and mCDFs for both the passive solute z and the reactive species A in case of bimolecular heterogeneous or homogeneous reaction, in case of finite $(0.1I_Y \times 0.1I_Y)$ instantaneous injection at time $t' = tU/I_Y = 0.5$. The dimensionless concentration of species A, C_1, is normalized over $\sqrt{K_{\text{eq}}}$ for the heterogeneous reaction, and over K_{eq} for the homogeneous reaction. A combination of color and line type is used to distinguish between Peclet number (Pe = 100 and Pe = 1000) and log-conductivity variance σ_Y^2 (v0.2 and v1).

$c_{\text{i,max}}$ represents the upper limit of the admissible range for c_i.

In the framework of local statistics, $mF(c_i^*)$ is somehow related to the concept of Expected Mass Fraction (EMF) proposed by Heagy and Sullivan, 1996 in the context of atmospheric physics, and recently used in risk assessment by Andricevic, Srzic, and Gotovac, 2012. For an assigned location $\mathbf{x_0}$, $mF(c_i^*;\mathbf{x_0})$ represents in fact the probability rate of the expected value of the mass above c_i^*. A further integration of $(1 - mF(c_i^*))$ over time exposure provides the amount of mass which gets through $\mathbf{x_0}$ with $c_i > c_i^*$ by computing:

$$\int_{c_i^*}^{c_{i,max}} \frac{1}{\bar{d}(\mathbf{x_0})} \int_0^\infty c_i f(c_i, \mathbf{x_0}, t) dt dc_i \tag{4.29}$$

where $\bar{c}_i(\mathbf{x}_0, t)$ is the expected concentration at $\mathbf{x}_0$ at time t, and $\bar{d}(\mathbf{x})dV = \int_0^\infty \bar{c}_i(\mathbf{x_0}, t)$ represents the expected total mass passing $\mathbf{x_0}$. The variable C_i refers to the detec-

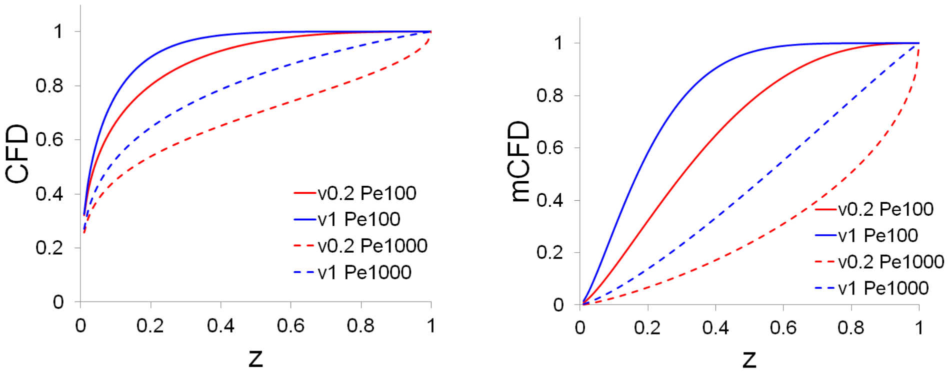

(a) CFD for the passive solute

(b) mCFD for the passive solute

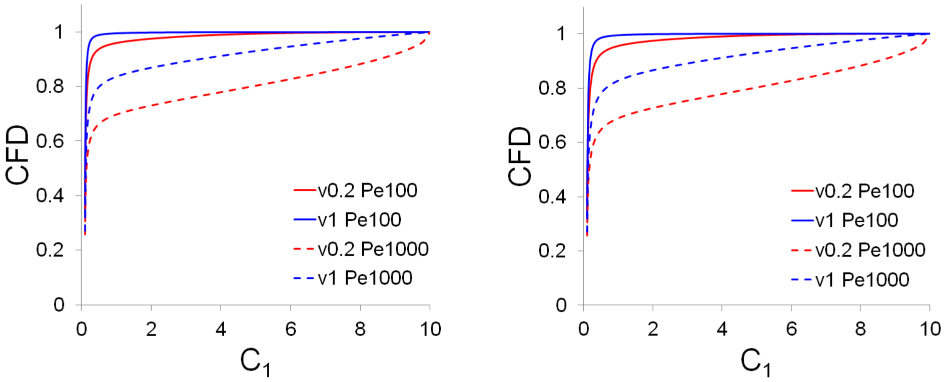

(c) CFD for $C_{1,\text{het}}$

(d) CFD for $C_{1,\text{hom}}$

Figure 4.11: Theoretical global CFDs and mCFDs for both the passive solute z and the reactive species A in case of bimolecular heterogeneous or homogeneous reaction, in case of finite $(I_Y \times I_Y)$ instantaneous injection at time $t' = tU/I_Y = 5$. The dimensionless concentration of species A, C_1, is normalized over $\sqrt{K_{\text{eq}}}$ for the heterogeneous reaction, and over K_{eq} for the homogeneous reaction. A combination of color and line type is used to distinguish between Peclet number (Pe = 100 and Pe = 1000) and log-conductivity variance σ_Y^2 (v0.2 and v1).

tion volume dV, whereas the pdf $f_{C_i}(\mathbf{x_0}, t)$ describes also the time variations of the probability distribution of concentration. The EMF is useful for assessing human risk in terms of dosage in case of accidental instantaneous solute injection of toxic or harmful compounds.

On the contrary, in the framework of global statistics $mF(c_i^*)$ represents the total amount of mass (with respect to the total plume's mass) with $c_i < c_i^*$:

$$mF(c_i^*) = \frac{\int_0^{c_i^*} c_i f_{C_i}(c_i) V_s dc_i}{\int_0^{c_{\text{i,max}}} c_i f(c_i) V_s dc_i} \tag{4.30}$$

where V_s represents the plume's volume. All quantities, namely mF, f_{C_i} and V_s, can depend also on time. The numerator represents the cumulated solute mass up to $c_i = c_i^*$, and the denominator represents the total amount of solute mass within the plume.

Once we assume the passive solute z to be distributed according to the Beta distribution, we can directly compute $mF(z)$ as follows:

$$mF(z^*) = \frac{\int_0^{z^*} zB(z;p_1,p_2)dz}{\int_0^1 zB(z;p_1,p_2)dz} = B(z;p_1+1,p_2) \tag{4.31}$$

where $B(z;p_1,p_2)$ is the Beta PDF of z and p_1 and p_2 its shape parameters which are analytically related to the z first two moments.
The extension to the reactive species is straightforward; for the heterogeneous case:

$$mF(c_i^*) = \frac{1}{2}\left[\pm\Delta u B(z^*;p_1+1,p_2) + u_0 B(z^*;p_1,p_2) + \beta_0(z^*)\right], \qquad i = 1,2 \tag{4.32}$$

and for the homogeneous case:

$$\begin{aligned} mF(c_i^*) =& \frac{1}{2}\left[\pm(\Delta u_1 - \Delta u_2)B(z^*;p_1+1,p_2) + (\pm u_{1,0} \mp u_{2,\mathrm{inj}} - K_{\mathrm{eq}})B(z^*;p_1,p_2)\right. \\ & \left. +\delta_0(z^*)\right] \qquad i = 1,2 \qquad (4.33) \\ mF(c_3^*) =& \frac{1}{2}\left[-(\Delta u_1 + \Delta u_2)B(z^*;p_1+1,p_2) + (u_{1,0} + u_{2,inj} + K_{eq})B(z^*;p_1,p_2)\right. \\ & \left. -\delta_0(z^*)\right] \qquad (4.34) \end{aligned}$$

where $z^* = z(c_i^*)$ is the inverse function of each speciation equation $c_i = \mathsf{c}_\mathsf{i}(z)$ computed for $c_i = c_i^*$ and:

$$\beta_0(z^*) = \int_0^{z*} \sqrt{(\Delta u z + u_0)^2 + 4K_{\mathrm{eq}}}B(z;p_1,p_2)dz \tag{4.35}$$

$$\delta_0(z^*) = \int_0^{z*} \sqrt{\rho(z)}B(z;p_1,p_2)dz. \tag{4.36}$$

The computation of the mFs for the reactive species is slightly more complicated because it involves the integrals $\beta_0(z^*)$ and $\delta_0(z^*)$ which have to be solved numerically for each value of z^*. As a result, it is cumbersome to compute this integration for all the values of c_i in its range of variability. Nevertheless we can easily compute single values of mFs for a specific concentration threshold value.

In the following graphs, we show both F and mF for z and F for species A in case of bimolecular equilibrium homogeneous and heterogeneous reactions. Figures 4.10 refer to local statistics in case of uniform $0.1I_Y \times 0.1I_Y$ injection. While the CDF for both the conservative and the reactive species expresses the probability that the concentration at the centroid is lower than each concentration threshold value, mF represents the expected instantaneous mass fraction at time $t' = 0.5$ in $\mathbf{x_C}$ and it is the first step for estimating dosage in terms of cumulated mass above a given concentration threshold. All CDFs display a similar pattern which confirms what already emerged from the analysis of the pdfs (Section 4.4). Dilution has already eroded high concentration values (close to the injection concentration), helped by the reaction. As a result, the growth is more anticipated for species A than for the passive tracer. Notice that the x axis is in log-scale for species A. mF

amplifies the distance between the curves at high concentration, where the expected mass difference is larger, and reduces the gap at low concentration. In case of larger $I_Y \times I_Y$ injection, all distributions display a similar trend, although there is a softer separation between cases with different Pe number.
On the other hand, Figures 4.11 refer to global statistics in case of $(I_Y \times I_Y)$ injection. Cumulative Frequencies represent the volume fractions with respect to the total plume volume where concentration is lower than a specific threshold, while mF represent the mass fraction of the plume where concentration is lower than a given threshold. Both quantities are important for plume or field scale risk assessment, for example in case of large receptors such as rivers or well fields, or in general in order to assess the impact of the whole plume on the aquifer. Also in this case, the reaction anticipates the growth of the CFDs for the reactive species A compared to the conservative solute. Cumulative distributions in case of smaller $(0.1 I_Y \times 0.1 I_Y)$ injection reflect the fact that pdfs in this case assume at very early times an almost Dirac shape centered on C_{amb}. In case of large line injection $(0.25 I_Y \times 80 I_Y)$, spatial cumulative distributions present a very similar pattern as the one shown in Fig. 4.11. Generally, in this second case the dilution process proceeds faster, as an effect of a larger ratio between the whole interface of the plume and its volume. As well known, dilution takes place along plume fringes, promoted by concentration gradients.

4.7 Global statistics: Theoretical predictions and numerical simulations

The theoretical predictions for the moments and the probability distributions of reactive species presented in the previous Sections (4.5 and 4.6) can be compared to numerical simulations on deterministic heterogeneity fields. Unlike local statistics, global statistics aims at reproducing single-realization scenarios rather than ensembles.
The comparison between the theoretical a-priori predictions and the numerical correspondent simulations for conservative transport has already been presented in Chapter 3 for a comprehensive set of numerical transport scenarios in 2D formations. In general, the comparison between the numerical results and the theoretical a-priori predictions is good for the passive tracer, for both the moments and the probability distributions. In that case low Peclet number and larger initial injection area improve the agreement between the two. For the same set of simulations, we compare also the moments and the probability distributions in case of bimolecular equilibrium reactions, taking advantage of the mathematical manipulations carried out in the present chapter. The numerical simulations are performed on deterministic heterogeneity fields with log-conductivity variance equal to $\sigma_Y^2 = 0.2$ and $\sigma_Y^2 = 1$. Coherently with the theoretical basis of the semianalytical formulae, the Y fields have a exponential isotropic covariance structure, characterized by an integral scale I_Y which is the length scale used for normalizing spatial quantities. The Peclet number $\mathrm{Pe} = U I_Y / D$ is set as equal to 100 and 1000 in order to test different conditions. The initial conditions for the simulations are of uniform initial concentration within A_0, with dimensionless $C_{1,\mathrm{inj}} = 10$, $C_{2,\mathrm{inj}} = 0.1$ and $C_{3,\mathrm{inj}} = 10$ within A_0, and $C_{1,0} = 0.1$, $C_{2,0} = 10$ and $C_{3,0} = 10$ outside. The permeameter-like flow field is

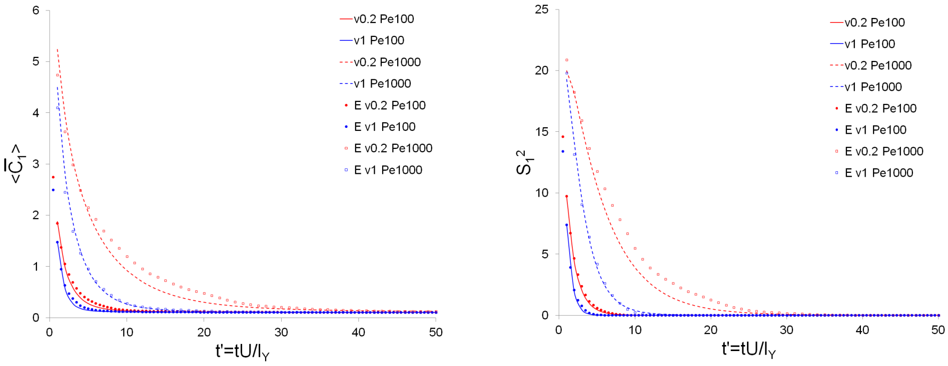

(a) $\langle \bar{C}_{1,\mathrm{hom}} \rangle$ **(b)** $S^2_{\mathrm{C1,hom}}$

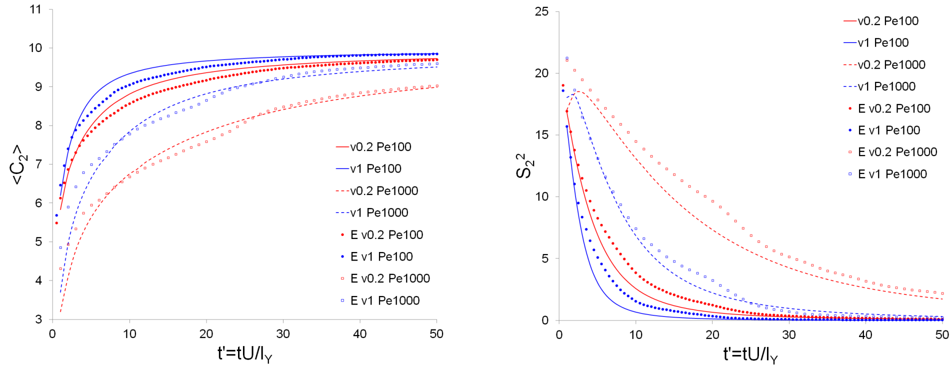

(c) $\langle \bar{C}_{2,\mathrm{hom}} \rangle$ **(d)** $S^2_{\mathrm{C2,hom}}$

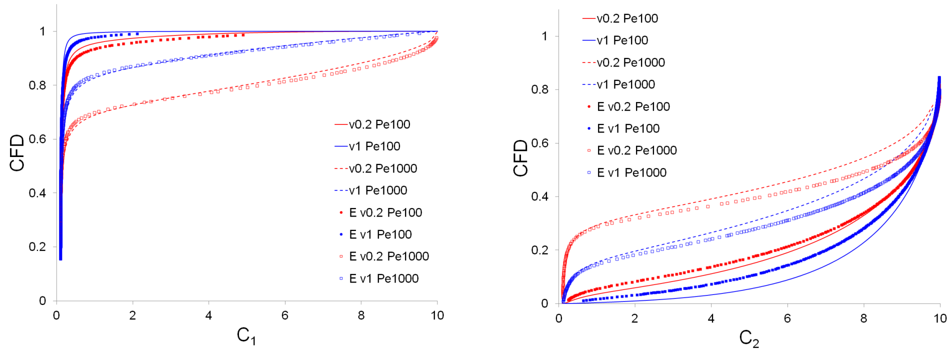

(e) CFD for $C_{1,\mathrm{hom}}$ **(f)** CFD for $C_{2,\mathrm{hom}}$

Figure 4.12: Theoretical and numerical global moments (mean $\langle \bar{C} \rangle$ and variance S^2_C) and CFD for the reactive species A and B involved in the bimolecular equilibrium homogeneous reaction $A + B \rightleftharpoons C$, in case of finite $(I_Y \times I_Y)$ instantaneous injection at time $t' = tU/I_Y = 5$. The dimensionless concentrations of species A and B, C_1 and C_2, are normalized over K_{eq}. A combination of color and plot type is used to distinguish between Peclet number (Pe = 100 and Pe = 1000) and log-conductivity variance σ^2_Y (v0.2 and v1); discontinuous dots represent the results of numerical simulations, whereas lines represent the theoretical predictions.

driven by a mean hydraulic gradient of $J = 0.03$ which determines a dimensionless effective velocity U along the longitudinal direction.

In Fig. 4.12 we present the comparison between theoretical predictions and numerical results in case of intermediate ($I_Y \times I_Y$) injection. All statistics are computed with reference to the concentration of the reactive species A and B in case of bimolecular homogeneous reaction. The Advection Dispersion Equations for the components u_1 and u_2 are solved by means of SPH simulation (see Chapter 2 for the implementation details), whereas reactive concentration maps are obtained through mathematical post-processing of the numerical conservative tracer results. The theoretical models for both the moments and the CFDs of the reactive species concentration are the ones presented in the previous sections (Sec. 4.5 and 4.6). Hence the theoretical CFDs are obtained by assuming a Beta distribution for the standard passive tracer z, with z moments obtained with the semianalytical Lagrangian relations presented in Chapter 3.

Despite being referred to non-ergodic transport scenarios, the comparison of the statistical quantities is good for both species. The match is slightly worst for the global variance, and for the highest Peclet number Pe = 1000, probably because in this case the plume is still rather influenced by the very local heterogeneity structures experienced by the solute body. Similar conclusions can be drawn for different initial source sizes, with generally a better comparison in case of large ergodic injection, and a slightly worst comparison for a smaller injection (not shown here). Analogous results are obtained in case of bimolecular equilibrium heterogeneous reaction.

Joining the Lagrangian statistical tools for predicting the moments of the passive tracer, and the mathematical manipulation shown in this Chapter can provide useful a-priori information on the fate of reactive species in the aquifer. Information about the consumption of the injected species (species A) or of the species which is predominant in the ambient water (species B) have a direct implication in remedial systems, since species A can be either interpreted as spilled contaminant or reactive chemical delivered into the aquifer for remediation purposes.

4.8 Conclusions

We analyzed the case of mixing-controlled bimolecular equilibrium reactions in groundwater. The reactive system has been deeply investigated in the past, hence the literature provides the analytical speciation equations which link the concentration of a reference passive tracer z to the concentration of the solute reactive species which take part in the reaction. Moreover, as stated by Bellin, Severino, and Fiori, 2011, among others, statistics can provide the analytical tools for dealing with reactive transport, which decisively depends on local processes. In particular, they provided an analytical procedure for linking the local pdf of z to the pdf of the concentrations C_i of the species reacting upon mixing in case of an heterogeneous equilibrium reaction, under the assumption of the validity of the Beta distribution as pdf of z. They also suggested the use of Lagrangian estimates of local moments for determining the shape parameters of these pdfs.

In this chapter we found similar expressions for both the moments (mean and variance) and the pdfs of solutes reacting upon a bimolecular homogeneous reaction, relying on the same assumption of the validity of the Beta distribution to describe the pdf of the passive tracer concentration. Lagrangian estimates for both local and global moments were used to analyze the response of the pdfs to the dilution process, and consequently, to the reaction. Statistical Lagrangian tools provide the analytical or semianalytical means for estimating the moments as well as the probability distributions once we assess, on the basis of aquifer characterization, the main statistical features of the formation, the local dispersion tensor and the equilibrium constant of the reaction.

Local mean and variance of C_i are not representative of dilution but rather of the uncertainty which depends on the irregular spreading of the plume. These moments have a fully statistical meaning, since they represent probability estimates representative of the whole range of possibilities for the plume space and time evolution. The progress of the dilution process, driven by the local scale dispersion and enhanced by the heterogeneity level, reduces the amount of uncertainty which affects local moments, as well as a larger initial size of the plume. Thus local moments become significant at asymptotic times, when pdfs become unimodal and centered on the ambient values of concentration; in this way local means are closer to actual concentration values, and local variances tend to zero.

On the other hand, global statistics are more representative of the mixing process, although they lose any precise reference to spatial locations. This lumped nature makes them suitable to represent actual, single-realization scenarios. The global variance, for example, is an inverse measure of dilution, which tends to zero as the concentration distribution within the plume volume progressively homogenizes towards the ambient concentration. At the same time the global pdf becomes unimodal, and centered around concentration values close to the ambient values of concentration $C_{\mathrm{i,amb}}$. Hence also the global mean concentration acquires a meaning which is closer to actual concentration values registered within the plume. Clearly the homogenization process progresses at different rates for different values of local dispersion (expressed by the Peclet number) or heterogeneity levels (epitomized by the log-hydraulic conductivity variance σ_Y^2).

Finally we considered for both local and global statistics the quantities $F = \int f_C dC$ and $mF = \int C f_C dC$ (where f_C is the pdf of concentration C), and explored their usefulness for risk assessment purposes. Theoretical models provide, under the first order approximation (that is, weakly heterogeneous formations), the parameters for these distributions. Numerical bidimensional simulations confirmed the good match between the predicted global statistics, and the empirical statistics obtained through numerical modeling.

Chapter 5

Numerical Investigation of Mixing Processes in Highly Heterogeneous Formations

5.1 Introduction

The distribution of solute concentration within a plume transported in a heterogeneous saturated formation is known to be very disordered and dependent on the complex and nonlinear interplay between local dispersion and spatially variable advection. Given this complexity, most of the early studies (Dagan, 1984, 1989; Gelhar and Axness, 1983; Kitanidis, 1988; Neuman, Larrabee Winter, and Newman, 1987) dealt with the stochastic representation of the concentration field under the assumption that hydraulic property variations can be described as Stationary Random Space Functions (RSFs). In fact, the randomness of the hydraulic-conductivity field is reflected in the velocity field and then in the concentration field. However, local statistics provides a deceptive representation of the real distribution of the solute concentration, because it is strongly affected by the uncertainty related to the unknown hydraulic and geochemical properties of the medium and their spatial distribution. As a consequence, local estimates are indeed hardly representative of the actual values that we can find in a real aquifer, especially when they refer to locations close to plume fringes (Cirpka *et al.* [2008]) or far from ergodicity. Moreover ensemble quantities often overestimate the actual value of these variables (Cirpka *et al.*, 2008; Kapoor and Kitanidis, 1998). The situation is even worse for multi-species solute transport because the reaction between solute species depends, often non-linearly, on the local concentration of reactive species. Therefore, as clearly evidenced by Kapoor, Gelhar, and Miralles-Wilhelm, 1997, using in the reaction terms the ensemble mean concentrations instead of the unknown local concentration leads to large errors in the global transformation rate. However evaluating local statistics is important for risk assessment, when we need to establish the probability to reach a certain point or to overcome a certain concentration threshold in a particular location within the aquifer (among others, Cirpka *et al.*, 2011; Dentz, 2012; Rubin, Cushey, and Bellin, 1994; Tartakovsky, Nowak, and Bolster, 2012).

In order to have a more faithful picture of how dilution and heterogeneity interact in real formations, we need to refer to the single realization and to the global statistical representation of transport processes. The distance between the ensemble of realizations and the single realization reduce as we approach the ergodic condition, that is when we experience all the spatial features of the formation in each realization (Dagan, 1989).

We consider here, on a single realization basis, several transport scenarios occurring on bi-dimensional formations with different heterogeneity levels (quantified by the log-conductivity variance σ_Y^2) but the same spatial structure of hydraulic conductivity variability. We compute and compare several classic global measures of mixing, referring either to conservative and reactive solutes, as well as local quantities and whole statistical distributions of concentration at the plume scale, in order to analyze the dilution process up to large heterogeneity ($\sigma_Y^2 = 10$). The main aim here is to numerically explore the interplay between dilution, velocity non-uniformities and possibly reaction kinetics. As far as we are aware there is no predictive theory nor systematic numerical investigation which analyzes dilution processes at such a high heterogeneity level in multi-Gaussian Y fields, where both mixing and spreading are highly non-Fickian (LeBorgne *et al.*, 2010; Neuman and Tartakovsky, 2009; Salandin and Rinaldo, 1989). In order to obtain numerical results not biased by numerical diffusion, we adopt a Smoothed Particle Hydrodynamics model (Chapter 2), and use it for modeling different test cases with different injection sizes, initial distributions of concentration, hydrodynamic dispersion models and reaction kinetics.

The mathematical framework, the numerical set-up and the reaction types are described in Section 5.2. Sections 5.3 and 5.4 contain the numerical results and the discussion. Besides several phenomenological observations of the physical and chemical processes, we consider the frequency distribution which can be used, for example, to obtain the probability of exceeding a target concentration at any position within the plume. This is an incomplete, but important, information for risk assessment, which is more reliable than performing risk assessment with the ensemble mean concentration as is currently done in most applications. In particular we numerically prove that the frequency distribution of the solute concentration is well represented by a Beta distribution up to the largest Y variances, thus requiring to know only the first two spatial moments of the plume. Our systematic numerical analyses do not cover all the situations, the main limitation being the bi-dimensionality of the numerical simulations, which is left to future work because of current computational resources limitation. However the wide variety of conditions that we consider and their combination allow to distinguish and analyze their interplay.

5.2 Simulation set-up and numerical schemes for flow and transport

We simulate flow and transport of a passive tracer and two aqueous species reacting upon mixing in a two-dimensional heterogeneous formation with a Gaussian distribution of the hydraulic log-conductivity $Y = \ln K$, where K is the hydraulic conductivity. Y is treated as a RSF with mean m_Y and variance σ_Y^2, both constant, and an exponential isotropic covariance function:

$$C_Y(r'_1, r'_2) = \sigma_Y^2 exp\left[-\frac{\sqrt{r'^2_1 + r'^2_2}}{I_Y}\right] \tag{5.1}$$

where I_Y is the log-conductivity integral scale. Simulations are performed with σ_Y^2 varying between 0.2 and 10, i.e., from weakly to strongly heterogeneous formations, in a squared flow domain with side equal to $L = 100I_Y$. A single realization of the log-conductivity field is generated by using Hydro_Gen, a RSF generator developed by Bellin and Rubin, 1996 as an evolution of the classic Sequential Gaussian Simulator (SGS). The governing equation for the hydraulic head H is the following:

$$\frac{\partial}{\partial x_1}\left[\mathbf{K}(x_1, x_2)\frac{\partial H(x_1, x_2)}{\partial x_1}\right] + \frac{\partial}{\partial x_2}\left[\mathbf{K}(x_1, x_2)\frac{\partial H(x_1, x_2)}{\partial x_2}\right] = 0 \tag{5.2}$$

Boundary conditions are of imposed hydraulic head at the upstream and downstream sides of the computational domain, and no flow conditions at the remaining two sides, parallel to the mean flow direction. In addition, the vertically averaged velocity field $\mathbf{u} = (u_1, u_2)$ is given by the Darcy's law:

$$u_i(x_1, x_2) = \frac{K(x_1, x_2)}{\phi b}\frac{\partial H(x_1, x_2)}{\partial x_i} \qquad i = 1, 2 \tag{5.3}$$

where ϕ is the formation's porosity, assumed constant, and b is the aquifer's thickness. We solve Equations 5.2 and 5.3 by using MODFLOW (Harbaugh, Banta, and McDonald, 2000), which implements a finite volume scheme with equal square cells of side $\Delta = I_Y/12$. The velocities within the computational cells are interpolated linearly by using the edge values in order to obtain a locally conservative continuous velocity field (LaBolle, Fogg, and Tompson, 1996). The resulting velocity field is used to simulate transport of a solute instantaneously injected into the aquifer. In all cases we consider both a uniform initial distribution of concentration (mode I) and a flux-proportional initial distribution (mode II), guaranteeing the same amount of total solute mass in both conditions (Demmy, Berglund, and Graham, 1999). Recent studies have numerically investigated the role of the injection mode on the solute behavior. In particular Frampton and Cvetkovic [2009] focused on the impact of the injection mode on macrodispersion for advective transport in bi-dimensional fracture networks, whereas Jankovic and Fiori [2010] analyzed solute arrival at downstream control planes in case of three-dimensional formations with a multi-indicator structure (Jankovic, Fiori, and Dagan, 2006). Although the flux-proportional injection mode resembles more closely most field situations, it results in an initial concentration variance that varies (increases) with σ_Y^2 (see e.g. LeBorgne *et al.*, 2010), thereby hindering the effect of heterogeneity on the concentration distribution and other global measures of dilution, such as the dilution index. We consider a large line injection, with an initial volume $0.25I_Y$ long and $80I_Y$ large, and a smaller square injection ($I_Y \times I_Y$), both centered at $\bar{\mathbf{a}} = (5I_Y, 50I_Y)$. The former guarantees ergodic conditions (Dagan, 1991; Salandin and Fiorotto, 1998), such that spatial and ensemble averages converge. Finally, local pore-scale dispersion D is set such as to obtain a Peclet number of $\text{Pe} = UI_Y/D = 1000$ in both longitudinal and transverse directions. U is the effective mean velocity $U = Q/(\phi L)$, where Q is the total flux entering through the upstream boundary of length L. We include two local dispersion models: A) uniform and isotropic hydrodynamic dispersion coefficients D, which take into account both molecular diffusive effects and velocity non-uniformities at the sub-Darcy scale; B) Scheidegger local dispersion model (Bear, 1972), with uniform and isotropic dispersivity coefficients α: $D = \alpha u + D_m$, where u is the local module of velocity and D_m is the effective molecular diffusion. We put $D_m = 3/10\alpha U$. Models A and B provide similar results in weak heterogeneity conditions (see Section 3). Besides, laboratory and field evidence show the non-linear dependence of local dispersion coefficients on the local velocity, on temperature, and also their dependence on direction and on the specific compound (see e.g.Chiogna *et al.*, 2011; Delgado, 2006; Olsson and Grathwohl, 2007). For the sake of simplicity these dependencies are not considered here.

Transport of a non reactive tracer is governed by the following dimensionless mass balance equation:

$$\frac{\partial c}{\partial t} + \mathbf{u} \cdot \nabla c = \nabla \cdot (\mathbf{D} \nabla c) \tag{5.4}$$

which can be normalized once we define appropriate reference quantities for space, time, concentration and velocity. In particular, concentration can be made dimensionless dividing c by the initial concentration c_0 of the solute injected instantaneously at the initial time $t = 0$.

The reference initial concentration c_0 in the injection volume V_0 is the same for both injection modes, although it represents the maximum concentration at time 0 only if the injection is uniform within V_0. The two injection modes considered here differ in the amount of mass Δm which is injected in the streamtubes which cross V_0. In fact, following Demmy, Berglund, and Graham [1999], each streambtube i with transverse section Δa_i receives an amount of solute mass Δm_i which depends either on the length of the solute parcel Δs which belongs to V_0 (injection mode I, $\Delta m_i = c_0 \phi \Delta a_i \Delta s$) or on the local velocity u_0 and the finite injection time Δt (injection mode II, $\Delta m_i = c_{0,i} \phi u_0 \Delta a \Delta t$). Since we decided to instantaneously inject the same total amount of solute mass through V_0, in case of flux-proportional injection the initial distribution of concentration at time 0 is non-uniform.

The solution of Equation 5.4, with a suitable initial condition, can be substituted in an algebraic speciation equation to obtain the concentrations of two aqueous species, A and B, reacting instantaneously upon mixing to produce a precipitate C according to the bimolecular equilibrium reaction $A + B \rightleftarrows C \downarrow$ (see e.g., De Simoni *et al.*, 2005, 2007; Rubin, 1983). We refer to the cited literature for the speciation equation for c_1 and c_2 (respectively, the dimensional concentration of species A and B) and the analytical expressions for the reaction rate r. These relations have already been reported in the previous chapters (Ch. 2 and 4). As well documented in the literature (see e.g., Kapoor, Gelhar, and Miralles-Wilhelm, 1997) bimolecular reactions are strongly dependent on mixing, with the reaction that does not occur when local dispersion is turned off. Therefore, the importance of studying how mixing depends on the interplay between non uniform advection and local dispersion goes beyond the interest for transport of a passive tracer to involve cases in which two aqueous species react upon mixing.

Furthermore, kinetically-controlled reactions depend also on the kinetic rate of the reaction as well as on the mixing rate. In this cases an adequate reaction term has to be added as a source/sink in Equation 5.4. The ratio between the diffusion/dispersion timescale τ_D and the overall time scale of the reaction τ_r is the Damköhler number $\mathrm{Da} = \tau_D/\tau_r$. We include the following reaction term (Steefel and Lasaga, 1994):

$$r = -\tau_r^{-1}\sqrt{K_{\mathrm{eq}}}(1 - \Omega_{\mathrm{eq}}) \tag{5.5}$$

with $\tau_r = \frac{\sqrt{K_{\mathrm{eq}}}}{k_0 S}$ where k_0 is the rate constant, S is the specific reactive surface and K_{eq} is the local equilibrium constant. Also $\Omega_{\mathrm{eq}} = c_1 c_2/K_{\mathrm{eq}}$, where c_1 and c_2 refer to the concentration of species A and B, respectively. Sanchez-Vila, Dentz, and Donado, 2007 demonstrated how this representation collapses on the instantaneous equilibrium model when Da becomes high. For both equilibrium and kinetically-controlled reactions, we set initial dimensionless conditions imposing the injection of predominant species A within V_0 by assuming: $C_{1,\mathrm{inj}} = C_{2,\mathrm{amb}} = 10$ and $C_{1,\mathrm{amb}} = C_{2,\mathrm{inj}} = 0.1$, with dimensionless equilibrium constant equal to 1. Dimensional values can be recovered by considering that concentration in the reactive case is normalized over $\sqrt{K_{\mathrm{eq}}}$. The analysis of kinetically-controlled reactions, that is, reactions which are both controlled by mixing rate and kinetics, is important not only for itself but also because some papers suggest that segregation and incomplete mixing within the pores can be mathematically mimicked by pseudo-kinetic processes (Binning and Celia, 2008).

Given the importance of correctly reproducing mixing, it is crucial to adopt in the simulations numerical schemes not affected by artificial (numerical) diffusion. Among the different available schemes we choose to work with Smoothed Particle Hydrodynamics (Monaghan, 2005) in the formulation proposed by Herrera, Massabó, and Beckie, 2009 (see Chapter 2). Applications of SPH to Equation 5.4 have been proposed for example also in the works by Cleary and Monaghan, 1999; Tartakovsky *et al.*, 2007a, 2008 and Tartakovsky, Tartakovsky, and Meakin, 2008. According to this meshless scheme, concentration is computed by means of kernel integral interpolation on a moving set of nodes, which represent fluid particles. The inflow along the upgradient boundary is modeled through the injection of particles proportionally to the local velocity. The advective component of Equation 5.4 is obtained by particle tracking, which is inherently free of numerical diffusion, whereas local dispersion is added through an approximation of the local diffusive fluxes among particles with different concentration.

The numerical solution for instantaneously reacting species can be directly drawn by algebraic manipulation from the numerical solution of Eq. 5.4. Both cases share the same underlying assumption, that is well-mixed reference volume (Li, Peters, and Celia, 2006; Lichtner and Kang, 2007; Steefel, DePaolo, and Lichtner, 2005). Reaction rates r_i can be computed by estimating local concentration gradients coherently with the SPH algorithm, or by exploting mass conservation of species A or B. If reactions are kinetically controlled, we include the reaction rate into the SPH discretization algorithm as an implicit term, in order to avoid stiffness problems. Convergence is sought through a fully implicit Newton-Raphson method (Istok, 1989). The convergence tolerance is set to $c_{\mathrm{lim}}/c_0 = 10^{-8}$.

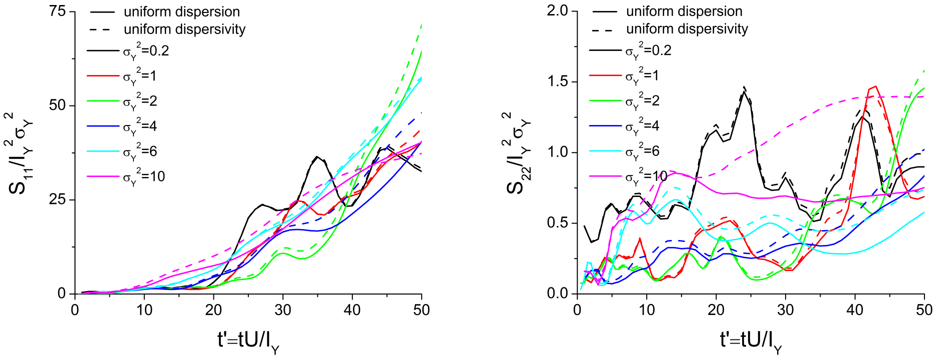

(a) S_{11} - Inj.Mode I **(b)** S_{22} - Inj.Mode I

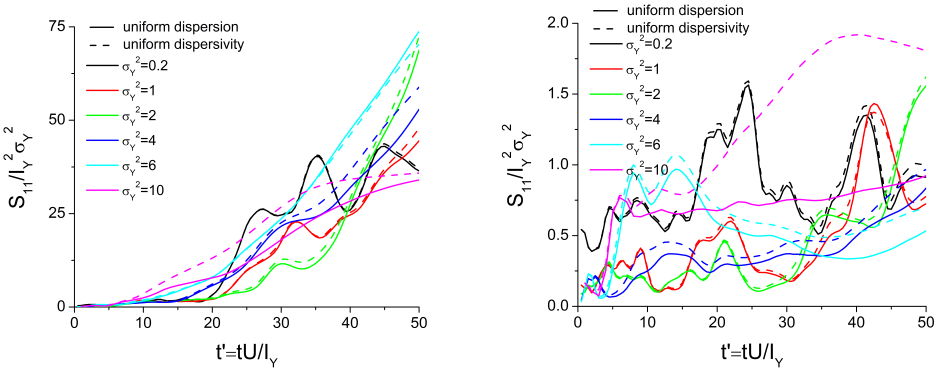

(c) S_{11} - Inj.Mode II **(d)** S_{22} - Inj.Mode II

Figure 5.1: Second central moments S_{ii} for the $(I_Y \times I_Y)$ case, for both dispersion models (line type) and both injection modes (upper row vs lower row) as a function of time $t' = tU/I_Y$. Color refers to the log-conductivity σ_Y^2 of the Y field.

5.3 Results and discussion: Conservative transport

In the following we present a few results of our numerical simulations with the aim of investigating how the interplay between spatially variable advection and local pore-scale dispersion influences the spatial distribution of the passive solute concentration. Results are organized on a quantity basis.

5.3.1 Second central moments

The second central moments S_{ij} can be computed on a deterministic plume as follows:

$$S_{ij} = \frac{1}{M(t)} \int_\Omega \phi\, c(\mathbf{x}, t)\,(x_i - R_i)\,(x_j - R_j)\, d\mathbf{x} \tag{5.6}$$

where i and j are the reference directions, $M(t) = \int_\Omega \phi c(\mathbf{x}, t) d\mathbf{x}$ is the total mass, and the coordinates R_i of the centroid of the plume $\mathbf{R}$ can be computed as follows:

$$R_i(t) = \frac{1}{M(t)} \int_\Omega x_i\, c(\mathbf{x}, t)\, d\mathbf{x}. \tag{5.7}$$

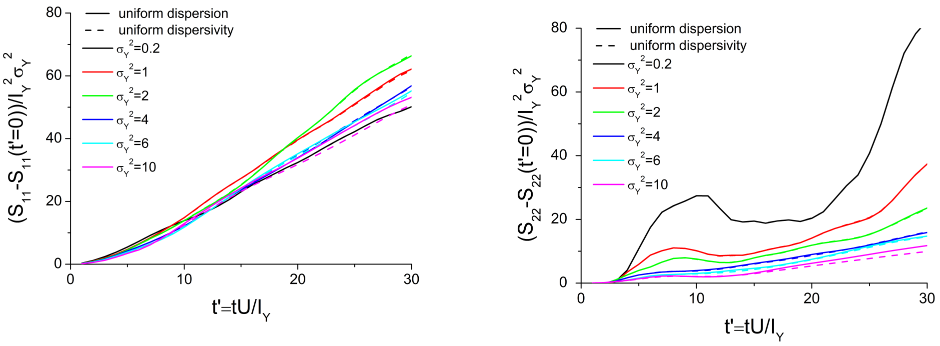

(a) S_{11} - Inj.Mode I **(b)** S_{22} - Inj.Mode I

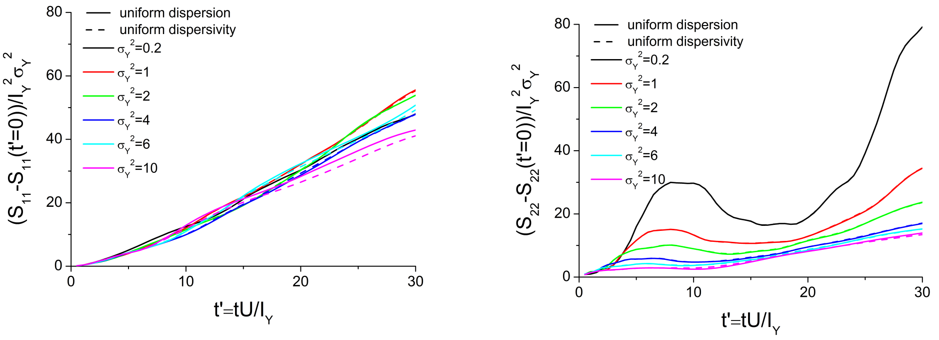

(c) S_{11} - Inj.Mode II **(d)** S_{22} - Inj.Mode II

Figure 5.2: Second central moments for the ergodic case, for both dispersion models (line type) and both injection modes (upper row vs lower row), as a function of time $t' = tU/I_Y$. Color refers to the log-conductivity σ_Y^2 of the Y field.

Although widely used, especially in the past, to estimate the spatial extent of a solute body, the spatial second central moments are now regarded more as a measure of the spreading experienced by the plume rather than of its dilution. In fact, the second central moments can be directly related to the plume volume only in case of plume moving in a homogeneous medium, or in case of well-developed plume, close to Gaussianity. In all other cases, moments are sensitive to the irregular solute mass distribution due to the non-uniform velocity field.

As a result, second central moments of deterministic plumes are neither monotonic increasing nor directly proportional to plume volume, since different mass distributions over the same volume can determine dramatically different spatial moments S_{ij}. Moreover, in the absence of pore scale dispersion (which is the primary cause of dilution and of volume increase) the second central moments in non-homogeneous medium are not constant, as a result of the disorder in the distribution of solute masses due to spreading. Nevertheless, the pore scale dispersion has a non-negligible effect on S_{ij}, mainly in the transverse direction, because it causes solute mass exchanges between adjacent streamtubes. S_{ij} are also related to the actual axial direction of the plume, which is not, especially at early times, aligned with the main longitudinal direction of the flow field. If the plume is in non-ergodic conditions (Fig. 5.1), the actual longitudinal axis of the plume and the main longitudinal direction (the x axis, parallel to S_{11}) do not coincide. As a result, both the longitudinal and the transverse S_{ij} display a pulsating behavior, which is anyway stronger in the transverse direction. This non-monotonic behavior occurs regardless of the dispersion model and of the injection mode. The influence of the dispersion model is evident as heterogeneity increases, especially in the transverse direction, because it determines more considerable mass exchanges among streamtubes, thus enlarging the transverse spatial extent of the non-ergodic plume. At low to intermediate σ_Y^2, the effect of the dispersion model is almost negligible in the longitudinal direction. The injection mode does not influence significantly the behavior of the moments in either direction, because the spatial distribution over V_0 is not so different in the two cases.

The moments'trend is rather different in case of ergodic plume (Fig. 5.2). Notice that in this case we subtract to S_{ii} the value of the spatial moments at time 0, because of the large $S_{22}(t' = 0)$ due to the initial width of the plume, which would have hidden the time variations of S_{22} related to the meandering of the plume. For the non-ergodic case this is not needed since both S_{11} and S_{22} are very small at time 0. The rate of growth is very regular in the longitudinal direction, with monotonically increasing S_{11}; the slope is almost constant in time, as it would occur in a homogeneous setting for a Gaussian plume. The difference between the injection modes increases with heterogeneity. In fact, larger deviations occur in case of very large heterogeneity, with also larger differences between the two dispersion models. In general, longitudinal moments are larger in case of injection mode I, probably because of the entrapment of solute mass in low permeability regions belonging to V_0. In the transverse direction the behavior is rather different. The smaller σ_Y^2 cases still keep a pulsating behavior of S_{22} as for the non-ergodic case, though with a less noisy trend. At higher heterogeneity, S_{22} display a monotonically increasing behavior, with an effect of σ_Y^2 on the lateral spreading which decreases as heterogeneity increases. This does not happen in the non-ergodic case, where the effect of σ_Y^2 is not regular. The dispersion models and the injection modes do not exert a crucial effect on S_{22}.

5.3.2 Dilution index and related quantities

A widely used global measure of dilution for the single realization is the dilution index E:

$$E(t) = \exp\left[- \int_{\Omega} p(\mathbf{x}, t) \ln(p(\mathbf{x}, t)) d\mathbf{x} \right] \tag{5.8}$$

where $p(\mathbf{x}, t) = c(\mathbf{x}, t) / \int_{\Omega} c(\mathbf{x}, t) d\mathbf{x}$ is the ratio between the point concentration and the total mass of injected solute, either conservative or reactive. A similar index has long been used in information theory as an indicator of the amount of information contained in a source, and later in several different fields as a measure of the trend of a system toward a maximum entropy - or equilibrium - condition (Kitanidis, 1994 and references therein). Kitanidis, 1994, used the index to quantify the cumulative dilution status of a system, dependent on the time-increasing number of locations where a certain solute particle can be found with a certain probability. He showed that E is proportional to the volume of the plume, thereby providing a reliable global measure of dilution in case of instantaneous injection when the total mass of solute is constant. E measures the capability of the system of smoothing out the concentration gradients.

In this sense the dilution index is analytically related, as shown by Kitanidis, 1994, to the scalar dissipation rate which is defined as the following quantity

$$\chi(t) = \int_{\Omega} \nabla c \mathbf{D} \nabla c d\mathbf{x} \tag{5.9}$$

and expresses the mixing rate of the system (Bilger, 2004; Bolster *et al.*, 2011). E and χ have been alternatively or together used to quantify the mixing capability of the system, respectively as a cumulated or instantaneous measure of dilution (Dentz *et al.*, 2011). Both quantities are very sensitive to the shape of the plume; shearing, fingering and spreading increase the interface of the plume and the region where dilution, through local dispersion, acts promoted by the concentration gradients. Clearly if the local dispersion is zero E remains constant and equal to the initial volume of the plume, whereas χ is zero. While E is rather simple to compute numerically, χ is harder since it directly depends on the local concentration gradients which can be highly variable, especially along plume fringes. Unless solute flux is zero along the boundaries of Ω (in this case χ would be equal to the spatial mean of the squared local concentration, as shown by LeBorgne *et al.*, 2010), the numerical computation of χ is scarcely reliable, especially at early times when ∇c can be locally very high.

The term $(\nabla c \mathbf{D} \nabla c)$ is included in two other quantities: (1) the reaction rate expression in case of bimolecular equilibrium reactions (De Simoni *et al.*, 2005, 2007) and (2) the PDE which governs the time evolution of the global variance (Kapoor and Gelhar, 1994a,b; Kapoor and Kitanidis, 1998), thus highlighting the central role of the parabolic operator in the AD(R)E. The reaction rate expression, as obtained by De Simoni *et al.*, 2005, is in fact the product of a mixing term, $(\nabla c \mathbf{D} \nabla c)$, which governs the rate at which molecules meet, and a stoichiometric term, which depends on chemistry. Moreover, as shown by Kapoor and Gelhar, 1994b, the global variance of a system (computed as the average of the local values of concentration variance), dissipates according to a $(\nabla c \mathbf{D} \nabla c)$ term which smoothes the concentration gradients and thus the variance.

Unfortunately, as far as we are aware, we do not have any analytical procedure which can provide reliable estimates of the dilution index or its related quantities. Their usefulness is thus limited to the comparison of synthetic cases, or as a compact global measure of dilution from Monte Carlo analysis. Moreover the amount of information carried by the dilution index is not so different from what we can get from the spatial mean concentration. Analytical asymptotic formulas are available once we assume the medium to be homogeneous. The time behavior of these quantities is useful to predict the Fickian asymptotic trend: in a 2D domain E increases with t and χ decreases with $t^{-3/2}$. Variations from this asymptotic pattern individuate non-Fickian behavior (LeBorgne *et al.*, 2010).

Despite the inability to predict or estimate either the dilution index and all the other quantities related to it, we compare the temporal evolution of the dilution index for all our cases, in order to quantify the amount of dilution in each case and distinguish the role of the different variables in the overall dilution process. For all the cases considered in the present work E, and thus dilution, increases with time

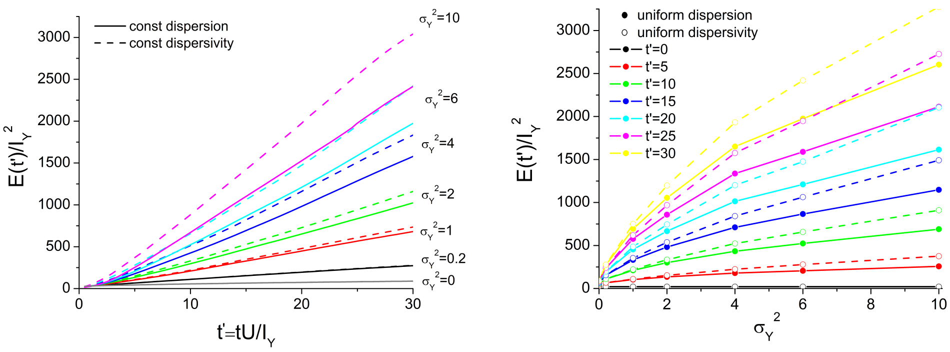

(a) Time evolution of the dilution index E. Color refers to the log-hydraulic conductivity variance σ_Y^2 of the field, whereas line type refers to the local dispersion model.

(b) Evolution of the dilution index E as a function of the log-hydraulic conductivity σ_Y^2 of the field. Color refers to the timestep, whereas the line type refers to the local dispersion model.

Figure 5.3: Dilution index E for the line flux-proportional injection case.

and with the heterogeneity level. The time rate of growth is less than linear at early times, and becomes linear at later times. The non linear behavior at early times is much more pronounced whenever the non-uniformities of the velocity field have a stronger role, that is, at larger σ_Y^2 values, in case of a non-uniform local dispersion model or in case of small injection. This late time behavior is in agreement with the asymptotic analysis of Kitanidis, 1994. The asymptotic rate of growth, which is reached at later times, is not linearly dependent on the heterogeneity level.

Figure 5.3a shows this time evolution of E for a passive solute in the case of flux-proportional initial concentration distribution (injection mode II) line injection for the different heterogeneity fields; the line type refers to the local dispersion model. As heterogeneity increases, E increases as well, reaching an almost linear time increasing slope at intermediate and late times.

Figure 5.3b shows in the same case for a few time steps the dependence of E on the log-conductivity variance σ_Y^2 of the field. For a given dimensionless time, E increases with σ_Y^2, but at a rate that attenuates progressively with σ_Y^2. This attenuation is very strong in the line uniform injection case, as small to negligible differences are observed for $\sigma_Y^2 \geq 4$ in the uniform injection case (in fact curves are almost flat for the uniform dispersion model), suggesting an upper limit to the increase of E due to plume's distortion.

At weak to moderate heterogeneity an increase of σ_Y^2 results in larger concentration gradients, but does not change significantly the shape of the plume, except that it becomes more elongated. The rather regular distribution of the velocity field, that characterizes the mildly heterogeneous formations, leads to a small dilution index, which shows a moderate linear increase with time, also at the early times. In this situation the plume develops thin fingers along interconnected paths with relatively high velocity, resulting in spatially well distributed high concentration gradients across these fingers.

On the contrary, in highly heterogeneous formations the plume tends to split in

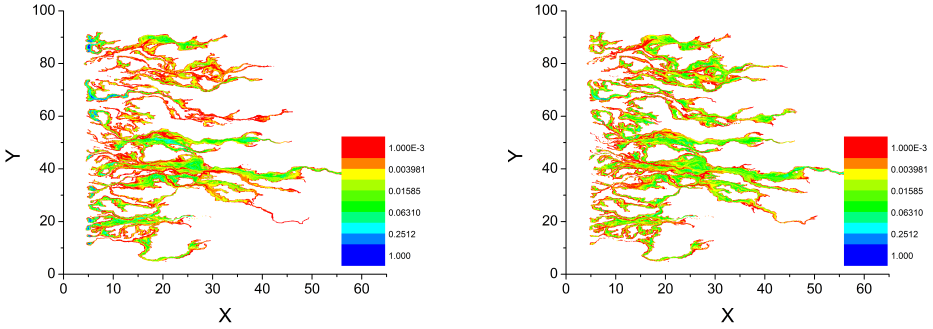

(a) D model A - Inj.Mode I **(b)** D model A - Inj.Mode II

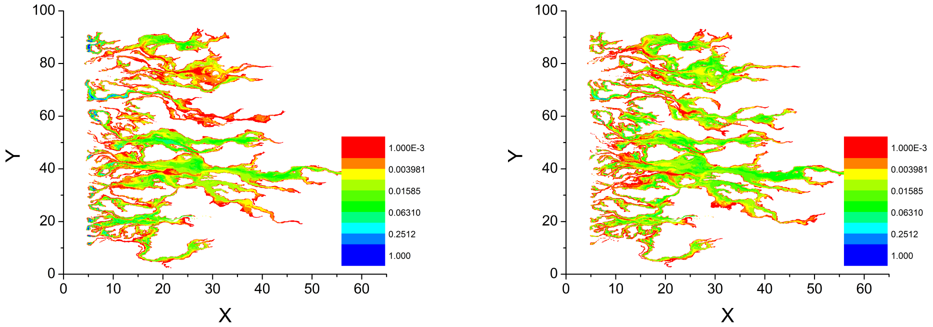

(c) D model B - Inj.Mode I **(d)** D model B - Inj.Mode II

Figure 5.4: Snapshots of the concentration field C for the passive tracer at time $t' = 10$. They refer to the line injection with both dispersion models (upper row vs lower row) and injection modes (left column vs right column). The hydraulic log-conductivity field has variance equal to 10. Notice that the color palette is logarithmic. All quantities are dimensionless: $X = x/I_Y$, $Y = y/I_Y$, $C = c/c_0$.

separate portions, whose transverse size is larger than the fingers observed at lower heterogeneity. These portions tend to remain compact within channels with relatively high velocity showing large dilution at the fringes, where the concentration gradients are large, but with small or almost no dilution inside, where the concentration varies much less than in the corresponding weakly heterogeneous formations (see also Fig. 5.4). This polarizing of mixing around two extremes of small to negligible mixing and very large mixing has the final effect of reducing the increase of disorder, as measured by E. This effect is weaker in case of non-uniform dispersion coefficients, since the velocity-dependent local dispersion coefficients keep high the rate of dilution in the fast fingers despite smoother concentration gradients.

If the initial distribution of concentration is flux-proportional, the solute mass which is injected in each point is proportional to the local value of velocity, so that most of the mass is injected in high permeability regions. Fingers develop quickly, creating large interface areas where the combined action of local dispersion and high concentration gradients determine a rather fast dilution process, which involves also

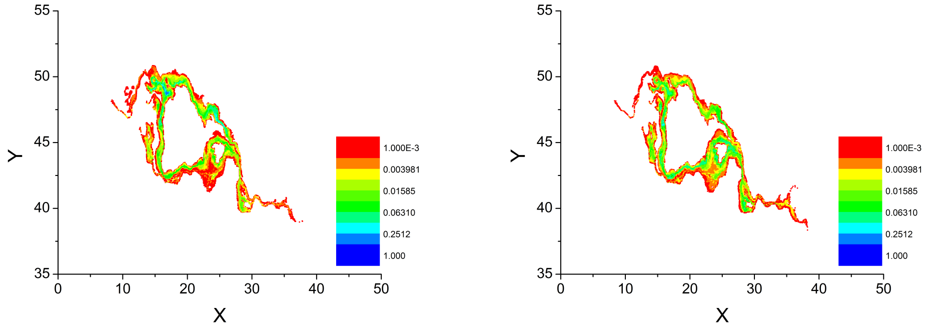

(a) D model A - Inj.Mode I

(b) D model A - Inj.Mode II

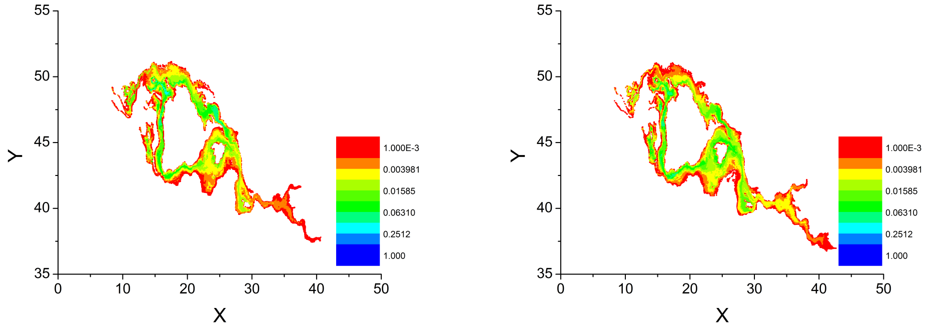

(c) D model B - Inj.Mode I

(d) D model B - Inj.Mode II

Figure 5.5: Snapshots of the concentration field C for the passive tracer at time $t' = 10$. They refer to the $(I_Y \times I_Y)$ injection with both dispersion models (upper row vs lower row) and injection modes (left column vs right column). The hydraulic log-conductivity field has variance equal to 10. Notice that the color palette is logarithmic. All quantities are dimensionless: $X = x/I_Y$, $Y = y/I_Y$, $C = c/c_0$.

the inner portions of the fingers. As a result E increases as an effect of larger σ_Y^2 with a higher rate than with injection mode I. In fact, if the initial distribution of concentration is uniform, we assist to a twofold effect. First a smaller amount of the total solute mass takes advantage of the rapid dilution along the fast fingers. Second a larger amount of mass is injected in the low-permeability regions, from which the solute can escape only thanks to the action of local diffusion. This segregation effect is stronger when the local dispersion values are velocity-dependent (dispersion model B).

In case of smaller injection, the shape of the plume and the evolution of its volume are highly dependent on the hydraulic conductivity variance of the medium, but also on the particular structures that are involved by the plume as it moves downgradient, thus on the single realization that we are considering as our synthetic setting. De Barros and Nowak, 2010, for example, proposed to introduce, in ensemble studies, the concept of effective source width in order to account for the uncertainty about the fluid flux through the source volume. The average hydraulic conductivity value

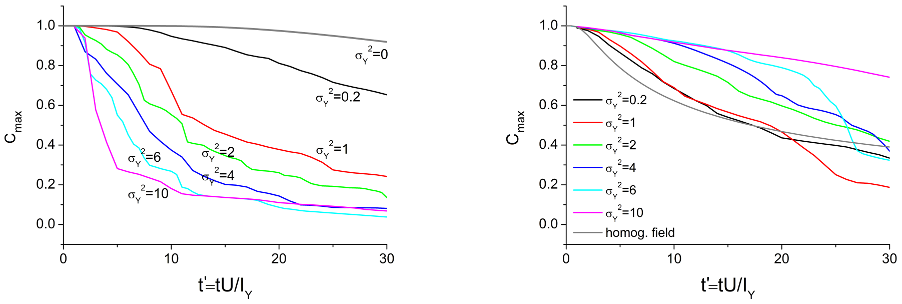

(a) $I_Y \times I_Y$ injection **(b)** Line Injection

Figure 5.6: Temporal evolution of the peak concentration $C_{\max} = c_{\max}/c_0$ for the non ergodic (a) and the ergodic (b) cases for the uniform injection case (I) and the Scheidegger dispersion model (B). As shown on the graphs, color refers to the heterogeneity level of the formation.

of the source area in our reference realizations is slightly larger than the average of the whole formation. In all our non ergodic simulations the initial size of the plume is equal to the integral scale of the formation. The velocity variance as well as the initial concentration variance within the injection volume is not large. Hence there is no big difference between the uniform and flux-proportional initial distribution of concentration. The attenuating effect on E of an increasing σ_Y^2 is weaker than in the ergodic cases, emerges at later times and becomes evident only at $\sigma_Y^2 \geq 6$. This effect is stronger for dispersion model B and injection mode II, mainly because solute entrapment in low permeability regions and fingers width are reduced as an effect of plume's size (Figure 5.5).

Overall, the analysis of the dilution index confirms that heterogeneity has a boosting effect on dilution, as high permeability areas promote dilution by means of both deformation and local scale dispersion. Dilution is also favored by a non uniform injection of solute in the source area, as well as by a non uniform dispersion model. Both effects enhance dilution along the fast fingers: the former because most solute mass moves and dilutes along the fast paths along whose fringes concentration gradients are very high, the latter because in these zones the velocity-proportional local hydrodynamic dispersion is larger. Moreover, the flux-proportional injection avoids the entrapment of solute mass in low permeability regions, from which mass can escape only by means of local dispersion which typically acts slowly, especially in case of velocity dependent dispersion.

5.3.3 Peak concentration

In Figures 5.6 we show the time evolution of the maximum concentration $C_{\max} = c_{\max}/c_0$ of a passive solute, which is also a quantity of interest in risk assessment, and an index of dilution (Fiori, 2001a), for both the non ergodic (Fig. 5.6a) and ergodic (Fig. 5.6b) injection cases. These Figures refer to simulations with dispersion model B and injection mode I. The inherently local nature of the maximum concentration makes it more sensitive to local dynamics than global indexes such as

the dilution index or the scalar dissipation rate. Generally speaking, the dynamics of the decrease of the maximum concentration depends on the size of the larger cluster of solute masses and thus strongly depends on the size and on the distribution of the initial concentration (Fiori, 2001a). As already pointed out by Kapoor and Kitanidis, 1998, these blobs of solute are less subject to the action of local dispersion, which is the mechanism which makes local concentration to decrease. They also pointed out that, unlike the homogeneous case where the peak concentration decreases with $t^{-m/2}$ (where m is the dimensionality of the problem), the peak concentration is not necessarily inversely proportional to the plume volume, but it can decrease at a much slower rate because of the interplay between velocity non-uniformities (especially related to the small heterogeneity scale) and dilution.
If the injection volume is small (see Figures 5.5), the maximum concentration, which most likely is recorded close to the centroid of the plume, decreases with regularity as shown by Figure 5.6a, that is, the larger the heterogeneity level the faster the decrease in the recorded value of maximum concentration. The rate of reduction of C_{max} increases with σ_Y^2. This is an expected result since the plume dilutes faster in ore heterogeneous formations, as an effect of plume deformation induced by spatially variable advection.
The injection mode does not vary significantly this picture, except at early times since the initial variance of the concentration is not 0 in case II, so that $c_{max}(t = 0) > c_0$, where c_0 is the initial concentration (Demmy, Berglund, and Graham, 1999). If both the injection mode and the dispersion model are non uniform, the decrease rate of the maximum value of concentration is rather regular, and stronger the higher the heterogeneity of the formation. The role of the non-uniform dispersion model is stronger at early times, when it determines a faster decrease of the maximum concentration in the high-permeability regions, where the maximum concentration is located. For both injection modes, a non-uniform hydrodynamic dispersion model increases (especially at $\sigma_Y^2 \geq 4$) the decreasing rate of the maximum value of concentration, thus confirming that the maximum concentration is located in zones where velocity, and thus the value of the velocity-dependent dispersion coefficients, is high.

On the other hand, if the injection area is large as in Fig. 5.6b, the behavior of the maximum concentration is less regular and strongly depends on the space and time evolution of the single cluster of particles (see also Fig. 5.4). The higher the log-hydraulic conductivity value, the more difficult to dilute are the clusters of particles which take off from low-permeability regions within the source area. This effect is much stronger when the initial distribution of concentration is uniform, that is, we are injecting a larger amount of solute mass in low permeability zones than in the flux-proportional injection case, or when the local dispersion coefficients depend on the local velocity. This result is consistent with what we observed for the dilution index, and may reflect the fact that in highly heterogeneous formations portions of the plume may remain entrapped in low conductive zone where concentration gradients are smaller, and where therefore mixing is locally smaller. This leads to an attenuated reduction of the maximum concentration which results affected by the local variability of low hydraulic transmissivity zones; as a result, $c_{\max}$ can decrease slowly also in highly heterogeneous formations, which are in general characterized by a overall stronger dilution. This suggests that the maximum concentration can be affected by the model of spatial variability and in particular on the distribution of low and high transmissivity zones and their internal variability. The effect of a velocity dependent hydrodynamic dispersion model depends on the location where the maximum concentration value is recorded. If, as in the uniform injection case (Fig. 5.4a,5.4b), the maximum values of concentration are recorded up to late times close to the injection area, considering also a velocity dependent dispersion tensor reduces the smoothing effect of local dispersion and increases $C_{\max}$ for B simulations with respect to A simulations. In addition, in the flux-proportional case, model A exerts an effective dilution on the small amount of solute mass entrapped in the low-permeability regions within the source area; so as time advances the maximum value of concentration in this case is recorded downstream, in the middle of the thicker fingers (Fig. 5.4b,5.4d). This does not happen in model B simulations, since the diffusive/dispersive effect within the source area is much slower. When injection is flux-proportional, the segregation effect of solute mass in low permeability areas is less pronounced since we are injecting a smaller amount of mass in these zones which can then be reached or left only by means of local dispersion. That is why the decrease of the maximum concentration is much more regular and predictable in the flux proportional injection case and for the uniform dispersion model than for the other cases.

5.3.4 Cumulative distribution functions of concentration

The dilution index and the related indicators are difficult to use in practical applications, where, to the contrary, we need to know for example if somewhere within a plume, or at a given target, the concentration can exceed a given threshold. The Cumulative Frequency Distribution (CFD) $F(C \leq \mathsf{c})$ can be used for this purpose. It represents the probability (for a given sample of concentration punctual values) that the concentration is below a given value c in any point within the plume, or in other words, the fraction of the actual plume's volume whose concentration is below c. The complement to 1 of F represents the fraction of the plume with concentration higher than the given threshold, which is a valuable piece of information, although not exhaustive, in applications. Notice that $F(C \leq \mathsf{c})$ is inherently different from the local Cumulative probability Distribution Function (CDF) of point concentration, which is computed by statically averaging over independent realizations of the conductivity field. The CDF shows dramatic space variability and reflects mainly uncertainty in the point concentration, which is very high except at exceedingly high times, when local dispersion overwhelms macrodispersion and the plume becomes Gaussian (Fiori and Dagan, 2000).

This spatial, plume-scale, statistics are conceptually and operatively different from the local statistics. Statistics is the means we have for addressing the uncertainty in the spatial distribution of the hydraulic properties of the formation. A large part of the literature has been focusing on the prediction of local statistics, both in terms of probability distributions and in terms of moments, as widely reviewed in Chapter 3. Strong, although not universal, convergence is on the use of the Beta distribution as a reliable analytical model for the local probability distribution of concentration (among others, Cirpka *et al.*, 2008; Fiori, 1996; Fiorotto and Caroni, 2002). Its usage has been numerically tested up to $\sigma_Y^2 = 2$ cases (Caroni and Fiorotto, 2005), and also theoretically supported (Bellin and Tonina, 2007).

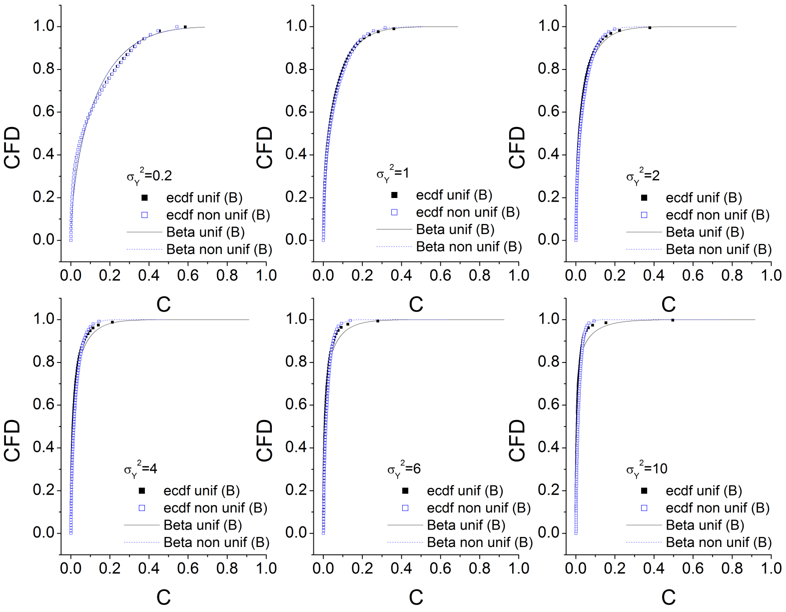

Figure 5.7: CFD for the concentration C of the passive tracer in case of line injection and dispersion model B at time $t' = 10$. Dots refer to the empirical CFDs, while lines refer to the Beta distribution model with shape parameters obtained from the empirical mean and variance. Color refers to the injection mode: Uniform (black) and Flux-Proportional (blue).

Unfortunately these local statistics are very sensitive to local uncertainty due to the non-uniformity of the hydraulic properties and give little information on the actual presence of solute mass in a certain location. When we deal with reactive transport this is a problem since reaction occurs only when we have the overlapping of plumes with different chemical characteristics, that is when we have actual mixing between chemical species. As opposed to local statistics, we focused on the spatial statistics of the plume. Both the global mean and the global variance (which is conceptually different from the global variance proposed by Kapoor and Gelhar, 1994a and mentioned above) are much more significant with respect to the real behavior of the plume. We have no local information, since we do not refer to a specific location, but we gain information on the global plume with more resemblance of the actual behavior of a real plume. Coherently we also considered single realization transport scenarios, as opposed to Monte Carlo series of realizations, with the aim of interpreting the actual phenomena which occur in real aquifers. The global statistics can be modeled by means of the Beta distribution as well (Bellin and Tonina, 2007), as its flexibility make it capable of reproducing the time evolution of the global cumulative frequency of concentration. Bellin and Tonina, 2007, observed that in weakly to moderate heterogeneous formations the frequency (space) distribution of the concentration of a passive solute is well represented by a Beta distribution with the parameters depending on the spatial mean and variance of the solute concentration.

Relying on an analytical shape of the global cumulative frequency helps when we deal with reactive transport scenarios which can be traced back to the conservative case by algebraic manipulation (Rubin, 1983). Along these lines Bellin, Severino, and Fiori, 2011, provided an analytical relation between the local mean and variance and the global cumulative frequency of the conservative reference species and the reactive species reacting upon heterogeneous equilibrium bimolecular reactions. In Chapter 4 we extended this procedure to the homogeneous case. This analytical manipulation is not valid only for the local statistics, but also for the global statistics once we ensure complete mixing within the pore, that is chemical species meet and actually react with no subscale segregation effect which could prevent reactions to occur (see also Chapter 6).

In this section we verify numerically that the Beta model of F holds also for large and very large heterogeneous formations, taking advantage of the good performance of the numerical SPH code. SPH is in fact free of artificial diffusion, resistant to highly heterogeneous velocity field and also robust with respect to the initial distribution of concentration and to the model of local hydrodynamic dispersion. According to the Beta model the concentration pdf assumes the following expression:

$$f_Z(C) = \frac{\Gamma(p_1+p_2)}{\Gamma(p_1)\Gamma(p_2)} C^{p_1-1}(1-C)^{p_2-1} \tag{5.10}$$

where C is the passive solute concentration varying in the range $(0,1)$, Γ is the Gamma function and the parameters p_1 and p_2 assume the following expressions: $p_1 = \bar{C}/\beta$, $p_2 = (1-\bar{C})/\beta$ where $\beta = (S_C^2)/(\bar{C}(1-\bar{C})-S_C^2)$; $\bar{C}(t) = 1/\Omega \int_\Omega C(\mathbf{x},t)d\mathbf{x}$ and $S_C^2 = 1/\Omega \int_\Omega (C(\mathbf{x},t)-\bar{C}(t))^2 d\mathbf{x}$ are the spatial moments of the concentration.

Figure 5.7 shows the CFDs of a passive solute at the dimensionless time $t' = tU/I_Y = 10$ for $\sigma_Y^2 = (0.2, 1, 2, 4, 6, 10)$ in the case of line (ergodic) uniform injection, considering model B for the hydrodynamic dispersion. This is the case where the match between the empirical CFDs and the Beta model is worst. In all other cases the match is better. Solid squared symbols indicate the empirical CFD as obtained numerically with the simulations described above, while the solid line indicate the Beta model obtained by replacing into the expressions for p_1 and p_2 the spatial concentration moments provided by the numerical simulations. Inspection of Figure 5.7 shows that a larger σ_Y^2 leads to a sharper CFD. The shape of the CFD depends on the stage of the dilution process which has been reached by the plume. At the initial time in case of uniform injection the concentration distribution is the Heaviside step-function, because $C \neq 0$ only within the plume. Successively, the frequency distributions broaden as an effect of dispersion. However, as time proceeds further the range of concentration narrows again as dilution attenuates concentration peaks. Both E and the empirical CFDs show that at a given time from injection the plumes are more diluted in the high variance than in the low variance cases. Consequently, in the former case the distribution of the concentration is closer to the concentration of the ambient water, which is the final condition at which the plumes tend for time tending to infinity. In all cases we observe a good match between the numerical results and the analytical reference models.

Either a smaller size of the injection plume, a flux-proportional initial distribution of concentration within the initial volume, a uniform dispersion tensor model or a weaker heterogeneity level make the match between the analytical reference and

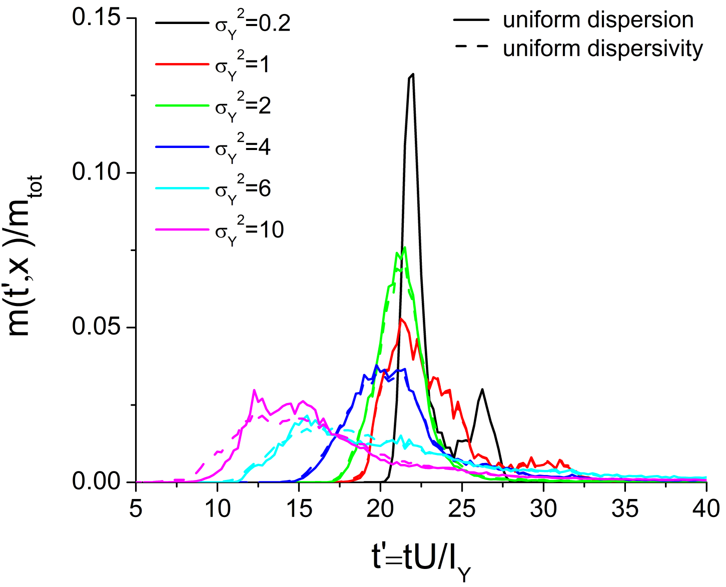

Figure 5.8: Transverse BTCs (amount of mass which crosses the control plane located in x^* in time, normalized over the total injected mass) for the passive tracer; finite $(I_Y \times I_Y)$ injection with non-uniform concentration distribution (II). The control plane is located at $x^* = 30I_Y$ which means $25I_Y$ downstream of the centroid of the injection area. Line type refers to the hydrodynamic dispersion model whereas line color refers to the Y variance of the field as shown in the figure.

the empirical CFD better, probably because all these conditions reduce segregation effects and the disaggregation of the plume. This suggests that the Beta distribution model is not limited to weakly heterogeneous formations and can be applied also to high and very high heterogeneous formations provided that a reliable model for the concentration first two spatial concentration moments is available. We also tested non-Gaussian permeability fields (not shown here) as in Zinn and Harvey, 2003, and the Beta distribution model holds also in this cases, proving that the representativeness of the Beta model is not an artificial effect of the Gaussian model of spatial variability of Y. The robustness of the Beta distribution in representing the behavior of solute concentration is confirmed also by the numerical experiments presented in Section 5.4.4.

5.3.5 Break Through Curves

Last we quantify the transverse breakthrough curves (BTCs) at several control planes located downstream of the injection area at different distances from the injection area. The analysis of the BTCs is important for several reasons. From an application point of view, BTCs represent the amount of solute mass which reaches a certain distance downstream, possibly hitting large receptors such as well fields or rivers. From the point of view of the nature of transport, the temporal behavior of the BTCs allows to detect the non-Fickian behavior which is typical of transport in heterogeneous media at preasymptotic times, and which emerges as early arrivals of solute and late tails (see e.g. Haggerty, McKenna, and Meigs, 2000; Harvey and Gorelick, 2000; Luo and Cirpka, 2011; Neuman and Tartakovsky, 2009; Seelros and Cvektovic, 1992). Finally, from a methodological point of view, transverse BTCs are often used to compare lumped or effective models of transport, such as macroscale models or traveltime methods. Luo and Cirpka, 2011 pointed out how the good representation of conservative transverse BTCs does not ensure the correct reproduction of reactive species BTCs, although analytically related to the conservative species, because they cannot reproduce concentration variations at the control plane. Here we show that this effect is due to the bad reproduction of the dilution properties of the system already in the conservative case. Despite this fact, a lot of academic work relies on cross-sectional BTCs to distinguish between different numerical approaches (Willmann *et al.*, 2010) or to evaluate traveltime methods (Luo and Cirpka, 2008; Simmons, Ginn, and Wood, 1995). Our simulations show that there is no big difference in the shape of the BTCs at control planes located downstream of the injection area when considering different local dispersion models and, after a certain distance from the source, also different initial distributions of concentration, regardless of the heterogeneity level. The cross-sectional BTCs average out the local effects of transport and the actual mixing that the plume experiences upstream of the control plane, by averaging across the control plane. There is no way to distinguish between mixing and spreading only relying on the shape of these cross sectional BTCs (Luo and Cirpka, 2011).

The shape of the numerical BTCs (Figure 5.8 is an example) is definitely non-Fickian, with evident early arrival times and late tails as heterogeneity increases. Heterogeneity is responsible for the fast fingers which carry solute mass downstream rather fast, and also for the entrapment of solute mass in low permeability regions. In case of flux-proportional injection, the early arrivals are reinforced with respect to the uniform injection, whereas tails are less fat; this is evident in case of line injection, where the solute mass distribution over V_0 is significantly different between the two injection modes. BTCs also display multiple peaks which are smoothed out as the dilution process progresses; in case of line injection the multiple peaks effect is still present 50 I_Y downgradient. It takes several integral scales to damp the effect of a different initial concentration distribution, especially at the highest Y variances for both the ergodic and the non ergodic injection cases (Fiori, Jankovic, and Dagan, 2011; Jankovic and Fiori, 2010). As the distance between V_0 and the control plane increases, BTCs present lower peaks and become much more broadened, as an effect of plume elongation and disaggregation. The effect of the hydrodynamic dispersion model is not large: it is distinguishable only for the highest Y variance cases and it is stronger for the small injection case, as evident in Figure 5.8. As clearly appears, for the non ergodic case the local dispersion model begins to display its influence only at the largest heterogeneity variance, where a non-uniform dispersion model (dashed line) determines earlier arrivals and a lower peak. This is probably due to the stronger dilution experienced along the fast advective fingers which move downgradient bringing a large amount of mass, thus further boosting dilution with high gradients at early times. In all other cases there is no relevant difference between the dispersion models which have been considered, despite a big role of the dispersion model in the dilution process itself. For instance, if we consider the

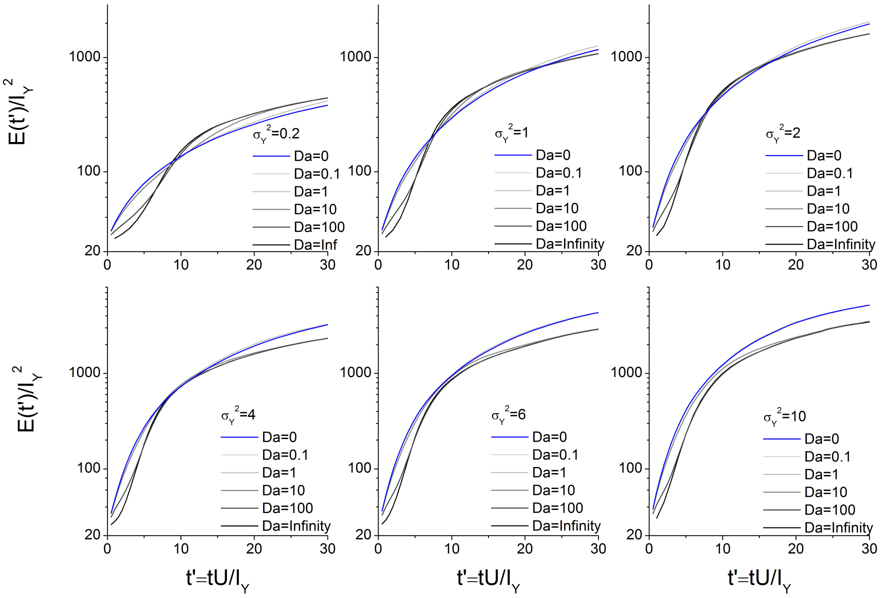

Figure 5.9: Dilution index E for the injected species A for the ergodic case (line injection) and the non-uniform dispersion model (B). The greyscale refers to the Da number, whereas the blue line represent the non-reactive case (Da = 0). For all fields, the line injection is uniform in space (injection mode I).

$\sigma_Y^2 = 6$ case and injection mode II, different dispersion models do not determine significant differences in the shape of the BTC, as shown in Figure 5.8. In the same condition, the dilution index E shows a difference between dispersion models A and B of 27% at time 20 which grows up to 40% at time 40.

5.4 Results and discussion: Reactive transport

In this section we focus on the effect of reaction kinetics on the classic dilution indicators as well as on quantities more strictly related to risk assessment regulations. The reference species is generally the injected species A, for the reactive cases listed in section 5.2. In all the following graphs the greyscale refers to the Damköhler number of the simulation. Black lines refer to the instantaneous (equilibrium) reactive case which is analytically related to the conservative case, and represents a lower limit for dilution since this is the case in which we have the stronger A consumption due to reaction. An upper limit for dilution (blue lines) is represented by the conservative transport case (Da = 0), which is approached by the low Da number cases.

5.4.1 Dilution index

We compute the dilution index (5.8) for the injected species A considering only the locations where C_1 is larger than the ambient concentration $C_{1,amb}$. The two extreme cases are analytically predictable from a conservative transport simulation.

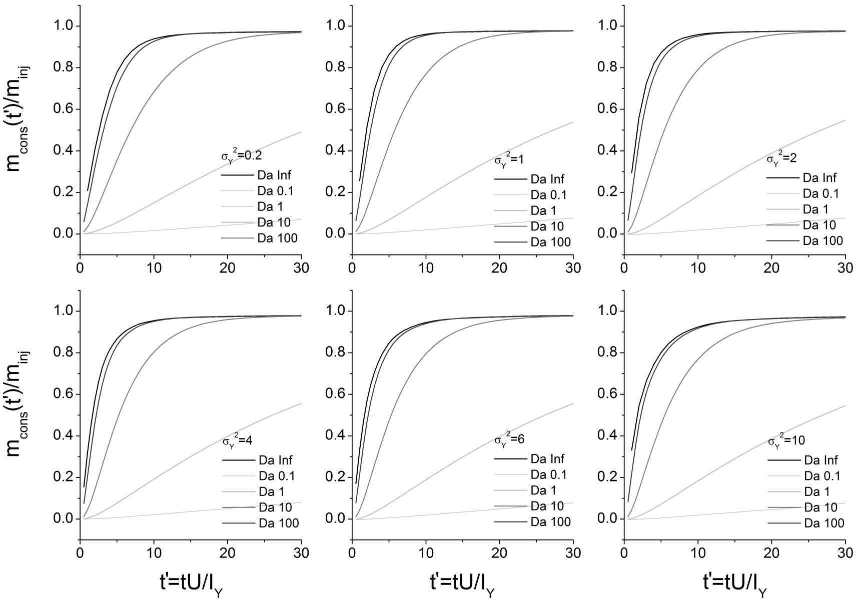

Figure 5.10: Time evolution of the total mass consumption m_{cons} of species A, normalized over the total injected A mass m_{inj}. The greyscale color refers to the Da number. For all fields, the line injection is uniform in space (I); the dispersion model is Scheidegger's (B).

Figure 5.9 represents the dilution index for species A for the ergodic uniform injection case, and dispersion model B. This case is instructive since it shows a twofold effect: (1) E grows as an effect of the interplay between velocity non-uniformities and local dispersion, as in the conservative transport case; the low Da cases display a growth rate which is similar to the E growth of the purely conservative case; (2) the stronger the reaction rate (that is, the larger the Da number, the smaller the time and the higher the heterogeneity level), the weaker the growth slope of E, since the plume volume increase is hampered by the solute consumption by the reaction. During the early stages of the dilution process (which lasts longer for weakly heterogeneous formations), E does not vary much at different Da. At this stage, plumes are constituted by a total amount of solute mass A which varies considerably with Da, as a result of very different reaction rates, as shown in Figure 5.10. Despite this fact, both plume's volume and solute mass distribution within the plume are not very different, once we normalize (as in the computation of E) over the total solute mass which characterizes each single time and value of Da. At later times the lower the Da number, the higher the dilution index E. This may be due to the fact that residual solute blobs determine high concentration gradients which feed dilution (see Figure 5.15).

The effect of Da determines large differences in the overall dilution effect, the largest gap being verified for the $\sigma_Y^2 = 10$ case where it reaches 40 %. It is interesting to note how despite the considered Da numbers span over four orders of magnitude, the largest differences occur around the intermediate orders of magnitude, since for Da < 1 the prediction is very close to the conservative case (Da $= 0$) and for

Da = 100 the dilution index is very close to the infinite Da case, except at the very early times. Hence for slow or fast reaction kinetics we can rely on conservative transport simulations with slight differences on the prediction of dilution.

The dilution index is a weighted measure of volume, since it takes into account also the concentration distribution within the plume volume. The inspection of the snapshots (see Fig. 5.15) shows how the Da = ∞ case and the Da = 0 provide the same isoconcentration border for the solute body, thus the same volume. But these extreme cases correspond to very different dilution, evidenced by a very different solute mass distribution within the plume. In confirmation of that, we include in the figures also the concentration CFDs which represent the concentration distribution in terms of fraction of the plume's volume which is characterized by a concentration lower than a given threshold.

5.4.2 Peak concentration

The effect of segregation can be also quantified by looking at the behavior of the maximum concentration of the injected reactive species. As a local indicator of mixing it is the most sensitive to local effects. Obviously, the slower the reaction kinetics the slower the decrease of the maximum concentration. This decrease is slower for the non-uniform dispersion model, because the solute mass can leave the low-permeability regions only as an effect of the molecular diffusion D_m. The effect of reaction kinetics could resemble the effect of local segregation effects and incomplete mixing within the pore, with a strong effect on the maximum value of concentration which is recorded locally (Binning and Celia, 2008).

5.4.3 Distribution of the cumulated precipitated mass as a function of Y

When species react upon a bimolecular heterogeneous reaction, a certain amount of mass precipitates. From an applicative point of view, the precipitated mass can be interpreted as either the fate of chemicals delivered into the aquifer for remediation purposes, or as the fate of a contaminant accidentally injected into the aquifer and degraded by natural attenuation processes. This kind of reactions strongly depends on mixing as the necessary condition which makes molecules of reactants meet. Then kinetics and kinetic reaction rates may reduce the rate of encounters which determine the precipitation of the reaction product. Mapping where the reactions occur spatially localizes where the hot spots of mixing are positioned in terms of relative log-conductivity. Figures 5.11 and 5.12 show the distribution of the total amount of precipitated species C at a given timestep, as a function of the normalized log-hydraulic conductivity of the location where precipitation occurs.

In Figure 5.11 we present the distribution for the ergodic case. All cases are negatively skewed due to the fact that solute mass moves earlier and faster along the highest permeability paths. As a result precipitation occurs first along the high conductivity fingers, whose fringes are characterized by high concentration gradients, and which represent hot spots of mixing (Werth, Cirpka, and Grathwohl, 2006; Willingham *et al.*, 2010). For the same reason the negative skewness is stronger for the flux-proportional injection and for the non uniform dispersion model. The former condition enhances early concentration gradients, while the latter uses higher

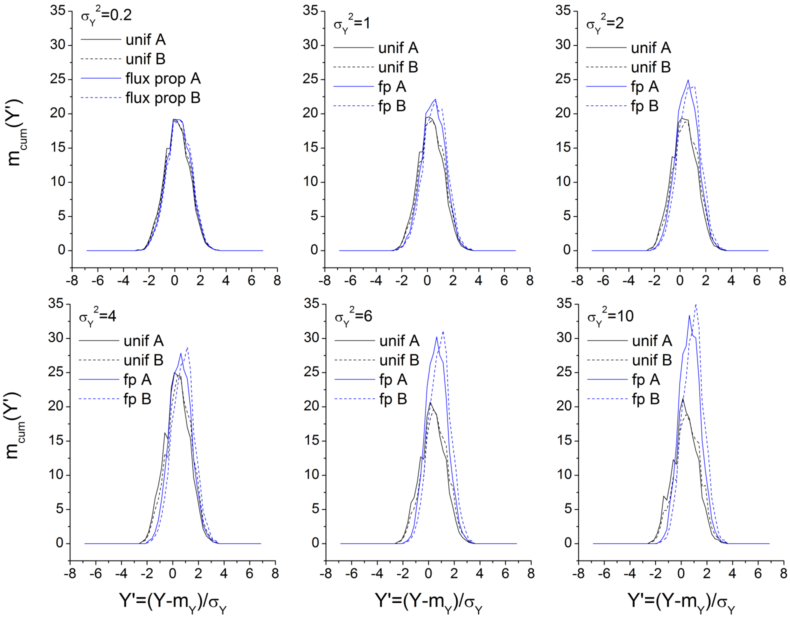

Figure 5.11: Amount of cumulated precipitated mass of species C as a function of the normalized value of log-conductivity of the regions where precipitation occurs, at time $t' = tU/I_Y = 10$. m_Y and σ_Y refer to the mean and the standard deviation of the log-conductivity field. Line type refers to the hydrodynamic dispersion model (A or B), whereas color refer to the injection mode (I, uniform, or II, flux-proportional). The values refer to the line injection case in case of the equilibrium reaction $A + B \leftrightharpoons C\downarrow$.

dispersion coefficients.

The shape of the distribution remains almost the same, except for the Y classes very close to the peaks, in case of uniform initial concentration injection, with also slight differences between the local dispersion models. This is due to the ergodicity of the plume, that is, the solutes experience all the Y structures of the multi-Gaussian system. When the initial concentration is flux-proportional, differences are more pronounced. Moreover the dispersion model affects the descending part of the curve related to the higher permeability regions, which are involved because a larger portion of the injected mass is introduced in these regions.

For both the ergodic and the non ergodic cases, the effect of the medium heterogeneity determines an increase in the total amount of precipitated mass (integral of the distribution), but with a rate which slows down as heterogeneity increases ($\sigma_y^2 \geq 6$). Also the flux-proportional injection of mass in the source area determines an increase of the total solute mass which precipitates, whereas different dispersion models do not make a huge difference. As opposed to the ergodic case, the non-ergodic simulations are more noisy since the plume experiences only a small portion of the domain. Curves are still negatively skewed, especially for injection mode II and dispersion model B, but distributions are typically multi-peaked at least at early

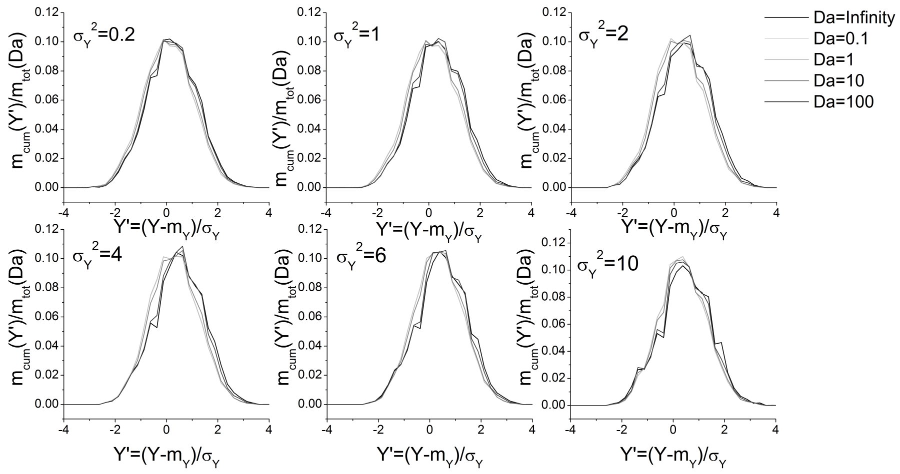

Figure 5.12: Amount of relative cumulated precipitated mass of species C as a function of the normalized value of log-conductivity of the regions where precipitation occurs at time $t' = 10$. m_{cum} is normalized over the integral of each curve, which represents the total cumulated precipitated mass in each case up to the current t' time. m_Y and σ_Y refer to the mean and the standard deviation of the field. Simulations are performed for the different Da numbers with dispersion model B and injection mode I.

and intermediate times.

For the same ergodic case, Figure 5.12 shows the distribution of the normalized cumulated mass also considering a wide range of Da numbers (injection mode I, dispersion model B). The Da number affects the total amount of precipitated mass but not its distribution, that is, it does not affect where the precipitation occurs. A similar result is obtained for the small, non-ergodic, injection case.

5.4.4 Cumulative distribution functions of concentration

As stated in Section 5.3 and deepened in Chapter 4, once we assume that the Beta distribution correctly reproduces the empirical CFDs of the concentration for a passive solute, we can also derive by mathematical manipulation analytical probability models for the reactive species in case of homogeneous or heterogeneous bimolecular equilibrium reactions (Chapter 4). Figure 5.13 shows the empirical and theoretical Cumulative Frequencies for the line injection case with dispersion model B for both injection modes I and II. The match between the empirical distributions and the theoretical model, whose shape is defined by the empirical global mean and variance, is good up to the highest log-conductivity variance, despite the nonlinear speciation relations between the passive solute concentration C and the reactive concentrations C_1 and C_2 which could enhance discrepancies between the empirical values and the theoretical prediction. The largest gaps are obtained for $\sigma_Y^2 \geq 6$ in case of uniform injection within V_0, because this condition enhances the disaggregation of the plume and the entrapment of solute mass in the low-permeability regions which belong to V_0. This does not happen for injection mode II.

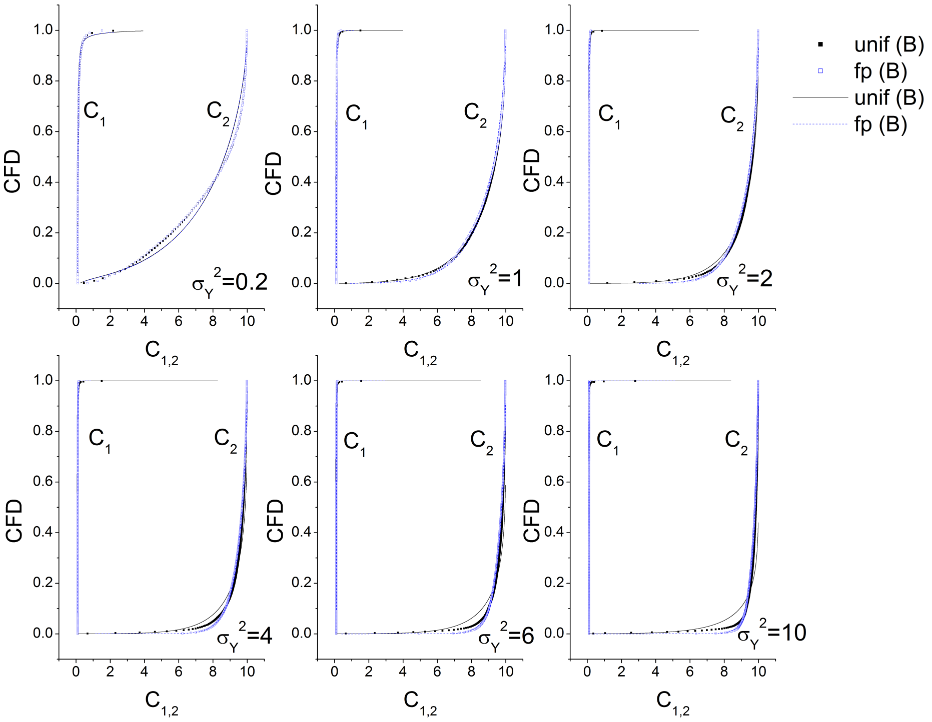

Figure 5.13: CFDs for the reacting species in the heterogeneous case. Simulations refer to instantaneous line injection and dispersion model B at time $t' = 10$. Dots refer to the empirical CFDs, while lines refer to the Beta distribution model with shape parameters obtained from the empirical mean and variance. Color refers to the injection modes: Uniform (I) and Flux-Proportional (II).

For the sake of completeness we also report the Cumulative Frequencies computed for the bimolecular equilibrium homogeneous reaction (see Chapter 4 for a description of the reactive system). The flow and transport initial conditions (in dimensionless form) and parameters are equal to the heterogeneous case, the only difference being the phase of the product of the reaction C. As evident in Figure 5.14, the match is equally good up to $\sigma_Y^2 = 10$ for all the three species involved with similar conclusions on the role of the injection mode on the goodness-of-fit of the theoretical model.

In case of kinetically controlled reactions, we do not have any analytical relation which links the concentration of passive species and the concentration of reactive species. However the CFD of concentration in this cases is severely affected by reaction kinetics as shown in Figure 5.15d. In general slower reaction rates determine higher CFD values for higher A concentrations, because concentration dilutes, and thus diminishes, as an effect of local dispersion, but mass A is also slowly consumed by the reaction.

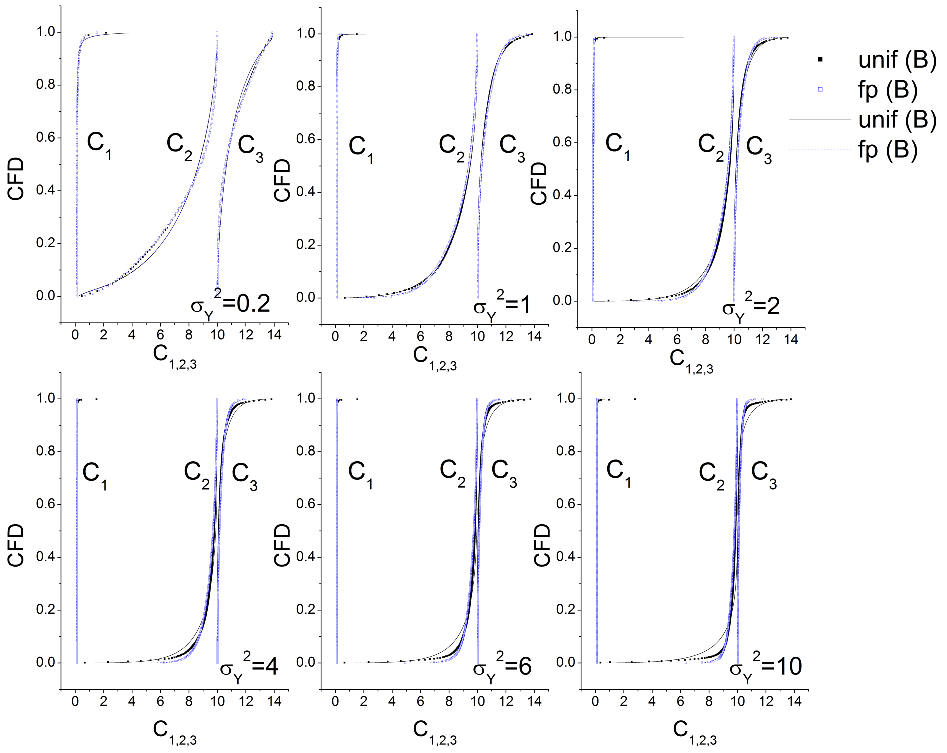

Figure 5.14: CFDs for the reacting species in the homogeneous case. Simulations refer to instantaneous line injection and dispersion model B at time 10. Dots refer to the empirical CFDs, while lines refer to the Beta distribution model with shape parameters obtained from the empirical mean and variance. Color refers to the injection mode: Uniform (I) and Flux-Proportional (II).

5.4.5 Break Through Curves

Finally we consider also the effect of reactions on the BTCs. Mass refers to the mass of species A which crosses the control plane with a concentration higher than the ambient water concentration $C_{1,amb}$. Also the total mass refers to the total mass of injected A above the ambient water concentration. Figure 5.16 refers to the control plane located 25 I_Y downstream of the line injection. All cases refer to injection mode I and dispersion model B. The effect of reaction kinetics is very strong. In the lower variance case the (Da = 0.1) case carries a peak mass through the control plane which is almost four times the amount of mass which crosses the plane for the higher (Da = 100) value. Both extremes, Da = 0.1 and Da = 100, substantially collapse on the limit cases Da = 0 and Da = ∞, respectively. The difference between the curves at different Da numbers is lower as heterogeneity increases. Moreover, the integral of each curve is different in all cases because it is different the amount of A mass consumed by the reaction.

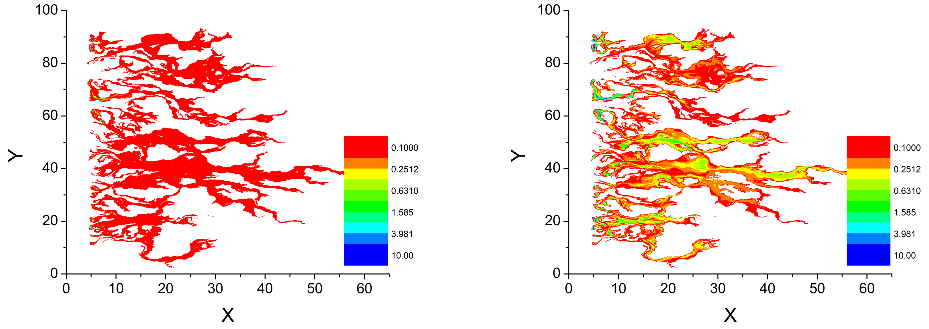

(a) Equilibrium reaction (Da)

(b) Conservative case (Da = 0)

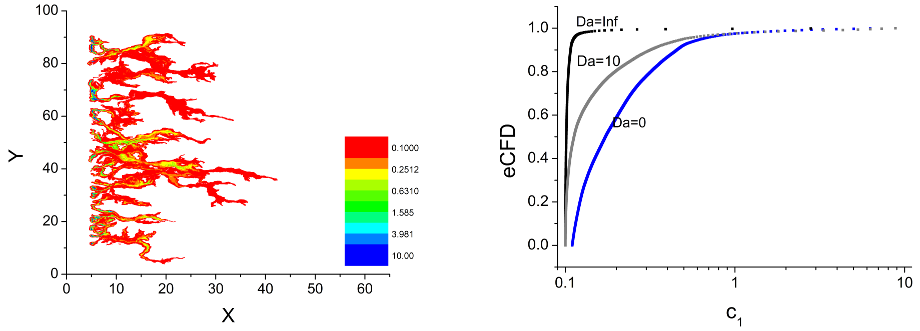

(c) Kinetic reactive case (Da = 10)

(d) Empirical CFDs

Figure 5.15: Snapshots of the concentration field for the reactive species A at time $t' = 10$ for different Da numbers (a) Da $= \infty$, (b) Da $= 0$, (c) Da $= 10$, and correspondent empirical CFDs (panel d). Figures refer to the line uniform injection with dispersion model B in the $\sigma_Y^2 = 10$ field. Notice that the color palette is logarithmic. All quantities are dimensionless: $X = x/I_Y$, $Y = y/I_Y$, $C_1 = c_1/\sqrt{K_{\mathrm{eq}}}$.

5.5 Conclusions

We analyzed numerically the role of high heterogeneity on dilution processes both in conservative and in reactive conditions. Different indicators of dilution have been considered, in order to highlight the interplay among heterogeneity structures, velocity non-uniformities and injection modes (both in terms of source size and initial concentration distribution within the source).

The general conclusion is that heterogeneity enhances the overall dilution of the plume. Velocity non-uniformities create preferential paths where water moves faster, thus advecting solute and developing protruding plume fingers. The high concentration gradients which develop along fingers'fringes feed dilution, which is also proportional to the local value of the dispersion coefficients. The higher the velocity contrasts, the more irregular the shape of the solute body. Thus local dispersion is activated in trying to smoothen the concentration gradients.

A clear image is provided by the dilution index (Kitanidis, 1994) of the concentration of the injected species. The effect of increasing heterogeneity on the overall dilution

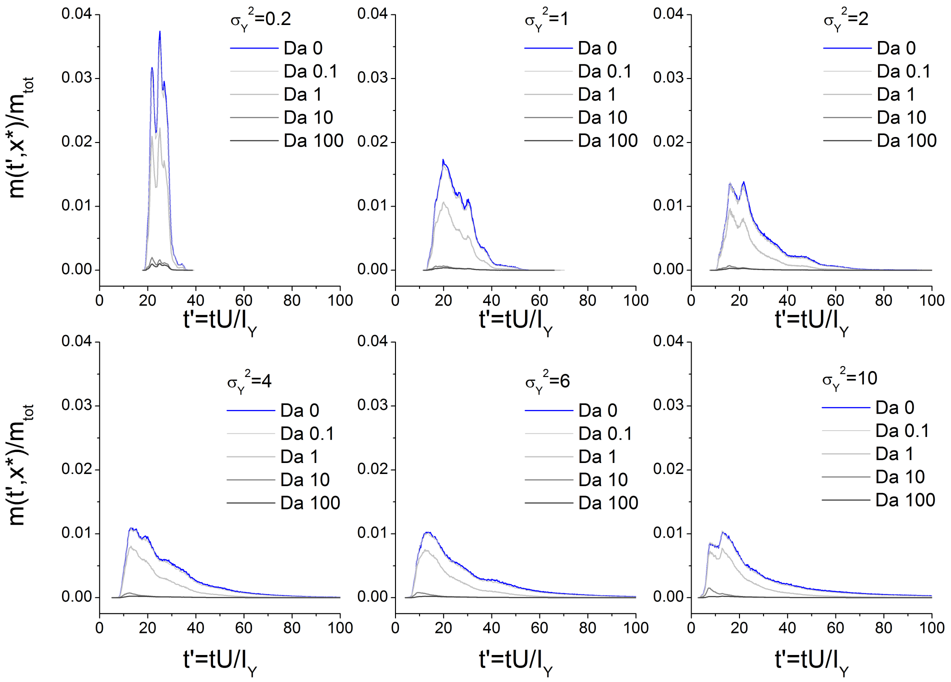

Figure 5.16: Transverse BTCs (amount of mass $m(t', x^*)$ which cross the control plane located at x^* in time t', normalized over the total injected mass m_{tot}) for the reactive species A; line injection with uniform concentration distribution (I) and non-uniform dispersion model (B). The control plane is set at $x^* = 30I_Y$, that is located $25I_Y$ downstream of the injection area. Line color refers to the Da number.

is generally stronger at intermediate heterogeneity levels, whereas it diminishes at $\sigma_Y^2 \geq 6$ in all analyzed conditions, as a result of both the irregular shape of the plume and the disordered mass distribution within the plume's volume. Fast kinetic rates determine a shrinking of the regions of the plume where concentrations are higher, thus promoting the homogenization of the solute body.

A similar behavior is displayed by the amount of total mass of species C which precipitates as a result of a mixing-controlled bimolecular reaction of the type $A + B \leftrightarrows C \downarrow$, as well as by the consumption time dynamics of species A. Precipitation displays also a different spatial mapping which depends on the source size and on the heterogeneity of the medium. Generally, these distributions are negatively skewed, that is, precipitation takes place mostly in high-conductivity regions which act as hot spots of mixing.

Besides, the peak concentration is not strictly inversely proportional to dilution. As directly sensitive to local dynamics, it is highly influenced by the injection mode as well as by the fate and transport of single solute blobs.

Differences in the overall dilution experienced by the plume are only partially evidenced by the shape of the Break Through Curves, which record the amount of solute mass which crosses downstream control planes in time. BTCs are sensitive to both heterogeneity level and reaction kinetics, but negligible differences result from

different dispersion models or injection modes up to the highest σ_Y^2.
Finally, we considered the evolution of the Cumulative Frequency Distribution of the concentration, as a meaningful measure for risk assessment at the plume/field scale. The instantaneously injected concentration can both represent the accidental release of contaminant into the aquifer, as well as the chemical delivery for remediation purposes. Literature analytical models (namely the Beta distribution) fit well the empirical conservative CFDs up to very high levels of heterogeneity ($\sigma_Y^2 = 10$), once we substitute the numerical moments of the passive tracer. The good match stands the transfer to reactive species concentration through analytical speciation equations in case of equilibrium reactions. These results open interesting perspectives in the application of the stochastic approach in risk assessment, thus contributing to reduce the gap between theory and applications.

Chapter 6

On the upscaling of multicomponent reactive transport processes from the pore-scale to the continuum-scale

6.1 Introduction

The continuum (or Darcy's scale) models of transport of solutes in groundwater can be inadequate to describe the complex phenomena which determine the fate and transport of chemicals while they move in porous formations. At this scale we can define continuous properties (i.e. hydraulic conductivity) for the porous medium. These models refer to Reference Elementary Volumes (REVs) where solute mass is considered as well-mixed, neglecting sub-scale fluctuations of concentration (Meakin and Tartakovsky, 2009; Steefel, DePaolo, and Lichtner, 2005). Regardless of the upscaling technique used to go from the pore-scale to the continuum scale, the Darcy's scale Advection-Dispersion-Reaction equations are based on a set of closure hypotheses. These assumptions allow to give a simple mathematical shape to the effective upscaled parameters, which should mimic the effects of the neglected sub-scale variability. But these lumped parameters cannot always guarantee the correct reproduction of the transport features.

It is recognized that the traditional continuum-scale Advection-Dispersion-Reaction equation with local effective coefficients adequately describes conservative and reactive transport if the timescale of the diffusion processes within the pores is sufficiently small, such that the liquid volume within the pore is indeed well-mixed (Dentz *et al.*, 2011). Besides, it is also necessary that the timescale of the reactions is larger than the timescale of diffusion, so that the reaction rate is not affected by impediments to molecule collisions due to transport mechanisms within the pore. This means that the microscale Damköhler number, which expresses the ratio between the timescale of diffusion within the pore $\tau_{d,mic} = l_p^2/D_m$ (where l_p is the length scale of the pore and D_m the molecular diffusion coefficient) and the timescale of reaction τ_r (Dentz *et al.*, 2011), has to be low. The well-mixed hypothesis is most likely verified in case of homogeneous reactions, which do not take place across liquid-solid interfaces (Meile and Tuncay, 2006). In general, highly localized chemical or physical processes, such as heterogeneous reactions which occur across liquid-solid interfaces, challenge the well-mixed pore-volume hypothesis. Moreover, because of the ubiquitous heterogeneity which characterizes the porous media, real transport develops anomalous non-Fickian features of transport, which affect the overall dilution experienced by the solutes as well as the reaction rates, and which cannot be reproduced by Fickian continuum-scale models despite the calibration of effective dispersion and reaction parameters.

Hence upscaling may not be allowed in all transport conditions, and resorting to pore-scale modelization can be required, at least in regions where physical and chemical processes are highly localized. However, pore-scale models are not feasible since they require huge computational resources as well as the detailed knowledge of the porous medium structure, which is never available. Hybrid models (see e.g. Kechagia *et al.*, 2002; Steefel, DePaolo, and Lichtner, 2005; Tartakovsky *et al.*, 2008) offer a natural solution to this kind of problems, applying a pore-scale resolution where processes are highly localized, and relying on upscaled models elsewhere. Alternatively, other methods introduce non-local formalism, such as non-local parameters (see e.g. Mikelic, Devigne, and Van Dujin, 2006; Morales-Casique, Neuman, and Guadagnini, 2006; Moyne, 1997; Porta, Riva, and Guadagnini, 2012) or non-local procedures (see e.g. Berkowitz *et al.*, 2006; Cushman, Bennethum, and Hu, 2002; Dentz, Gouze, and Carrera, 2011; Ginn, 2001; Haggerty and Gorelick, 1995; Neuman and Tartakovsky, 2009; Willmann *et al.*, 2010).

But how can we determine where (and when) solving at the pore-scale is necessary? Answering such a question requires to explore the validity conditions for the assumptions and hypotheses at the base of the upscaled equations. The type and entity of the requirements depend on the choice of the upscaling procedure, which can be various (Brenner, 1987; Cushman, Bennethum, and Hu, 2002), e.g. the method of moments (Brenner, 1980), the volume averaging technique (Battiato *et al.*, 2009; Kechagia *et al.*, 2002; Porta, Riva, and Guadagnini, 2012; Whitaker, 1999), the multi-scale expansion or homogenization procedure (Auriault and Adler, 1995; Battiato and Tartakovsky, 2011; Bensoussan, Lions, and Papanicolaou, 1978; Mikelic, Devigne, and Van Dujin, 2006).

Recently a few works tried to quantitatively identify the regions where upscaling is safe, and where else we need to use different solutions. Auriault and Adler, 1995, for example, identified sufficient conditions for upscaling conservative transport in terms of the Peclet number and a scale ratio parameter within the framework of the homogenization procedure. Battiato *et al.*, 2009 upscaled the Reaction-Diffusion Equation in case of a bimolecular precipitation/dissolution process $A + B \leftrightharpoons C \leftrightharpoons C\downarrow$ relying on a volume averaging procedure; their reference parameters are the ratio between the microscale and the macroscale length, and the Damköhler number for the homogeneous reaction $A + B \rightarrow C$. Battiato and Tartakovsky, 2011 found a homogenizability region for a one-species crystallization $C \leftrightharpoons C\downarrow$ process in terms of Peclet and Damköhler through multi-scale expansion analysis.

We aim here at delineating a region in a multi-dimensional phase space for the upscaling of a bimolecular reactive system which involves both homogeneous and heterogeneous reactions $A+B \leftrightharpoons C \leftrightharpoons C\downarrow$ in the presence of a fully developed transport scenario, which includes advection, diffusion and reactions. Here the transport scenario is controlled by one Peclet number and three Damköhler numbers. So the cases explored by Auriault and Adler, 1995, Battiato *et al.*, 2009 and Battiato and Tartakovsky, 2011 can be drawn as special cases.

First we recall in Section 6.2 the pore-scale differential system for both flow and transport for the different species. Second, in Section 6.3, we state the sufficient homogenizability conditions as derived with a multiscale expansion procedure, and point out how scenarios previously reported in the literature can be obtained from our general results as special cases. The complete development of the procedure is listed in Appendix A. In Section 6.4 we numerically explore the limits which represent sufficient conditions for the homogenization in a simplified bidimensional fracture setting. For this geometry we derive effective coefficients for the macroscale equations (Appendix B), and compare the pore-scale and the macroscale numerical results for a few cases. Finally in Section 6.5 we comment the results presented in the previous chapters of the present thesis, obtained under the assumption of a well-mixed REV, in the light of these last considerations.

6.2 Pore-scale description of the reactive problem

We analyze the upscaling from the pore-scale to the continuum scale of a reactive problem which implies a bimolecular precipitation/dissolution reaction sequence which is both mixing-controlled and kinetically-controlled:

$$\mathrm{A} + \mathrm{B} \underset{k_C}{\overset{k_{\mathrm{AB}}}{\rightleftharpoons}} \mathrm{C} \underset{k_d}{\overset{k_p}{\rightleftharpoons}} \mathrm{C}\downarrow \tag{6.1}$$

The reactions are characterized by a different reaction rate k and thus by different timescales.

Transport of solute species occurs in a porous media setting, thus it is controlled by both advective and diffusive mechanisms. The local velocity field is complex since it is diverted by the pore geometry, and influences the encounter rates between the mobile molecules in the fluid. This means that reactions in the liquid phase are mixing-controlled. Instead the heterogeneous reaction $\mathrm{C} \underset{k_d}{\overset{k_p}{\rightleftharpoons}} \mathrm{C}\downarrow$ occurs across the interface between the liquid and the solid phase. We are assuming here that precipitation occurs only across existing interfaces, and that the solid matrix is impermeable. In the presence of the solid phase, the reaction rate of dissolution coincides with k_d, whereas the reaction rate of precipitation depends on the concentration of species C in the liquid phase.

At this small scale (we will refer to it as microscale, local scale or pore-scale), we can describe the behavior of the solutes A, B and C through the solution of the following differential system for both flow and transport. Differently from the previous chapters, here the apices identify the dimensional variables.

The saturated stationary flow of an incompressible fluid within a geometrically complex system is governed by the Stokes equation, which expresses the momentum conservation as a simplified version of the Navier Stokes equations, and by the continuity equation, which imposes fluid mass conservation:

$$\mu \nabla' \tilde{\mathbf{v}}'(\mathbf{x}')^2 = \nabla' \tilde{p}'(\mathbf{x}'), \quad \mathbf{x}' \in \Omega_L \tag{6.2a}$$

$$\nabla' \cdot \tilde{\mathbf{v}}'(\mathbf{x}') = 0, \quad \mathbf{x}' \in \Omega_L \tag{6.2b}$$

where $\tilde{\mathbf{v}}'(\mathbf{x}')$ represents the stationary local velocity, $\tilde{p}'(\mathbf{x}')$ represents the dynamic pressure (including also the contribution of gravity), and μ represents the uniform viscosity of the fluid. All quantities are regarded as dimensional. Here Ω_L represents the fluid phase of the domain, whereas Γ_Ω represents the interface between the fluid phase and the solid phase. Along Γ_Ω no-slip boundary conditions hold, that is:

$$\tilde{\mathbf{v}}'(\mathbf{x}') = 0, \quad \mathbf{x}' \in \Gamma \tag{6.3}$$

The mass conservation of the solutes dissolved in the fluid phase is expressed by the following Advection-Diffusion-Reaction equation:

$$\frac{\partial \tilde{c}'_i(\mathbf{x}', t')}{\partial t'} + \tilde{\mathbf{v}}'(\mathbf{x}') \cdot \nabla' \tilde{c}'_i(\mathbf{x}', t') = \nabla' \left(\mathbf{D}'_{m,i} \nabla' \tilde{c}'_i(\mathbf{x}', t) \right) + \tilde{r}'_i(\mathbf{c}') \tag{6.4}$$

where $\tilde{c}'_i$ is the concentration of species i and $\mathbf{D}'_{m,i}$ is the molecular diffusion tensor for species i. $\mathbf{D}'_{m,i}$ is generally uniform and isotropic, but compound-dependent. Referring to the reactive system which represents a precipitation/dissolution process, the reaction term reads for species A and B:

$$\tilde{r}'_{\mathrm{A,B}}(\mathbf{x}', t') = -k_{AB} \tilde{c}'_A(\mathbf{x}', t') \tilde{c}'_B(\mathbf{x}', t') + k_C \tilde{c}'_C(\mathbf{x}', t') \tag{6.5}$$

Reaction terms depend non-linearly on the concentration of the other solute species. C in the liquid phase is regulated by an opposite reaction term:

$$\tilde{r}'_C(\mathbf{x}', t') = +k_{\mathrm{AB}} \tilde{c}'_A(\mathbf{x}', t') \tilde{c}'_B(\mathbf{x}', t') - k_C \tilde{c}'_C(\mathbf{x}', t') \tag{6.6}$$

The dynamics of the heterogeneous reaction is governed by a boundary condition which holds along Γ_Ω:

$$-\mathbf{n} \cdot \left(\mathbf{D}'_C \nabla' \tilde{c}'_C \right) = k_p \left(\tilde{c}'^{a}_C - \bar{c}'^{a} \right), \quad \text{on } \Gamma_\Omega \tag{6.7}$$

where $\mathbf{n}$ is a vector orthogonal to the interface Γ_Ω, a is the positive integer parameter which defines the order of the heterogeneous reaction and $\bar{c}'$ is the equilibrium concentration which controls the dissolution/precipitation behavior of species C and is related to the kinetic rates through $\bar{c}'^{a} = k_d / k_p$. The boundary conditions for species A and B read:

$$-\mathbf{n} \cdot (\mathbf{D}'_i \nabla' \tilde{c}'_i) = 0, \quad i = A, B, \quad \text{on } \Gamma_\Omega \tag{6.8}$$

stating the impermeability of the interface with regards to A and B.

In order to make the system dimensionless, we need to define a series of scales for each quantity of interest. We consider the following scales: the length scale of the pore ℓ, the length scale of the macroscale domain L, the effective pore-scale velocity U', a reference molecular diffusion D'_m, and a concentration scale c'^*. Each process, i.e. advection, molecular diffusion and the reactions, is characterized by a specific timescale:

$$T_d = \frac{L^2}{D_{m,i}}, \qquad T_a = \frac{L}{U}, \qquad T'_r = \frac{L}{k \bar{c}^{a-1}}, \qquad T''_r = \frac{1}{k_{\mathrm{AB}} c'^*}, \qquad T'''_r = \frac{1}{k_C} \tag{6.9}$$

where the dimensional timescales T refer to diffusion (T_d), advection (T_a), heterogeneous reaction (T'_r) and homogeneous reactions (T''_r and T'''_r).
All these reference quantities allow to define the following dimensionless quantities:

$$\hat{\mathbf{x}} = \frac{\mathbf{x}'}{L}, \qquad \tilde{\mathbf{v}} = \frac{\tilde{\mathbf{v}}'}{U'}, \qquad \tilde{p} = \frac{\tilde{p}'\ell^2}{\nu U' L}, \qquad \mathbf{D} = \frac{\mathbf{D}'}{D'_m}, \qquad \tilde{c} = \frac{\tilde{c}'}{c'^*} \tag{6.10}$$

and set the dimensionless time variables as follows:

$$\tau_d = \frac{t'}{T_d} \quad \tau_a = \frac{t'}{T_a} \quad \tau'_r = \frac{t'}{T'_r} \quad \tau''_r = \frac{t'}{T''_r} \quad \tau'''_r = \frac{t'}{T'''_r} \tag{6.11}$$

In the following we drop the $\sim$ in order to deal with a lighter formalism.
A few dimensionless numbers are given by the ratio between the timescales, namely the Peclet number

$$\mathrm{Pe} = \frac{T_a}{T_d} = \frac{U'L}{D'_{m,i}} \tag{6.12}$$

and the Damköhler numbers for each of the three concentration-dependent reactions:

$$\mathrm{Da}' = \frac{T_d}{T'_r} = \frac{L^2 k_p \bar{c}'^{a-1}}{D'}, \quad \mathrm{Da}'' = \frac{T_d}{T''_r} = \frac{L^2 k_{\mathrm{AB}} c'^*}{D'}, \quad \mathrm{Da}''' = \frac{T_d}{T'''_r} = \frac{L^2 k_C}{D'} \tag{6.13}$$

Moreover, we define the ratio between the lengthscales $\varepsilon = \ell/L$, which is typically small. We look for homogenizability conditions in terms of these dimensionless numbers. In order to simplify the handling of the time variables, we choose $\hat{t} = \tau_d$ as the reference time variable. The resulting dimensionless differential systems for flow and transport read:

$$\varepsilon^2 \hat{\nabla}^2 \mathbf{v}(\hat{\mathbf{x}}) - \hat{\nabla} p(\hat{\mathbf{x}}) = 0, \qquad \hat{\mathbf{x}} \in \Omega_L \tag{6.14a}$$

$$\hat{\nabla} \cdot \mathbf{v} = 0, \qquad \hat{\mathbf{x}} \in \Omega_L \tag{6.14b}$$

$$\mathbf{v}(\hat{\mathbf{x}}) = 0, \qquad \hat{\mathbf{x}} \in \Gamma_\Omega \tag{6.14c}$$

and:

$$\begin{aligned} \frac{\partial c_i(\hat{\mathbf{x}}, \hat{t})}{\partial \hat{t}} + \mathrm{Pe}\ \mathbf{v}(\hat{\mathbf{x}}) \cdot \hat{\nabla} c_i(\hat{\mathbf{x}}, \hat{t}) =& \hat{\nabla} \cdot (\mathbf{D}_i \hat{\nabla} c_i(\hat{\mathbf{x}}, \hat{t})) - \mathrm{Da}'' c_A(\hat{\mathbf{x}}, \hat{t}) c_B(\hat{\mathbf{x}}, \hat{t}) \\ &+ \mathrm{Da}''' c_C(\hat{\mathbf{x}}, \hat{t}), \quad i = A, B,\ \hat{\mathbf{x}} \in \Omega_L \end{aligned} \tag{6.15a}$$

$$\begin{aligned} \frac{\partial c_C(\hat{\mathbf{x}}, \hat{t})}{\partial \hat{t}} + \mathrm{Pe}\ \mathbf{v}(\hat{\mathbf{x}}) \cdot \hat{\nabla} c_C(\hat{\mathbf{x}}, \hat{t}) =& \hat{\nabla} \cdot (\mathbf{D}_C \nabla c_C(\hat{\mathbf{x}}, \hat{t})) + \mathrm{Da}'' c_A(\hat{\mathbf{x}}, \hat{t}) c_B(\hat{\mathbf{x}}, \hat{t}) \\ &- \mathrm{Da}''' c_C(\hat{\mathbf{x}}, \hat{t}),\ \hat{\mathbf{x}} \in \Omega_L \end{aligned} \tag{6.15b}$$

$$-\mathbf{n} \cdot (\mathbf{D}_i \hat{\nabla} c_i(\hat{\mathbf{x}}, \hat{t})) = 0, \quad i = A, B, \quad \hat{\mathbf{x}} \in \Gamma_\Omega \tag{6.15c}$$

$$-\mathbf{n} \cdot (\mathbf{D}_C \hat{\nabla} c_C(\hat{\mathbf{x}}, \hat{t})) = \mathrm{Da}'(c_C(\hat{\mathbf{x}}, \hat{t})^a - \bar{c}^a), \quad \hat{\mathbf{x}} \in \Gamma_\Omega \tag{6.15d}$$

6.3 Upscaling via multiple scale expansion

6.3.1 Preliminaries and assumptions on the pore-scale geometry

We aim at upscaling the differential system via multiple-scale expansion. Pore-scale processes occur within a macroscale domain Ω with characteristic length L

which is characterized by a liquid phase Ω_L, given by the set of interconnected pores where flow and transport take place, and a discontinuous solid phase Ω_S, which is assumed as impermeable. Let us define Γ_Ω the interface between the liquid and the solid phase throughout the domain. Overall, the domain has also a general boundary $\partial\Omega$ where the boundary conditions of the macroscopic problem are posed.

The multi-scale expansion procedure takes off from the assumption that the structure of the porous domain is given by the repetition of a unit volume $\mathcal{Y}$ with characteristic length ℓ. Some kind of periodicity assumption is typical of a large part of analytical and numerical studies of upscaling (Ahmadi, Aigueperse, and Quintard, 2001; Chen, Deng, and Ye, 2005; Duijn *et al.*, 2007; Edwards, Shapiro, and Brenner, 1993; Whitaker, 1999; Wood, 2007, 2009; Wood *et al.*, 2003). Also the unit cell has a liquid part $\mathcal{B}$ and a solid matrix $\mathcal{G}$, as well as a interface Γ between the two phases, where the heterogeneous reactions take place.

Referring to $\mathcal{Y}$, we can distinguish between a slowly varying spatial variable $\mathbf{x}$, which identifies, from a macroscale perspective, the sequence of unit cells $\mathcal{Y}$ forming the whole domain Ω, and a fast varying spatial variable $\mathbf{y}$ which explores the interior of the unit cells. Clearly, $\mathbf{x}$ and $\mathbf{y}$ are related through the lengthscale ratio ε. The averages of the unknown quantities $\mathcal{A}$ over the unit cell, such as the velocity $\mathbf{v}$, the pressure p and the concentration c_i, can be differently defined through integration over $\mathcal{Y}$:

$$\langle \mathcal{A} \rangle = \frac{1}{|\mathcal{Y}|} \int_{\mathcal{B}(\mathbf{x})} A d\mathbf{y} \tag{6.16}$$

$$\langle \mathcal{A} \rangle_{\mathcal{B}} = \frac{1}{|\mathcal{B}|} \int_{\mathcal{B}(\mathbf{x})} A d\mathbf{y} \tag{6.17}$$

$$\langle \mathcal{A} \rangle_{\Gamma} = \frac{1}{|\Gamma|} \int_{\Gamma(\mathbf{x})} A d\mathbf{x} \tag{6.18}$$

$\langle \mathcal{A} \rangle$ and $\langle \mathcal{A} \rangle_{\mathcal{B}}$ average over the whole volume $|\mathcal{Y}|$ and the liquid volume $|\mathcal{B}|$ of the unit cell, respectively; their ratio depends on the porosity of the unit cell $\phi = \frac{|\mathcal{B}|}{|\mathcal{Y}|}$. $\langle \mathcal{A} \rangle_{\Gamma}$ averages over the interface between the liquid and the solid phase. Each quantity $\mathcal{A}$ varies among unit cells $\mathcal{Y}$ and within unit cells $\mathcal{Y}$, thus it is generally a function of both $\mathbf{x}$ and $\mathbf{y}$.

As a result the complete spatial derivatives in $\hat{\mathbf{x}}$ have both a slowly varying component, depending upon $\mathbf{x}$, and a fast varying component, depending upon $\mathbf{y}$:

$$\nabla_{\hat{x}} \mathcal{A} = \nabla_x \mathcal{A} + \varepsilon^{-1} \nabla_y \mathcal{A}$$

Similarly, also the multiple timescales require to expand temporal derivatives (in $\hat{t}$) according to the different signals, whose relative importance is given by the dimensionless Pe and Da numbers. Taken $t = \tau_d$ as the reference time variable, all the other time quantities are related to the reference t through the dimensionless numbers defined above:

$$\tau_a = \mathrm{Pe}\, t, \qquad \tau_r' = \mathrm{Da}' t, \qquad \tau_r'' = \mathrm{Da}'' t, \qquad \tau_r''' = \mathrm{Da}''' t \tag{6.19}$$

The chain rule of derivation gives:

$$\frac{\partial}{\partial \hat{t}} = \frac{\partial}{\partial t} + \mathrm{Pe} \frac{\partial}{\partial \tau_a} + \mathrm{Da}' \frac{\partial}{\partial \tau_r'} + \mathrm{Da}'' \frac{\partial}{\partial \tau_r''} + \mathrm{Da}''' \frac{\partial}{\partial \tau_r'''} \tag{6.20}$$

Finally we define the dimensionless characteristic number of our problem as functions of the small parameter ε, as follows:

$$\mathrm{Pe} = \varepsilon^{-\alpha},\ \mathrm{Da}' = \varepsilon^{\beta},\ \mathrm{Da}'' = \varepsilon^{\gamma},\ \mathrm{Da}''' = \varepsilon^{\delta} \tag{6.21}$$

In this way the behavior of the pore-scale system is driven by the choice of the four parameters α, β, γ and δ, as well as $\bar{c}$. The higher α, the higher the Pe number, that is, advection-dominated transport conditions. The higher β, γ and δ, the lower the Da number, that is, slow reactions with respect to diffusive properties of the system within the pore.

6.3.2 Upscaling of the flow equations

The upscaling of the flow equations is reported in Auriault and Adler, 1995, and we refer to that paper for the mathematical details. We expound here briefly the key points of the procedure and the final result.

We look for an upscaled flow system which regulates the behavior of the velocity and the pressure at the macroscale, with a first order accuracy in ε. Both the local velocity $\mathbf{v}$ and the local fluid dynamic pressure p are expanded in ε terms as follows:

$$\begin{aligned} \mathbf{v} &= \mathbf{v_0}\left(\mathbf{x},\mathbf{y}\right) + \varepsilon\mathbf{v_1}\left(\mathbf{x},\mathbf{y}\right) + \varepsilon^2\mathbf{v_2}\left(\mathbf{x},\mathbf{y}\right) + \mathcal{O}(\varepsilon^3) \\ p &= p_0 + \varepsilon p_1\left(\mathbf{x},\mathbf{y}\right) + \varepsilon^2 p_2\left(\mathbf{x},\mathbf{y}\right) + \mathcal{O}(\varepsilon^3) \end{aligned}$$

Each $\mathbf{v_m}$ or p_m indicates a contribution to the overall amount of $\mathbf{v}$ and p of the order m in ε, and is periodic in Ω with period $\mathcal{Y}$.

By substituting the variable expansion in ε and by applying the chain rule of derivation to the spatial derivatives in the original microscale flow system, the macroscale system reads:

$$\begin{cases} \langle\mathbf{v}\rangle = -\mathbf{K}\nabla_x p \\ \nabla\cdot\langle\mathbf{v}\rangle = 0 \end{cases} \tag{6.22}$$

where the effective conductivity tensor $\mathbf{K} = \langle\mathbf{k}(\mathbf{y})\rangle$ can be obtained by the solution of a boundary value problem which applies on the unit cell $\mathcal{Y}$:

$$\nabla_y^2\mathbf{k}(\mathbf{y}) + \mathbf{I} + \nabla_y\mathbf{a} = 0, \qquad \mathbf{y}\in\mathcal{B} \tag{6.23a}$$

$$\nabla\cdot\mathbf{k} = 0, \qquad \mathbf{y}\in\mathcal{B} \tag{6.23b}$$

$$\mathbf{k} = 0, \qquad \mathbf{y}\in\Gamma \tag{6.23c}$$

$$\langle\mathbf{a}(\mathbf{y})\rangle = 0, \qquad \mathbf{y}\in\mathcal{B} \tag{6.23d}$$

$\mathbf{k}(\mathbf{y})$ is periodic, with the unit cell $\mathcal{Y}$ as periodic unit. The system 6.22 is the well known system composed by the Darcy equation and the continuity equation at the Darcy's scale, and $\mathbf{K}$ is the hydraulic conductivity tensor (to be corrected for the effect of porosity in the general formulation of Darcy's law) which expresses the hydraulic properties of the Darcy's scale reference volume.

6.3.3 Upscaling the transport equations

In a similar fashion, we proceed to upscale the transport microscale differential system. We need to consider the ε expansion of concentration for each species:

$$c = c_0 + \varepsilon c_1\left(\mathbf{x},\mathbf{y}\right) + \varepsilon^2 c_2\left(\mathbf{x},\mathbf{y}\right) + \mathcal{O}(\varepsilon^3)$$

as well as applying the chain rule of derivation also on temporal derivatives, taking into account all the timescales of the process.
The detailed procedure is listed in Appendix A at the end of the chapter, and brings to the following upscaled version of the Advection-Diffusion-Reaction equations:

$$\begin{aligned}\frac{\partial\langle c_i\rangle_{\mathcal{B}}}{\partial t} =&\nabla_x\cdot\left(\phi^{-1}\mathbf{D}^*\nabla_x\langle c_i\rangle_{\mathcal{B}}\right)-\phi^{-1}\mathrm{Pe}\nabla_x\cdot\left(\langle c_i\rangle_{\mathcal{B}}\langle\mathbf{v}\rangle\right)-\mathrm{Da}''\langle c_A\rangle_{\mathcal{B}}\langle c_B\rangle_{\mathcal{B}}\\ &+\mathrm{Da}'''\langle c_C\rangle_{\mathcal{B}},\quad i=A,B\end{aligned}\tag{6.24}$$

$$\begin{aligned}\frac{\partial\langle c_C\rangle_{\mathcal{B}}}{\partial t} =&\nabla_x\cdot\left(\phi^{-1}\mathbf{D}^*\nabla_x\langle c_C\rangle_{\mathcal{B}}\right)-\phi^{-1}\mathrm{Pe}\nabla_x\cdot\left(\langle c_C\rangle_{\mathcal{B}}\langle\mathbf{v}\rangle\right)+\mathrm{Da}''\langle c_A\rangle_{\mathcal{B}}\langle c_B\rangle_{\mathcal{B}}\\ &-\mathrm{Da}'''\langle c_C\rangle_{\mathcal{B}}-\varepsilon^{-1}\mathrm{Da}'K^*\left(\langle c_C\rangle_{\mathcal{B}}^a-\bar{c}^a\right)\end{aligned}\tag{6.25}$$

The effective parameters K^* and $\mathbf{D}^*$ depend on the microscale. K^* depends on the geometrical relation $K^*=|\Gamma|/|\mathcal{B}|$, whereas $\mathbf{D}^*=\langle\mathbf{D}\left(\mathbf{I}+\nabla_y\boldsymbol{\chi}\right)\rangle+\varepsilon^{1-\alpha}\langle\boldsymbol{\chi}\mathbf{k}\rangle\nabla_x p_0$ can be obtained by solving the boundary value problems for the closure variables $\mathbf{k}(\mathbf{y})$ (see previous section) and $\boldsymbol{\chi}(\mathbf{y})$ over $\mathcal{Y}$:

$$-\nabla_y\cdot\mathbf{D}\left(\nabla_y\boldsymbol{\chi}+\mathbf{I}\right)+\varepsilon\mathrm{Pe}\mathbf{v_0}\cdot\nabla_y\boldsymbol{\chi}=\varepsilon\mathrm{Pe}\left(\langle\mathbf{v_0}\rangle-\mathbf{v_0}\right),\qquad \mathbf{y}\in\mathcal{B}\tag{6.26a}$$

$$-\left[\mathbf{n}\cdot\mathbf{D}\left(\nabla_y\boldsymbol{\chi}+\boldsymbol{I}\right)\right]=0,\qquad \mathbf{y}\in\Gamma\tag{6.26b}$$

The solution is periodic in Ω, with period $\mathcal{Y}$. The boundary value problem (6.26) for $\boldsymbol{\chi}$ is presented in decoupled form, that is, the microscale does not depend on the macroscale. The decoupling between the macroscale and the microscale is guaranteed by the following set of conditions:

I. $\varepsilon\ll 1$, that is, the microscale and the macroscale are conveniently separated;

II. $\alpha<2$, that is, $\mathrm{Pe}<\varepsilon^{-2}$;

III. $\beta>0$, that is, $\mathrm{Da}'<1$;

IV. $\alpha+\beta>1$, that is, $\mathrm{Da}'/\mathrm{Pe}<\varepsilon$;

V. $\gamma>-2$, that is, $\mathrm{Da}''<\varepsilon^{-2}$;

VI. $\alpha+\gamma>-1$, that is, $\mathrm{Da}''/\mathrm{Pe}<\varepsilon^{-1}$;

VII. $\delta>-2$, that is, $\mathrm{Da}'''<\varepsilon^{-2}$;

VIII. $\alpha+\delta>-1$, that is, $\mathrm{Da}'''/\mathrm{Pe}<\varepsilon^{-1}$;

IX. $\langle\boldsymbol{\chi}_\Gamma\rangle=\langle\boldsymbol{\chi}\rangle_{\mathcal{B}}$.

Conditions I-VIII refer to the parameters of the transport scenario and to the geometry of the setting, and constitute the set of sufficient conditions for upscaling. Condition IX is a operative condition which allows to write the boundary value problem for $\boldsymbol{\chi}$ and obtain the effective coefficients (see Appendix A).
Condition I is analogous to the constraints obtained by Auriault and Adler, 1995 who neglected any kind of reaction, and identified a limit in terms of the sole Pe number. Physically, this means that advection cannot be too fast as compared to

diffusion in order to be able to upscale the local equations with simple effective coefficients. Conditions I-IV and condition IX coincide with the conditions individuated by Battiato and Tartakovsky, 2011 for a simplified reactive system involving only species C. Our results thus generalize the previous works, which can be obtained as special cases of our set of conditions.
The conditions on γ and δ are equal, despite the fact that the homogeneous reaction pointing towards the right requires mixing between A and B before occurring. However mixing (of waters with a different chemical composition) and dilution (of a plume with a single compound) are subject to the same transport processes, which determine identical conditions for the homogeneity of the composition over the REV.
The conditions on β state that the heterogeneous reactions cannot be too fast as compared to diffusion because advection-dominated conditions are characterized by strong concentration gradients which occupy small width fringes.
The mixed conditions (i.e., on Pe and Da) compare advection and reaction timescale, and pose a limit on their ratio which states that when reactions are fast, also advection limitations are stronger, since the velocity field could obstacle the encounter between molecules, or their approaching the reactive walls, thus slowing down the reactions.

It is also interesting to note that the macroscale equations have the same shape of the upscaled equations obtained by Battiato *et al.*, 2009, who upscaled the same reactive system, but neglecting advection, via volume averaging. Moreover, also the limit between the decoupled condition and the coupling between the microscale and the macroscale identified by the two procedures coincides. Besides, our results are more generalized because with our procedure we did not need to assume nothing other than the periodic structure of the porous medium. On the contrary, the volume averaging procedure would have required to set a number of assumptions which cannot be verified a priori. Nevertheless the final condition on Da'' obtained through the two procedures coincides in the absence of advection, thus confirming that different upscaling procedures bring to the same results.

The homogenizability conditions can be graphically represented in a phase diagram with the dimensionless numbers Pe, Da', Da'' and Da''' along the axes. For graphical reasons and thanks to the fact that the constraints on γ and δ are identical, we represent the parameters for both homogeneous reactions along the same axis. The colors on Figure 6.1 identify also the shape of the macroscale equations, which in particular conditions can drop certain terms. We can identify six different sub-regions, as described in the following subsections. The limits between sub-regions are defined given for granted the exterior limits of the safe homogenizability region stated by conditions I-VIII.

The phase diagram developed by Battiato and Tartakovsky, 2011 represents a cross-section of our phase diagram, in the region where γ and δ do not modify the constraints on α and β. It is evident how the constraint related to the heterogeneous reaction is more stringent than the constraints on the homogeneous reaction parameters. This is because the pore geometry directly affects the heterogeneous reaction rate, since reactions occur only in the vicinity of the phase interfaces and are thus highly localized. On the contrary, homogeneous reactions are more related to the fluid-phase transport dynamics, and it is sufficient that diffusion is fast enough to

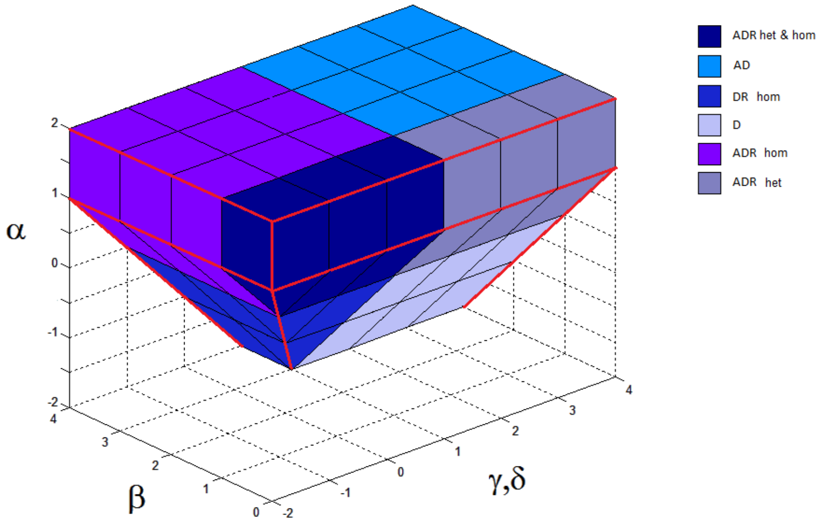

Figure 6.1: Phase diagram for the homogenizability. α, β, γ and δ are related to the dimensionless Pe and Da numbers of the transport scenario through the length-scale ratio ε.

make mixing within the pore almost complete, and thus to make the reaction occur at its full kinetic rate (Meile and Tuncay, 2006).
Outside the homogenizability region upscaling is not guaranteed, although it could be possible with modified effective parameters (see e.g. Dagan, 1988; Han, Bhakta, and Carbonell, 1985; Koch and Brady, 1987; Mikelic, Devigne, and Van Dujin, 2006; Porta, Riva, and Guadagnini, 2012) taking into account non-local effects.

6.3.4 Complete Macroscale Equation (ADR het&hom)

Within the homogenizability region identified by the colored volume in Fig. 6.1, the sub-region characterized by $\alpha > 0$, $\beta < 1$ and $\gamma, \delta < 1$ individuates the zone for which the microscale transport problem can be safely upscaled, despite the fact that all physical and chemical processes play a non-negligible role. The upscaled Advection-Diffusion-Reaction equation is thus complete (Eq. 6.24 for species A and B, and Eq. 6.25 for C) and includes effective terms for diffusion and reaction. The complete system is then completed by a set of boundary conditions to be posed along the macroscale boundary of the domain $\partial\Omega$.

6.3.5 Region where Advection and Heterogeneous Reaction are Negligible (DR hom)

If $\alpha < 0$, $\beta > 1$ and $\gamma, \delta < 1$ the complete macroscale system can be simplified by neglecting both the advective terms and the heterogeneous reaction. These supplemental conditions in fact describe a diffusion-dominated system, where also the heterogeneous reaction is slow enough to be neglected. The simplified macroscale differential system reads for A and B:

$$\frac{\partial \langle c_i \rangle_{\mathcal{B}}}{\partial t} = \nabla_x \cdot \left(\phi^{-1} \mathbf{D}^* \nabla_x \langle c_i \rangle_{\mathcal{B}} \right) - \mathrm{Da}'' \langle c_A \rangle_{\mathcal{B}} \langle c_B \rangle_{\mathcal{B}} + \mathrm{Da}''' \langle c_C \rangle_{\mathcal{B}}, \quad i = A, B$$

and for species C:

$$\frac{\partial \langle c_C \rangle_{\mathcal{B}}}{\partial t} = \nabla_x \cdot \left(\phi^{-1} \mathbf{D}^* \nabla_x \langle c_C \rangle_{\mathcal{B}} \right) + \mathrm{Da}'' \langle c_A \rangle_{\mathcal{B}} \langle c_B \rangle_{\mathcal{B}} - \mathrm{Da}''' \langle c_C \rangle_{\mathcal{B}}$$

6.3.6 Region where the Heterogeneous Reaction is Neglibible (ADR hom)

If $\alpha > 0$, $\beta > 1$ and $\gamma, \delta < 1$ only the heterogeneous reaction is negligible, so that the upscaled partial differential equations read:

$$\begin{aligned} \frac{\partial \langle c_i \rangle_{\mathcal{B}}}{\partial t} =& \nabla_x \cdot \left(\phi^{-1} \mathbf{D}^* \nabla_x \langle c_i \rangle_{\mathcal{B}} \right) - \phi^{-1} \mathrm{Pe} \nabla_x \cdot \left(\langle c_i \rangle_{\mathcal{B}} \langle \mathbf{v} \rangle \right) \mp \mathrm{Da}'' \langle c_A \rangle_{\mathcal{B}} \langle c_B \rangle_{\mathcal{B}} \\ & \pm \mathrm{Da}''' \langle c_C \rangle_{\mathcal{B}}, \quad i = A, B, C \end{aligned}$$

where the lower signs apply to species A and B and the upper signs apply to C.

6.3.7 Region where the Homogeneous Reactions are negligible (ADR het)

On the contrary, if $\alpha > 0$, $\beta < 1$ and $\gamma, \delta > 1$ we can neglect only the heterogeneous reaction terms to obtain for species A and B:

$$\frac{\partial \langle c_i \rangle_{\mathcal{B}}}{\partial t} = \nabla_x \cdot \left(\phi^{-1} \mathbf{D}^* \nabla_x \langle c_i \rangle_{\mathcal{B}} \right) - \phi^{-1} \mathrm{Pe} \nabla_x \cdot \left(\langle c_i \rangle_{\mathcal{B}} \langle \mathbf{v} \rangle \right), \quad i = A, B$$

and for species C:

$$\frac{\partial \langle c_C \rangle_{\mathcal{B}}}{\partial t} = \nabla_x \cdot \left(\phi^{-1} \mathbf{D}^* \nabla_x \langle c_C \rangle_{\mathcal{B}} \right) - \phi^{-1} \mathrm{Pe} \nabla_x \cdot \left(\langle c_C \rangle_{\mathcal{B}} \langle \mathbf{v} \rangle \right) - \varepsilon^{-1} \mathrm{Da}' K^* \left(\langle c_C \rangle_{\mathcal{B}}^a - \bar{c}^a \right)$$

6.3.8 Diffusion-dominated Region (D)

The simplest upscaled form for the transport equations is valid if the following conditions are fulfilled: $\alpha < 0$, $\beta > 1$ and $\gamma, \delta > 1$. In this cases the system is governed by diffusion solely and the concentration evolves according to:

$$\frac{\partial \langle c_i \rangle_{\mathcal{B}}}{\partial t} = \nabla_x \cdot \left(\phi^{-1} \mathbf{D}^* \nabla_x \langle c_i \rangle_{\mathcal{B}} \right), \quad i = A, B, C$$

6.3.9 Advection-Diffusion Region (AD)

Finally if $\alpha > 0$, $\beta > 1$ and $\gamma, \delta > 1$ the system is regarded as conservative, and all species are subject to advection and effective diffusion solely:

$$\frac{\partial \langle c_i \rangle_{\mathcal{B}}}{\partial t} = \nabla_x \cdot \left(\phi^{-1} \mathbf{D}^* \nabla_x \langle c_i \rangle_{\mathcal{B}} \right) - \phi^{-1} \mathrm{Pe} \nabla_x \cdot \left(\langle c_i \rangle_{\mathcal{B}} \nabla \mathbf{v} \rangle \right), \quad i = A, B, C$$

6.4 Numerical investigation

We numerically explore the sufficient conditions identified for the safe upscaling of the microscale transport equations, by comparing numerical simulations at the microscale and at the macroscale. We choose the simple setting of a bidimensional fracture, neglecting any geometry change due to species C precipitation. The ratio between half-width H_f of the fracture and its length L_f provides the lenghtscale ratio $\varepsilon = H_f/L_f$. Flow and transport are thus defined on the dimensionless domain $\Omega = \{(x,y) : x \in (0,1), |y| \leq \varepsilon\}$. The liquid-phase domain is $\mathcal{B} = \{(x,y) : x \in (0,1), |y| < \varepsilon\}$, whereas the liquid-solid interface is the wall of the fracture $\Gamma = \{(x,y) : x \in (0,1), y = \pm\varepsilon\}$. Reactions occur both in the liquid phase and across Γ. All the dimensionless numbers (namely, Peclet and the several Damköhler numbers which describe the reactive properties of the system) are expressed as powers of the parameter ε. The slow spatial variable x is one-dimensional and parallel to the longitudinal axis of the fracture. The fast spatial variable y is onedimensional and orthogonal to the longitudinal axis of the fracture. The average quantities are defined across the width of the fracture:

$$\langle \mathcal{A}(x,y,t) \rangle = \frac{1}{2\varepsilon} \int_{-\varepsilon}^{\varepsilon} \mathcal{A}(x,y,t) dy \tag{6.27}$$

where $\mathcal{A}(x,y,t)$ is a generic variable defined over the domain.
The initial conditions of concentration for each species are posed as follows:

$$c_A(x,y,t=0) = \begin{cases} c_{0,\mathrm{A}}, & \text{if } x \leq \bar{x} \\ 0, & \text{otherwise} \end{cases}$$

$$c_B(x,y,t=0) = \begin{cases} 0, & \text{if } x \leq \bar{x} \\ c_{0,\mathrm{B}}, & \text{otherwise} \end{cases}$$

$$c_C(x,y,t=0) = 0, \quad \text{everywhere}$$

In all tested cases we introduce species A continuously along the upstream boundary of the fracture with $c_A = c_{0,\mathrm{A}}$. The ambient water downstream of $\bar{x}$ contains initially only species B. C in the liquid phase is initially absent, and is produced only through dissolution from the solid phase or mixing-controlled production through $A + B \to C$.
Our numerical test cases share the same geometry ($\varepsilon = 0.00625$) and the same fluid flow, with $U' = 0.0\bar{6}\,\mathrm{mm/s}$ and the Reynolds number $\mathrm{Re} = U'H/\nu \approx 0.01$ guarantees laminar flow. The initial conditions impose $\bar{x}' = 5mm$ and $\tilde{c}'_{0,\mathrm{A}} = \tilde{c}'_{0,\mathrm{B}} = 1$. Moreover we assume the following parameters: $a = 1$, $\bar{c} = 1$ and $\tilde{c}'^{*} = 1$. For the sake of simplicity we impose equal molecular diffusion coefficients for all the three aqueous species. This condition could be easily modified. The value of D'_m varies in all cases according to the chosen value for the Peclet number.

6.4.1 Pore-scale solution

The problem is first solved numerically at the microscale. This solution is the reference solution for evaluating the accuracy of the upscaled models.

The solution $\mathbf{v}(y) = (v(y), 0)$ of the dimensionless flow problem is given analytically and reads:

$$v\left(y\right) = \begin{cases} \frac{3}{2}\left[1 - \left(\frac{y}{\varepsilon}\right)^2\right], & \text{if } y \leq |\varepsilon| \\ 0, & \text{otherwise} \end{cases} \tag{6.28}$$

The reference dimensionless effective velocity is simply the transverse average of the velocity profile:

$$U = \frac{1}{2\varepsilon}\int_{-\varepsilon}^{\varepsilon} v(y)dy = 1 \tag{6.29}$$

whereas the driving force ∇p has only the longitudinal component $\frac{\partial p}{\partial x} = -3$.
The solution of the complete flow system has also the following form (see Auriault and Adler, 1995):

$$\mathbf{v}\left(x, y\right) = -\frac{1}{\varepsilon^2}\mathbf{k}\cdot\nabla p \tag{6.30}$$

In this case $\mathbf{k}(\mathbf{y}) = (k(y), 0)$ and:

$$k(y) = \begin{cases} \frac{1}{2}\left(1 - \frac{y^2}{\varepsilon^2}\right), & \text{if } y \leq |\varepsilon| \\ 0, & \text{otherwise} \end{cases} \tag{6.31}$$

The complete dimensionless transport problem needs to be solved numerically. The pore-scale problem is solved in the simple geometry by means of Smoothed Particle Hydrodynamics. Flow is included analytically as the movement of the computational nodes, thus providing also the advective contribution to transport. Molecular diffusion is modeled via kernel integral interpolation. Homogeneous reactions are included as an implicit reaction term among fluid particles (see Chapter 5), whereas the heterogeneous reaction term is modeled as solute mass exchanges between solid particles and fluid particles/computational nodes (Tartakovsky *et al.*, 2007a,b) when they approach the reactive surface Γ. The temporal variation of concentration of species A and B is computed as follows:

$$\left.\frac{dc_s}{dt}\right|_i = \sum_{j\in fluid}\frac{1}{\omega_{ij}}D(c_{s,i}-c_{s,j})\frac{\mathbf{r}_{ij}}{|\mathbf{r}_{ij}|^2}\cdot\nabla W(\mathbf{r}_{ij}, h) - \mathrm{Da}'' c_{A,i}c_{B,i} + \mathrm{Da}''' c_{C,i}, \quad s = A, B \tag{6.32}$$

Coherently with the symbols used in the presentation of the SPH method in Chapter 2, $c_{s,i}$ refers to the concentration for species s of the particle located in $\mathbf{x}_i$ at time t, $\mathbf{r}_{ij} = \mathbf{x}_i - \mathbf{x}_j$ is the distance between the location of particles i and j, j indicates the fluid particles located within the smoothing area $\mathcal{H}$ centered in $\mathbf{x}_i$ with radius proportional to the smoothing length h, and ω_{ij} is the harmonic mean of the local particle density $\omega_i = \sum_{j\in fluid} W(\mathbf{r}_{ij}, h)$ in the smoothing areas centered in $\mathbf{x}_i$ and $\mathbf{x}_j$. W is the kernel function which is defined over $\mathcal{H}$, and whose value depends on $\mathbf{x}_i$, where W is centered, and on $\mathbf{x}_j$, where its value is sought. We assume a cubic-B spline shape for W (Monaghan, 2005).
For species C the algorithm has to consider also the heterogeneous reaction term,

which is included when the fluid particle i is sufficiently close to the border Γ:

$$\begin{aligned}\frac{dc_i}{dt} = \sum_{j\in fluid} \frac{D(c_i - c_j)}{\omega_{ij}} \frac{\mathbf{r}_{ij}}{|r_{ij}|^2} \cdot \nabla W(r_{ij}, h) - \mathrm{Da}'' c_{i,A} c_{i,B} + \mathrm{Da}''' c_{i,C} \\ - R_{\mathrm{eff}} \sum_{k\in solid} (c_i - \bar{c})\delta_{ik}\end{aligned} \tag{6.33}$$

k spans over the solid particles which constitute the interface between the liquid and the solid phase (in our case, the walls of the fracture), whereas the vicinity to the border is regulated by

$$\delta_{ik} = \begin{cases} 1, & \text{if } |\mathbf{x}_i - \mathbf{x}_k| \leq d \\ 0, & \text{otherwise} \end{cases} \tag{6.34}$$

The parameter d is chosen according to the recommendations by Tartakovsky *et al.*, 2007b, who suggested to adopt a reaction boundary layer thickness d larger than the physical reactive layer, and of the order of magnitude of the smoothing length h. In particular they suggest to fulfill the following relation: $dx < d < h$, where dx is the mean particle-particle distance and h is the smoothing length. Besides, the choice of d is less significant if we neglect the surface growth/erosion due to the precipitation/dissolution process. We impose $h = \sigma\sqrt{dx^2 + dy^2}$, where dx and dy are respectively the mean spacing in x and y directions, and $\sigma = 1.75$, and choose $dx = dy = 0.00025$ and $d = 0.001$. The effective reaction parameter R_{eff} is computed as follows:

$$R_{\mathrm{eff}} = \frac{k_p}{d\, N_{int}} \tag{6.35}$$

where N_{int} is the mean number of fluid particles which interact with each solid particle. Given the rigid movement of the fluid particles, N_{int} can be computed exactly according to the geometry of the problem and the initial configuration of the fluid and solid particles. All the reaction terms are implemented implicitly; convergence is sought with a fully implicit Newton-Raphson method (Istok, 1989). The geometry variations due to precipitation are neglected.

Upscaling the exact pore-scale solution provides exact averaged values at the macroscale:

$$\langle c_i\rangle_{\mathrm{exact}} = \frac{1}{2\varepsilon}\int_{-\varepsilon}^{\varepsilon} c_i(y)dy \tag{6.36}$$

$\langle c_i\rangle_{\mathrm{exact}}$ can be estimated by averaging the numerical results at the pore-scale. Smoothed Particle Hydrodynamics computes local c_i values at nodes whose configuration varies in time. In order to compute $\langle c_i\rangle_{\mathrm{exact}}$ estimates at precise $x = x^*$, we need to compute the values of $c_i(x^*, y)$ along y as follows:

$$c_i(x^*, y) = \sum_{j\in fluid} \frac{c_j W_{ij}(\mathbf{r}_{ij}, h)}{\omega_{ij}} \tag{6.37}$$

by considering all the j particles located within $\mathcal{H}$ centered in (x^*, y). The $\langle c_i\rangle_{\mathrm{exact}}$ estimates are thus obtained through:

$$\langle c_i\rangle_{\mathrm{mic}} = \frac{1}{N}\sum_i c_i(x^*, y_i) \tag{6.38}$$

where N is the number of points y_i with which the transverse section at $x = x^*$ is divided along the y direction.

6.4.2 Macroscale solution

Macroscale flow is given by a constant one-dimensional velocity U along the fracture longitudinal axis. As regards transport, we consider the complete and general form of the upscaled transport system which is rigorously valid only in the homogenizability region which is represented in the phase diagram in Figure 6.1. The solution of the macroscale system requires the determination of the following effective parameters: $K^* = \frac{|\Gamma|}{|\mathcal{B}|}$ and $\mathbf{D}^* = \langle \mathbf{D} \left(\mathbf{I} + \nabla_y \boldsymbol{\chi} \right) \rangle + \epsilon^{1-\alpha} \langle \boldsymbol{\chi} \mathbf{k} \rangle \nabla_x p_0$. The particular geometry of the problem provides an analytical solution for these effective parameters, as shown in Appendix B. Thus:

$$K^* = 1 \qquad \text{and} \qquad D^* = D + \frac{2}{105} \frac{(\varepsilon^{1-\alpha})^2}{D} \tag{6.39}$$

D^* is larger than the microscale molecular diffusion coefficient D as an effect of velocity non-uniformities at the scale smaller than the continuum scale. Generally, the higher the Pe number, the larger the gap between D^* and D, that is, the subscale distortion due to the non-uniform velocity field is less mitigated by the action of local diffusion.

K^* and D^* are included in the following one-dimensional system for the approximate upscaled $\langle c_i \rangle$:

$$\frac{\partial \langle c_i \rangle}{\partial t} = \frac{\partial}{\partial x} \left(D^* \frac{\partial c_i}{\partial x} \right) - \mathrm{Pe} \frac{\partial}{\partial x} \left(\langle c_i \rangle U \right) - \mathrm{Da}'' \langle c_A \rangle_{\mathcal{B}} \langle c_B \rangle_{\mathcal{B}} + \mathrm{Da}''' \langle c_C \rangle_{\mathcal{B}}, \; i = A, B \tag{6.40}$$

$$\begin{aligned} \frac{\partial \langle c_i \rangle}{\partial t} =& \frac{\partial}{\partial x} \left(D^* \frac{\partial c_i}{\partial x} \right) - \mathrm{Pe} \frac{\partial}{\partial x} \left(\langle c_i \rangle U \right) + \mathrm{Da}'' \langle c_A \rangle_{\mathcal{B}} \langle c_B \rangle_{\mathcal{B}} - \mathrm{Da}''' \langle c_C \rangle_{\mathcal{B}} \\ & - \varepsilon^{-1} \mathrm{Da}' K^* \left(\langle c_C \rangle_{\mathcal{B}}^a - \bar{c}^a \right) \end{aligned} \tag{6.41}$$

which can be solved provided the one-dimensional initial conditions for the concentration of the three species, and the boundary conditions at $x = 0$ and $x = 1$.

The macroscale system of equations is solved by means of Smoothed Particle Hydrodynamics, in order to provide a similar level of numerical accuracy at both scales. The longitudinal spacing among the particles dx is equal to the pore-scale problem, in order to have the same spatial resolution across the initial discontinuity between concentration values, whereas the timestep dt is subject to a slightly different condition because of a different diffusion coefficient:

$$dt \leq \frac{\epsilon h^2}{D} \quad \text{vs} \quad dt \leq \frac{\epsilon h^2}{D^*}$$

where $\epsilon = 0.1$ is an empirical factor. The uniform flow is analytically given, whereas at this scale reactions occur - mathematically speaking - only in the fluid phase since the heterogeneous reaction contribution is considered by means of an effective reaction parameter. The reaction terms are included implicitly following a similar procedure as the one used at the pore scale, and described in Chapter 5.

As in the previous case, the punctual value at specific x^* has to be derived by kernel interpolation. Here, $\langle c_i \rangle_{\text{mac}}$ is supposed to approximate $\langle c_i \rangle_{\text{exact}}$ within terms of order ε^2:

$$\langle c_i \rangle_{\text{exact}} = \langle c_i \rangle_{\text{mac}} + \mathcal{O}(\varepsilon^2) \tag{6.42}$$

Table 6.1: Parameters for the test cases.

Parameter	TC 1	TC 2	TC 3	TC 4
α	1	1	1	2
β	1	1	-1	-1
γ	-1	-3	0	-1
δ	-1	-3	0	-1

except for numerical approximation errors. That is why we use the same algorithm and the same resolution for both the microscale and the macroscale numerical simulations.

6.4.3 Test cases

In the following we include the results of the illustrative comparison for a few test cases, located both inside and outside the homogenizability region delineated by the sufficient conditions stated above. In Table 6.1 we list the parameters which characterize each couple of simulations.

Figures 6.2 and 6.3 refer to Test Case 1 (TC 1), whose parameters are located within the homogenizability region enclosed in the colored volume represented in Fig. 6.1. The upper row in Fig. 6.2 represents the longitudinal profile for the averaged concentration. Black solid lines refer to the averaged microscale solution $\langle c\rangle_{\mathrm{mic}}$ for each species, whereas the thinner grey lines refer to the macroscale solution $\langle c\rangle_{\mathrm{mac}}$, which is supposed to approximate the exact, averaged pore-scale solution, within terms of order ε^2. This condition is respected by all species, as evidenced in the lower row which represents $E_i = |\langle c\rangle_{\mathrm{mic}} - \langle c\rangle_{\mathrm{mac}}|$. It is noticeable the good match for the logitudinal profile for species C which confirms the good choice of the numerical parameters for the implementation of the heterogeneous reactive term at the microscale. The production of species C is concentrated across the moving front, as shown in Fig. 6.3, whereas along the boundaries the C production is negligible because of a slow heterogeneous reaction kinetics. Notice also that Fig. 6.3 covers a different x axis range, in order to zoom on the reactive mobile front.

Figures 6.4 and 6.5 represent the same quantities for the Test Case 2 (TC 2), which is located just outside the homogenizability region, because of the values assigned to the parameters γ and δ which define the Damköhler numbers for the homogeneous reactions. This time the rate of production of C through the homogeneous reactions is much larger, hence species C reaches not negligible values at the fringe. Although Test Case 2 does not fulfill the sufficient conditions for homogenizability, the errors are low, thus confirming that the safe region could be larger than what determined through the multiscale procedure.

On the contrary, Figures 6.6 and 6.7 represent a case (TC 3) whose parameters are located outside the homogenizability region, for which upscaling is indeed not possible within $\mathcal{O}(\varepsilon)$ errors. Test case 3 is characterized by a fast heterogeneous reaction kinetics, which causes large errors in the prediction of the upscaled behavior of c_C. The predominant role of the heterogeneous reaction is evident from the analysis of the concentration field in Fig. 6.7. This time we do not need to focus on a small range along x because the production of species C occurs mainly along

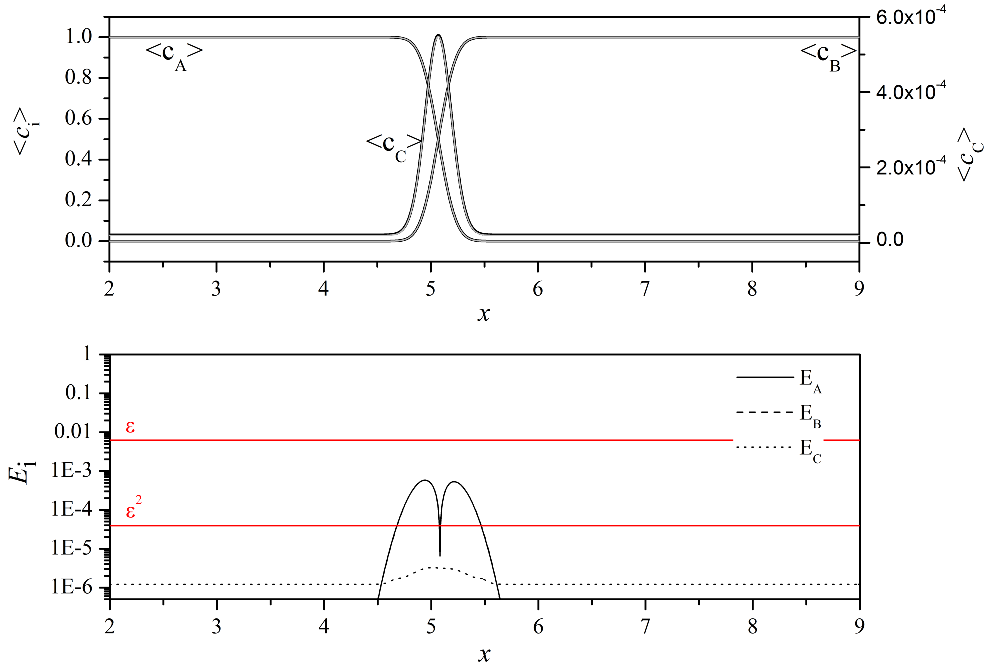

Figure 6.2: Test Case 1: Comparison of the longitudinal profiles of $\langle c_i \rangle$ and errors $E_i = |\langle c_i \rangle_{\text{mic}} - \langle c_i \rangle_{\text{mac}}|$ computed as the difference between the averaged microscale solution and the solution of the macroscale problem. $\langle c_i \rangle_{\text{mic}}$ is represented with thick black lines, whereas $\langle c_i \rangle_{\text{mac}}$ is represented with thinner grey lines in the upper panel. The parameters of this test case ($\alpha = 1, \beta = 1, \gamma = -1, \delta = -1$) belong to the homogenizability region, and require a complete form for the upscaled equation (Eq. 6.24 and 6.25). The reference dimensional time is $t' = 1$. The x axis is in dimensional form.

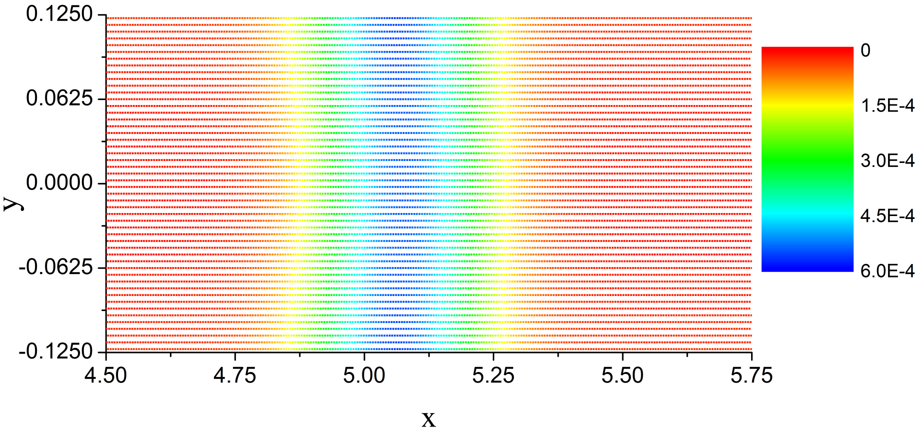

Figure 6.3: Test Case 1: Concentration field for species C across the discontinuity at time $t' = 1$. Notice that the x axis range (dimensional) is smaller than in Fig. 6.2

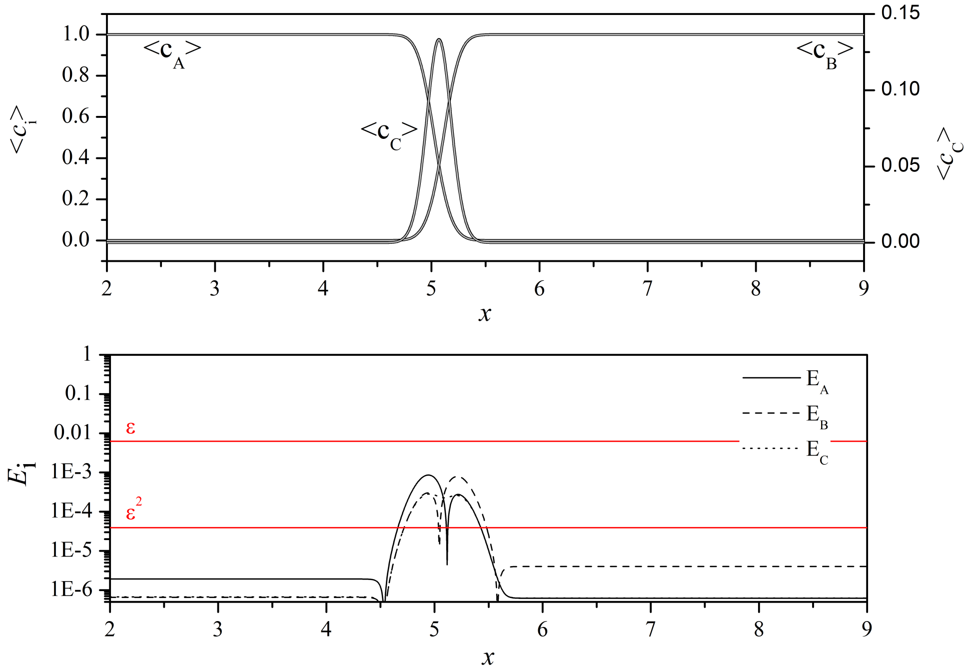

Figure 6.4: Test Case 2: Comparison of the longitudinal profiles of $\langle c_i \rangle$ and errors $E_i = |\langle c_i \rangle_{\text{mic}} - \langle c_i \rangle_{\text{mac}}|$ computed as the difference between the averaged microscale solution and the solution of the macroscale problem. $\langle c_i \rangle_{\text{mic}}$ is represented with thick black lines, whereas $\langle c_i \rangle_{\text{mac}}$ is represented with thinner grey lines in the upper panel. The parameters of this test case ($\alpha = 1, \beta = 1, \gamma = -3, \delta = -3$) do not belong to the homogenizability region, because of fast homogeneous reactions. The reference dimensional time is $t' = 1$. The x axis is in dimensional form.

the walls of the fracture. With respect to this massive dissolution of solid C, the production of C by the homogeneous mixing-controlled reaction is negligible.

Finally, Test Case 4 (TC 4) is analyzed in Figures 6.8 and 6.9. This test case is characterized by a high Peclet number, which locates its state point outside the colored region in the phase diagram in Fig. 6.1. The high distortion of the velocity field, which is caused by a rapid advective timescale as opposed to the diffusive timescale, causes a bad performance of the upscaling system of equations for all species, whose errors are larger than ε for all species. Also in this case, the production of C along the walls largely exceeds the mixing-controlled production due to the interaction of A and B in the fluid phase. Such a scenario calls for a different shape of the upscaled equations, capable of taking into account the non-negligible coupling between the microscale and the macroscale.

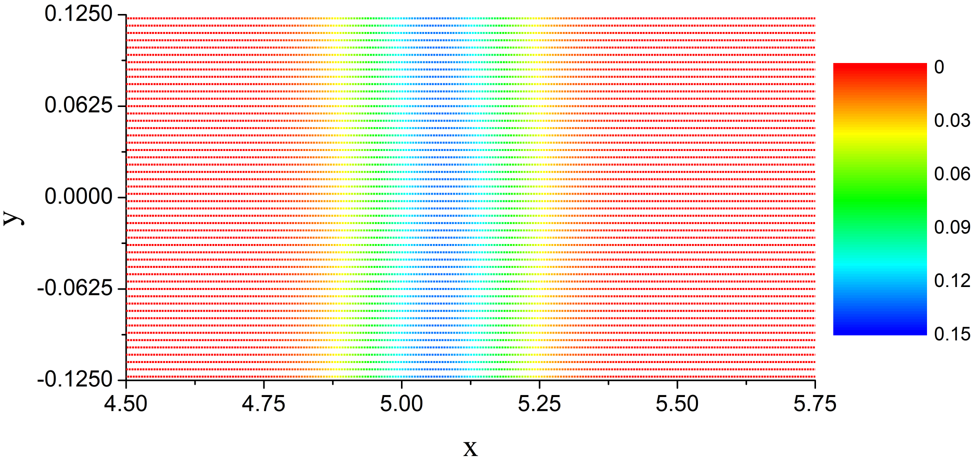

Figure 6.5: Test Case 2: Concentration field for species C across the discontinuity at time $t' = 1$. Notice that the x (dimensional) axis range is smaller than in Fig. 6.4

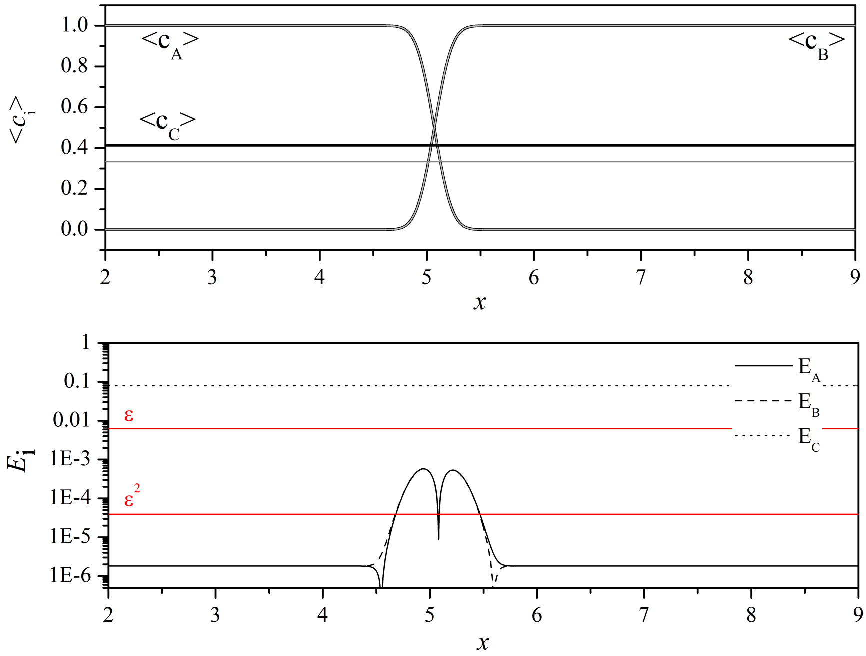

Figure 6.6: Test Case 3: Comparison of the longitudinal profiles of $\langle c_i \rangle$ and errors $E_i = |\langle c_i \rangle_{\text{mic}} - \langle c_i \rangle_{\text{mac}}|$ computed as the difference between the averaged microscale solution and the solution of the macroscale problem. $\langle c_i \rangle_{\text{mic}}$ is represented with thick black lines, whereas $\langle c_i \rangle_{\text{mac}}$ is represented with thinner grey lines in the upper panel. The parameters of this test case ($\alpha = 1, \beta = -1, \gamma = 0, \delta = 0$) do not belong to the homogenizability region, because of a fast heterogeneous reaction. The reference dimensional time is $t' = 1$. The x axis is in dimensional form.

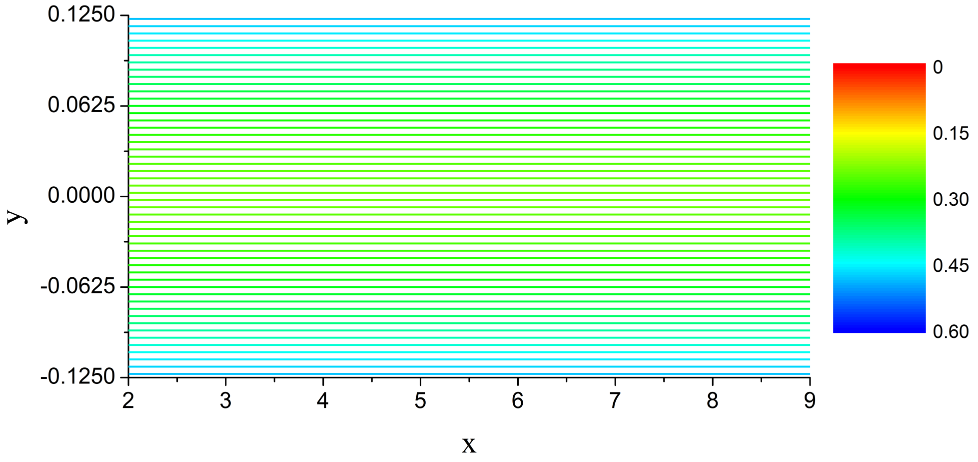

Figure 6.7: Test Case 3: Concentration field for species C across the discontinuity at time $t' = 1$. The x axis is in dimensional form.

6.5 Implications for the numerical solution of reactive transport at the Darcy scale

The multi-scale expansion procedure applied to a reactive system which includes both homogeneous and heterogeneous kinetic reactions provides a set of sufficient conditions which identifies the region within the flow and transport domain where the upscaling of the pore-scale equations to an adequate continuum scale is possible. The microscale and the macroscale need to be sufficiently separated in terms of order of magnitude. In this region the pore-scale and the upscaled equations can be decoupled, that is, the effective coefficients that we need in the upscaled equations can be determined a-priori from the solution of a single pore-scale problem on a unit cell. The periodic solution of this boundary value problem depends only on the geometry of the unit cell, and not on the solution of the upscaled problem, as could happen instead outside the homogenizability region. The boundaries of the 4D homogenizability region are stated in terms of four dimensionless numbers, which express the characteristics of reactive transport.

In the previous chapters, and in particular in Chapter 5, we modeled upscaled bimolecular reactive processes in a variety of conditions. We considered:

1. bimolecular homogeneous equilibrium reaction $\mathrm{A} + \mathrm{B} \overset{\mathrm{eq}}{\rightleftharpoons} \mathrm{C}$;
2. bimolecular heterogeneous equilibrium reaction $\mathrm{A} + \mathrm{B} \overset{\mathrm{eq}}{\rightleftharpoons} \mathrm{C}\downarrow$;
3. bimolecular kinetically-controlled reaction $\mathrm{A} + \mathrm{B} \overset{\mathrm{kin}}{\rightleftharpoons} \mathrm{C}\downarrow$.

All these reactive mechanisms can be traced back to the bimolecular reactive mechanism at the pore-scale described in this chapter as special cases.

Case 1 for example neglects the precipitation/dissolution part of the reaction, whereas

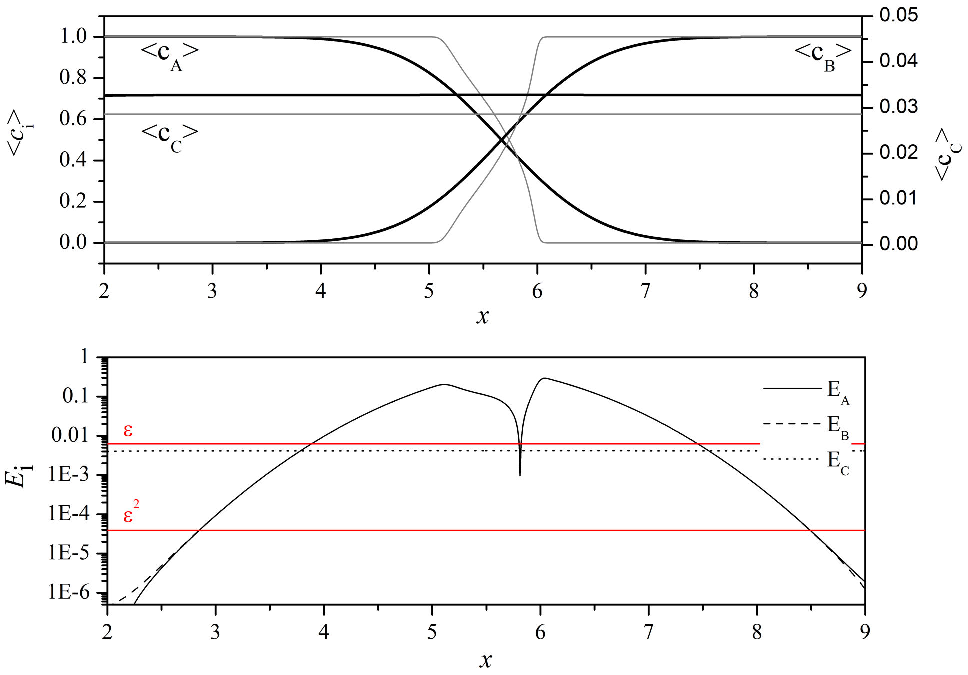

Figure 6.8: Test Case 4: Comparison of the longitudinal profiles of $\langle c_i \rangle$ and errors $E_i = |\langle c_i \rangle_{\mathrm{mic}} - \langle c_i \rangle_{\mathrm{mac}}|$ computed as the difference between the averaged microscale solution and the solution of the macroscale problem. $\langle c_i \rangle_{\mathrm{mic}}$ is represented with thick black lines, whereas $\langle c_i \rangle_{\mathrm{mac}}$ is represented with thinner grey lines in the upper panel. The parameters of this test case ($\alpha = 2, \beta = -1, \gamma = -1, \delta = -1$) do not belong to the homogenizability region, mainly because of strong advection. The reference dimensional time is $t' = 10$. The x axis is in dimensional form.

both Cases 2 and 3 neglect the intermediate step involving species C. For the equilibrium cases (Cases 1 and 2) we can take advantage of the widely used algebraic simplification, which holds only if the concentration can be considered well-mixed over the reference macroscale volume (Li, Peters, and Celia, 2006; Lichtner and Kang, 2007; Steefel, DePaolo, and Lichtner, 2005). As we can see here, this is not always guaranteed, and pseudokinetic effects can arise.

We need to compare the dimensionless numbers which characterize our simulations with the limits identified in this Chapter. In all cases, given our choice of initial conditions, the limits which apply are the ones posed on the Peclet number and on the Damköhler number which governs the homogeneous reaction $A + B \rightarrow C$, that is:

$$\mathrm{Pe} = \frac{U'L}{D'_m} < \varepsilon^{-2}$$

$$\mathrm{Da} = \frac{L^2}{D'_m T''_r} < \varepsilon^{-2}$$

where L is the macro-lengthscale, U' is the reference velocity, D'_m is the molecular diffusion coefficient and T''_r is the timescale of the reaction. We need to compute the

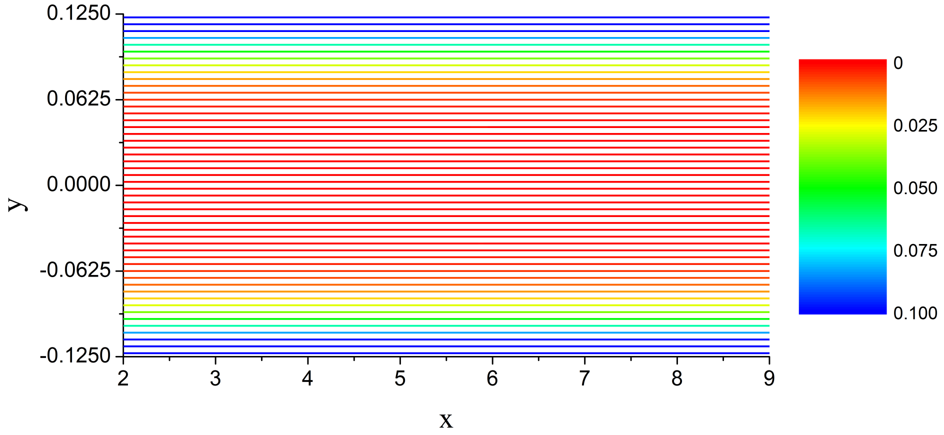

Figure 6.9: Test Case 4: Concentration field for species C across the discontinuity at time $t' = 10$. The x axis is in dimensional form.

reference Pe and Da numbers for our macroscale numerical simulations coherently with the formulations used in the present chapter. In the previous chapters we used the value of dispersion rather than the value of molecular diffusion for computing the timescale of the diffusive/dispersive processes. On the contrary, the reaction timescale is the same. In Table 6.2 we compare the dimensionless numbers of the simulations and the limits identified by the multiscale analysis. In order to assign a value to the limits, we choose a reasonable value for ε, coherent with the reference dimensional quantities which govern our transport scenarios: $\varepsilon = 10^{-3}$.

In all kinetically controlled cases both limits are respected. The largest Pe and Da numbers considered are of the order of ε^1, so upscaling is allowed as well as the well-mixed REV hypothesis used for the numerical simulations. Clearly, the instantaneous reaction case does not respect the upscaling conditions, because $\mathrm{Da} = \infty$. However, our numerical simulations show that there is no big difference between the numerical results for $\mathrm{Da} = 100$ and $\mathrm{Da} = \infty$ (see Ch. 5), thus indirectly validating the numerical results obtained for the instantaneous injection case. Besides, it is necessary to note that the limits obtained by the multiscale analysis are sufficient conditions, thus, as evidenced also by the test cases in the previous section, it is possible that scenarios located outside the homogenizability region work reasonably well. However, these results act as a warning against the careless use of algebraic manipulation (see e.g. De Simoni *et al.*, 2005, 2007; Rubin, 1983), which could result in erroneous prediction of transport and reaction rates in particular transport conditions.

6.6 Conclusions

The balance between the timescales of the physical and chemical processes, which lead fate and transport of chemicals in porous formations, influences the possibility

Table 6.2: Comparison of the homogenizability conditions and the numerical parameters used in the numerical simulations. The first column identifies the reference dimensionless parameters of transport: Peclet and Damköhler. The second column refers to the homogenizability threshold, below which it is guaranteed the decoupling between the microscale and the macroscale; we used $\varepsilon = 10^{-3}$. The third column lists the dimensionless parameters used in the equilibrium and kinetic simulations of Chapter 5; all simulations share the same Pe number, but different Da which cover several orders of magnitude. The last column expresses the same dimensionless numbers in terms of dispersion rather than molecular diffusion, in order to be coherent with the definition of Pe and Da used in the previous chapter; hence it expresses the correspondence between the symbols used in this chapter and the ones used in the previous chapter.

Parameter	Homogenizability Condition	Correspondent Sim. Parameter	Original Sim. Parameter
Pe	10^6	$3.\bar{3} \cdot 10^3$	10^3
Da	10^6	$3.\bar{3} \cdot 10^{-1}$	0.1
		$3.\bar{3} \cdot 10^0$	1
		$3.\bar{3} \cdot 10^1$	10
		$3.\bar{3} \cdot 10^2$	100
		∞	∞

to upscale pore-scale transport equations to a continuum scale. Upscaled equations in fact introduce effective coefficients which epitomize sub-scale effects relying on several assumptions which cannot be always verified a-priori. We focused here on a precipitation/dissolution reactive system $A + B \leftrightharpoons C \leftrightharpoons C \downarrow$ which includes both homogeneous mixing-controlled reactions ($A + B \leftrightharpoons C$) and heterogeneous reactions ($C \leftrightharpoons C \downarrow$), which occur across solid-liquid interfaces. The timescales of the involved processes (i.e. advection, molecular diffusion and four reactions) can be expressed through four dimensionless Peclet and Damköhler numbers. We performed the upscaling via a multiple-scale expansion procedure, and we individuated a set of sufficient conditions for the upscaling as a function of the dimensionless Pe and Da numbers, which are expressed as powers of a lengthscale ratio parameter $\varepsilon = \ell/L$, comparing the microscale ℓ (pore-scale) and the macroscale L of the formation. Such a set of conditions delimits a safe homogenizability region in a 4D phase diagram, where we provided a definite shape for the upscaled transport equations which results to be decoupled from the solution of transport at the pore-scale. Outside this region, resorting to different upscaled representations of transport is needed, because of the coupling between the microscale and the macroscale. The obtained limits are coherent with the results of Battiato *et al.*, 2009, in the absence of advection, and with the limits individuated by Auriault and Adler, 1995, in the absence of reactions. We obtained more severe conditions for the heterogeneous reaction and for advection than for the homogeneous reactions, since the former are the main cause of localized phenomena. In fact homogeneous reactions are less demanding, since apparently once it is guaranteed that the Peclet number is low enough, concentration gradients cannot be so high, and when they are (for example for a discontinuous initial conditions), diffusion smoothens them out in a reasonable time, so that mixing-controlled reactions do not suffer segregation effects. However instantaneous or equilibrium reactions do not belong to the homogenizability region. These results thus warn to use consciously the algebraic simplification procedures which rely on the assumption of fast reactions, so that the complexity of the problem can be reduced to the numerical solution of conservative transport equations. Although upscaled equations could work well in the non-reactive case (provided low enough Peclet values), this is not guaranteed once also reactions are implied. Relying on the conservative transport results and on the well-mixed hypothesis over the REV could result in the overestimation of dilution and thus of reaction rates.

6.7 Appendix A: Upscaling Pore-Scale Transport Differential System by Multiple Scale Expansion

6.7.1 Orders of magnitude

Substituting 6.3.1 and 6.20 into the original dimensionless system 6.15 we obtain the following equations for species $i = A, B$:

$$\begin{aligned}&\frac{\partial c_i}{\partial t} + \mathrm{Pe}\frac{\partial c_i}{\partial \tau_a} + \mathrm{Da}'\frac{\partial c_i}{\partial \tau_r'} + \mathrm{Da}''\frac{\partial c_i}{\partial \tau_r''} + \mathrm{Da}'''\frac{\partial c_i}{\partial \tau_r'''} + \nabla_x \cdot \left[-\mathbf{D}_i\left(\nabla_x c_i + \varepsilon^{-1}\nabla_y c_i\right)\right.\\ &\left.+\mathrm{Pe}\ \mathbf{v}c_i\right] + \varepsilon^{-1}\nabla_y \cdot \left[-\mathbf{D_i}\left(\nabla_x c_i + \varepsilon^{-1}\nabla_y c_i\right) + \mathrm{Pe}\ \mathbf{v}c_i\right] = -\mathrm{Da}'' c_A c_B + \mathrm{Da}''' c_C \end{aligned} \tag{6.43}$$

$$-\,\mathbf{n}\cdot\left[\mathbf{D}_i\left(\nabla_x c_i + \varepsilon^{-1}\nabla_y c_i\right)\right] = 0, \qquad \text{on } \Gamma \tag{6.44}$$

and for species C:

$$\begin{aligned}&\frac{\partial c_C}{\partial t} + \mathrm{Pe}\frac{\partial c_C}{\partial \tau_a} + \mathrm{Da}'\frac{\partial c_C}{\partial \tau_r'} + \mathrm{Da}''\frac{\partial c_C}{\partial \tau_r''} + \mathrm{Da}'''\frac{\partial c_C}{\partial \tau_r'''} + \nabla_x \cdot \left[-\mathbf{D}_C\left(\nabla_x c_C + \varepsilon^{-1}\nabla_y c_C\right)\right.\\ &\left.+\ \mathrm{Pe}\ \mathbf{v}c_C\right] + \varepsilon^{-1}\nabla_y \cdot \left[-\mathbf{D_C}\left(\nabla_x c_C + \varepsilon^{-1}\nabla_y c_C\right) + \mathrm{Pe}\ \mathbf{v}c_C\right] = +\mathrm{Da}'' c_A c_B - \mathrm{Da}''' c_C \end{aligned} \tag{6.45}$$

$$-\,\mathbf{n}\cdot\left[\mathbf{D}_i\left(\nabla_x c_i + \varepsilon^{-1}\nabla_y c_i\right)\right] = \mathrm{Da}'\left(c_C^a - \bar{c}^a\right), \qquad \text{on } \Gamma \tag{6.46}$$

Substituting into Eq. 6.43 and 6.45 the following expansions for the unknowns c^i and $\mathbf{v}$:

$$c^i(\mathbf{x},\mathbf{y},t,\tau_a,\tau_r',\tau_r'',\tau_r''') = \sum_{m=0}^{\infty} \varepsilon^m c_m^i(\mathbf{x},\mathbf{y},t,\tau_a,\tau_r',\tau_r'',\tau_r'''), \quad i = A, B, C \tag{6.47}$$

$$\mathbf{v}(\mathbf{x},\mathbf{y},t,\tau_a,\tau_r',\tau_r'',\tau_r''') = \sum_{m=0}^{\infty} \varepsilon^m \mathbf{v_m}(\mathbf{x},\mathbf{y},t,\tau_a,\tau_r',\tau_r'',\tau_r''') \tag{6.48}$$

where the terms c_m and $\mathbf{v_m}$ are periodic on the unit cell $\mathcal{Y}$, we obtain for species$A$ and B:

$$
\begin{array}{ll}
\varepsilon^{-2} & \Big\{\nabla_y \cdot \left(-\mathbf{D}\nabla_y c_0 + \varepsilon^{1-\alpha} c_0 \mathbf{v_0}\right) + \varepsilon^{2+\gamma}\left(\frac{\partial c_0}{\partial \tau_r''} + c_{0,A}c_{0,B}\right) + \varepsilon^{2+\delta}\left(\frac{\partial c_0}{\partial \tau_r'''} - c_{0,C}\right)\Big\} \\
+\varepsilon^{-1} & \Big\{ - \nabla_x \cdot \mathbf{D}\nabla_y c_0 - \nabla_y \cdot \mathbf{D}\left(\nabla_y c_1 + \nabla_x c_0\right) + \varepsilon^{1-\alpha}\Big[\frac{\partial c_0}{\partial \tau_a} + \varepsilon^{\alpha+\beta}\frac{\partial c_0}{\partial \tau_r'} \\
\multicolumn{2}{l}{\qquad\qquad + \nabla_x \cdot (c_0\mathbf{v_0}) + \nabla_y \cdot (c_1\mathbf{v_0} + c_0\mathbf{v_1})] + \varepsilon^{2+\gamma}\Big[\frac{\partial c_1}{\partial \tau_r''} + c_{0,A}c_{1,B} + c_{1,A}c_{0,B}\Big]} \\
\multicolumn{2}{l}{\qquad\qquad + \varepsilon^{2+\delta}\Big[\frac{\partial c_1}{\partial \tau_r'''} - c_{1,C}\Big]\Big\}} \\
+\varepsilon^0 & \{\frac{\partial c_0}{\partial t} - \nabla_x \cdot \mathbf{D}\left(\nabla_x c_0 + \nabla_y c_1\right) - \nabla_y \cdot \mathbf{D}\left(\nabla_x c_1 + \nabla_y c_2\right) \\
\multicolumn{2}{l}{\qquad\qquad +\varepsilon^{1-\alpha}\Big[\frac{\partial c_1}{\partial \tau_a} + \varepsilon^{\alpha+\beta}\frac{\partial c_1}{\partial \tau_r'} + \nabla_x \cdot (c_1\mathbf{v0} + c_0\mathbf{v_1}) + \nabla_y \cdot (c_1\mathbf{v_1} + c_0\mathbf{v_2} + c_2\mathbf{v_0})\Big]} \\
\multicolumn{2}{l}{\qquad\qquad + \varepsilon^{2+\gamma}\Big[\frac{\partial c_2}{\partial \tau_r''} + c_{0,A}c_{2,B} + c_{0,B}c_{2,A} + c_{1,A}c_{1,B}\Big] + \varepsilon^{2+\delta}\Big[\frac{\partial c_2}{\partial \tau_r'''} - c_{2,C}\Big]\ \Big\}} \\
= \mathcal{O}(\varepsilon) &
\end{array}
\tag{6.49}
$$

with the boundary condition:

$$
\begin{aligned}
&\varepsilon^{-1}\left[-\mathbf{n} \cdot \mathbf{D}\nabla_y c_0\right] \\
&+\varepsilon^{0}\left[-\mathbf{n} \cdot \mathbf{D}\left(\nabla_x c_0 + \nabla_y c_1\right)\right] \\
&+\varepsilon^{1}\left[-\mathbf{n} \cdot \mathbf{D}\left(\nabla_x c_1 + \nabla_y c_2\right)\right] = \mathcal{O}\left(\varepsilon^2\right)
\end{aligned}
\tag{6.50}
$$

and for species C:

$$
\begin{array}{ll}
\varepsilon^{-2} & \Big\{\nabla_y \cdot \left(-\mathbf{D}\nabla_y c_0 + \varepsilon^{1-\alpha} c_0 \mathbf{v_0}\right) + \varepsilon^{2+\gamma}\left(\frac{\partial c_0}{\partial \tau_r''} - c_{0,A}c_{0,B}\right) + \varepsilon^{2+\delta}\left(\frac{\partial c_0}{\partial \tau_r'''} + c_{0,C}\right)\Big\} \\
+\varepsilon^{-1} & \Big\{-\nabla_x \cdot \mathbf{D}\nabla_y c_0 - \nabla_y \cdot \mathbf{D}\left(\nabla_y c_1 + \nabla_x c_0\right) + \varepsilon^{1-\alpha}\Big[\frac{\partial c_0}{\partial \tau_a} + \varepsilon^{\alpha+\beta}\frac{\partial c_0}{\partial \tau_r'} + \nabla_x \cdot (c_0\mathbf{v_0}) \\
\multicolumn{2}{l}{\qquad\qquad +\nabla_y \cdot (c_1\mathbf{v_0} + c_0\mathbf{v_1})] + \varepsilon^{2+\gamma}\Big[\frac{\partial c_1}{\partial \tau_r''} - c_{0,A}c_{1,B} - c_{1,A}c_{0,B}\Big]} \\
\multicolumn{2}{l}{\qquad\qquad + \varepsilon^{2+\delta}\Big[\frac{\partial c_1}{\partial \tau_r'''} + c_{1,C}\Big]\Big\}} \\
+\varepsilon^0 & \Big\{\frac{\partial c_0}{\partial t} - \nabla_x \cdot \mathbf{D}\left(\nabla_x c_0 + \nabla_y c_1\right) - \nabla_y \cdot \mathbf{D}\left(\nabla_x c_1 + \nabla_y c_2\right) \\
\multicolumn{2}{l}{\qquad\qquad +\varepsilon^{1-\alpha}\Big[\frac{\partial c_1}{\partial \tau_a} + \varepsilon^{\alpha+\beta}\frac{\partial c_1}{\partial \tau_r'} + \nabla_x \cdot (c_1\mathbf{v0} + c_0\mathbf{v_1}) + \nabla_y \cdot (c_1\mathbf{v_1} + c_0\mathbf{v_2} + c_2\mathbf{v_0})\Big]} \\
\multicolumn{2}{l}{\qquad\qquad + \varepsilon^{2+\gamma}\Big[\frac{\partial c_2}{\partial \tau_r''} - c_{0,A}c_{2,B} - c_{0,B}c_{2,A} - c_{1,A}c_{1,B}\Big] + \varepsilon^{2+\delta}\Big[\frac{\partial c_2}{\partial \tau_r'''} + c_{2,C}\Big]\Big\}} \\
= \mathcal{O}(\varepsilon) &
\end{array}
\tag{6.51}
$$

with the boundary condition:

$$
\begin{array}{ll}
\varepsilon^{-1} & \left[-\mathbf{n} \cdot \mathbf{D}\nabla_y c_0\right] \\
+\varepsilon^{0} & \left[-\mathbf{n} \cdot \mathbf{D}\left(\nabla_x c_0 + \nabla_y c_1\right) - \varepsilon^{\beta}\left(c_0^a - \bar{c}^a\right)\right] \\
+\varepsilon^{1} & \left[-\mathbf{n} \cdot \mathbf{D}\left(\nabla_x c_1 + \nabla_y c_2\right) - \varepsilon^{\beta} a c_0^{a-1} c_1\right] = \mathcal{O}\left(\varepsilon^2\right)
\end{array}
\tag{6.52}
$$

Such a subdivision of the orders of magnitude is implied by the necessity to find the stricter condition for which microscale and macroscale can be decoupled.

6.7.2 Terms of order $\mathcal{O}(\varepsilon^{-2})$

Next we need to separate the microscale equations by order of magnitude, and consider each level separately. Considering the terms of order $\mathcal{O}(\varepsilon^{-2})$ we obtain for species A and B:

$$\nabla_y \cdot \left(-\mathbf{D}\nabla_y c_0 + \varepsilon^{1-\alpha} c_0 \mathbf{v_0}\right) + \varepsilon^{2+\gamma}\left(\frac{\partial c_0}{\partial \tau_r''} + c_{0,\mathrm{A}} c_{0,\mathrm{B}}\right) + \varepsilon^{2+\delta}\left(\frac{\partial c_0}{\partial \tau_r'''} - c_{0,\mathrm{C}}\right) = 0 \tag{6.53}$$

and for species C:

$$\nabla_y \cdot \left(-\mathbf{D}\nabla_y c_0 + \varepsilon^{1-\alpha} c_0 \mathbf{v_0}\right) + \varepsilon^{2+\gamma}\left(\frac{\partial c_0}{\partial \tau_r''} - c_{0,\mathrm{A}} c_{0,\mathrm{B}}\right) + \varepsilon^{2+\delta}\left(\frac{\partial c_0}{\partial \tau_r'''} + c_{0,\mathrm{C}}\right) = 0 \tag{6.54}$$

and the same analytical shape for the boundary condition for all species:

$$-\mathbf{n} \cdot \mathbf{D}\nabla_y c_0 = 0, \qquad \text{on } \Gamma \tag{6.55}$$

Since both the Partial Differential Equation System (Eq. 6.53 and 6.54) and the Boundary Conditions (Eq. 6.55) are homogeneous, the Neumann type boundary conditions ensure that $\nabla_y c_0 = 0$, that is, c_0 does not depend on $\mathbf{y}$:

$$c_0 = c_0 \left\{\mathbf{x}, t, \tau_a, \tau_r', \tau_r'', \tau_r'''\right\}$$

6.7.3 Terms of order $\mathcal{O}(\varepsilon^{-1})$

In order to investigate the relation between the microscale and the macroscale let us consider the terms of order ε^{-1}. For the sake of shortness, the following relations are valid for species A, B, and C; the only difference is given by the sign of the homogeneous reaction terms. Lower signs refer to species A and B, whereas upper signs refer to species C.

$$\begin{aligned} &-\nabla_x \cdot (\mathbf{D}\nabla_y c_0) - \nabla_y \cdot \mathbf{D}\left(\nabla_y c_1 + \nabla_x c_0\right) \\ &+\varepsilon^{1-\alpha}\left[\frac{\partial c_0}{\partial \tau_a} + \varepsilon^{\alpha+\beta}\frac{\partial c_0}{\partial \tau_r'} + \nabla_x \cdot (c_0 \mathbf{v_0}) + \nabla_y \cdot (c_1 \mathbf{v_0} + \mathbf{v_1} c_0)\right] \\ &+\varepsilon^{2+\gamma}\left[\frac{\partial c_1}{\partial \tau_r''} \pm (c_{0,A} c_{1,B} + c_{1,A} c_{0,B})\right] + \varepsilon^{2+\delta}\left[\frac{\partial c_1}{\partial \tau_r'''} \mp c_{1,C}\right] = 0 \end{aligned} \tag{6.56}$$

with the following boundary conditions for species A and B:

$$-\mathbf{n} \cdot \mathbf{D}\left(\nabla_x c_0 + \nabla_y c_1\right) = 0, \qquad \text{on } \Gamma \tag{6.57}$$

and for species C:

$$-\mathbf{n} \cdot \mathbf{D}\left(\nabla_x c_0 + \nabla_y c_1\right) = \varepsilon^{\beta}\left(c_0^a - \bar{c}^a\right), \qquad \text{on } \Gamma \tag{6.58}$$

Then integrating equation 6.56 over $\mathcal{B}$, which is the liquid volume of the unit cell $\mathcal{Y}$, and considering the boundary conditions 6.57 and 6.58, the no-slip boundary condition along Γ and that $\nabla_y c_0 = 0$, we obtain for species A and B:

$$\begin{aligned} &\varepsilon^{1-\alpha}\tfrac{\partial c_0}{\partial \tau_a} + \varepsilon^{1+\beta}\tfrac{\partial c_0}{\partial \tau_r'} = -\varepsilon^{1-\alpha}\nabla_x \cdot (c_0 \langle \mathbf{v_0} \rangle_{\mathcal{B}}) - \varepsilon^{2+\gamma}\left[\tfrac{\partial \langle c_1 \rangle_{\mathcal{B}}}{\partial \tau_r''} + c_{0,A}\langle c_{1,B}\rangle_{\mathcal{B}}\right. \\ &\left. + c_{0,\mathrm{B}}\langle c_{1,\mathrm{A}}\rangle_{\mathcal{B}}\right] - \varepsilon^{2+\delta}\left[\tfrac{\partial \langle c_1 \rangle_{\mathcal{B}}}{\partial \tau_r'''} - \langle c_{1,C}\rangle_{\mathcal{B}}\right] \end{aligned} \tag{6.59}$$

and for species C:

$$\varepsilon^{1-\alpha}\frac{\partial c_0}{\partial \tau_a}+\varepsilon^{1+\beta}\frac{\partial c_0}{\partial \tau_r'}=-\varepsilon^{1-\alpha}\nabla_x\cdot\left(c_0\left\langle \mathbf{v_0}\right\rangle_{\mathcal{B}}\right)-\varepsilon^{\beta}K^*\left(c_0^a-\bar{c}^a\right)-\varepsilon^{2+\gamma}\left[\frac{\partial\langle c_1\rangle_{\mathcal{B}}}{\partial \tau_r''}\right. \\ \left.-c_{0,A}\left\langle c_{1,B}\right\rangle_{\mathcal{B}}-c_{0,B}\left\langle c_{1,A}\right\rangle_{\mathcal{B}}\right]-\varepsilon^{2+\delta}\left[\frac{\partial\langle c_1\rangle_{\mathcal{B}}}{\partial \tau_r'''}+\left\langle c_{1,C}\right\rangle_{\mathcal{B}}\right] \tag{6.60}$$

where $K^*=\frac{|\Gamma|}{|\mathcal{B}|}$ is an effective parameter which depends on the geometry of the unit cell.

Then combining 6.56 and 6.59 for species A and B, and 6.56 and 6.60 for species C, and considering that $\nabla_y\cdot\mathbf{v_0}=0$, $\nabla_x\cdot\langle\mathbf{v_0}\rangle_{\mathcal{B}}=0$, $\nabla_y\cdot\mathbf{v_1}+\nabla_x\cdot\mathbf{v_0}=0$ (Auriault and Adler, 1995) and $\nabla_y c_0=0$, we obtain the following boundary value problems for species A and B:

$$\begin{aligned}&-\nabla_y\cdot\mathbf{D}\left(\nabla_y c_1+\nabla_x c_0\right)+\varepsilon^{1-\alpha}\left[\left(\mathbf{v_0}-\langle\mathbf{v_0}\rangle_{\mathcal{B}}\right)\cdot\nabla_x c_0+\mathbf{v_0}\cdot\nabla_y c_1\right]\\&+\varepsilon^{2+\gamma}\left[\frac{\partial}{\partial\tau_r''}\left(c_1-\langle c_1\rangle_{\mathcal{B}}\right)+c_{0,A}\left(c_{1,B}-\langle c_{1,B}\rangle_{\mathcal{B}}\right)+c_{0,B}\left(c_{1,A}-\langle c_{1,A}\rangle_{\mathcal{B}}\right)\right]\\&+\varepsilon^{2+\delta}\left[\frac{\partial}{\partial\tau_r'''}\left(c_1-\langle c_1\rangle_{\mathcal{B}}\right)-c_{1,C}+\langle c_{1,C}\rangle_{\mathcal{B}}\right]=0,\quad\text{in }\mathcal{B}\end{aligned}\tag{6.61a}$$

$$-\mathbf{n}\cdot\mathbf{D}\left(\nabla_x c_0+\nabla_y c_1\right)=0,\qquad\text{on }\Gamma\tag{6.61b}$$

and for species C:

$$\begin{aligned}&-\nabla_y\cdot\mathbf{D}\left(\nabla_y c_1+\nabla_x c_0\right)+\varepsilon^{1-\alpha}\left[\left(\mathbf{v_0}-\langle\mathbf{v_0}\rangle_{\mathcal{B}}\right)\cdot\nabla_x c_0+\mathbf{v_0}\cdot\nabla_y c_1\right.\\&+\varepsilon^{2+\gamma}\left[\frac{\partial}{\partial\tau_r''}\left(c_1-\langle c_1\rangle_{\mathcal{B}}\right)-c_{0,A}\left(c_{1,B}-\langle c_{1,B}\rangle_{\mathcal{B}}\right)-c_{0,B}\left(c_{1,A}-\langle c_{1,A}\rangle_{\mathcal{B}}\right)\right]\\&+\varepsilon^{2+\delta}\left[\frac{\partial}{\partial\tau_r'''}\left(c_1-\langle c_1\rangle_{\mathcal{B}}\right)+c_{1,C}-\langle c_{1,C}\rangle_{\mathcal{B}}\right]-\varepsilon^{\alpha+\beta-1}K^*\left(c_0^a-\bar{c}^a\right)=0\end{aligned}\tag{6.62a}$$

$$-\mathbf{n}\cdot\mathbf{D}\left(\nabla_x c_0+\nabla_y c_1\right)=\varepsilon^{\beta}\left(c_0^a-\bar{c}^a\right),\qquad\text{on }\Gamma\tag{6.62b}$$

The boundary value problems can be manipulated by considering that the first order term c_1 in the expansion of the unknown concentration c has the form:

$$c_1(\mathbf{x},\mathbf{y},t,\tau_a,\tau_r',\tau_r'',\tau_r''')=\boldsymbol{\chi}\left(\mathbf{y}\right)\cdot\nabla_x c_0(\mathbf{x},t,\tau_a,\tau_r',\tau_r'',\tau_r''')+\bar{c}_1(\mathbf{x},t,\tau_a,\tau_r',\tau_r'',\tau_r''')\tag{6.63}$$

thanks to the linearity of the partial differential transport equation. In Eq. 6.63 the dependence upon $\mathbf{y}$ is isolated in the closure variable $\boldsymbol{\chi}$, which is modulated by the macroscale forcing $\nabla_x c_0$ and summed to the macroscale variable $\bar{c}_1$.
Thanks to 6.63, we can write:

$$c_1\left(\mathbf{x},\mathbf{y},t,\tau_a,\tau_r',\tau_r'',\tau_r'''\right)-\left\langle c_1\left(\mathbf{x},\mathbf{y},t,\tau_a,\tau_r',\tau_r'',\tau_r'''\right)\right\rangle_{\mathcal{B}}=\boldsymbol{\chi}\left(\mathbf{y}\right)\cdot\nabla_x c_0\tag{6.64}$$

Then the boundary value problems read for species A and B:

$$\begin{aligned}&\left[-\nabla_y\cdot\mathbf{D}\left(\nabla_y\boldsymbol{\chi}\left(\mathbf{y}\right)+\mathbf{I}\right)+\varepsilon^{1-\alpha}\mathbf{v_0}\cdot\nabla_y\boldsymbol{\chi}\right]\cdot\nabla_x c_0\\&+\varepsilon^{2+\gamma}\left[\frac{\partial}{\partial\tau_r''}\left(\boldsymbol{\chi}\left(\mathbf{y}\right)\cdot\nabla_x c_0\right)+c_{0,A}\left(\boldsymbol{\chi}_B(\mathbf{y})\cdot\nabla_x c_{0,B}\right)+c_{0,B}\left(\boldsymbol{\chi}_A(\mathbf{y})\cdot\nabla_x c_{0,A}\right)\right]\\&+\varepsilon^{2+\delta}\left[\frac{\partial}{\partial\tau_r'''}\left(\boldsymbol{\chi}(\mathbf{y})\cdot\nabla_x c_0\right)-\boldsymbol{\chi}_C(\mathbf{y})\cdot\nabla_x c_{0,C}\right]=\varepsilon^{1-\alpha}\left(\langle\mathbf{v_0}\rangle_{\mathcal{B}}-\mathbf{v_0}\right)\cdot\nabla_x c_0\end{aligned}\tag{6.65a}$$

$$-\left[\mathbf{n}\cdot\mathbf{D}\left(\nabla_y\boldsymbol{\chi}\left(\mathbf{y}\right)+\mathbf{I}\right)\right]\cdot\nabla_x c_0 = 0, \qquad \text{on } \Gamma \tag{6.65b}$$

and for species C:

$$\begin{aligned}&\left[-\nabla_y\cdot\mathbf{D}\left(\nabla_y\boldsymbol{\chi}\left(\mathbf{y}\right)+\mathbf{I}\right)+\varepsilon^{1-\alpha}\mathbf{v_0}\cdot\nabla_y\boldsymbol{\chi}\right]\cdot\nabla_x c_0-\varepsilon^{\beta}K^*\left(c_0^a-\bar{c}^a\right)\\&+\varepsilon^{2+\gamma}\left[\frac{\partial}{\partial\tau_r''}\left(\boldsymbol{\chi}\left(\mathbf{y}\right)\cdot\nabla_x c_0\right)-c_{0,A}\left(\boldsymbol{\chi}_B(\mathbf{y})\cdot\nabla_x c_{0,B}\right)-c_{0,B}\left(\boldsymbol{\chi}_A(\mathbf{y})\cdot\nabla_x c_{0,A}\right)\right]\\&+\varepsilon^{2+\delta}\left[\frac{\partial}{\partial\tau_r'''}\left(\boldsymbol{\chi}(\mathbf{y})\cdot\nabla_x c_0\right)+\boldsymbol{\chi}_C(\mathbf{y})\cdot\nabla_x c_{0,C}\right]=\varepsilon^{1-\alpha}\left(\langle\mathbf{v_0}\rangle_{\mathcal{B}}-\mathbf{v_0}\right)\cdot\nabla_x c_0\end{aligned} \tag{6.66a}$$

$$-\left[\mathbf{n}\cdot\mathbf{D}\left(\nabla_y\boldsymbol{\chi}+\mathbf{I}\right)\right]\cdot\nabla_x c_0=\varepsilon^{\beta}\left(c_0^a-\bar{c}^a\right), \qquad \text{on } \Gamma \tag{6.66b}$$

In general, these boundary value problems express the coupling between the microscale and macroscale solutions of the transport problem. In fact the solution of the boundary value problem within $\mathcal{Y}$ depends on the solution of the macroscale problem through c_0 and $\nabla_x c_0$. If the terms which depend on the macroscale were negligible, the microscale boundary value problem could be decoupled from the macroscale solution. In such conditions, we would have the means for obtaining the effective coefficients neglecting the coupling between the microscale and the macroscale systems. This happens if the following conditions are fulfilled:

I. $\alpha < 2$

II. $\beta > 0$

III. $\beta > \max\{0, 1-\alpha\}$

IV. $2+\gamma > \max\{0; 1-\alpha\}$

V. $2+\delta > \max\{0; 1-\alpha\}$

These constraints determine a homogeneizability region in a 4D phase diagram, whose axes are the dimensionless numbers which characterize reactive transport: $\mathrm{Pe}=\varepsilon^{-\alpha}$, $\mathrm{Da}'=\varepsilon^{\beta}$, $\mathrm{Da}''=\varepsilon^{\gamma}$, $\mathrm{Da}'''=\varepsilon^{\delta}$.

6.7.4 Terms of order $\mathcal{O}(\varepsilon^0)$

If the homogenizability conditions are fulfilled, we can determine a macroscale version of the transport system by considering the terms of order ε^0. Isolating the $\mathcal{O}(\varepsilon^0)$ terms for species A and B we obtain:

$$\begin{aligned}&\frac{\partial c_0}{\partial t}-\nabla_x\cdot\mathbf{D}\left(\nabla_x c_0+\nabla_y c_1\right)-\nabla_y\cdot\mathbf{D}\left(\nabla_x c_1+\nabla_y c_2\right)\\&+\varepsilon^{1-\alpha}\left[\frac{\partial c_1}{\partial\tau_a}+\varepsilon^{\alpha+\beta}\frac{\partial c_1}{\partial\tau_r'}+\nabla_x\cdot\left(c_1\mathbf{v_0}+c_0\mathbf{v_1}\right)+\nabla_y\cdot\left(c_1\mathbf{v_1}+c_0\mathbf{v_2}+c_2\mathbf{v_0}\right)\right]\\&+\varepsilon^{2+\gamma}\left[\frac{\partial c_2}{\partial\tau_r''}+c_{0,A}c_{2,B}+c_{0,B}c_{2,A}+c_{1,A}c_{1,B}\right]+\varepsilon^{2+\delta}\left[\frac{\partial c_2}{\partial\tau_r'''}-c_{2,C}\right]=0\end{aligned} \tag{6.67a}$$

$$-\mathbf{n}\cdot\mathbf{D}\left(\nabla_x c_1+\nabla_y c_2\right)=0, \qquad \text{on } \Gamma \tag{6.67b}$$

and for species C we have:

$$\begin{aligned}&\frac{\partial c_0}{\partial t} - \nabla_x \cdot \mathbf{D}\left(\nabla_x c_0 + \nabla_y c_1\right) - \nabla_y \cdot \mathbf{D}\left(\nabla_x c_1 + \nabla_y c_2\right)\\ &+\varepsilon^{1-\alpha}\left[\frac{\partial c_1}{\partial \tau_a} + \varepsilon^{\alpha+\beta}\frac{\partial c_1}{\partial \tau_r'} + \nabla_x \cdot \left(c_1\mathbf{v_0} + c_0\mathbf{v_1}\right) + \nabla_y \cdot \left(c_1\mathbf{v_1} + c_0\mathbf{v_2} + c_2\mathbf{v_0}\right)\right]\\ &+\varepsilon^{2+\gamma}\left[\frac{\partial c_2}{\partial \tau_r''} - c_{0,A}c_{2,B} - c_{0,B}c_{2,A} - c_{1,A}c_{1,B}\right] + \varepsilon^{2+\delta}\left[\frac{\partial c_2}{\partial \tau_r'''} + c_{2,C}\right] = 0\end{aligned} \tag{6.68a}$$

$$-\mathbf{n}\cdot\mathbf{D}\left(\nabla_x c_1 + \nabla_y c_2\right) = a\varepsilon^{\beta}c_0^{a-1}c_1, \qquad \text{on } \Gamma \tag{6.68b}$$

Then integrating over $\mathcal{B}$, using the boundary conditions 6.67b and 6.68b, the no-slip boundary condition on Γ, the trivial integration of equations 6.53 and 6.54 over $\mathcal{B}$ and the following relation:

$$\begin{aligned}\frac{\partial \langle c\rangle_{\mathcal{B}}}{\partial t} &= \frac{\partial \langle c_0\rangle_{\mathcal{B}}}{\partial t} + \varepsilon^{\beta}\frac{\partial \langle c_0\rangle_{\mathcal{B}}}{\partial \tau_r'} + \varepsilon^{-\alpha}\frac{\partial \langle c_0\rangle_{\mathcal{B}}}{\partial \tau_a} + \varepsilon^{\gamma}\frac{\partial \langle c_0\rangle_{\mathcal{B}}}{\partial \tau_r''} + \varepsilon^{\delta}\frac{\partial \langle c_0\rangle_{\mathcal{B}}}{\partial \tau_r'''}\\ &+\varepsilon\left\{\frac{\partial \langle c_1\rangle_{\mathcal{B}}}{\partial t} + \varepsilon^{\beta}\frac{\partial \langle c_1\rangle_{\mathcal{B}}}{\partial \tau_r'} + \varepsilon^{-\alpha}\frac{\partial \langle c_1\rangle_{\mathcal{B}}}{\partial \tau_a} + \varepsilon^{\gamma}\frac{\partial \langle c_1\rangle_{\mathcal{B}}}{\partial \tau_r''} + \varepsilon^{\delta}\frac{\partial \langle c_1\rangle_{\mathcal{B}}}{\partial \tau_r'''}\right\}\\ &+\varepsilon^2\left\{\frac{\partial \langle c_2\rangle_{\mathcal{B}}}{\partial t} + \varepsilon^{\beta}\frac{\partial \langle c_2\rangle_{\mathcal{B}}}{\partial \tau_r'} + \varepsilon^{-\alpha}\frac{\partial \langle c_2\rangle_{\mathcal{B}}}{\partial \tau_a} + \varepsilon^{\gamma}\frac{\partial \langle c_2\rangle_{\mathcal{B}}}{\partial \tau_r''} + \varepsilon^{\delta}\frac{\partial \langle c_2\rangle_{\mathcal{B}}}{\partial \tau_r'''}\right\} + \mathcal{O}\left\{\varepsilon^3\right\}\end{aligned} \tag{6.69}$$

we obtain for species A and B:

$$\begin{aligned}&\frac{\partial \langle c_0\rangle_{\mathcal{B}}}{\partial t} + \varepsilon^{1-\alpha}\frac{\partial \langle c_1\rangle_{\mathcal{B}}}{\partial \tau_a} + \varepsilon^{1+\beta}\frac{\partial \langle c_1\rangle_{\mathcal{B}}}{\partial \tau_r'} + \varepsilon^{2+\gamma}\frac{\partial \langle c_2\rangle_{\mathcal{B}}}{\partial \tau_r''} + \varepsilon^{2+\delta}\frac{\partial \langle c_2\rangle_{\mathcal{B}}}{\partial \tau_r'''} =\\ &\nabla_x \cdot \left[\phi^{-1}\mathbf{D}^*\nabla_x c_0\right] - \phi^{-1}\varepsilon^{1-\alpha}\nabla_x \cdot \left(c_0\left\langle \mathbf{v_1}\right\rangle + \bar{c_1}\left\langle \mathbf{v_0}\right\rangle\right)\\ &-\varepsilon^{2+\gamma}\left(c_{0,A}\left\langle c_{2,B}\right\rangle_{\mathcal{B}} + c_{0,B}\left\langle c_{2,A}\right\rangle_{\mathcal{B}} + \left\langle c_{1,A}c_{1,B}\right\rangle_{\mathcal{B}}\right) + \varepsilon^{2+\delta}\left\langle c_{2,C}\right\rangle_{\mathcal{B}}\end{aligned} \tag{6.70}$$

where $\mathbf{D}^* = \langle \mathbf{D}\left(\mathbf{I} + \nabla_y \boldsymbol{\chi}\right)\rangle + \varepsilon^{1-\alpha}\langle \boldsymbol{\chi}\mathbf{k}\rangle \nabla_x p_0$. The sum of Eq. 6.70 and Eq. 6.59 multiplied by ε^{-1}, and also considering the integrated equation of order $\mathcal{O}(\varepsilon^{-2})$, gives:

$$\begin{aligned}&\frac{\partial \langle c\rangle_{\mathcal{B}}}{\partial t} - \left[-\varepsilon^{-\gamma}c_{0,A}c_{0,B} + \varepsilon^{\delta}c_{0,C}\right] = \nabla_x \cdot \left[\phi^{-1}\mathbf{D}^*\nabla_x c_0\right] - \phi^{-1}\varepsilon^{1-\alpha}\nabla_x \cdot \left(c_0\left\langle \mathbf{v_1}\right\rangle\right.\\ &\left.-\bar{c_1}\left\langle \mathbf{v_0}\right\rangle\right) - \varepsilon^{2+\gamma}\left(c_{0,A}\left\langle c_{2,B}\right\rangle_{\mathcal{B}} + c_{0,B}\left\langle c_{2,A}\right\rangle_{\mathcal{B}} + \left\langle c_{1,A}c_{1,B}\right\rangle_{\mathcal{B}}\right) + \varepsilon^{2+\delta}\left\langle c_{2,C}\right\rangle_{\mathcal{B}}\\ &-\varepsilon^{-\alpha}\nabla_x \cdot \left(c_0\left\langle \mathbf{v_0}\right\rangle_{\mathcal{B}}\right) - \varepsilon^{1+\gamma}\left(c_{0,A}\left\langle c_{1,B}\right\rangle_{\mathcal{B}} + c_{0,B}\left\langle c_{1,A}\right\rangle_{\mathcal{B}}\right) - \varepsilon^{1+\delta}\left\langle c_{1,c}\right\rangle_{\mathcal{B}}\end{aligned} \tag{6.71}$$

Then using $c_0 = \langle c_0\rangle_{\mathcal{B}}$, $\hat{c_1} = \langle c_1\rangle_{\mathcal{B}}$, $\langle c\rangle_{\mathcal{B}}\langle \mathbf{v}\rangle = \langle c_0\rangle\langle \mathbf{v_0}\rangle_{\mathcal{B}} + \varepsilon c_0\langle \mathbf{v_1}\rangle_{\mathcal{B}} + \varepsilon\bar{c_1}\langle \mathbf{v_0}\rangle + \mathcal{O}(\varepsilon^2)$, $\varepsilon\langle c\rangle_{\mathcal{B}} = \varepsilon\langle c_0\rangle_{\mathcal{B}} + \mathcal{O}(\varepsilon^2)$ and considering that:

$$\begin{aligned}\langle c_A c_B\rangle_{\mathcal{B}} = \;& c_{0,A}c_{0,B} + \varepsilon\left(c_{0,A}\langle c_{1,B}\rangle + c_{0,B}\langle c_{1,A}\rangle\right) + \varepsilon^2\left(c_{0,A}\langle c_{2,B}\rangle + c_{0,B}\langle c_{2,A}\rangle +\right.\\ &\left.\langle c_{1,A}c_{1,B}\rangle\right) + \mathcal{O}(\varepsilon^3)\end{aligned} \tag{6.72}$$

is equal to $\langle c_A\rangle_{\mathcal{B}} \langle c_B\rangle_{\mathcal{B}}$ up to order ε^1 terms, we obtain for species A and B:

$$\frac{\partial \langle c\rangle_{\mathcal{B}}}{\partial t} = \nabla_x \cdot \left(\phi^{-1}\mathbf{D}^*\nabla_x c_0\right) - \phi^{-1}\mathrm{Pe}\nabla_x \cdot \left(\langle c\rangle_{\mathcal{B}} \langle \mathbf{v}\rangle\right) - \mathrm{Da}'' \langle c_A\rangle_{\mathcal{B}} \langle c_B\rangle_{\mathcal{B}} + \mathrm{Da}''' \langle c_C\rangle \tag{6.73}$$

Similarly for C, further assuming that $\langle \boldsymbol{\chi}\rangle_{\Gamma} = \langle \boldsymbol{\chi}\rangle_{\mathcal{B}}$ so that $\langle c_1\rangle_{\Gamma} = \langle c_1\rangle_{\mathcal{B}}$ we have:

$$\begin{aligned}\frac{\partial \langle c\rangle_{\mathcal{B}}}{\partial t} &= \nabla_x \cdot \left(\phi^{-1}\mathbf{D}^*\nabla_x c_0\right) - \phi^{-1}\mathrm{Pe}\nabla_x \cdot \left(\langle c\rangle_{\mathcal{B}} \langle \mathbf{v}\rangle\right) - \mathrm{Da}'' \langle c_A\rangle_{\mathcal{B}} \langle c_B\rangle_{\mathcal{B}} + \mathrm{Da}''' \langle c_C\rangle \\ &\quad - \varepsilon^{-1}\mathrm{Da}' K^*(\langle c\rangle_{\mathcal{B}}^a - \bar{c}^a)\end{aligned} \tag{6.74}$$

Summarizing for Equations 6.73 and 6.74 provide a macroscale description of transport coherent with the microscale up to order ε^2 if the following conditions are respected:

I. $\varepsilon << 1$;

II. $\alpha < 2$, that is $\mathrm{Pe} < \varepsilon^{-2}$;

III. $\beta > 0$, that is $\mathrm{Da}' < 1$;

IV. $\alpha + \beta < 1$, that is $\mathrm{Da}/\mathrm{Pe} < \varepsilon$;

V. $\langle \boldsymbol{\chi}\rangle_{\Gamma} = \langle \boldsymbol{\chi}\rangle_{\mathcal{B}}$;

VI. $\gamma, \delta > -2$, that is $\mathrm{Da}'', \mathrm{Da}''' < \varepsilon^{-2}$;

VII. $\alpha + \gamma > -1$ and $\alpha + \delta > -1$, that is $\mathrm{Da}''/\mathrm{Pe} < \varepsilon^{-1}$ and $\mathrm{Da}'''/\mathrm{Pe} < \varepsilon^{-1}$.

6.8 Appendix B: Effective parameters for the test case

In this appendix we find an expression for the effective parameters K^* and D^* for the simple geometrical setting which constitutes our test case. The results are coherent with the result by Mikelic, Devigne, and Van Dujin, 2006, who developed a rigorous upscaled Advection-Diffusion-Reaction Equation for the same flow field under conditions of dominant Peclet and Damköhler number in case of a first order reaction at the pore walls.

K^* is introduced because, by using the divergence theorem, we are shifting from a volume integral to a surface integral. This is not necessary in our simple onedimensional case, thus $K^* = 1$. K^* emerges from the simplification of the following term

$$\frac{1}{2\varepsilon}\int_{-\varepsilon}^{\varepsilon} -\partial_y D\left(\partial_x c_0 + \partial_y c_1\right) dy \tag{6.75}$$

by taking advantage of the boundary condition $-D\left(\partial_x c_0 + \partial_y c_1\right) = \varepsilon^{\beta}\left(c_0 - \bar{c}\right)$. Eq. 6.75 is is the one-dimensional version of the term $\nabla_y \mathbf{D}(\nabla_y c_1 + \nabla_x c_0)$ in Eq. 6.56 after applying the divergence theorem. The general form of the term is $-\varepsilon^{\beta} K^*\left(c_0 - \bar{c}\right)$, whereas in our case it simplifies to $-\varepsilon^{\beta}\left(c_0 - \bar{c}\right)$, thus $K^* = 1$.

As regards D^*, we need to solve the decoupled boundary value problem, which, fulfilled the constraints on the transport parameters, reads:

$$-\nabla_y \cdot \mathbf{D}\left(\nabla_y c_1 + \nabla_x c_0\right) + \varepsilon^{1-\alpha}\left[\left(\mathbf{v_0} - \langle \mathbf{v_0} \rangle_{\mathcal{B}}\right) \cdot \nabla_x c_0 + \mathbf{v_0} \cdot \nabla_y c_1\right] = 0 \qquad \text{in } \mathcal{B} \quad (6.76)$$

$$-\mathbf{n} \cdot \mathbf{D}\left(\nabla_x c_0 + \nabla_y c_1\right) = 0 \qquad \textit{on } \Gamma \quad (6.77)$$

Considering the particular geometry of the problem, the form of the solution $c_1(x, y) = \chi(y)\partial_x c_0 + \bar{c_1}(x)$ and an isotropic molecular diffusion tensor $\mathbf{D} = D\mathbf{I}$ the BVP reads:

$$-D\frac{\partial^2 \chi}{\partial y^2} + \varepsilon^{1-\alpha}\left[\frac{3}{2}\left(1 - \frac{y^2}{\varepsilon^2}\right) - 1\right] = 0 \quad (6.78)$$

$$\frac{\partial \chi\left(\pm\varepsilon\right)}{\partial y} = 0 \quad (6.79)$$

The problem has an analytical solution:

$$\chi = \frac{\varepsilon^{1-\alpha}}{D}\left(\frac{1}{4}y^2 - \frac{1}{8}\frac{y^4}{\varepsilon^2}\right) - \frac{7}{120}\frac{\varepsilon^{1-\alpha}}{D}\varepsilon^2 \quad (6.80)$$

The constant value which is required for the complete χ formulation is obtained by imposing $\langle \chi \rangle = 0$, that is $\frac{1}{2\varepsilon}\int_{\varepsilon}^{\varepsilon} \chi(y)dy = 0$.
Coherently with the symmetry of the unit cell geometry, also χ is symmetric.

D^* depends on χ through the following definition:

$$\mathbf{D}{*} = \langle \mathbf{D}\left(\mathbf{I} + \nabla_y \boldsymbol{\chi}\right) \rangle + \varepsilon^{1-\alpha}\langle \boldsymbol{\chi}\boldsymbol{k} \rangle \nabla_x p_0 \quad (6.81)$$

In our geometry the longitudinal effective dispersion coefficient $D*$ reads:

$$D{*} = \left\langle D\left(1 + \frac{\partial \chi}{\partial x}\right)\right\rangle + \varepsilon^{1-\alpha}\left\langle \chi\frac{1}{\varepsilon^2}k \right\rangle \frac{\partial p}{\partial x} \quad (6.82)$$

Since $k = \frac{1}{2}\left(1 - \frac{y^2}{\varepsilon^2}\right)$ and $\frac{\partial p}{\partial x} = -3$ (see section above) we have:

$$D{*} = D + \frac{2}{105}\frac{\left(\varepsilon^{1-\alpha}\right)^2}{D} \quad (6.83)$$

The effective dispersion parameter is larger than the molecular diffusion coefficient, thus taking into account the effect of the velocity fluctuations. Besides D^*, Mikelic, Devigne, and Van Dujin, 2006, also found effective reaction and velocity coefficients which correct the upscaled form of the transport equations in this simplified setting.

Chapter 7

Conclusions and Future Work

In the present thesis we addressed a few issues related to the quantification of dilution in heterogeneous formations, and its effect on mixing-controlled processes. The topic is relevant for manifold reasons. First, the knowledge of the physical and chemical processes which lead to dilution is still lacking, with significant negative impacts on both contamination assessment and remediation intervention planning. Second, it should be considered for determining the potential of an aquifer in terms of remediation capabilities related to natural attenuation and biodegradation processes. As a consequence, also risk assessment is decisively influenced by dilution and mixing. Because of the inaccessibility of the setting where transport processes take place, uncertainty plagues any attempt to quantify dilution and reactions. In particular, hydrogeological uncertainty is epistemic, thus there is a conceptual dualism between the stochastic tools typically used for dealing with uncertainty, and the intrinsic determinism of the geological formations. We focused here on synthetic realizations of formations' hydraulic properties. Working on single-realization stands aside from the usual academic practice, which is generally based on Monte Carlo series of realizations, or equivalent ensemble analysis. Unfortunately, Monte Carlo procedures are compatible with the stochastic investigation of the actual groundwater processes, but often fail in reproducing important local features, leading to the inaccurate representation of the reality. On the other hand, also single realization modeling does not reproduce what indeed occurs in the real aquifer, but it is more likely that single-realization scenarios would share with actual plumes similar aggregated statistics.

First we implemented a few Lagrangian numerical tools for the solution of the transport equation at the Darcy scale, and compared them to more popular numerical schemes. We considered advection-dominated instantaneous injection scenarios in porous formations with heterogeneity spanning from weak ($\sigma_Y^2 = 0.2$) to high ($\sigma_Y^2 = 10$). Such a set of conditions poses several numerical challenges to numerical schemes, mainly related to the accurate reproduction of the highly irregular and mobile plume's fringes, characterized by strong concentration gradients. Besides, these regions represent the areas where mixing-controlled reactions focus because of the favored mixing between waters with different chemical composition. Our numerical tests provided a set of guidelines for the well-informed choice of the numerical scheme according to the objectives of the investigation and to the heterogeneity level, highlighting the drawbacks of the numerical schemes on both the evaluation of dilution and of the overall effect of reactions. We also proposed a modification to the hybrid Streamline-Based method introduced by Herrera, Valocchi, and Beckie, 2010 in order to make it more suitable to the comparison in terms of global quantities with the other numerical methods. This new SB based model could be useful for implementing relatively fast three-dimensional fate and transport scenarios with a rather regular flow field. SPH resulted to be the most reliable method for the simulation of mixing-related problems, despite its computational burden and its being limited to isotropic dispersion tensors.

Such a code was used to test new semianalytical formulations to a-priori estimate plume-scale global moments. Our numerical validation was performed in a two-dimensional setup, although a 3D testing is desirable. The use of our SPH code on three dimensional formations is straightforward but unfortunately numerically cumbersome, requiring to resort to supercomputer facilities. However, the comparison between the semianalytical moments and the correspondent empirical quantities referred to single-realization synthetic scenarios is very good, at least for the tested model of log-conductivity covariance (exponential), and represents a significant step forward with respect to classic stochastic theories at the global scale. Semianalytical relations are limited to weak and intermediate heterogeneity conditions. These semianalytical formulations have the further advantage to be simple and to require a limited, yet relevant, amount of information about the geological properties of the medium, the geometry of the aquifer and the reactive system. Nevertheless coherently derived estimates of peak concentration values do not perform equally well. This is expected, since maximum concentration depends on the interplay of several mechanisms with a highly local connotation, whereas the other global statistics have a lumped, aggregated nature which make them more suitable to a-priori estimation. Therefore a different statistical apparatus is required to hope to predict also the peak values of concentration, at least in simplified conditions such as in case of very large or very small source areas. We promoted here the use of plume-scale global moments (mean and variance) and Cumulative Frequency Distributions of concentration, which are undoubtedly representative of the dilution processes for conservative tracer plumes. The global mean concentration represents the average mean concentration considering the whole plume volume, which is defined as the region where local concentration is larger than a small threshold value, for example the detection limit of the method used to determine concentration. Once we set a sufficiently low concentration threshold, such that most of the total injected mass is included in the plume volume, also the plume volume can be quantified. The variance provides higher order statistical information about the actual distribution of concentration within the plume, allowing to distinguish between rather homogenized plumes or strongly disordered concentration distributions which are typical of highly heterogeneous formations. The CFDs reinforce this information, modeling the concentration distribution over the whole admissible concentration range. The time variation of these global statistics offers a dynamic, though aggregated, a-priori description of the evolution of a solute body which develops from the instantaneous injection of a contaminant over a source volume V_0.

Statistical information, at the global scale but also at the local scale, can be transferred from nonreactive tracers to reactive aqueous species reacting upon mixing in a reactive system characterized by fast kinetics. In this cases we can take advantage of speciation relations between reference conservative components (or tenads) and actual reactive species concentrations to provide analytical formulations for the moments and the probability distributions of concentrations. We obtained such relations for the bimolecular homogeneous reaction case, illustrating also the difference between local statistics, referred to a single point in the space, and global statistics; in particular we highlighted the conceptual difference in the handling of uncertainty and in the physical meaning of the statistical quantities. Along these lines we could also attempt to improve the distinction between mixing and spreading at specific locations. Local statistics have been in fact derived here according to the classic formulations proposed by Fiori, 2001a, which belong to the Lagrangian framework (as they are based on particle displacement statistics), but still have an Eulerian connotation (since they provide estimates and probability distributions referring to deterministic spatial points). By moving to a fully Lagrangian framework we could aim at distinguishing between the mixing contribution to the local evolution of concentration and the spreading, uncertainty-related, contribution. The former could be assessed relying on relative solute mass particle displacements in a mobile reference system moving with the actual, although unknown, centroid of the solute body (Fiori, 2001a); the latter could be quantified by dealing with geological uncertainty separately, thus estimating the potential role of spreading.

Extending the previous considerations to high heterogeneity implies resorting to numerical simulations. Furthermore, a whole set of conditions, i.e. the source size, the dispersion model, the reaction kinetics, and the injection mode, requires numerical investigation as well, because they cannot be included straightforwardly into analytical or semianalytical procedures. Our systematic phenomenological analysis shed some light on the actual physical and chemical mechanisms which occur in groundwater environments, and in particular on their interplay with heterogeneity features. The results of our numerical simulations could be compared with simplified formulas, aiming at predicting actual transport processes also in non-ideal conditions.

Describing transport at the continuum scale implies accepting that at the reference scale (REV) well-mixed conditions are fulfilled. In general, this entails verifying that the action of diffusion within the pore is fast enough to cancel the inhomogeneities created by the local velocity field, or by the interference of reactive processes. We quantified sufficient conditions for this upscaling in terms of a set of dimensionless numbers for an articulate reactive system. This set of conditions represents a step forward for the rationalized implementation of hybrid models (e.g. Tartakovsky and Winter, 2008), distinguishing the regions where pore-scale resolution is required and where we can rely on larger scale refinement. A suitable numerical instrument for the implementation of hybrid models is represented by the SPH algorithm, which can handle multi-resolution by its very nature. Moreover, such a numerical tool could also give the possibility to simulate time-variable pore geometries due to precipitation or dissolution of solid matter, or for example include also the concentration effect on fluid density, thereby allowing to analyze its effect on fate and transport of solute concentration.

Overall, the path to the complete understanding and consequently the development of reliable predictive tools for estimating accidental contamination events in groundwater is still long. Our numerical instruments represent a valid toolbox for investigating a whole set of physical and chemical processes which is not always treated correctly in the literature and in practice, with misleading conclusions due to numerical errors. We believe that considerable effort should be devoted to bridge the gap between the academic world and the applications, because sophisticated statistical theories are often disregarded by practitioners, who need reliable and easy-to-use instruments to support them in the decision-making process.

Bibliography

Ahmadi, A., A. Aigueperse, and M. Quintard [2001], “Upscaling of nonwetting phase residual transport in porous media: A network approach”, *Transport in porous media*, 43, 2, pp. 309–353. (Cited on p. 126.)

Andricevic, R., V. Srzic, and H. Gotovac [2012], “Risk characterization for toxic chemicals transported in aquifers”, *Advances in Water Resources*, 36, pp. 86–97. (Cited on p. 84.)

Aris, R. [1956], “On the dispersion of a solute in a fluid flowing through a tube”, *Proceedings of the Royal Society A, London*, 235, pp. 67–77. (Cited on pp. 3, 35.)

Attinger, S. *et al.* [1999], “Temporal behavior of a solute cloud in a chemically heterogeneous porous medium”, *Journal of Fluid Mechanics*, 386, pp. 77–104. (Cited on pp. 35, 43.)

Auriault, J.L. and P.M. Adler [1995], “Taylor dispersion in porous media: Analysis by multiple scale expansions”, *Advances in Water Resources*, 18, 4, pp. 217–226. (Cited on pp. 122, 123, 127, 128, 133, 143, 147.)

Battiato, I. and D.M. Tartakovsky [2011], “Applicability regimes for macroscopic models of reactive transport in porous media”, *Journal of Contaminant Hydrology*, 120-121, pp. 18–26. (Cited on pp. 4, 122, 123, 129.)

Battiato, I. *et al.* [2009], “On breakdown of macroscopic models of mixing-controlled heterogeneous reactions in porous media”, *Advances in Water Resources*, 32, pp. 1664–1673. (Cited on pp. 3, 4, 122, 123, 129, 143.)

Battiato, I. *et al.* [2011], “Hybrid Simulations of Reactive Transport in Fractures”, *Advances in Water Resources*, 34, 9, pp. 1140–1150. (Cited on p. 3.)

Bear, J. [1972], *Dynamics of Fluids in Porous Materials*, American Elsevier. (Cited on pp. 2–4, 13, 14, 19, 22, 94.)

— [1979], *Hydraulics of Groundwater*, McGraw Hill. (Cited on p. 13.)

Bear, J. and Y. Bachmat [1990], *Introduction to modeling of transport phenomena in porous media*, Springer. (Cited on p. 2.)

Bellin, A. and Y. Rubin [1996], “HYDRO _GEN: A spatially distributed random field generator for correlated properties”, *Stochastic Hydrology and Hydraulics*, 10, 4, pp. 2913–2924. (Cited on pp. 21, 46, 93.)

Bellin, A., Y. Rubin, and A. Rinaldo [1994], “Eulerian-Lagrangian approach for modeling of flow and transport in heterogeneous geological formations”, *Water Resources Research*, 30, 11, pp. 2913–2924. (Cited on pp. 30, 41.)

Bellin, A., G. Severino, and A. Fiori [2011], “On the local concentration probability density function of solutes reacting upon mixing”, *Water Resources Research*, 47, W01514. (Cited on pp. 5, 68, 71, 74, 76, 89, 107.)

Bellin, A. and D. Tonina [2007], “Probability density function of non-reactive solute concentration in heterogeneous porous formations”, *Journal of Contaminant Hydrology*, 94, 1–2, pp. 109–125. (Cited on pp. 36, 41, 50, 68, 70, 105, 106.)

Benson, D.A., S.W. Wheatcraft, and M.M. Meerschaert [2000], “The fractional-order governing equation of Levy motion”, *Water Resources Research*, 36, 6, pp. 1413–1423. (Cited on pp. 4, 6.)

Bensoussan, A., J.L. Lions, and G. Papanicolaou [1978], *Asymptotic analysis for periodic structures*, North-Holland, Amsterdam. (Cited on p. 122.)

Berkowitz, B. and H. Scher [1998], “Theory of anomalous chemical transport in fracture networks”, *Physical Review E*, 57, 5, pp. 5858–5869. (Cited on pp. 4, 6.)

Berkowitz, B. *et al.* [2006], “Modeling non-Fickian transport in geological formations as a Continuous Time Random Walk”, *Review of Geophysics*, 44, RG2003, DOI: `doi:10.1029/2005RG000178`. (Cited on pp. 4, 6, 122.)

Bilger, R.W. [2004], “Some aspects of scalar dissipatio”, *Flow, Turbulence and Combustion*, 72, pp. 93–114. (Cited on p. 99.)

Binning, P.J. and M.A. Celia [2008], “Pseudo-kinetics arising from the upscaling of geochemical equilibrium”, *Water Resources Research*, 44, W07410. (Cited on pp. 3, 95, 112.)

Bolster, D. *et al.* [2011], “Mixing in confined stratified aquifers”, *Journal of Contaminant Hydrology*, 120–121, pp. 198–212. (Cited on p. 99.)

Brenner, H. [1980], “Dispersion resulting from flow through spatially periodic porous media.”, *Philosopycal transactions of the Royal Society A, London*, 297, pp. 81–133. (Cited on pp. 3, 122.)

— [1987], *Transport processes in porous media*, McGraw Hill. (Cited on p. 122.)

Brenner, H. and P. Adler [1980], “Dispersion resulting from flow through spatially periodic porous media. II. Surface and intraparticle transport”, *Proceedings of the Royal Society A, London*, 307, pp. 149–200. (Cited on p. 3.)

Brookshaw, L. [1985], “A method of calculating radiative heat diffusion in particle simulations”, *Proceedings of the Astronomical Society of Australia*, 6, 2, pp. 207–210. (Cited on p. 18.)

Cabezon, R.M., D. Garcia-Senz, and A. Relano [2008], “A one-parameter family of interpolation kernels for SPH studies”, *Journal of Computational Physics*, 227, pp. 8523–8540. (Cited on p. 23.)

Cainelli, O., A. Bellin, and M. Putti [2011], “On the accuracy of finite element schemes for computing the flow field in heterogeneous formations”, *Advances in Water Resources*, 0, pp. 0–0. (Cited on p. 22.)

Cao, J. and P.K. Kitanidis [1998], “Pore-scale dilution of conservative solutes: An example”, *Water Resources Research*, 34, pp. 1941–1949. (Cited on pp. 2, 3.)

Caroni, E. and V. Fiorotto [2005], “Analysis of concentration as sampled in natural aquifers”, *Transport in Porous Media*, 59, 1, pp. 19–45. (Cited on pp. 41, 50, 70, 105.)

Carrera, J. *et al.* [1998], “On matrix diffusion: Formulations, solution methods and qualitative effects”, *Hydrogeology Journal*, 6, 1, pp. 178–190. (Cited on pp. 4, 6.)

Chen, Z.M., W.B. Deng, and Y.H. Ye [2005], “A new upscaling method for the solute transport equations”, *Discrete and continuous dynamical systems*, 13, 4, pp. 941–960. (Cited on p. 126.)

Chilakapati, A. and S. Yabusaki [1999], "Nonlinear reactions and nonuniform flows", *Water Resources Research*, 35, 8, pp. 2427–2438. (Cited on p. 27.)

Chiogna, G. *et al.* [2011], "Relevance of local compound-specific transverse dispersion for conservative and reactive mixing in heterogeneous porous media", *Water Resources Research*, 47, W07540. (Cited on p. 94.)

Cirpka, O.A. [2002], "Choice of dispersion coefficients in reactive transport calculations on smoothed fields", *Journal of Contaminant Hydrology*, 58, pp. 261–282. (Cited on pp. 35, 43.)

— [2010], "Simplified simulation of steady state bioreactive transport with kinetic solute uptake by the biomass", *Water Resources Research*, 46, W07534. (Cited on pp. 6, 68.)

Cirpka, O.A., R. Helmig, and E.O. Frind [1999], "Numerical methods for reactive transport on rectangular and streamline-oriented grids", *Advances Water Resources*, 22, 7, pp. 711–728. (Cited on p. 12.)

Cirpka, O.A. and P.K. Kitanidis [2000a], "An advective-dispersive stream tube approach for the transfer of conservative-tracer data to reactive transport", *Water Resources Research*, 36, 5, pp. 1209–1220. (Cited on p. 6.)

— [2000b], "Characterization of mixing and dilution in heterogeneous aquifers by means of local temporal moments", *Water Resources Research*, 36, 5, pp. 1221–1236. (Cited on pp. 2, 41.)

Cirpka, O.A. and A.J. Valocchi [2007], "Two-dimensional concentration distribution for mixing-controlled bioreactive transport in steady state", *Advances in Water Resources*, 30, pp. 1668–1679. (Cited on pp. 6, 67.)

Cirpka, O.A. *et al.* [2008], "Concentration statistics for mixing-controlled reactive transport in random heterogeneous media", *Journal of Contaminant Hydrology*, 98, pp. 61–74. (Cited on pp. 6, 36, 41, 50, 68, 70, 91, 105.)

Cirpka, O.A. *et al.* [2011], "Probability density function of steady state concentration in two-dimensional heterogeneous porous media", *Water Resources Research*, 47, W15523. (Cited on p. 91.)

Cleary, P.W. and J.J. Monaghan [1999], "Conduction Modelling Using Smoothed Particle Hydrodynamics", *Journal of Computational Physics*, 148, pp. 227–264. (Cited on pp. 18, 95.)

Cortis, A. *et al.* [2004], "Numerical simulation of non-Fickian transport in geological formations with multiple-scale heterogeneities", *Water Resources Research*, 40, W04209. (Cited on p. 4.)

Csanady, G.T. [1973], *Turbulent diffusion in the environment*, D. Reidel Publishing Company. (Cited on p. 1.)

Cushman, J.H., L.S. Bennethum, and B.X. Hu [2002], "A primer on upscaling tools for porous media", *Advances in Water Resources*, 25, pp. 1043–1067. (Cited on pp. 6, 122.)

Cushman, J.H. and T.R. Ginn [1993], "Nonlocal dispersion in media with continuously evolving scales of heterogeneity", *Transport in Porous Media*, 13, 1, pp. 123–138. (Cited on pp. 6, 35, 43.)

Dagan, G. [1982], "Stochastic modeling of groundwater flow by unconditional and conditional probabilities: 2. The solute transport", *Water Resources Research*, 18, 4, pp. 835–848. (Cited on p. 41.)

— [1984], “Solute transport in heterogeneous formations”, *Journal of Fluid Mechanics*, 145, pp. 151–177. (Cited on pp. 5, 35, 38, 41, 91.)

— [1988], “Time-dependent macrodispersion for solute transport in anisotropic heterogeneous aquifers”, *Water Resources Research*, 24, 9, pp. 1491–1500. (Cited on pp. 4, 130.)

— [1989], *Flow and Transport in Porous Formations*, Springer-Verlag. (Cited on pp. 5, 22, 30, 33, 38, 40, 68, 91, 92.)

— [1990], “Transport in heterogeneous porous formations: Spatial moments, Ergodicity and Effective Dispersion”, *Water Resources Research*, 26, 6, pp. 1281–1290. (Cited on pp. 35, 41.)

— [1991], “Dispersion of a passive solute in non-ergodic transport by steady velocity fields in heterogeneous formations”, *Journal of Fluid Mechanics*, 233, pp. 197–210. (Cited on p. 93.)

Dagan, G. [2003], “Flow and transport in highly heterogeneous formations: 1. Conceptual framework and validity of the first order approximation”, *Water Resources Research*, 39, 9. (Cited on p. 46.)

De Barros, F.P.J., A. Fiori, and A. Bellin [2011], “A simple closed-form solution for assessing concentration uncertainty”, *Water Resources Research*, 47, W12603. (Cited on p. 36.)

De Barros, F.P.J. and W. Nowak [2010], “On the link between contaminant source release conditions and plume prediction uncertainty”, *Journal of Contaminant Hydrology*, 116, 1–4, pp. 24–34. (Cited on p. 102.)

De Simoni, M. *et al.* [2005], “A procedure for the solution of multicomponent reactive transport problems”, *Water Resources Research*, 41, W11410. (Cited on pp. 6, 13, 14, 67–69, 94, 99, 142.)

De Simoni, M. *et al.* [2007], “A mixing ratios-based formulation for multicomponent reactive transport”, *Water Resources Research*, 43, W07419. (Cited on pp. 6, 67–69, 94, 99, 142.)

Delgado, J.P.Q.M. [2006], “A critical review of dispersion in packed beds”, *Heat and mass transfer*, 42, pp. 279–310. (Cited on pp. 4, 94.)

Demmy, G., S. Berglund, and W. Graham [1999], “Injection mode implications for solute transport media: Analysis in a stochastic Lagrangian framework”, *Water Resources Research*, 35, 7, pp. 1965–1973. (Cited on pp. 93, 94, 104.)

Denbigh, K. and K.G. Denbigh [1981], *The principles of chemical equilibrium*, Cambridge University Press. (Cited on pp. 14, 67, 69.)

Dentz, M. [2012], “Concentration statistics for transport in heterogeneous media due to stochastic fluctuations of the center of mass velocity”, *Advances in Water Resources*, 36, pp. 11–22. (Cited on pp. 41, 91.)

Dentz, M. and J. Carrera [2007], “Mixing and spreading in stratified flow”, *Physics of Fluids*, 1–17. (Cited on p. 2.)

Dentz, M., P. Gouze, and J. Carrera [2011], “Effective non-local reaction kinetics for transport in physically and chemically heterogeneous media”, *Journal of Contaminant Hydrology*, 120–121, pp. 222–236. (Cited on p. 122.)

Dentz, M. and D.M. Tartakovsky [2006], “Delay mechanisms of non-Fickian transport in heterogeneous media”, *Geophysical Research Letters*, 33, L16406. (Cited on p. 4.)

Dentz, M. *et al.* [2000], "Temporal behavior of a solute cloud in a heterogeneous porous medium 2. Point like injection", *Water Resources Research*, 36, 12, pp. 3591–3604. (Cited on pp. 35, 43.)

Dentz, M. *et al.* [2004], "Time behavior of solute transport in heterogeneous media: Transition from anomalous to normal transport", *Advances in Water Resources*, 27, 2, pp. 155–173. (Cited on p. 4.)

Dentz, M. *et al.* [2011], "Mixing, spreadig and reaction in heterogeneous media: A brief review", *Journal of Contaminant Hydrology*, 120–121, 017107. (Cited on pp. 3, 6, 99, 121.)

Duijn, C.J. van *et al.* [2007], "Effective equations for two-phase flow in porous media: the effect of trapping on the microscale", *Transport in porous media*, 69, pp. 411–428. (Cited on p. 126.)

Dumbser, M. and M. Käser [2007], "Arbitrary high order non-oscillatory Finite Volume schemes on unstructured meshes for linear hyperbolic systems", *Journal of Computational Physics*, 221, pp. 693–723. (Cited on p. 12.)

Dumbser, M. *et al.* [2007], "Quadrature-Free Non-Oscillatory Finite Volume Schemes on Unstructured Meshes for Nonlinear Hyperbolic Systems", *Journal of Computational Physics*, 226, pp. 204–243. (Cited on p. 12.)

Edwards, D.A., M. Shapiro, and H. Brenner [1993], "Dispersion and reaction in two-dimensional model porous media", *Physics of Fluids A*, 5, pp. 837–848. (Cited on pp. 4, 126.)

Ferrari, A. *et al.* [2009], "A new 3D parallel scheme for free surface flows", *Computers & Fluids*, 38, 6, pp. 1203–1217. (Cited on pp. 19, 23.)

Fiori, A. [1996], "Finite Peclet extensions of Dagan's solutions to transport in anisotropic heterogeneous formations", *Water Resources Research*, 32, 1, pp. 193–198. (Cited on pp. 36, 38, 50, 68, 105.)

— [2001a], "The Lagrangian concentration approach for determining dilution in aquifer transport: Theoretical analysis and comparison with field experiments", *Water Resources Research*, 37, 12, pp. 3105–3114. (Cited on pp. 36, 40, 41, 44, 50, 52, 79, 103, 104, 155.)

— [2001b], "The relative dispersion and mixing of passive solutes in transport in geologic media", *Transport in porous media*, 42, pp. 69–83. (Cited on p. 43.)

Fiori, A. and G. Dagan [2000], "Concentration fluctuations in aquifer transport: A rigorous first-order solution and applications", *Journal of Contaminant Hydrology*, 45, 1–2, pp. 139–163. (Cited on pp. 38, 39, 74, 105.)

Fiori, A. and I. Jankovic [2005], "Can we determine the transverse macrodispersivity by using the method of moments?", *Advances in Water Resources*, 28, pp. 589–599. (Cited on p. 43.)

Fiori, A., I. Jankovic, and G. Dagan [2011], "The impact of local diffusion upon mass arrival of a passive solute in transport through three-dimensional highly heterogeneous aquifers", *Advances in Water Resources*, 34, 1563–1573. (Cited on p. 109.)

Fiori, A. *et al.* [2010], "An indirect assessment on the impact of connectivity of conductivity classes upon longitudinal asymptotic macrodispersivity", *Water Resources Research*, 46, W08601. (Cited on p. 46.)

Fiorotto, V. and E. Caroni [2002], “Solute concentration statistics in heterogeneous aquifers for finite Peclet values”, *Transport in porous media*, 48, pp. 331–351. (Cited on pp. 36, 41, 50, 68, 70, 105.)

Frampton, A. and V. Cvetkovic [2009], “Significance of injection modes and heterogeneity on spatial and temporal dispersion of advecting particles in two-dimensional discrete fracture networks”, *Advances in Water Resources*, 32, pp. 649–658. (Cited on p. 93.)

Friedly, J.C. and J. Rubin [1992], “Solute transport with multiple equilibrium-controlled or kinetically-controlled chemical reactions”, *Water Resources Research*, 28, 6, pp. 1935–1953. (Cited on pp. 14, 67.)

Gelhar, L.W. and C.L. Axness [1983], “Three-dimensional stochastic analysis of macrodispersion in aquifers”, *Water Resources Research*, 19, 1, pp. 161–180. (Cited on pp. 6, 37, 41, 91.)

Gelhar, L.W. and M.A. Collins [1971], “General Analysis of Longitudinal Dispersion in Nonuniform Flow”, *Water Resources Research*, 7, 6, pp. 1511–1521. (Cited on p. 19.)

Gelhar, L.W., C. Welty, and K.R. Rehefeldt [1992], “A critical review of data on fieldscale dispersion in aquifers”, *Water Resources Research*, 28, 7, pp. 1955–1974. (Cited on p. 4.)

Ginn, T.R. [2001], “Stochastic-convective transport with nonlinear reactions and mixing: Finite streamtube ensemble formulation for multicomponent reaction systems with intra-streamtube dispersion”, *Journal of Contaminant Hydrology*, 47, 1, pp. 1–28. (Cited on pp. 4, 6, 122.)

Ginn, T.R., C.S. Simmons, and B. Wood [1995], “Stochastic-convective transport with nonlinear reaction: Biodegradation with microbial growth”, *Water Resources Research*, 31, pp. 2689–2700. (Cited on p. 6.)

Girimaji, S.S. [1991], “Assumed Beta pdf model for turbulent mixing: Validation and extension to multiple scalar mixing”, *Combustion Science and Technology*, 78, 1–6. (Cited on pp. 36, 41.)

Gomez-Hernandez, J.J. and R.M. Srivastava [1990], “Isim3D: An ANSI C threedimensional multiple indicator conditional simulation program”, *Computers and Geosciences*, 16, 4, pp. 395–440. (Cited on p. 21.)

Gramling, C.M., C.F. Harvey, and L.C. Meigs [2002], “Reactive transport in porous media: A comparison of model prediction with laboratory visualization”, *Environmental Science and Technology*, 36, 2, pp. 2508–2514. (Cited on p. 42.)

Guadagnini, A. *et al.* [2009], “Application of a mixing-ratios based formulation to model mixing-driven dissolution experiments”, *Advances in Water Resources*, 32, pp. 756–766. (Cited on p. 67.)

Haggerty, R. and S.M. Gorelick [1995], “Multiple-rate mass transfer for modeling diffusion and surface reactions in media with pore-scale heterogeneity”, *Water Resources Research*, 31, pp. 2383–2400. (Cited on pp. 4, 6, 122.)

Haggerty, R., S.A. McKenna, and L.C. Meigs [2000], “On the late-time behavior of tracer test breakthrough curves”, *Water Resources Research*, 36, 12, pp. 3467–3479. (Cited on pp. 4, 6, 109.)

Ham, P.A.S. *et al.* [2004], “Effects of hydrodynamic dispersion on plume lengths for instantaneous bimolecular reactions”, *Advances in Water Resources*, 27, pp. 803–813. (Cited on pp. 4, 67.)

Han, N.W., J. Bhakta, and R.G. Carbonell [1985], "Longitudinal and lateral dispersion in packed beds: Effect of colum length and particle size distribution", *AIChE Journal*, 31, pp. 277–287. (Cited on pp. 4, 130.)

Harbaugh, A.W., M.C. Banta E.R. Hill, and M.G. McDonald [2000], *MODFLOW-2000, The U.S. Geological Survey Modular Ground-Water Model - User guide to modularization concepts and the Ground-Water Flow Process: U.S. Geological Survey Open-File Report 00-92, 121 p.* (Cited on pp. 15, 21, 46, 93.)

Harten, A. *et al.* [1987], "Uniformly high order essentially non-oscillatory schemes, III", *Journal of Computational Physics*, 71, pp. 231–303. (Cited on p. 12.)

Harvey, C. and S.M. Gorelick [1995], "Temporal Moment-Generating Equations: Modeling Transport and Mass Transfer in Heterogeneous Aquifers", *Water Resources Research*, 31, 8, pp. 1895–1911. (Cited on p. 4.)

— [2000], "Rate-limited mass transfer or macrodispersion: Which dominates plume evolution at the Macrodispersion Experiment (MADE) Site?", *Water Resources Research*, 36, pp. 637–650. (Cited on p. 109.)

Heagy, W.K. and P.J. Sullivan [1996], "The expected mass fraction", *Atmospheric Environment*, 30, 1, pp. 35–47. (Cited on p. 84.)

Hellferich, F.G. and G. Klein [1970], *Multicomponent chromatography, theory of interference*, Marcel Dekker. (Cited on p. 14.)

Herrera, P.A., M. Massabó, and R.D. Beckie [2009], "A meshless method to simulate solute transport in heterogeneous porous media", *Advances Water Resources*, 32, pp. 413–429. (Cited on pp. 7, 15, 18, 22, 26, 95.)

Herrera, P.A., A.J. Valocchi, and R.D. Beckie [2010], "A multidimensional streamline-based method to simulate reactive solute transport in heterogeneous porous media", *Advances Water Resources*, 33, pp. 711–727. (Cited on pp. 7, 12, 15, 19, 22, 33, 154.)

Hornung, U. [1997], *Homogenization and porous media*, Springer, New York. (Cited on p. 8.)

Hu, B.X., J.H. Cushman, and F.W. Deng [1997], "Nonlocal reactive transport with physical, chemical, and biological heterogeneity", *Advances in Water Resources*, 20, 5–6, pp. 293–308. (Cited on p. 43.)

Hu, C. and C.W. Shu [1999], "Weighted essentially non-oscillatory schemes on triangular meshes", *Journal of Computational Physics*, 150, pp. 97–127. (Cited on p. 12.)

Hubbard, S.S. and Y. Rubin [2000], "Hydrogeological parameter estimation using geophysical data: a review of selected techniques", *Journal of Contaminant Hydrology*, 1–2, pp. 3–34. (Cited on p. 5.)

Istok, J.D. [1989], *Groundwater modeling by the Finite Element Method*, AGU Water Resources monograph, vol. 13. (Cited on pp. 95, 134.)

Jankovic, I. and A. Fiori [2010], "Analysis of the impact of injection mode in transport through strongly heterogeneous aquifers", *Advances Water Resources*, 33, pp. 1199–1205. (Cited on pp. 93, 109.)

Jankovic, I., A. Fiori, and G. Dagan [2006], "Modeling flow and transport in highly heterogeneous three-dimensional aquifers: Ergodicity, Gaussianity and anomalous behavior 1. Conceptual issues and numerical simulations", *Water Resources Research*, 42, W06D12. (Cited on p. 93.)

Jiang, G.-S. and C.W. Shu [1996], "Efficient Implementation of Weighted ENO Schemes", *Journal of Computational Physics*, 126, pp. 202–228. (Cited on p. 12.)

Jubelgas, M., V. Springel, and K. Dolag [2004], "Thermal conduction in cosmological SPH simulations", *Monthly Notices of the Royal Astronomical Society*, 351, 2, pp. 423–435, ISSN: 1365-2966, DOI: `10.1111/j.1365-2966.2004.07801.x`, `http://dx.doi.org/10.1111/j.1365-2966.2004.07801.x`. (Cited on p. 18.)

Kapoor, V. and L.W. Gelhar [1994a], "Transport in three-dimensionally heterogeneous aquifers 1. Dynamics of concentration fluctuations", *Water Resources Research*, 30, 6, pp. 1775–1788. (Cited on pp. 99, 106.)

— [1994b], "Transport in three-dimensionally heterogeneous aquifers 2. Predictions and observations of concentration fluctuations", *Water Resources Research*, 30, 6, pp. 1789–1801. (Cited on pp. 36, 99.)

Kapoor, V., L.W. Gelhar, and F. Miralles-Wilhelm [1997], "Bimolecular second-order reactions in spatially varying flows: Segregation induced scale-dependent transformation rates", *Water Resources Research*, 33, 4, pp. 527–536. (Cited on pp. 6, 42, 91, 94.)

Kapoor, V. and P.K. Kitanidis [1998], "Concentration fluctuations and dilution in aquifers", *Water Resources Research*, 34, 5, pp. 1181–1193. (Cited on pp. 29, 38, 91, 99, 104.)

Kechagia, P.E. *et al.* [2002], "On the upscaling of reaction-transport processes in porous media with fast or finite kinetics", *Chemical Engineering Science*, 57, pp. 2565–2577. (Cited on pp. 3, 4, 122.)

Kinzelbach, W. [1987], "The random walk method in pollutant transport simulation. Advances in analytical and numerical groundwater flow and quality modelling.", in *NATO ASI Series C*, ed. by E. et al. Custodio, vol. 224, pp. 227–246. (Cited on p. 17.)

Kitanidis, P.K. [1988], "Prediction by the method of moments of transport in heterogeneous formations", *Journal of Hydrology*, 102, 453. (Cited on pp. 6, 35, 42, 91.)

— [1992], "Analysis of macrodispersion through volume-averaging: Moment equations", *Stochastic Hydrology and Hydraulics*, 6, pp. 5–25. (Cited on p. 43.)

— [1994], "The concept of dilution index", *Water Resources Research*, 30, 7, pp. 2011–2026. (Cited on pp. 27, 42, 98–100, 117.)

Koch, D.L. and J.F. Brady [1987], "A non-local description of advection-diffusion with application to dispersion in porous media", *Journal of Fluid Mechanics*, 180, pp. 387–403. (Cited on pp. 4, 43, 130.)

Koochesfahani, M.M. and P.E. Dimotakis [1986], "Mixing and chemical reactions in a turbulent liquid mixing layer", *Journal of Fluid Mechanics*, 170, pp. 83–112. (Cited on p. 2.)

Kubo, R., M. Toda, and N. Hashitsume [1991], *Statistical Physics II, Non Equilibrium Statistical Mechanics*, Springer Verlag, Berlin, Heildelberg. (Cited on p. 4.)

LaBolle, E.M., G.E. Fogg, and A.F.B. Tompson [1996], "Random-walk simulation of transport in heterogeneous porous media: Local mass-conservation problem and implementation methods", *Water Resources Research*, 32, 3, pp. 583–593. (Cited on pp. 12, 17, 19, 93.)

LeBorgne, T. *et al.* [2010], "Non-Fickian mixing: Temporal evolution of the scalar dissipation rate in heterogeneous porous media", *Advances in Water Resources*, 33, pp. 1468–1475. (Cited on pp. 92, 93, 99.)

Li, L., C.A. Peters, and M.A. Celia [2006], "Upscaling geochemical reaction rates using pore-scale network modeling", *Advances in Water Resources*, 29, pp. 1351–1370. (Cited on pp. 4, 95, 141.)

Lichtner, P.C. [1993], "Scaling properties of time-space kinetic mass transport equations and the local equilibrium limit", *American Journal of Science*, 293, pp. 257–296. (Cited on p. 4.)

Lichtner, P.C. and Q. Kang [2007], "Upscaling pore-scale reactive transport equations using a multiscale continuum formulation", *Water Resources Research*, 43, W12S15. (Cited on pp. 95, 141.)

Liu, G.R. and M.B. Liu [2003], *Smoothed Particle Hydrodynamics - A Meshfree Particle Method*, World Scientific. (Cited on p. 18.)

Luo, J. and O.A. Cirpka [2008], "Traveltime-based descriptions of transport and mixing in heterogeneous domains", *Water Resources Research*, 44, W09407. (Cited on pp. 6, 109.)

— [2011], "How do well mean breakthrough curves predict mixing-controlled reactive transport?", *Water Resources Research*, 47, W02520. (Cited on p. 109.)

Luo, J. *et al.* [2008], "Effective reaction parameters for mixing controlled reactions in heterogeneous media", *Water Resources Research*, 44, W02416. (Cited on p. 6.)

MacQuarrie, K.T.B. and E.A. Sudicky [1990], "Simulation of biodegradable organic contaminants in groundwater: 2. Plume behavior in uniform and random flow fields", *Water Resources Research*, 26, 2, pp. 223–239. (Cited on pp. 6, 42.)

Meakin, P. and A.M. Tartakovsky [2009], "Modeling and simulation of pore-scale multiphase fluid flow and reactive transport in fractured and porous media", *Review of Geophysics*, 47, RG3002. (Cited on p. 121.)

Meerschaert, M.M., D.A. Benson, and B. Baumer [1999], "Multidimensional advection and fractional dispersion", *Physical Review E*, 59, 5, pp. 5026–5028. (Cited on pp. 4, 6.)

Meile, C. and K. Tuncay [2006], "Scale dependence of reaction rates in porous media", *Advances in Water Resources*, 29, pp. 62–71. (Cited on pp. 3, 4, 121, 130.)

Metzler, R. and J. Klafter [2000], "The random walk's guide to anomalous diffusion: A fractional dynamics approach", *Physical Reports*, 339, pp. 1–77. (Cited on p. 4.)

Mikelic, A., V. Devigne, and C.J. Van Dujin [2006], "Rigorous upscaling of the reactive flow through a pore, under dominant Peclet and Damkohler numbers", *Advances in Water Resources*, 38, 4, pp. 1262–1287. (Cited on pp. 122, 130, 150, 151.)

Molins, S. *et al.* [2004], "A formulation for decoupling components in reactive transport problems", *Water Resources Research*, 40, W10301. (Cited on p. 67.)

Molz, F. and M. Widdowson [1988], "Internal inconsistencies in dispersion-dominated models that incorporate chemical and microbial kinetics", *Water Resources Research*, 24, 4, pp. 615–619. (Cited on pp. 6, 42.)

Monaghan, J.J. [2005], "Smoothed Particle Hydrodynamics", *Reports on Progress in Physics*, 68, pp. 1703–1759. (Cited on pp. 12, 17, 18, 95, 133.)

Montroll, E.W. and G.H. Weiss [1965], "Random Walks on lattices, II", *Journal of Mathematical Physics*, 6, 167, DOI: `doi:10.1063/1.1704269`. (Cited on pp. 4, 6.)

Morales-Casique, E., S.P. Neuman, and A. Guadagnini [2006], "Non-local and localized analyses of non-reactive solute transport in bounded randomly heterogeneous porous media: Theoretical framework", *Advances in Water Resources*, 29, pp. 1238–1255. (Cited on p. 122.)

Moyne, C. [1997], "Two equation model for a diffusive process in porous media using volume averaging method with an unsteady closure", *Advances in Water Resources*, 20, pp. 63–76. (Cited on p. 122.)

Neuman, S.P., C. Larrabee Winter, and C.M. Newman [1987], "Stochastic theory of field-scale Fickian dispersion in anisotropic porous media", *Water Resources Research*, 23, 3, pp. 453–466. (Cited on pp. 42, 91.)

Neuman, S.P. and D.M. Tartakovsky [2009], "Perspective on theories of non-Fickian transport in heterogeneous media", *Advances in Water Resources*, 32, pp. 670–680. (Cited on pp. 6, 92, 109, 122.)

Obi, E.O. and M.J. Blunt [2004], "Streamline-based simulation of Advective-Dispersive solute transport", *Advances in Water Resources*, 27, pp. 913–924. (Cited on p. 12.)

Olsson, A. and P. Grathwohl [2007], "Transverse dispersion of non-reactive tracers in porous media: A new nonlinear relationship to predict dispersion coefficients", *Journal of Contaminant Hydrology*, 92, pp. 149–161. (Cited on pp. 4, 94.)

Ottino, J.M. [1989], *The kinematics of mixing: stretching, chaos, and transport*, Cambridge University Press. (Cited on pp. 1, 2, 6.)

Pappenberger, F. and K.J. Beven [2006], "Ignorance is bliss: Or seven reasons not to use uncertainty analysis", *Water Resources Research*, 42, W05302. (Cited on pp. 7, 36.)

Pope, S.B. [1994], "Lagrangian PDF methods for turbulent flows", *Annual Review of Fluid Mechanics*, 26, pp. 23–63. (Cited on p. 41.)

— [2000], *Turbulent flows*, Cambridge University Press. (Cited on pp. 2, 36, 41.)

Porta, G.M., M. Riva, and A. Guadagnini [2012], "Upscaling solute transport in porous media in the presence of an irreversible bimolecular reaction", *Advances in Water Resources*, 35, pp. 151–162. (Cited on pp. 4, 122, 130.)

Quarteroni, A. and A. Valli [1994], *Numerical approximation of Partial Differential Equations*, Springer-Verlag. (Cited on p. 12.)

Quintard, M. and S. Whitaker [1994], "Convection, dispersion and interfacial transport of contaminants: Homogeneous media", *Advances in Water Resources*, 17, pp. 221–239. (Cited on p. 4.)

Rajaram, H. and L.W. Gelhar [1993a], "Plume scale-dependent dispersion in heterogeneous aquifers 1. Lagrangian analysis in a stratified aquifer", *Water Resources Research*, 29, 9, pp. 3249–3260. (Cited on p. 42.)

— [1993b], "Plume scale-dependent dispersion in heterogeneous aquifers 2. Eulerian analysis and three-dimensional aquifers", *Water Resources Research*, 29, 9, pp. 3261–3276. (Cited on pp. 35, 42, 43.)

Raje, D.S. and V. Kapoor [2000], "Experimental study of bimolecular reaction kinetics in porous media", *Environmental Science and Technology*, 34, pp. 1234–1239. (Cited on p. 42.)

Rhodes, R.P. [1975], “A probability distribution function for turbulent flows”, in *Turbulent mixing in nonreactive and reactive flows*, ed. by S.N.B. Murthy, New York/London Plenum, pp. 235–241. (Cited on p. 41.)

Rubin, J. [1983], “Transport of reacting solutes in porous media: Relation between mathematical nature of problem formulation and chemical nature of reactions”, *Water Resources Research*, 19, 5, pp. 1231–1252. (Cited on pp. 14, 22, 67–69, 94, 107, 142.)

Rubin, Y. [2003], *Applied Stochastic Hydrogeology*, Oxford University Press. (Cited on pp. 22, 37, 38.)

Rubin, Y., A. Bellin, and A.E. Lawrence [2003], “On the use of block-effective macrodispersion for numerical simulations of transport in heterogeneous formations”, *Water Resources Research*, 39, 9 (1242). (Cited on p. 43.)

Rubin, Y., M.A. Cushey, and A. Bellin [1994], “Modeling of transport in groundwater for environmental risk assessment”, *Stochastic Hydrology and Hydraulics*, 8, 1, pp. 57–77. (Cited on p. 91.)

Rubin, Y., M.A. Cushey, and A. Wilson [1997], “The moments of the breakthrough curves of instantaneously and kinetically sorbing solutes in heterogeneous geologic media: Predication and parameter inference from field measurements”, *Water Resources Research*, 33, pp. 2465–2481. (Cited on p. 6.)

Rubin, Y. *et al.* [1999], “The concept of block-effective macrodispersivity and a unified approach for grid-scale and plume-scale dependent transport”, *Journal of Fluid Mechanics*, 395, pp. 161–180. (Cited on pp. 35, 43.)

Saaltink, M.W., C. Ayora, and J. Carrera [1998], “A mathematical formulation for reactive transport that eliminates mineral concentrations”, *Water Resources Research*, 34, 7, pp. 1649–1656. (Cited on p. 14.)

Salamon, P., D. Fernández-Garcia, and J. Jaime Gómez-Hernandez [2006], “A review and numerical assessment of the random walk particle tracking method”, *Journal of Contaminant Hydrology*, 87, pp. 277–305. (Cited on pp. 16, 17.)

Salandin, P. and V. Fiorotto [1998], “Solute transport in highly heterogeneous aquifers”, *Water Resources Research*, 34, 5, pp. 949–961. (Cited on p. 93.)

Salandin, P. and A. Rinaldo [1989], “The influence of the form of the log-conductivity covariance on non-Fickian dispersion in random permeability fields”, *International Journal for Numerical Methods in Engineering*, 27, 1, pp. 185–193. (Cited on p. 92.)

Sanchez-Vila, X., M. Dentz, and L.D. Donado [2007], “Transport-controlled reaction rates under local non-equilibrium conditions”, *Geophysical Research Letters*, 34 (10), L10404. (Cited on pp. 6, 67, 95.)

Sanchez-Vila, X., A. Guadagnini, and D. Férnandez Garcia [2009], “Conditional probability density functions of concentrations for mixing-controlled reactive transport in heterogeneous aquifers”, *Mathematical Geosciences*, 41, pp. 323–351. (Cited on p. 68.)

Sanchez-Vila, X. *et al.* [2010], “A solution for multicomponent reactive transport under equilibrium and kinetic reactions”, *Water Resources Research*, 46, W07539. (Cited on pp. 6, 67.)

Scheibe, T.D. *et al.* [2008], “Hybrid numerical methods for multiscale simulations of subsurface biogeochemical processes”, *Proceedings of SciDAC 2008: Journal of Physics*, 125, 012054. (Cited on p. 3.)

Scheidegger, A.E. [1957], *The physics of flow through porous media*, University of Toronto Press. (Cited on p. 19.)

Scher, H. and M. Lax [1973], "Stochastic transport in a disordered solid. I. Theory.", *Physical Review B*, 7, 1, pp. 4491–4502. (Cited on pp. 4, 6.)

Schwede, R.L. *et al.* [2008], "Impact of sampling volume on the probability density function of steady state concentration", *Water Resources Research*, 44, W12433. (Cited on pp. 36, 41, 50, 68.)

Seelros, J.O. and V. Cvektovic [1992], "Modeling solute advection coupled with sorption kinetics in heterogeneous formations", *Water Resources Research*, 28, pp. 1271–1278. (Cited on p. 109.)

Shapiro, A.M. and V.D. Cvektovic [1988], "Stochastic-analysis of solute arrival time in heterogeneous porous media", *Water Resources Research*, 24, pp. 1711–1718. (Cited on p. 6.)

— [1990], "Mass arrival of sorptive solute in heterogeneous porous media", *Water Resources Research*, 26, pp. 2057–2067. (Cited on p. 6.)

Simmons, C.S., T. Ginn, and B. Wood [1995], "Stochastic-convective transport with nonlinear reaction: Mathematical framework", *Water Resources Research*, 31, pp. 2675–2688. (Cited on pp. 6, 109.)

Steefel, C.I., D.J. DePaolo, and P.C. Lichtner [2005], "Reactive transport modeling: An essential tool and a new research approach for the Earth Sciences", *Earth and Planetary Science Letters*, 240, pp. 539–558. (Cited on pp. 3, 95, 121, 122, 141.)

Steefel, C.I. and A.C. Lasaga [1994], "A coupled model for transport of multiple chemical species and kinetic precipitation/dissolution reactions with application to reactive flow in single phase hydrothermal systems", *American Journal of Science*, 294, pp. 529–592. (Cited on p. 95.)

Tartakovsky, A.M. [2010], "Langevin model for reactive transport in porous media", *Physical Review E*, 82, 026302. (Cited on p. 3.)

Tartakovsky, A.M., D.M. Tartakovsky, and P. Meakin [2008], "Stochastic Langevin model for flow and transport in porous media", *Physical Review Letters*, 101, 044502. (Cited on pp. 3, 95.)

Tartakovsky, A.M., G.D. Tartakovsky, and T.D. Scheibe [2009], "Effects of incomplete mixing on multicomponent reactive transport", *Advances in Water Resources*, 32, pp. 1674–1679. (Cited on pp. 3, 19.)

Tartakovsky, A.M. *et al.* [2007a], "A smoothed particle hydrodynamics model for reactive transport and mineral precipitation in porous and fractured porous media", *Water Resources Research*, 43, W05437. (Cited on pp. 18, 21, 95, 133.)

Tartakovsky, A.M. *et al.* [2007b], "Simulations of reactive transport and precipitation with smoothed particle hydrodynamics", *Journal of Computational Physics*, 222, pp. 654–672. (Cited on pp. 133, 134.)

Tartakovsky, A.M. *et al.* [2008], "Hybrid simulations of Reaction-Diffusion systems in porous media", *SIAM Journal on Scientific Computing*, 30, 6, pp. 2799–2816. (Cited on pp. 3, 95, 122.)

Tartakovsky, D.M. [2007], "Probabilistic risk analysis in subsurface hydrology", *Geophysical Research Letters*, 34, L05404. (Cited on pp. 5, 7.)

Tartakovsky, D.M., P.C. Lichtner, and R.J. Pawar [2003], "PDF methods for reactive transport in porous media", in *Calibration and Reliability in Groundwater*

Modeling: A few steps closer to reality, ed. by Proceedings of ModelCARE 2002. (Cited on p. 41.)

Tartakovsky, D.M., W. Nowak, and D. Bolster [2012], "Introduction to the special issue on uncertainty quantification and risk assessment", *Advances in Water Resources*, 36, pp. 1–2. (Cited on pp. 7, 36, 41, 91.)

Tartakovsky, D.M. and C.L. Winter [2008], "Uncertain Future of Hydrogeology", *ASCE Journal of Hydrologic Engineering*, 13, 1, pp. 37–39. (Cited on pp. 36, 83, 155.)

Taylor, S.G. [1953], "Dispersion of soluble matter in solvent flowing slowly through a tube", *Proceedings of the Royal Society, London*, 219, pp. 186–203. (Cited on p. 3.)

Tonina, D. and A. Bellin [2008], "The influence of pore scale dispersion, formation heterogeneity, source size, and sampling volume on the concentration of conservative tracers", *Advances in Water Resources*, 31, 2, pp. 339–354. (Cited on pp. 16, 17, 30, 43.)

Toro, E.F. [1999], *Riemann Solvers and Numerical Methods for Fluid Dynamics - A practical introduction*, Springer-Verlag. (Cited on p. 12.)

Valocchi, A.J., R.L. Street, and P.V. Roberts [1981], "Transport of ion-exchanging solutes in groundwater. Chromatographic theory and field simulation", *Water Resources Research*, 15, 5, pp. 1517–1527. (Cited on p. 14.)

Wang, J. and P.K. Kitanidis [1999], "Analysis of macrodispersion through volume averaging: Comparison with stochastic theory", *Stochastic Environmental Research and Risk Assessment*, 13, pp. 66–84. (Cited on p. 43.)

Werth, C.J., O.A. Cirpka, and P. Grathwohl [2006], "Enhanced mixing and reaction through flow focusing in heterogeneous porous media", *Water Resources Research*, 42, W12414. (Cited on pp. 3, 4, 112.)

Whitaker, S. [1999], *The method of volume averaging*, Springer. (Cited on pp. 2, 4, 122, 126.)

Willingham, T. *et al.* [2010], "Using dispersivity values to quantify the effects of pore-scale flow focusing on enhanced reaction along a transverse mixing zone", *Advances in Water Resources*, 33, pp. 525–535. (Cited on pp. 3, 4, 112.)

Willmann, M., J. Carrera, and X. Sanchez-Vila [2008], "Transport upscaling in heterogeneous aquifers: What physical parameters control memory functions?", *Water Resources Research*, 44, W12437. (Cited on p. 4.)

Willmann, M. *et al.* [2010], "Coupling of mass transfer and reactive transport for nonlinear reactions in heterogeneous media", *Water Resources Research*, 46, W07512. (Cited on pp. 4, 6, 109, 122.)

Wood, B.D. [2007], "Inertial effects in dispersion in porous media", *Water Resources Research*, 43, 12. (Cited on p. 126.)

— [2009], "The role of scaling laws in upscaling", *Advances in Water Resources*, 32, pp. 723–736. (Cited on pp. 4, 126.)

Wood, B.D. *et al.* [2003], "Volume averaging for determining the effective dispersion tensor: Closure using periodic unit cells and comparison with ensemble averaging", *Water Resources Research*, 39, 8. (Cited on p. 126.)

Zheng, C. and P. Wang [1999], *MT3DMS, A Modular Three-Dimensional Multi-Species transport model for simulation of advection, dispersion and chemical reactions of contaminants in groundwater systems; documentation and user's* *guide. U.S. Army Engineer Research and Development Center Contract Report SERDP-99-1. U.S. Army Engineer Research and Development Center, Vicksburg, Mississippi.* (Cited on pp. 7, 12, 15.)

Zinn, B. and C.F. Harvey [2003], "When good statistical models of aquifer heterogeneity go bad: A comparison of flow, dispersion, and mass transfer in connected and multivariate Gaussian hydraulic conductivity fields", *Water Resources Research*, 39 (3), 1051. (Cited on p. 108.)